CRANFIELD UNIVERSITY

MICHAEL E. MAYO

INTERACTION OF LASER RADIATION WITH URINARY CALCULI

CRANFIELD DEFENCE AND SECURITY

PhD THESIS

CRANFIELD UNIVERSITY

CRANFIELD DEFENCE AND SECURITY

DEPARTMENT OF APPLIED SCIENCE,
SECURITY AND RESILIENCE

PhD THESIS

Academic Year 2008-2009

Michael E. Mayo

Interaction of laser radiation with urinary calculi

Supervisors: Dr S. R. Ahmad
Dr J. M. Bellerby

April 2009

ABSTRACT

Urolithias, calculus formation in the urinary system, affects 5 – 10% of the population and is a painful and recurrent medical condition. A common approach in the treatment of calculi is the use of laser radiation, a procedure known as laser lithotripsy, however, the technique has not yet been fully optimised. This research examines the experimental parameters relevant to the interactions of the variable microsecond pulsed holmium laser (λ = 2.12 μm, τ_p = 120 – 800 μs, I ~ 3 MW cm^{-2}) and the Q-switched neodymium laser (λ = 1064 nm, τ_p = 6 ns, I ~ 90 GW cm^{-2}) with calculi.

The laser-calculus interaction was investigated from two perspectives: actions that lead to calculus fragmentation through the formation of shockwave and plasma, and the prospect of material analysis of calculi by laser induced breakdown spectroscopy (LIBS) to reveal elemental composition. This work is expected to contribute to improved scientific understanding and development of laser lithotripsy.

The results support the general model of thermal and plasma processes leading to vaporization and pressure pulses. Nd:YAG laser interaction processes were found to be plasma-mediated and shockwave pressure (~ 12 MPa) dependent on plasma and strongly influenced by metal ions. Ho:YAG laser-induced shockwaves (~ 50 MPa) were found to be due to direct vaporisation of water and dependent on laser pulse duration. The characteristics of the pressure pulse waveforms were found to be different, and the efficiency and repeatability of shockwave and the nature of the dependencies for the lasers suggest different bubble dynamics.

For the Nd:YAG laser, LIBS has been demonstrated as a potential tool for in situ analysis of calculus composition and has been used for the identification of major and trace quantities of calcium, magnesium, sodium, potassium, strontium, chromium, iron, copper, lead and other elements.

ACKNOWLEDGEMENTS

Completion of the research and the writing of this thesis on a part time basis has been a real challenge. Without doubt I would not have made it to the end if it was not for the assistance and support from a number of people, and the following are those who I owe the greatest thanks to.

My Supervisor, Dr S Rafi Ahmad, for his much valued expertise and guidance, and above all friendship and encouragement, without which this work would have made no headway at all. Also to Dr John Bellerby, for his support and encouragement, particularly in the final year when giving up seemed like a real possibility.

Dr Xiao Fang for his expertise and help with the experimental work and many useful discussions in particular on laser induced plasma, and to Mr Edwin Billiet for his assistance with the laser equipment and spectroscopy instrumentation.

My former colleagues, Mr Alun Davies and Prof Malcolm Sperrin, of the Medical Physics Department at the Great Western Hospital, Swindon, who gave me the opportunity, encouragement, and support to embark on this research work. Also to the staff of the Pathology Laboratory for providing samples and the Department of Urology for further samples and the use of the holmium laser.

Dr Andy Nevill, Director of Healthcare Science and Technology at Derriford Hospital, Plymouth, who has supported my aims which has allowed me to continue with this research following my decision to relocate from Swindon to Plymouth.

An especially big thank you to my wife Nicky, and daughter Rebecca, who have supported my desire to embark on a PhD. I shall endeavour to make up for all the lost weekends and get back to completing the refurbishment of our house!

And finally, to my parents, to whom this thesis is dedicated.

CONTENTS

5.13 Variation of pressure amplitude with laser pulse frequency …….. 162
5.13.1 Nd:YAG laser ……..…..…..…

LIST OF TABLES

LIST OF FIGURES

Chapter 6

No figures

GLOSSARY

Absorption coefficient	A number (μ) with units of reciprocal distance indicating the propensity of a material to attenuate an incident intensity
Acoustic impedance	The resistance of a material to resist the passage of an acoustic wave and calculated as the product of material density and acoustic velocity
Acoustic-wave	A pressure transient that travels at the speed of sound
Apatite	A generic name for one type of material found to comprise calculi
Architecture	A descriptive term for the structural arrangement of the materials comprising urinary calculi
Brushite	One of a range of materials found in urinary calculi and is found in approximately 3%
Calculus	A generic term for any agglomeration of calcium rich deposits leading to stone-type structures
Cavitation	The appearance of bubbles in fluid or tissues as a result of the passage of a high intensity wave
COD	Calcium oxalate dihydrate
COM	Calcium oxalate monohydrate
Cystine	A type of urinary stone associated with hormonal imbalance
CW	Continuous wave
Dihydrate	One of three possible forms of oxalate, the others being the monohydrate and trihydrate
Dye laser	A laser in which a fluorescent dye is used as the resonant material. It is unique in that the dye defines the wavelength range and hence can be tuned.
Emission centre	A reference point in space taken as being the centre of the laser interaction zone: for the Ho:YAG at the tip of the optical fibre and for the Nd:YAG at the focal point of the focussing lens.
Fragmentation	The process whereby energy is given to a solid in order to reduce the size of the individual particles such that they may then be spontaneously removed
FT-IR	Fourier Transform Infra-red Spectroscopy

Gall bladder	A region of the hepatic system which concentrates bile produced by the liver. It can also form large cholesterol rich stones.
Ho:YAG laser	A type of laser in which the resonant cavity comprises a YAG crystal doped with holmium. The output wavelength is 2.12 μm (2100 nm).
Hydrophone	A device which produces a potential difference as a result of pressure being applied. There are a number of different types, but the two most important are needle hydrophones and membrane hydrophones.
Hz	Hertz - units of frequency
Irradiance	The rate of energy falling onto unit area (W m^{-2}).
LASER	An acronym for 'Light amplification by stimulated emission of radiation'. Also refers to the generic name for a device emitting a laser beam.
Lasertripter	A generic name for a laser used for lithotripsy
LISL	Laser induced shock wave lithotripsy. A technique in which a shockwave-inducing laser is used to deliver energy to the calculus such that fragmentation can occur.
Lithotripsy	A generic urological technique for the destruction and removal of calcifications, usually in the urinary system, but also in the gall bladder.
MAPH	Magnesium ammonium phosphate dihydrate, an infection stone also known as struvite (the mineral name)
mJ	10^{-3} Joule – common units of laser pulse energy
Monohydrate	A form of oxalate which is frequently found as a component of calculi and is often found in incidence with its dihydrate form
MPa	10^{6} Pascals - units of pressure
n (nano)	10^{-9}
Nd:YAG	Neodymium yttrium aluminium garnet laser. A type of laser in which the resonant cavity comprisies a YAG crystal doped with neodymium. The output wavelength is 1064 nm.
Oxalate	A common constituent of urinary calculi
Photomechanical	An interaction process involving the conversion of optical energy into mechanical energy such as pressure pulses (shockwaves and acoustic waves)

Photon	A quantised ‘packet’ of energy with a value proportional to the frequency of the electromagnetic wave
Photothermal	An interaction process involving the conversion of optical energy into thermal energy
Plasma	A state of matter comprising free electrons and ions at high temperature
Pulse duration	The time the pulse is ‘on’, usually expressed as the full width half maximum of the pulse profile
PVdF	A plastic material displays piezo-electric properties and is well suited to the measurement of underwater pressures
Q-switch	A component in the laser cavity which permits short pulse durations e.g. nanosecond pulses
Shock-wave	A wave that travels faster than the speed of sound having sufficient amplitude for different sections of the wave to travel at different velocities. The effect is for the wave to distort until there is a very rapid transition from the negative to positive pressure. The shock wave evolves by the creation of harmonics which decay preferentially thus reducing the shock-wave amplitude.
Stones	The generic term for in-vivo calcifications
Struvite	One of the common constituents of urinary calculi often associated with bacterial infection
Ureter	The connecting duct between the bladder and kidney and in which urinary calculi are frequently found
Urethra	The duct which enables voiding of urine from the bladder to the air
Uric acid	A common constituent of urinary calculi formed from the crystallisation of salts from the urine
Urolith	The generic term for stones found in the urinary system
Urolithias	The generic term for stone disease in the urinary system
Urologist	A medical specialist in techniques associated with the urinary system
Weddelite	The mineral name for calcium oxalate dihydrate
Whewelitte	The mineral name for calcium oxalate monoydrate
μ (micro)	10^{-6}

Chapter 1
Introduction

On July 7th 1960 Theodore Maiman unveiled the world's first working laser device (Maiman, 1960), as shown in Figure 1.1. Generating light more than a billion times brighter than the sun, the laser (the name LASER is an acronym for Light Amplification by Stimulated Emission of Radiation, the physical process by which the high intensity light is created) caused much excitement. However, no one was quite sure of what use it had, indeed, it was popularly referred to as 'a tool looking for applications' (Radziemski, 2002). Applications it did have, and the speed and scope of such applications within a few decades have surpassed that of any other technological breakthroughs so far. One such area was the medical speciality of urology, and within a few years of the development of the laser, studies into its ability to fragment urinary calculi had been reported. By the mid 1980's the use of the laser to carry out clinical procedures in the treatment of stone disease had become established, and the era of laser lithotripsy had begun (Gross et al, 2007).

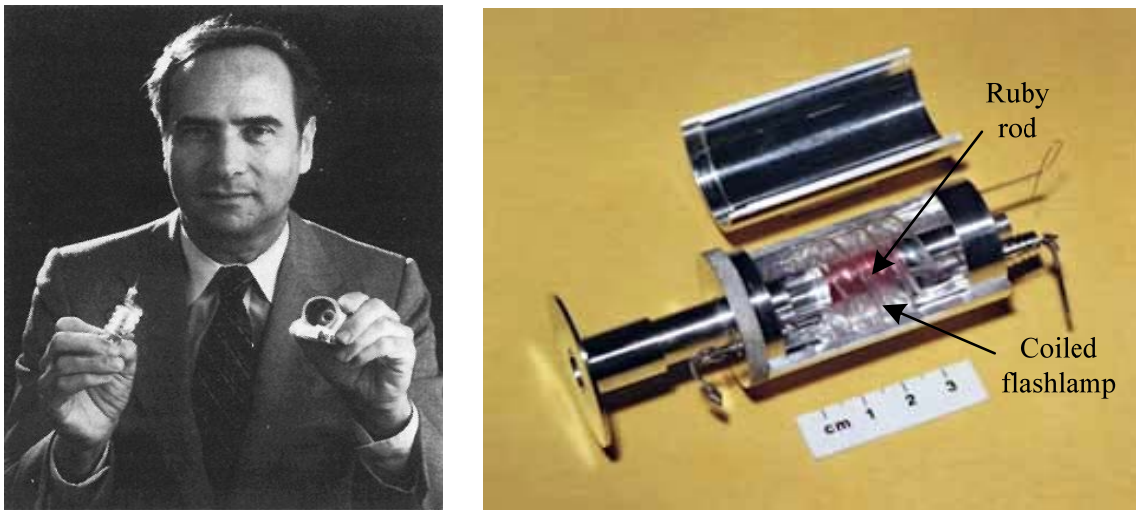

Figure 1.1: (Left) Physicist Dr. Theodore Maiman holds the original first laser which he devised, demonstrated, and patented in 1960. (Right) The laser consisted of a ruby rod inside a reflective cavity containing a flashlamp. (Images taken with permission; Left: University of Alaska website, 05.02.09; Right: IEEE website, 05.02.09)

1.1 Overview of developments in laser applications in medicine

While laser technology was still in its infancy, lasers found applications as a tool for medical procedures as well as many other diverse fields. Within a decade the use of lasers had become standard for a range of eye treatments and dermatological conditions (Carruth and McKenzie, 1986). During the past 20 years or so the use of lasers has expanded to most fields of medicine and, in many cases, has revolutionized the way the illnesses are treated, and in some cases, diagnosed (Peng et al, 2008). There are many medical disciplines where lasers are now used routinely for a variety of purposes and with much success. There is, however, a need for further research in laser applications in medicine in order to achieve optimal outcomes for the patient (e.g. Vogel and Venugopalan, 2003).

Key to improving laser techniques in medical application is a better understanding of the nature of the laser-biomaterial interaction processes. The kinetics and dynamics of laser interactions with biological tissues and materials are still to be fully understood, and basic and applied researches are being actively pursued in laboratories all over the world to underpin further technological developments for more effective clinical applications (e.g. conference proceedings of SPIE). Such knowledge of the laser-tissue interaction will help guide clinical operators in identifying optimal laser parameters for the application so that a more efficient and safer outcome may be achieved (Müller et al, 2006).

The applications of lasers in medicine can be categorized into two major disciplines: diagnostic and therapeutic. The vast majority of applications are in the therapeutic field, making use of laser as an efficient and effective tool for controlled and precise ablation, for example in the surgical removal of tissues. In recent years, there has also been much interest in the use of the laser as a diagnostic tool and this has resulted in some exciting developments across all medical specialities (Johansson et al, 2008). Gaining clinical diagnostic information by the use of a laser probe, for example for the analysis of tissue and bio materials, may better guide the treatment and may also be helpful in optimizing the therapeutic technique (Crow, 2003).

One application where the use of lasers has achieved huge success is in the treatment of calculi, a procedure known as laser lithotripsy (e.g. Watson et al, 1983; Schmidt-Kloiber, 1991; Floratos and Rosette, 1999; Waidelich, 2005). In this application a laser beam is introduced into the body via optical fibre and used to fragment the calculi. The treatment alleviates pain and discomfort caused by the condition, which left untreated could potentially lead to kidney failure and even death (Tiselius, 2003). Today laser lithotripsy is a commonly practiced minimally invasive technique although further work is needed to gain a better understanding of the interaction and fragmentation processes so that treatment can be optimised.

A number of lasers are commercially available and this presents the urologist with a bewildering choice of wavelengths, pulse energies, pulse durations, pulse repetition rates, and fibre sizes (Marks and Teichman, 2007). The output parameters determine the nature of the laser-calculus interaction and this is crucial in order to understand and optimise the application. Some laser lithotripters are referred to as 'LISL' systems – Laser Induced Shockwave Lithotripsy - such as those using a Q-switched neodymium YAG laser, on account of the observed shockwave effects during fragmentation (Schmidt-Kloiber et al, 1985). Other laser lithotripsy systems, such as those employing holmium YAG lasers, have been reported as possibly having a different mechanism of interaction (Chan et al, 1999a,b), although shock waves are still very much evident (Sperrin, 2000). What is not clear is how these devices differ in their action on calculi (Sperrin et al, 1999), and furthermore with the availability of variable pulsed holmium lasers, how the choice of pulse duration affects the ability of the laser to generate plasma and shockwave effects for calculus destruction.

There is also another potential application in this field, that is, to use the laser as part of a spectroscopic system to obtain data on the composition of the calculi. Analysis of laser-induced plasma on calculus material may provide elemental identification particularly the presence of certain metals, and this information may be useful, for example, in identifying environmental factors (Al-Kofahi and Hallak, 1996; Abboud, 2008). Significant differences have been reported in the level of lead found in kidney

stones between geographical regions, suggesting exposure to lead in the environment (Galassini et al, 1989).

The presence of various metal elements in the calculus may also guide treatment. The concentration of zinc, manganese and magnesium has been suggested to affect the outcome of stone treatment by shockwaves (Turgut et al, 2008). There has also been a suggested link in the role of trace elements, in particular metals, in the process of calculus formation (Hofbauer, 1991; Pineda and Peisach, 1994; Golovanova et al, 2003; Atakan et al, 2007; Chaudhri et al, 2007). Calcium and magnesium are known to be important in stone formation, and it has been suggested that zinc, strontium, and copper are also connected to stone nucleation (Lin et al, 1987). Therefore, a laser technique that allows the detection of elements such as metals in calculi is very much of interest (Bazin et al, 2007).

The work described in this thesis has been carried out by the author in the pursuit of contributing further knowledge in the laser-calculus interaction and the fragmentation process, and also to investigate the potential for using a laser to analyse elemental composition of calculi. The following sections provide background information on laser technology, urinary calculi, and the application of lasers to calculus destruction.

1.2 Laser physics and technology

The basic principle of operation of a laser can be described in terms of Maiman's laser, which generated visible light from a ruby crystal. An energized flashlamp coiled around a rod of ruby was used to pump the crystal with optical energy, raising the majority of its chromium atoms to an excited state, achieving a so-called population inversion. Spontaneous de-excitation of atoms releases photons in random directions, some of which travel along the axis of the rod and induced stimulated emission of further photons also in the same direction, thereby amplifying the intensity of the light. The ends of the rod were silvered to reflect the light back and forth through the material, enabling the process of simulated emission to repeat over and over, with one end partially transmitting such that a portion of light passed through and exited from one end as a beam. Generated in this way, the laser light had a much higher intensity than

ordinary light sources including the sun, and the light generated was at a specific wavelength corresponding to the photon energy released on atomic de-excitation, in this case a wavelength of 694 nm (Carruth and McKenzie, 1986).

The following describes the basic physics of the two lasers that were used for experimental work in this thesis; the neodymium YAG laser and the holmium YAG laser.

1.2.1 The neodymium YAG laser (Nd:YAG)

In 1961, soon after Maiman had demonstrated the ruby laser, Johnson and Nassau reported laser action by neodymium ions (Nd^{3+}) incorporated as an impurity in a host crystal. The yttrium aluminium garnet ($Y_3Al_5O_{12}$) crystal matrix emerged as the host with the best performance, as it allowed continuous wave (CW) operation at room temperature. The neodymium ions are excited by illumination with radiation from a krypton flashlamp, which has an optical output that is reasonably well matched to the absorption spectrum of the Nd^{3+} ions. The neodymium ions then relax and emit at infrared wavelengths, with 1064 nm being the wavelength of the strongest emission line and this is the laser transition. A population inversion is maintained as the lower laser level has rapid transitions to the ground state through interaction with the lattice; also it is sufficiently above the ion ground state so that thermal pumping to this level is negligible. The incorporation of Q-switching, an electrically operated shutter/switch in the laser cavity, allows the population inversion to build-up by obscuring one of the mirrors whilst pumping the active medium. The Q-switch device is then opened and the rapid de-excitation processes produce a laser pulse of nanosecond duration.

1.2.2 The holmium YAG laser (Ho:YAG)

Holmium lasers have been known since the early 1970's, however, the experimental arrangements for this laser were only workable at very low temperatures, for example, at 77 K, the temperature of liquid nitrogen. The development of holmium lasers for medical applications was made possible by the introduction of more efficient laser materials with thermal properties suitable for operation at closer to room temperature (Berlien and Müller, 2003). As with the Nd:YAG laser the holmium laser is a solid state

laser, with an active medium which is a mix of chromium, thulium and holmium in the host YAG crystal. The chromium atoms absorb white light produced by a xenon or krypton flashlamp, and transfer the absorbed energy to the thulium ions. Excited thulium ions transfer half of their energy to adjacent thulium ions in the ground state, thereby doubling the number of excited ions. This process of energy transfer is known as cross-relaxation. At this lower energy level, energy is transferred to holmium ions which give rise to laser transitions. The emitted radiation has a wavelength of 2.12 μm and typically has a "free-running" pulse duration of 300 μs – 500 μs. Transfer of energy between Thulium ions is of paramount importance for the holmium laser. Without this process, the laser crystal would overheat and its efficiency would be dramatically reduced due to the thermal population of the lower laser level and the spontaneous depopulation of the upper laser level. The cross relaxation process moderates the generation of heat and allows the holmium laser to operate at the room temperature. The laser output is characterized by short spikes of around 1 μs duration. These relaxation oscillations, particularly at the beginning of the pulse, are a consequence of light generation by the stimulated emission process. These spikes limit the maximum pulse energy to avoid destruction of optical resonator components or fibre materials. However, intense short spikes support the ablation of materials as the energy density reaches the ablation threshold, and are therefore desirable (Teichmann et al, 2007).

1.3 Urinary calculi

Urinary calculi are crystalline deposits, also known as kidney stones or uroliths, which occur in the urinary system. The condition causes the individual severe discomfort and pain, and can lead to renal failure if left untreated. Their formation is not fully understood although a number of risk factors including diet, age, gender, genetics and certain pathologies have been indicated (Robertson and Peacock,1979; Tiselius, 2003).

The formation of stones in the urinary tract, which includes the bladder, ureters, urethra and kidneys (as shown schematically in Figure 1.2), affects 5 – 10 % of the population in the Western world, and an even higher proportion has been reported from other parts of the world. The disease occurs more frequently in white populations, and the occurrence rate is 2 – 3 times higher in men than in women. Stone recurrence amongst

stone formers is very common, at a rate of around 50% and increasing (Rizvi et al, 2002; Tiselius, 2003).

Calculus composition depends upon the underlying cause that leads to their precipitation. For this reason it is particularly critical to know exactly which kind of stone is present in order to consider the best treatment, and also to guide prognosis and preventative measures. For example, dietary changes may serve to slow the growth of certain stones, but they could conceivably accelerate growth of other types of stones. Analysis of stone composition is therefore essential (Kasidas, 2004).

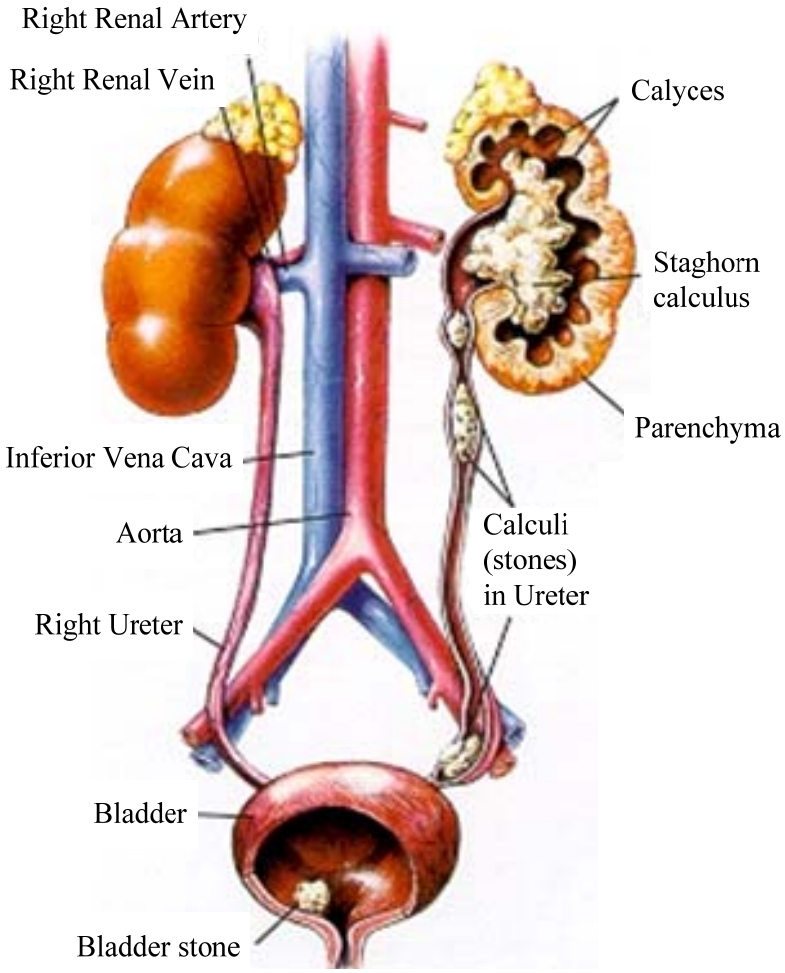

Figure 1.2: Basic anatomy showing the main components of the human urinary system and potential sites of calculus formation (image taken with permission from nymc.edu, 01.07.09)

An imbalance or excess of certain chemicals in the urine is known to trigger their deposition and growth, resulting in the formation of what is known as a primary stone.

Secondary-type calculi, also known as a concrements, form around a solid object such as a foreign body or biological matter in the urine, or indeed a primary stone (Sabot et al, 1999). Urinary calculi may occur where there is a high level of calcium, oxalate or uric acid in the urine; a lack of citrate in the urine (which is an inhibitor); or insufficient water in the kidneys to dissolve waste products. The compositions of the most common types are comprised of forms of calcium oxalate, magnesium phosphate, uric acid, and cystine. Table 1.1 shows the different compositions of urinary calculi and their mineral name and chemical formulae.

Table 1.1: Common human urinary calculi and their major constituent(s)

Constituent	Mineral Name	Chemical Formula	Description
Calcium Oxalate Monohydrate (COM)	Whewellite	$CaC_2O_4.H_2O$	Primary stone Brown
Calcium Oxalate Dihydrate (COD)	Weddellite	$CaC_2O_4.2H_2O$	Rough surface, very hard, laminated structure
Magnesium Ammonium Phosphate Hexahydrate (MAPH)	Struvite	$MgNH_4PO_4.2H_2O$	Secondary stone Mixed composition White
Calcium Phosphate, Carbonate Form	Carbonate Apatite	$Ca_{10}(PO_4CO_3OH)_6(OH)_2$	Smooth, soft friable consistency
Calcium Phosphate, Hydroxyl Form	Hydroxylapatite	$Ca_{10}(PO_4)_6(OH)_2$	Primary stone Colour varies off white to brown
Calcium Hydrogen Phosphate Dihydrate	Brushite	$CaHPO_4.2H_2O$	Variable hardness
Tricalcium Phosphate	Whitlockite	$Ca_3(PO_4)_2$	
Magnesium Hydrogen Phosphate Trihydrate	Newberyite	$MgHPO_4.3H_2O$	
Uric Acid	N/A	$C_5H_4N_4O_3$	Primary stone
Sodium Acid Urate		$NaHC_5H_2O_3N_4.H_2O$	Brown
Ammonium Acid Urate		$NH_4H.C_5H_2O_3N_4.H_2O$	Smooth, hard, concentric lamination
Cystine	N/A	$(SCH_2CH(NH_2)COOH)_2$	Primary stone Yellowish-brown Very firm

The micro-architecture of calculi has an influence on their physical properties and varies between stone types (Kim, 1982; Söhnel and Grases, 1993; Sperrin and Rodgers, 1998).

For example, calcium oxalate and uric acid calculi generally have a more crystalline structure, built up of concentric laminations, which gives rise to their relative hardness. Other calculi that are a conglomeration of crystalline and organic components tend to be more friable. In general, however, calculi tend to have an inhomogeneous structure with inherent weaknesses, and this is exploited in their treatment such as with lasers (Singh and Agarwal, 1990; Agarwal and Singh, 1991; Chuong et al, 1993). A laser-generated pressure pulse travelling through the bulk calculus material will encounter regions of different acoustic impedance and be partially reflected as a tensile stress wave. These waves have high damage potential, since calculi are approximately five times more susceptible to break-up under tension than compression (Vogel, 1997). This laser-induced process may lead to cracks and rupture of the calculus.

1.4 Laser lithotripsy

Laser lithotripsy, as described in section 1.1, is the fragmentation of calculi using a laser beam, and the technique is used in the removal of urinary calculi and also billiary calculi in the gall bladder (e.g. Langhorst and Neuhaus, 2000; Rosin et al, 2000). The surgeon locates the calculus using a flexible endoscope attached to a viewing monitor and advances the tip of the optical fibre to touch the stone surface, or with a small separation. The laser energy is then imparted to the surface of the calculus to generate an action that will lead to the bulk disintegration of the calculus. Fragmentation is performed until either the calculus is dis-impacted, or until breakdown is complete, so that the fragments can be extracted using a wire basket, or left in situ to be passed naturally. The procedure is carried out under local anaesthesia. A schematic of the arrangement of the apparatus during the procedure is shown in Figure 1.3.

The advantage of using a laser is that the beam has an effect only in the region where it is absorbed. In some situations, such as blockage of the ureter caused by an impacted calculus, precise targeting afforded by a laser beam is necessary to avoid surrounding tissues. Compared to ultrasound and electrohydraulic techniques, laser lithotripsy has several important advantages. In particular, the small diameter of the flexible laser fibre within the optical scope overcomes difficulties encountered with rigid ultrasonic probes

and larger diameter electrohydraulic systems. Improved tissue safety has been reported to be another advantage with the laser (Coptcoat, 1987), minimising the risk of ureteral perforation compared to electrohydraulic lithotripsy. The practitioner has direct visualisation of the calculus, thus improving control and reducing the risk of accidental injury. Additionally, laser lithotripsy requires less energy to attain a similar fragmentation effect, generates less heat, and causes less calculus retro-propulsion (a ballistic effect seen when powerful shockwaves cause stones to recoil).

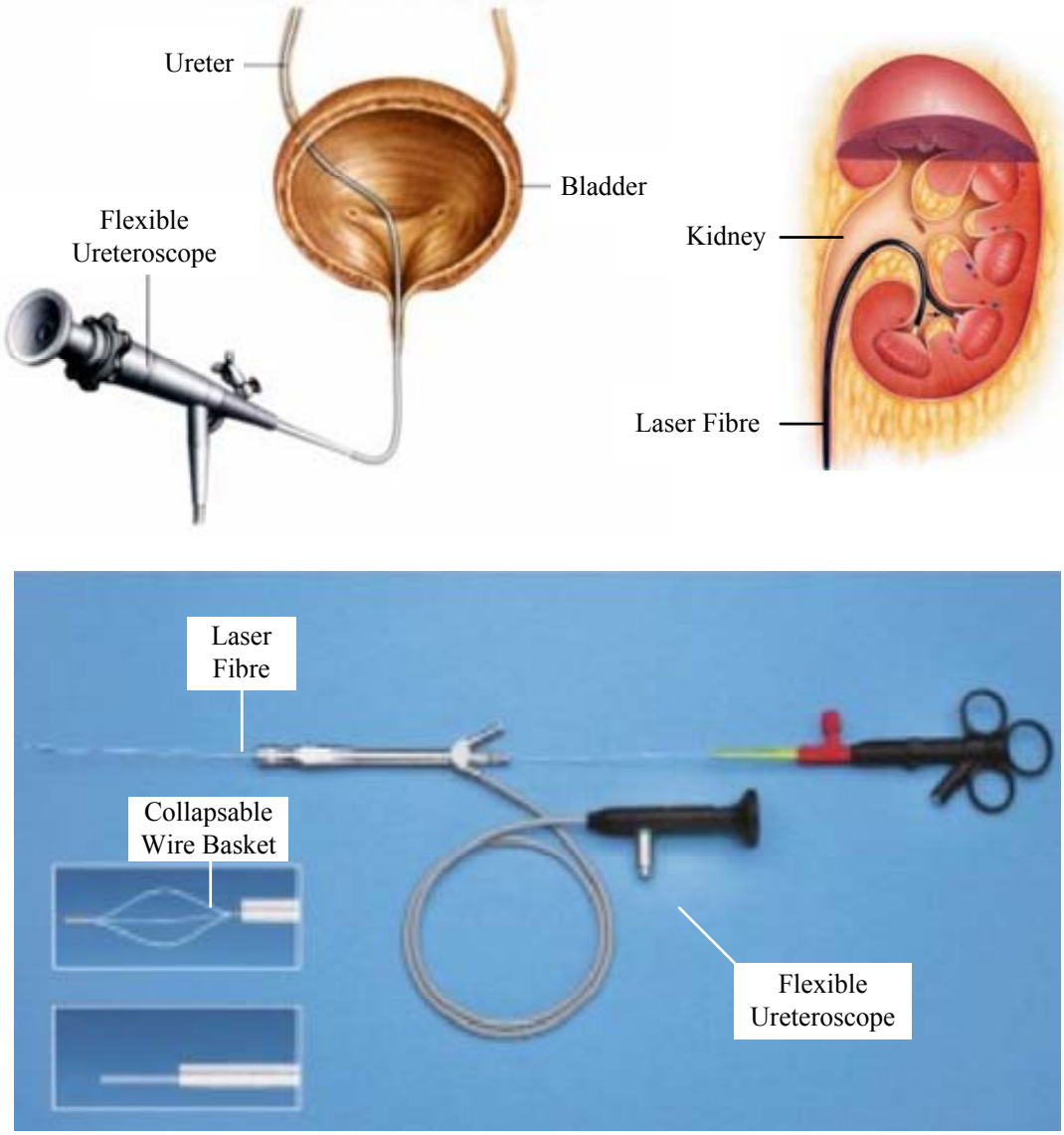

Figure 1.3: Images showing the basic arrangement of apparatus for the delivery of laser energy to the calculus during laser lithotripsy procedure. (Images taken with permission; Top: kidneystoneindia.com 01.07.09; Bottom: sosromandie.ch 01.07.09).

The principle of laser destruction of calculi is by direct effect of laser radiation, or by shockwaves produced when the laser is absorbed in a thin layer of liquid near the fibre end-face. Although a full description is complex and not yet fully understood, in general, when the fibre touches the stone direct ablation is dominant and a slight pressing of the fibre against the stone results in a drilling action. If the distance between the fibre end-face and the stone surface is greater than the thickness of the water layer that can be penetrated by the laser radiation, the laser energy is absorbed in the water and the destruction runs due to the shock waves. For certain values of the distance the two mechanisms are simultaneous and a combined action is possible.

The action of laser radiation on calculi depends on several laser light properties, i.e. wavelength, duration of exposure, delivered energy, and intensity (rate of delivery of energy over the focussed area of the target). The effect of laser wavelength is very important as it determines the amount of absorption by the calculus and intervening liquid, and therefore the following energy transfer/ dissipation dynamics. However, the wavelength of the laser light must be from the region of the spectrum where flexible fibres having good transmission are available.

The duration of the laser pulse or the exposure time (in the case of CW lasers) plays a vital role in the energy balance dynamics of optical interaction with calculi. Depending on the extent of duration three identifiable different processes take place. These are categorised as:

- Continuous wave (CW) lithotripsy
- Long pulse lithotripsy (pulse duration: μs to ms)
- Short pulse lithotripsy (pulse duration: ns)

Continuous wave laser action results in a temperature rise leading to melting and vaporisation of the material. After several holes have been drilled into the calculus bulk it may break apart. As this effect is relatively slow, some of the heat is conducted into the surroundings and collateral damage can result. The necessary energy to minimise this is too high to be afforded by most commercial lasers, and therefore the method is

not practical for in vivo application. Pulsed laser energy allows the application of high instantaneous pulse power i.e. higher rate of energy delivery, to fracture the calculus. Application of these pulses with a low duty cycle reduces the average power needed for calculus fracture. Therefore, stone fragmentation can be done without harmful thermal effects to the surrounding tissues.

The mechanical action on the calculus must be strong and most importantly of short duration, so that the inertia becomes important and an overall motion of the calculus is prevented. Therefore, conservation of momentum is only done with a small part of the calculus and if by this action the breaking point of the calculus material is exceeded, fragmentation starts. Mechanical action can be generated by pressure pulses arising from pulsed laser radiation. Long pulse lithotripsy makes use of the optical absorption properties of the calculus to produce mechanical stress transients within the bulk material, and, therefore, this method is dependent on calculus composition. In short pulse lithotripsy, the laser pulses are absorbed by plasma and shockwaves are released, which then act on the calculus. This method is independent of any optical properties of the stone.

Laser light energy and intensity also determine the fragmentation rate. Besides laser parameters the optical and mechanical properties of the calculi are also important for the conversion efficiency of optical energy into mechanical stress. Calculi may vary widely in contents and composition and thus show different hardness and absorption coefficients.

1.5 Laser induced breakdown spectroscopy (LIBS)

Most calculi occur due to dietary factors or metabolic disorders, where abnormally high levels of certain elements (e.g. Ca, Mg and also Sr, Cu, Zn, etc.) are present (Kasidas et al, 2004). It is possible that the chemical compositions of the calculi are influenced by the elements present as active catalysts or chelating agents. A variety of spectroscopic analytical techniques has been widely used to identify and analyse the structural and elemental compositions of urinary calculi. Infrared and Raman spectroscopy (Carmona

et al, 1997; Estepa and Daudon, 1997; Paluszkiewicz et al, 1997) and X-ray diffraction have been applied for the analysis of structural composition, while inductively coupled plasma atomic emission spectroscopy, graphite furnace atomic absorption spectroscopy and particle induced X-ray emission spectroscopy have been used for the analysis of elemental composition (Hofbauer et al, 1992). All of these analytical techniques, particularly the ones for elemental analysis, require time and labour intensive specialist sample preparation and presentation protocols. For fast and in situ analysis, laser induced breakdown spectroscopy (LIBS) has been found to be a suitable technique for elemental analysis in solid materials (Radziemski, 2002). The technique involves the use of a high power laser pulse focussed on a sample to create plasma emission, which is collected and analysed to identify the constituent elements, in particular metals. This is a similar arrangement as carried out with laser lithotripsy but with the incorporation of spectroscopic instrumentation, and the application of LIBS for urinary stone analysis has recently become of interest. The advantage of the LIBS technique is that it does not require any special sample preparation and presentation efforts, and could therefore potentially be used as an in-situ method of investigation.

1.6 Aims of the research

The research examines the laser interaction process with calculi and water and the effect of laser parameters for a medical Ho:YAG laser that has variable pulse duration (λ = 2.12 μm, τ_p = 120 – 800 μs, I ~ 3 MW cm^{-2}). The Ho:YAG interaction process will be contrasted with a Q-switched Nd:YAG laser (λ = 1064 nm, τ_p = 6 ns, I ~ 90 GW cm^{-2}), which has applications in laser induced breakdown spectroscopy (LIBS). The study will investigate the interaction process by means of detection of optical emissions from the interaction site i.e. plasma generation, using spectroscopy instrumentation, and also the measurement of laser-induced shockwaves using a needle hydrophone to obtain highly accurate pressure measurements. The study aims to clarify the interaction process, in particular the effect of pulse duration with the Ho:YAG laser, and to reveal the magnitude of pressure pulses and the formation of plasma for both Nd:YAG and Ho:YAG lasers. Laser generated plasma by LIBS technique is used to investigate the prospect of analysing elemental composition for calculus material as this has potential benefits in guiding treatment, particularly as specimens are not routinely analysed.

Chapter 2
Review of the Literature

2.1 Historical development of laser lithotripsy

By the 1990's several competing technologies were available for carrying out minimally invasive fragmentation of calculi: Electrohydraulic lithotripsy (EHL), ultrasonic lithotripsy, pneumatic lithotripsy, extracorporeal shockwave lithotripsy (ESWL), and laser lithotripsy (Bhatta, 1995). All these devices operated on the principle of generating a mechanical action, in particular shockwaves, to cause fragmentation. However, there were a number of problems, including their inability to break up hard calculi. In the case of ESWL where it is crucial that the patient is positioned under x-ray guidance with the calculus at the focus of the shockwave, certain types of calculi such as cystine compositions are not sufficiently radio-opaque and could not be visualised. EHL probes generated excessive heat, increasing the risk of injury to tissues including perforation of the ureter. Ultrasonic probes only offered limited access to the urinary tract because of their rigid construction. Furthermore, the large calibre of EHL, ultrasonic and pneumatic probes meant they were not compatible with small flexible ureteroscopes that were available and this limited their application (Reynard and Badenoch, 1997). In contrast, laser lithotripsy enabled fragmentation of calculi via small and highly flexible optical fibres with minimal risk of tissue damage (Bhatta, 1995).

The action of laser radiation on calculi was known to be different to the direct mechanical methods of stone fragmentation. Laser light requires processes to convert the optical energy into destructive mechanical effects, and in laser lithotripsy the main conversion process is via the formation of plasma. Investigations of the optical breakdown process and laser generated plasma (Felix and Ellis, 1971; Bloembergen, 1974), and the resulting mechanical effects such as stress waves arising from the generation of shockwaves (Anderholm, 1970) and cavitation processes (Lauterborn and Bolle, 1975) were the basis of the development of laser lithotripsy.

The first reported study on the interaction of laser radiation with calculi was carried out by Mulvaney and Beck (1968). Using a pulsed 694 nm wavelength ruby laser

generating high energy pulses of 50 – 300 J focused through quartz rods for potential endoscopic delivery, and also a 50W CO_2 laser emitting continuously at 10.6 μm, the ability of laser radiation to disintegrate calculi was demonstrated. The interaction generated considerable thermal effects including dehydration, decomposition, carbonisation, melting and vaporization, which precluded the laser from clinical use because of the potential for tissue damage. Excessive heating, however, is to be expected at such high laser output. Fragmentation was dependent on the calculus composition; some types of calculus were easily disintegrated, and others with difficulty. Calculus surface colouration was found to be important as the interaction was enhanced by the use of dye to stain the calculi. The production of shockwaves was also observed which were enhanced when the calculus was immersed in water, confining the laser energy. The potential of the laser as a tool for spectroscopic elemental analyses of calculus material, in particular for trace elements, was also noted in this study.

The problem of excessive heat production was addressed by Anderholm (1970), who showed that the effects of lasers are not only thermal. He demonstrated that short duration laser pulses could be used to generate strong shockwaves. This was possible because Q-switched lasers had become available, generating laser pulses of around 10 ns duration. The study highlighted the link between short pulse duration and shockwave intensity. However, the reported amplitude of the pressure pulse of 34 kbar (3.4 GPa) was obtained for high energy laser pulses focused onto a metal target in air, and therefore not directly applicable to a laser-calculus interaction.

The search began for a suitable laser to carry out in vivo disintegration of calculi. Tanahashi et al (1979) experimented with a CW CO_2 laser and reported its ability to drill holes in stones. However, the desired effect is bulk fragmentation into smaller particles that can be passed or extracted and this was not achieved. Furthermore, the action created too much heat and the wavelength could not be delivered via optical fibre, hence making endoscopic access to the urinary tract impossible. A CW Nd:YAG laser was tested by Pensel et al (1981), but the high energy levels required for calculus fragmentation caused fibre damage.

Watson et al (1983) concluded that although CW lasers do heat the stone surface eventually leading to some fragmentation of the calculus, they also result in thermal tissue injury and are therefore unsuitable. Noting that earlier studies had indicated short pulse durations yield less thermal effect and greater mechanical action, he investigated the Q-switched Nd:YAG laser as a potential laser lithotripter. The laser proved to be tissue-safe and was able to achieve fragmentation of calculi, however, the high peak power limited the energy which could be transmitted through the fibre making the laser less effective. Thicker fibres were used that allowed higher energy pulses to be transmitted but with the drawback of reduced flexibility. Attempts were later made to overcome this problem using specially adapted fibres either with focusing optics to achieve the fragmentation threshold at the distal end of the fibre (Frank et al, 1990), supported by special breakdown liquid (Reichel et al, 1991), or the use of a metal pin for plasma ignition known as an optomechanical coupler. These techniques produced shockwaves independent of the stone properties, but proved to be problematic in clinical use, in particular with their large size and inflexibility.

Microsecond duration pulses from flashlamp pumped pulsed dye lasers (PDL) could be transmitted through optical fibres down to 200 μm diameter and experimental studies were reported by Watson et al (1987a) and Bhatta et al (1989a). The effect of PDL wavelengths of 445, 504 and 577 nm, pulse duration, energy and repetition rate, and fibre diameter, were investigated to determine the optimum parameters (Watson, 1987b). It was found that the fragmentation ability of the PDL increased with shorter pulse durations and smaller fibres, indicating a dependence on peak power density. Although the fragmentation threshold was lower at 445 nm, for safety a wavelength of 504 nm was chosen to maximize the absorption differential between calculi and ureter. A relatively slow pulse repetition rate of 5 Hz was chosen to reduce the effect of residual heat accumulation of the previous pulses. Clinical studies reported the PDL to be effective in fragmentation of most stone types (Grasso et al, 1991) and also to have improved safety over EHL (Watson et al, 1987b). Since its introduction in the late 1980's, the pulsed dye laser has become one of the most popular commercial lithotripters available. The main disadvantages of the PDL are the inability to fragment

pale hard stones, and technical reliability and maintenance issues including the need to replace the coumarin green dye on a periodic basis.

The long pulsed Ho:YAG laser has been utilized extensively since 1995 and is widely regarded as the laser of choice for lithotripsy (Denstedt et al, 1995; Devarajan et al, 1998; Matsuoka et al, 1999; Pierre and Preminger, 2007). The laser emits at a wavelength of 2.12 μm, a typical pulse duration of around 300 μs, pulse repetition rate 5 – 20 Hz, and pulse energy 200 mJ – 2 J. The first in vitro studies were reported by Jiang et al (1991a) and Sayer et al (1993a, 1993b). Clinical application of Ho:YAG laser lithotripsy is technically relatively simple to perform and safe and effective (Peh et al, 2001; Sofer et al, 2002). The procedure is associated with minimal collateral thermal damage, although it is imperative that the optical fibre tip be visualized throughout the procedure to confirm the beam is directed at the stone and the fibre in close contact. As the laser produces relatively small particles during fragmentation the procedure is slower than other lithotripsy modalities, extending the surgical time (Teichman et al, 1998a).

A recently developed laser for lithotripsy is the frequency-doubled double-pulse Nd:YAG (FREDDY) laser (Koort et al, 2002; Bader et al, 2007). The FREDDY laser generates a synchronized double pulse at 1064 nm in tandem with the harmonic wavelength 532 nm, which is achieved by incorporating a KTP frequency-doubler crystal inside the Nd:YAG laser cavity. Clinical trials with the FREDDY laser have indicated that it is safer on tissues than the PDL and Ho:YAG lasers (Tischer et al, 2002). Fragmentation speed is better than the Ho:YAG laser for brittle stone compositions, however for hard calculi the process is slow and the low fragmentation efficiency is a major drawback (Marguet et al, 2005).

There has been recent interest in the potential of the Er:YAG laser in lithotripsy following studies with a Er:Cr:YSGG laser (D'Yakonov et al, 1991a; Bloch et al, 1993), and proposed optimal wavelengths of around 3 μm for calcium oxalate monohydrate calculi (Chan et al, 2000a). The Er:YAG laser emits pulsed radiation in the infrared at 2.94 μm, which also coincides with the water absorption peak. Investigators have

reported that compared to the Ho:YAG laser the Er:YAG more efficiently ablates a variety of calculi, and produces a more precise ablation and less thermal damage (Teichman et al, 2001; Chan et al, 2002). However, a fibre that will transmit at the Er:YAG wavelength and is also suitable for lithotripsy is not yet available, although the germanium oxide fibre with a sealing cap is reported to be a potential delivery system (Welch et al, 2004).

The search for a more efficient and cost effective laser solution to calculus fragmentation is ongoing. Developments in diode laser technology are promising and a compact solid state diode-pumped thulium fibre laser operating at 1.94 μm has been reported as capable of fragmenting calculi (Fried, 2005). However, such devices are not yet capable of delivering sufficiently high peak power pulses for rapid calculus fragmentation and further work is needed in this area. As such, the holmium laser currently remains the state of the art in laser lithotripsy although recent developments in variable pulse duration holmium lasers and their impact on optimising stone clearance are still to be investigated (Marks and Teichman, 2007).

2.2 Investigations into laser-calculus interactions

2.2.1 Ho:YAG laser

Holmium is a rare-earth element, which when doped in YAG can emit laser radiation at a wavelength of 2.12 μm with "free running" pulse duration of ~ 250 – 350 μs. The pulsed Ho:YAG emerged as a real alternative to the pulsed dye laser in the early 1990's (Brinkmann and Bauer, 1991; Jiang et al, 1991a; Sayer et al, 1993a). It was put into clinical use in 1994, and since then it has been used widely to fragment all types of calculi, including the hardest stones (Pierre and Preminger, 2007). On account of it's very high absorption in water (absorption coefficient 50 cm^{-1}, optical penetration ~ 400 μm), the laser energy is absorbed by water/bioliquid in front of the fibre and also by the surface of the hydrated calculus. This results in an intense localised vaporisation, giving rise to the possibility of shockwave interactions and direct material ablation.

Jiang et al (1991a) investigated the holmium laser-calculus interaction and reported the absence of laser-induced plasma formation, possibly as the peak power density was low,

but noted shockwaves which were attributed to the collapse of a vapour bubble, suggesting mechanical processes. However, unlike the explosive action of the PDL it was noted that calculus destruction was a drilling action, an observation that suggested a thermal effect. Brinkmann and Bauer (1991), however, using a shorter pulse duration (~ 6 μs) holmium laser and higher irradiance (> 180 J cm^{-2}) achieved plasma formation and concluded the fragmentation mechanism to be mechanical, but rather as a result of an expanding plasma. Plasma formation has also been reported as a possibility with the Ho:YAG laser as the laser pulse contains a series of high intensity spikes which may exceed the optical breakdown threshold in water (Vogel and Venugopalan, 2003). Watson et al (1993) noted a lack of propulsion effect on the calculus and the production of smaller fragments compared to shockwave-producing lasers such as the PDL, suggesting that mechanical effects were less significant with this laser.

Detailed studies by Schafer et al (1994), Zhong et al (1998), Chan et al (1999a, 1999b) and Vasser et al (1999) utilising high-speed imaging, simultaneous pressure measurements, and real-time optical emission spectroscopy presented new evidence. Directing the laser pulse freely into water, peak pressures of 20 bars (2 MPa) were reported (Chan et al, 1999b) but with the fibre positioned close to the calculus, as in the clinical situation, only relatively weak transients (< 2 bars) were detected (Beghuin et al, 1998). The results suggested that the laser induced pressures were insufficient to induce fragmentation. However, Sperrin (2000) investigated the variation of pressure with distance and found that the peak pressure falls off rapidly within a few millimetres from the point of interaction, and goes on to predict pressures of the order 600 MPa at the calculus surface. Such high pressures are in excess of the failure strength of calculi (Sperrin, 2000).

Image sequences of the interaction revealed the vapour bubble to be non-spherical, and elongated (Jansen et al, 1996). Zhong et al (1998) described the process as the ‘Moses effect’ as the laser effectively ‘parts the water’; a steam bubble is generated by the initial vaporisation of water and this is progressively vaporised on the distal side until an elongated void is formed. Bubble size was reported to be related to laser pulse

energy, however, the pressure spike from the bubble collapse was roughly constant over a range of pulse energies (Schafer et al, 1994). The close proximity of the delivery fibre to the calculus was believed to impede bubble expansion and further diminish shockwave pressures (Chan et al, 1999a), and ejected fragments were also thought to perturb the bubble dynamics (Beghuin et al, 1998). Chan et al (1999a) reported that fragmentation occurred ~ 50 μs after the initiation of the laser pulse, long before the collapse of the cavitation bubble, although Kokaj (2001) suggested that shock waves could be the bubble expansion phase. Shockwave formation arising from accelerated liquid jets following bubble implosion was also considered a possibility (Van Swol et al, 1998), although this has not been confirmed.

Investigators found that fragmentation only took place when the vapour bubble produced by the laser pulse actually contacts the stone surface (Schafer et al, 1994). It was proposed that the bubble serves as an open channel along the path of the beam through which the remaining laser energy can pass and directly ablate the calculus, possibly via explosive vaporisation of interstitial water and non-condensable gases production (Beghuin et al, 1998), although this mechanism has not been confirmed. Observations of an incandescent glow on the stone surface during the interaction are consistent with a predominantly thermal process (Schafer et al, 1994), however, this may be attributable to scattered light in the laser pulse originating from the laser flashlamp (Chan et al, 1999a), although the white glow has been reported to continue after the laser pulse has terminated (Dushinski and Lingeman, 1998). Photothermal breakdown products such as cyanide have been recovered through chemical analysis of the ejected fragments (Teichman et al, 1998; Glickman et al, 1999a, 1999b, 2000), suggesting that substantial heating occurred during the interaction. Vasser et al (1998) found that lithotripsy efficiency correlated with energy density, and Teichman et al (1998b) reported crater size to be related to calculus composition, providing further evidence for a predominantly thermal mechanism.

Evidence has also been presented for holmium laser induced mechanical effects on calculi. Beghuin et al (1998) noted that fragmentation efficiency was significantly better

for wet stones or stones immersed in water compared to dry stones, suggesting that there is better coupling of laser energy in a water environment which would be the case with shockwave action. Sperrin (2000) conducted detailed measurements of Ho:YAG induced shockwaves in water arising from a fixed pulse duration laser and found that the attenuation affects are significant. Accounting for the fall off with distance he estimated that, for optimised laser parameters, the peak pressures are considerably higher than previously reported (of the order several hundred MPa), and also found that the pressure pulse has a significant negative component (of the order -85 MPa) which is potentially more destructive to calculi. His investigations also found that the ablated crater size on simulated urinary stones correlated well with shockwave dynamics. The disparity in the shockwave amplitudes reported by Chan et al (1999b) and Sperrin (2000) may be explained by the different approaches in measurement, where the more detailed field characterisation and in particular the determination of the dependence with distance lends weight to Sperrin's findings.

The mechanism of pulsed Ho:YAG laser radiation on calculi is clearly disputed and still not fully understood. Short pulse systems have been shown to be capable of generating strong shockwaves (Jansen et al, 1996), however, from reports the long pulsed laser operating at ~ 250 μs that has been used clinically appears to have a photothermal action and a photomechanical contribution from shockwaves. Studies on variable pulsed Ho:YAG systems have indicated that mechanical effects on the calculus are increased with shorter pulse durations (Lee, 2003; Finley et al, 2005; Kang et al, 2006). These systems, with pulse durations selectable in the range ~ 100 – 800 μs, afford the operator greater flexibility and have the potential to provide further optimisation with the holmium laser.

2.2.2 Nd:YAG laser

Historically, the Nd:YAG laser (1064 nm) has been the most widely used in lithotripsy. Studies have been carried out with the long pulsed (100 μs) Nd:YAG, although most of the reported work has been on the use of the Q-switched (8 – 20 ns) Nd:YAG laser.

Using the long pulsed Nd:YAG, Batishche (1995) observed how after a few initial pulses which gave no visible results, a plasma appeared that grew in intensity with each successive pulse, accompanied by a loud sound pulse and the creation of gas bubbles and later a further shockwave. The laser interaction led to calculus fragmentation. His observations indicated that a combination of effects including initial heating, plasma expansion, hot gas expansion, water vaporisation, and bubble collapse contributed to the fragmentation process. The investigator concluded that although the initial absorption was low, enough absorption took place to create a local temperature rise which led to structural change and a corresponding increase of absorption (a non linear effect at high irradiances).

The Q-switched Nd:YAG laser has also been used successfully to fragment all types of calculi in air and water (Chan et al, 2001). Frank et al (1990) found that multiple laser pulses were required for all but dark calculi suggesting a thermal action where initial pulses are required to heat the target site. However, the investigators found no evidence of melting and deduced that this was due to the very rapid interaction resulting in a stress wave which fractures the bulk calculus.

One of the drawbacks with the Q-switched Nd:YAG laser as a laser lithotripter was found to be that the high peak power of the laser pulses caused damage to quartz glass fibres (threshold for optical breakdown ~ 5 GW cm^{-2}) leading to unacceptable fibre wear (Frank et al, 1990). Thicker fibres of 600 μm were able to overcome this problem, although with the drawback of reduced flexibility which made them unsuitable for some clinical situations.

Another approach to inducing fragmentation with the Q-switched Nd:YAG was to use focussing components at the distal end of the fibre, such as an optical fibre with either a cone (Hofmann et al, 1990), a spherical end (Maghraby et al, 1990) or an attached multiple lens system (Frank et al, 1990). This method increased the irradiance a few millimetres beyond the tip of the fibre to in excess of the free dielectric breakdown in water (~ 6 GW cm^{-2}) but without exceeding the damage threshold of the quartz glass.

Shockwaves of up to 50 bars (5 MPa) have been reported (Reichel et al, 1991). Sterenborg (1991a) used high speed photography to image a shockwave within a few microseconds of the onset of the laser pulse and determined that plasma expansion produced the greatest acoustic pulse. Rink et al (1995) reached the same conclusion but noted that a second shockwave was also produced following bubble collapse, albeit slightly weaker in magnitude.

The optically focused coupler (lens system) reported by Frank et al (1990) was advantageous in that the laser induced breakdown was independent of the target. However, the distance to the calculus had to be maintained at 0 – 2 mm to be effective as the front was formed to a spherical mirror to reflect and focus the generated shockwaves onto the stone surface. The durability of the coupler was limited by evaporation processes of the brass that formed the lens casing, which eventually formed thin layers on the lenses leading to their destruction. The outer diameter of 4.5 mm and total rigid length of 3.5 cm, along with the need for 600 μm fibre limited the clinical application owing to size and inflexibility.

Similar to the lens system, a spherical fibre tip was investigated (Frank et al, 1990). The fibre had to be held at a set distance from the calculus (2 – 4 mm) and so required visual control. The power density of the laser was increased over a distance of ~ 2 – 3 mm in front of tip, achieving dielectric breakdown when the calculus was brought into this area. However, the polished surface was fragile and easily fractured by the shockwave or damaged by contacting the calculus, and this would be expected in the clinical situation. Clinically, the Nd:YAG laser with spherical fibre tip gave reasonable results, although fragmentation efficiency was dependent on calculus absorption properties.

A further development with the use of focussing optical fibres was proposed by Reichel et al (1991, 1992a), whereby the breakdown threshold in saline could be lowered from 21 GW cm^{-2} to 5 GW cm^{-2} by using an irrigation fluid containing metal ions. The introduction of Fe^{3+} ions (at a concentration of 0.02 mmol L^{-1}) into the water provided

the necessary starting electrons at the beginning of the laser pulse to allow the electron avalanche effect to proceed to a plasma at a lower field strength and, therefore, a plasma and shockwaves could be generated with significantly lower laser pulse energy. This technique was shown to fragment even cystine or COM stones successfully. However, as described previously the problem of fibre damage was a major drawback.

Studies in the use of an optomechanical transducer have also been reported (Maghraby et al, 1990; Muschter et al, 1990; Reichel et al, 1992b). An optomechanical transducer attachment on the end of the fibre was used to convert the laser pulse into an acoustic shockwave. A tungsten metal target (with low work function) was attached to the end of the fibre to intercept the laser beam and generate a plasma. Thus breakdown was induced independent of the calculus composition. One advantage of this method was that the laser beam could not reach the surrounding tissues making the device relatively safe. Various shaped targets were developed including rods and wedges (to generate side-firing shockwaves). Clinical studies showed reasonable success, giving higher fragmentation rates for all stones compared to the focussing fibres, although calcium oxalate monohydrate, cystine, and brushite calculi proved difficult or impossible to fragment. Another drawback was that the coupler was not effective unless placed 0 – 3 mm from the calculus which required direct vision, and furthermore because the diameter was greater than the fibre it offered no advantage over large calibre instruments already available for ultrasonic or electrohydraulic lithotripsy. Also, the durability was limited to several thousand laser pulses and a suitable irrigation system was required with a continuous flow to flush away vaporisation products of the metal tip, otherwise the shockwaves were significantly weakened.

The results of studies have indicated the ‘long-pulsed’ mode of the Nd:YAG laser generates a mainly thermal interaction and does not reliably reduce calculi to a passable size. In contrast, the shockwave nature of the Q-switched mode is better at producing finer fragments but requires a thicker fibre. Thomas et al (1988) noted these problems and abandoned the Nd:YAG laser in favour of the pulsed dye laser.

2.2.3 FREDDY laser

The fragmentation process with the Frequency-doubled double pulse Nd:YAG laser (FREDDY) has been reported to be primarily due to photoacoustical mechanisms and similar to the PDL (Zorcher et al, 1999). The microsecond-duration 120 mJ pulses contain about 20% of their energy at 532 nm which is well absorbed by the calculus and initiates a low density plasma. The remainder of the pulse energy is at 1064 nm and this portion is well absorbed by the plasma causing it to expand and generate a cavitation bubble. Strong shockwaves sufficient to fragment most types of calculi have been reported both on plasma onset and cavitation collapse (Koort et al, 2002).

2.2.4 Er:YAG laser

The flashlamp-pumped solid state Erbium Yttrium Aluminium Garnet laser incorporates erbium, a rare-earth element, to create laser radiation at a wavelength of 2.94 μm. The Er:YAG laser (250 – 500 μs, 50 mJ per pulse) appears promising as a lasertripter, although so far it has only been tested on calculi in vitro (Chan et al, 2000c; Teichman et al, 2001; Chan et al, 2002; Lee et al, 2005) as there is a lack of clinically useful optical fibres for endoscopic delivery. This laser is closer to the absorption peaks of water than the holmium laser (penetration ~ 1 μm in water) and thus vaporises a channel through the water (the 'Moses effect') more efficiently than the Ho:YAG, thereby delivering more laser energy direct to the calculus. Chan et al (2000c, 2002) obtained Schlieren flash images of the interaction and suggested a photothermal mechanism of calculus destruction, possibly initiated by plasma formation, on the evidence of chemical decomposition, melting, and fine fragments, which are all indicative of thermal rather than shockwave events. Although multiple rapidly-expanding vapour bubbles are formed whilst the laser pulse is passing through water (formed into a torpedo shaped void), the absence of a high pressure acoustic shockwave was explained by unsynchronised collapse of these bubbles. Compared to the Ho:YAG laser, results of studies have indicated that for the same fluence the Er:YAG gives a more efficient and precise ablation (Teichman et al, 2001; Lee et al, 2005). However, these investigations were restricted by the damage threshold of the optical fibre for the Er:YAG, whereas commercially available Ho:YAG systems can be operated at much higher fluence levels and so are in fact more efficient clinically. It has been reported that it is important that

the fibre is in close contact with the calculus otherwise there is no plasma or optical breakdown of the material. Despite not being thermally confined, collateral tissue damage is minimised because of the low optical penetration, although the ablation volume is similar to the Ho:YAG because of heat diffusion. Teichman et al (2001) noted plasma formation but did not detect significant shockwaves, and they concluded that any photomechanical effects were secondary to thermal ablation.

2.2.5 Pulsed dye laser (PDL)

The flashlamp-pumped pulsed-dye laser (PDL) has been the most popular laser lithotripter and has been extensively studied. The use of PDL was considered to be advantageous as they can be tuned to emit at wavelengths where there is preferential absorption by the target, and pulses are of high energy and of short duration. The laser medium is an organic dye dissolved in alcohol, the choice of dye determines the wavelength range. Liquid dyes have complex sets of electronic and vibrational energy levels, and the wavelength emitted depends on the type of dye used. Coumarin dye generates green light at ~ 504 nm and this has been the most widely used, others have been tried including Rhodamine 6G (~ 590 nm) and Rhodamine 700 (~ 720 nm). A range of pulse durations have been investigated (1 – 300 μs) and the optimum laser parameters were found to be a wavelength of 504 nm, pulse duration of 1 μs, repetition rate of 5 Hz, fibre core diameter of 200 μm, and typical pulse energy of < 140 mJ. At 504 nm the differential in absorption between the calculus and the surrounding tissues was found to be greatest within the range of wavelengths available, and therefore the safest option. A 1 μs pulse was found to be long enough to permit adequate energy to be delivered to cause fragmentation, but sufficiently short to minimise collateral thermal tissue damage, and the relatively slow 5 Hz pulse rate minimised residual elevation in temperature caused by the previous laser pulse.

In an early study, Watson et al (1987a) suggested that fragmentation with the PDL is a photothermal effect attributable to highly localised temperature gradients, causing thermoelastic expansion of heated material followed by fracture. However, Teng et al (1987a, 1987b) observed that lithotripsy was more efficient when the calculus was

immersed in liquid than when it was in air, suggesting an advantageous coupling in liquid. According to the investigators, shockwaves generated in the surrounding liquid that propagate towards the calculus. Bubble formation by laser induced vaporisation of water was considered unlikely as there was more energy in the laser pulse than that required to form a steam bubble of the size observed (diameter ~ 4 mm). Therefore, shearing of water (cavitation) by the stress wave was suggested as a possible mechanism, which was later confirmed by Rink et al (1995). High speed flash photography revealed the mechanism to be photoacoustical, where a plasma was initiated on absorption of the laser light by the surface of the calculus. The plasma then absorbed all the subsequent laser energy and expanded, generating a shockwave and cavitation bubble. A model by Jiang et al (1992c) indicated the role of calcium ions liberated from the calculus material in the plasma formation. Shockwaves in excess of 100 bars (10 MPa) were recorded. Rink suggested that only the shockwave generated by the collapse of the cavitation bubble was strong enough to cause fragmentation, although this was contrary to evidence by Teng et al (1987) indicating that stone damage occurs before the bubble collapse. The investigators also suggested that jet formation played a role in the fragmentation process.

The mechanism of laser-calculus interaction proposed by Watson et al (1987a) above correlated well with the observation that the threshold fluence depended on the absorption properties of the calculus (i.e. better with pigmented calculi). Furthermore, the fibre was required to be either in contact with the calculus or no greater than ~ 3 mm separation, otherwise no effect took place. Watson et al (1987a) observed that fragmentation rate was proportional to the laser pulse energy and noted that the threshold for fragmentation was between 40 – 50 mJ, efficient at 60 – 70 mJ, although some calculi required up to 100 mJ laser energy. The fragmentation threshold increased with increasing pulse duration, indicating shorter pulses were slightly better.

Clinically, the PDL has delivered excellent results for pigmented calculi (Dretler, 1990), however, pale calculi such as cystine are not fragmented, brushite stones (calcium hydrogen phosphate dihydrate) are difficult, and 100 % COM stones are resistant.

Corbin et al (2000) noted fragments were larger and sharper compared to the Ho:YAG. Zerbib et al (1990) reported 78.3 % clearance with 80 mJ pulses, Dretler et al (1987) was less successful at 64% but with lower energy pulses of 60 mJ, and also noted that there was minimal effect on tissue.

To improve lithotripsy with pale stones, Rudhart and Hirth (1994) and Tasca et al (1993) investigated the use of sensitising methods (dyes) to improve absorption by the stone surface and hence enable plasma formation at lower energies, making the fragmentation independent of the stone coloration. Saline solution irrigation was substituted for 2% solution of rifamycin which was used to stain the surface of the calculi, enabling successful fragmentation of even cystine stones. Patients were given rifampicin (also improves the absorption) a few days before treatment which enabled lower concentrations of rifamycin in the irrigation fluid. However, there were problems in that as a side effect the urothelium was also stained and risked possible damage, although since the solutions are relatively transparent the urologist could target the stones with a degree of accuracy.

Bhatta et al (1989b, 1989c) noted problems with the PDL in that good vision was needed to ensure the laser fibre contacts the calculus, otherwise there is risk of tissue damage from the laser plasma and also the sharp fibre end. As an alternative technique, the investigators carried out tests using a metal cap on the fibre tip acting as a “plasma shield” that was also visible under fluoroscopy. The metal cap facilitated the conversion of the light pulse to a shockwave, and in contact mode a “jack hammer” type action resulted. Cystine calculi could be fragmented, albeit slowly. However, this approach was later abandoned as it had no significant advantages.

Another development with the pulsed-dye laser were studies utilising acoustic signals and plasma optical emissions to monitor and guide calculus fragmentation (Daidoh et al, 1991; Jiang et al, 1992b,1992c: Rosen et al, 1993). Using various targets including different urinary calculi, guidewires, catheters, tissue etc. it was shown that it was possible to target the calculus without direct vision. Calculi gave strong acoustic and

plasma signals, whereas a strong acoustic signal only indicated that the laser was striking blood or tissue, and when there were no signals detected the laser was targeting healthy tissue. As a result of these studies it was concluded that guided lasertripsy is a possibility.

In conclusion, the PDL pulse duration is at the transition between stress and thermal confinement implying both thermal and mechanical effects, although cavitation dynamics were found to the most significant. The advantages of the PDL laser are the small size of the optical fibres (core 200 μm), a pulse width short enough to prevent thermal damage and long enough to fragment calculi, and a wavelength where there is minimal effect on soft tissue. The drawbacks with the PDL are that the complexity of the technology contributes to its high cost as the dye in these lasers must be changed at regular intervals so limiting it to specialist centres. Crucially, the dye laser is affected by stone colour and it cannot fragment calculi that are pale and hard compositions. Also, the fibre is susceptible to damage at high energy levels making it difficult to maintain stable energy output. Overall, these considerations suggest that the PDL is not the optimum lasertripter.

2.2.6 KTP laser

Helfmann et al (1990) described the use of a double-pulse technique for lasertripsy, with an initial second harmonic pulse (532 nm, 6 ns, 15 mJ) followed by a delayed first harmonic pulse (1064 nm, 8 ns, 50 mJ, ~ 10ns delay), which were effectively superimposed to create a single 65 mJ pulse. Various calculi, including calcium oxalate stones, were successfully fragmented although with some variation in efficiency. However, fibre damage due to high peak power of the Q-switched 532 nm pulse was a problem, but longer pulse durations reduced this damage with only a small increase in the threshold for calculi fragmentation. The investigators reported the best outcomes when the 532nm pulse was fired first, followed by a ~ 10 ns delay before the 1064 nm pulse, although Zorcher et al (1999) used simultaneous 532/1064 nm pulses (1 – 1.4 μs) with similar results. As calculi absorb 532 nm better than 1064 nm, the intent of this technique was to use 532 nm light to initiate a plasma at the calculus surface which then

acts as a black body absorber, and the remainder of the light at both wavelengths pumps the plasma at high efficiency. The mechanism was not investigated, but it is likely that the plasma induces a cavitation bubble, which on collapse causes a shockwave (Müller et al, 1993). In a comparison with the excimer, PDL and Nd:YAG lasers, Müller et al (1993) proposed the double pulse 532/1064 nm as the laser of choice for calculus fragmentation although the Ho:YAG is, however, more efficient.

2.2.7 Ruby laser

Although the ruby laser was one of the first lasers to be studied for lithotripsy, there have been relatively few reports in the literature. Early investigations with a pulsed ruby laser (694 nm, 170 ns) revealed some difficulty in fragmenting pale calculi (Berenberg et al, 1996; Shkadarevich et al, 1996). It was found that staining calculi with blue or black dye significantly enhanced the speed of lithotripsy by a factor of 1.5 – 2 times, and also, that the action was more pronounced in wet calculi than dry (Mulvaney and Beck, 1968). It was suggested that the laser energy absorbed by the surface of the calculus leads to vaporisation of moisture, although Lauterborn (1974) produced cavitation bubbles and shockwaves indicating a photomechanical action.

Fair (1978) adopted a different approach, focussing a Q-switched ruby laser (20 ns) onto a metal target to generate shockwaves. Various urinary calculi, placed in direct contact with the metal, were successfully fragmented using 2 J laser pulses that reportedly generated pressure waves as high as 10 kbar (1 GPa), although this pressure is likely to be an overestimate.

Pupkova et al (1993, 1994) used the direct ruby laser beam (1 μs pulses) delivered via 400 μm fibre for clinical lithotripsy. As with previous studies, hard pale calculi (cystine and COM) could not be fragmented. This conventional approach did, however, overcome the disadvantage of the optomechanical coupler used by Fair where the calculus must be in direct contact.

Based on the ruby laser, Berenberger et al (1993a, 1993b, 1994) developed a theoretical model of the laser-calculus interaction process. They concluded that the dominant process is direct absorption by chromophores on the surface of the calculus, hence the improvement in using dyes, leading to local vaporisation and plasma. Fragmentation then occurs as a result of hot gas production at the site of the micropores, leading to material destruction. However, the proposed model does not offer a complete description, as events following the thermochemical changes such as shockwaves, and cavitation bubble formation are not incorporated.

2.2.8 Alexandrite laser

The alexandrite is a vibronic solid-state laser with a composition of chromium-doped $BeAl_2O_4$ (a mineral known as alexandrite). Its wavelength ranges from 380 – 830 nm, with the strongest laser emission between 700 – 830 nm. This provides the possibility of a tuning range.

The alexandrite laser (755 nm) has been studied for use in lithotripsy as both a Q-switched (30 – 1000 ns) laser system (Ubelacker, 1992), and as a pulse-stretched (2 – 3 μs) laser (Brinkmann et al, 1990). It combines the advantages of some other lasers, such as the ability to use thinner and more flexible fibres than the Nd:YAG, and better tissue safety than the PDL (Maghraby et al, 1990), although compared to the PDL more than twice the pulse energy is required (Zumbe et al, 1993). However, it cannot fragment harder compositions such as calcium oxalate monohydrate (Miller et al, 1991), calcium phosphate and 100 % uric acid (Zumbe et al, 1993), but has been found to be more successful if the surface is irregular (Miller et al, 1991) or a thicker fibre and higher energy are used (Mattioli et al, 1991). To overcome this deficiency, attempts have been made to pre-stain the calculus with dye that absorbs well at 755 nm, such as sterile indocyanine green (Cardio green), however, this also stains the urothelium thereby increasing the risk of accidental perforation.

There have been reports of fibre fragmentation with the short pulse alexandrite, and shards (up to 3mm) can become embedded in urinary tract leading to serious complications. The long pulse alexandrite laser, which was developed to match the dye laser, overcomes fibre damage problems because of its lower peak power and is also better suited for calculus fragmentation. However, long pulse lasers have problems such as temporal nonuniformity, and pulse inconsistency (Simons and Koschmann, 1992).

The fragmentation mechanism has been reported as an initial plasma dependent on the composition and colour of the calculus surface, followed by the development and expansion of a gas bubble, creating a shockwave which interacts acoustically with stone through reflection and transmission (Zumbe et al, 1993). Observers have noted a plasma flash and audible click (Steiger et al, 1990). Compared to the dye laser there appears to be a much longer plasma induction phase (Mattioli et al, 1991), and fragment size has been reported in some cases as smaller and larger in others (Corbin et al, 2000). These findings suggest that optical breakdown in water plays a significant role in the process, and therefore shockwaves are likely to be involved.

Clinically there have been mixed reports with the alexandrite, for example Pearle et al (1998) found the alexandrite laser to be effective, whereas Denstedt et al (1997) reported fibre burn off and the inability to fragment hard and pale stones, concluding that the laser was not the optimum lasertripter.

2.2.9 Ti:sapphire laser

Jiang et al (1993) investigated the potential use of the solid state flashlamp pumped Titanium-doped Sapphire laser (792 nm, 2 μs pulses, up to 160 mJ per pulse) for lithotripsy, as an alternative to the dye laser. In vitro lithotripsy in water resulted in a bright white flash of the plasma emission, a sharp “crack” sound, strong shock waves, fibre recoil and stone propulsion. The plasma thresholds were dependent on the colour of the stones and it often took several consecutive pulses to initiate, an effect attributed to the heating and eventual vaporisation of the surface which in turn induced plasma

formation. However, like the pulsed dye laser, this laser was unable to ablate cystine calculi and had a significantly higher ablation threshold. It did offer some advantages over the dye laser including that of reduced maintenance requirements, the possibility of higher pulse repetitive rate and also improved safety on tissue, although it is not the lasertripter of choice as it cannot fragment cystine calculi.

2.2.10 Nd:Glass laser

At 1055 nm (pulses 30 ns, 10J) the Nd:Glass laser is essentially identical to the traditional Nd:YAG laser. D'yakonov et al (1991a, 1991b) reported an Nd:Glass laser to trigger shockwaves from a focussing optoacoustical cell, and successfully fragmented calculi placed in the focal zone, although the calculus composition was not stated. Pressures were calculated to be ~ 2 kbar (200 MPa), but were, however, measured to be lower than predicted possibly due to the shockwave becoming non-linear at high pressure. The setup used was purely experimental and not suitable for clinical use.

2.2.11 Multi Nd:YAG laser

Wollin et al (1996a, 1996b) reported the use of a "multi-Nd:YAG" (1440 nm) with a pulse duration of 650 μs, and found that calculi were fragmented provided the optical fibre was within 1mm of contact. Although the study was not designed to determine the mechanism, it seems likely that both thermal and plasma mediated interactions were involved. Plasma formation was not always seen, however, although fragmentation was still effective, possibly since 1440 nm is well absorbed by water and the water held within the stone undergoes thermal vaporization leading to localised ablation of the calculus. Multiple drill holes were formed that eventually joined and the stones fragmented along natural cleavage lines.

2.2.12 Er:Cr:YSGG laser

The Er:Cr:YSGG laser (2.79 μm, 250 – 500 μs, <1J per pulse) has been studied for lithotripsy application using optical fibre delivery (Bloch et al, 1993). The laser was used in free-running pulsed mode and also in Q-switched mode, and in combination.

The calculus was first drilled using the longer free-running pulses, and then the fibre was inserted into the hole and Q-switched pulses fired to fragment the stone, probably by a shockwave mechanism although this was not investigated. The calculi were fragmented by the direct absorption of the laser energy, resulting in photothermal ablation. As with the Er:YAG, the main drawback at this wavelength is finding a suitable material for the optical fibre, although fluoride fibre was tried with some success and there are now new infrared fibres available.

2.2.13 Free electron laser

Using a free-electron laser, Chan et al (2000a) investigated the radiant threshold exposures for ablation across the range 2 – 10 μm. They concluded that urinary calculi have mid-infrared absorption bands where the ablation threshold is lowest i.e. the optimum laser wavelength for efficient ablation lies in this region. Although the free electron laser itself is not suitable as a clinical laser on account of its large size and cost, Wantanbe et al (2001) carried out an in vitro study on bilirubin calculi. The wavelength, in the infra red, was chosen to match the molecular oscillation of the ester molecules in bilirubin calculi, such that the bonds were selectively excited and broken, destroying the molecular structure of the stone. The investigators reported that the outcome was to disintegrate the laser-irradiated site on the gallstone to powder in a matter of seconds. This method indicated a possible way to target calculi without risk of injury to surrounding tissue, although currently the free electron laser is not a viable cost effective option.

2.2.14 Carbon dioxide laser

In the first studies of laser-calculus interaction by Mulvaney and Beck (1968), urinary calculi of various compositions were irradiated with a 50W CW CO_2 laser (10.6 μm). Predictably at such high power, all types of calculi were successfully melted and disintegrated, accompanied by significant shockwaves on account of the high absorption by the interstitial water which was vaporised to steam. Operating in continuous wave the CO_2 laser was not suitable clinically due to significant collateral damage from the build up of heat from the long exposure times, however, modern CO_2 lasers can be

operated in pulsed mode and so may become a possibility for lithotripsy in the future. The major remains the lack of a suitable optical fibre to transmit the far-infrared radiation, although there have been recent developments in this area.

2.2.15 Excimer laser

In an early study by Shi et al (1990, 1991), the XeCl excimer laser (308 nm, 160 ns, 80 – 110 mJ mm^{-2}) was used successfully for the fragmentation of biliary calculi and with a low threshold. Fragmentation was found to be significantly more efficient for pigmented stones, and also improved at higher pulse repetition rate and larger spot size. This indicated a dependence on the absorption properties of the calculus and implies direct laser interaction with the stone surface i.e. a thermal action. However, fragmentation in liquid produced larger fragments than in air, suggesting a contribution from shockwaves.

Benaim et al (1992) reported a different set of findings in their experiments using the XeCl laser (200 ns, 60 – 100 mJ) for the fragmentation of urinary stones. They observed two distinct phases during the laser-calculus interaction, first a threshold phase where pure ablation removed a portion of calculus material (~ 5 J cm^{-2}), followed by a second phase (~ 10 J cm^{-2}) where popping sounds and sparks were noted, indicating plasma formation. Compared to the dye laser, they noted that fragmentation thresholds were significantly lower by a factor of ~ 10, and also that the excimer laser created smaller fragments causing the stone to crumble. A basic mechanism was proposed, that organic molecule decomposition requires multiphoton absorption processes to initiate plasma, and increasing the fluence induces plasma formation followed by a very strong shockwave, which causes mechanical fragmentation.

Siano et al (1995) used time-resolved imaging to record bubble dynamics during excimer laser lithotripsy, identifying shockwave generation both on plasma formation and cavitation bubble collapse, although the relative magnitudes of the acoustic transients were not measured. Plasma was observed followed by a strong acoustic wave

travelling at ‘supersonic speed’, then after a few microseconds a cavitation bubble evolved. After the bubble had expanded and then collapsed, a rebound bubble was seen to form. Interestingly, they noted cavitation bubble size depended on calculus composition, similar sized bubbles were seen during fragmentation of calcium phosphate and xanthine stones whereas approximately double the laser energy was required for calcium phosphate compositions.

Scholz (1991) carried out a clinical study for the treatment of calculi in the salivary glands, and in all cases stones were completely fragmented. He concluded that the XeCl laser is particularly suitable for this purpose, although the pulsed dye laser was better for larger and more resistant stones.

2.2.16 Dual wavelength laser

Ultraviolet laser radiation has also been employed in lasertripsy using dual-wavelength lasers, where the fundamental wavelength is passed through a frequency doubling crystal to generate the second harmonic in the UV region. The purpose of utilising two overlapping pulses was initially for calculus/ureter identification via the detection of the fluorescence signal. If the beam impacts on a calculus a strong fluorescence signal is detected, whereas if the signal is weak or not present then it indicates that the beam is misdirected and tissue damage may result. In the latter case, by design the laser pulse is terminated before the full output is delivered. Shi et al (1990, 1991) investigated this technique using the alexandrite laser (755 nm), inducing fluorescence with the harmonic at 375 nm (16 J cm^{-2}, 100 ns), or by 308 nm excimer laser, although they determined the best calculus/tissue discrimination at 755 nm alone as there was no fluorescence signal from tissue, so the UV component was not required for this purpose.

Steiger et al (1991, 1994) and Steiner et al (1991) investigated a dual-wavelength alexandrite system for calculus fragmentation with an adjustable wavelength ratio (755:375 nm). The investigators found that all types of urinary stones could be fragmented with this laser although with varying efficiencies, and except for a pale

calcium oxalate stone all results were apparently better than published results for the dye laser.

A dual-wavelength ruby lasertripter (694 nm / 347 nm) was investigated by Shkadarevich et al (1996). Experiments were carried out injecting the second harmonic at the same time as the fundamental, delivering 3 mJ at 347 nm and 16 mJ at 694 nm with a pulse of 170 ns. This technique reportedly fragmented pale stones more efficiently, although there was no improvement for other calculi.

Investigators proposed the interaction process with the dual wavelength laser to be plasma mediated, with events triggered by photon absorption leading to an electron/ion plasma, and due to the higher surface absorption in the UV region the calculus material is more easily ionised and the UV produces an earlier and more consistent plasma with less energy (Steiger and Giesel, 1994). The plasma is formed by multiphoton ionisation in which free electrons are accelerated by "inverse Bremsstrahlung" causing multiplication by collision with atoms and molecules of the medium (Steiger et al, 1991). The remaining pulse energy is scattered and absorbed thus heating the plasma to a higher temperature, although UV is not as efficient at accelerating electrons as IR wavelengths and so does not drive the plasma to expand to the same extent (Muscheter et al, 1990). The heating of the plasma also heats the stone surface, and causes explosive boiling of bioliquid and optical breakdown (Maghraby et al, 1990). The expanding plasma drives a shockwave front through the medium, leaving behind a cavitation bubble, which expands against the static pressure of the liquid until eventually collapsing and generating a further shockwave. The resulting shockwaves are therefore largely independent of the surface colour of calculi (i.e. optical properties), although the fragmentation efficiency does depend on the hardness of the composition (i.e. mechanical properties).

2.3 Conclusions

The review of the literature has found that there have been a number of investigations into the interaction of laser radiation with calculi, and with many different laser systems. Significantly, many of the studies were conducted in the late 1980s and 1990s when lasers were first introduced clinically and there was much interest in finding the optimal laser lithotripter. During that period the pulsed dye laser emerged as the most popular but has since been overtaken by the holmium YAG laser which is generally accepted as the state of the art.

What are lacking, however, are published reports of experimental studies on the laser-calculus interaction of current laser systems, such as the variable pulsed holmium YAG laser, and yet there is a need for further basic research to optimise the clinical outcome. In particular, there has been some disagreement between investigators as to the magnitude of Ho:YAG laser-induced shockwaves and whether the process involves plasma formation. Chan et al (1999a, 1999b) have presented strong evidence for a dominant photothermal mechanism with the ~ 300 μs pulsed Ho:YAG laser, whereas Sperrin (2000) has reported significantly higher shockwave intensities for a similar laser, with pressures in excess of published failure strength of calculi and of magnitudes comparable to known shockwave action lasers (i.e. LISL lasers such as the Q-switched Nd:YAG laser).

This research is, therefore, partly aimed at furthering the work by Chan et al (1999b) and Sperrin (2000) and focussing on specific studies on the action of the variable pulsed holmium laser on calculi in water. In order to further characterise the dynamics of the interaction the use of a needle hydrophone will enable more precise spatial measurements of the shockwave and potentially at closer range compared to the limitations of the large area membrane hydrophone used by Sperrin (2000). Furthermore, comparing the variable pulsed Ho:YAG laser to a Q-switched Nd:YAG laser under identical conditions will reveal how the shockwave dynamics vary between a plasma mediated shockwave action laser and the Ho:YAG laser, for different pulse durations.

In addition, another area where there has been a lack of research is in the use of a laser as a spectroscopic tool for the study of plasma formation on calculi. As the use of a laser to fragment calculi has significantly advanced to a point where clinical success is more or less guaranteed, and that the calculus is completely destroyed in the process, there has been an important impact on the traditional management of the condition in that calculi samples are no longer routinely available for analysis. Thus, there is a need for basic research on the potential of using the laser to probe the calculus material for spectroscopic information on composition, as this could potentially be carried out on-line during lithotripsy. In particular, the use of a plasma-forming laser to carry out Laser Induced Breakdown Spectroscopy (LIBS) to reveal information on elemental composition of samples of human calculi is a focus of this research.

As new laser devices are continually being developed and in particular the range of wavelengths available with compact, low-cost, diode lasers is rapidly growing, there is potential for new lasers in lithotripsy application. As part of this research work the optical properties of a selection of calculi will be investigated as this will indicate, for the spectral range measured, the laser wavelengths that are suitably matched to absorption peaks. This will then give an indication for possible further work.

In the next section, the background theory of laser-calculus interaction is described. The processes of optical absorption, photothermal interaction, photomechanical interaction, and plasma processes are presented.

Chapter 3
Background Theory

3.1 Introduction

The mechanism of the laser-calculus interaction is dependent upon the laser parameters and the material properties. The laser parameters are characterised by the laser wavelength, the pulse duration, and the power density (Helfmann and Müller, 2001). In addition to the laser parameters, the properties of the calculus material have considerable effect on the mechanisms of the laser action process (Jiang and King, 1994). These material properties can be divided into optical and thermal properties, where the first set of properties determines the primary distribution of laser light inside the calculus material, while the second deals with the conversion of light energy into heat and the subsequent transport via thermal conduction (Welch et al, 2004). The laser, material and other relevant parameters referred to in this chapter are given in Table 3.1.

Table 3.1: Nomenclature of laser and material parameters

Type	Description	Symbol	Definition	Units
Laser parameters	Laser wavelength	λ	Inversely related to frequency ($v = f\lambda$)	nm or μm
	Laser pulse energy	Q_0	Optical energy delivered per pulse	mJ or J
	Laser pulse duration	τ_p	Time extent of laser pulse	μs or ms
	Fluence	F	Optical energy per unit area	J cm^{-2}
Material properties	Absorption coefficient	μ_a	Product of absorber concentration and absorption cross section	cm^{-1}
	Optical penetration depth	δ	Depth at which the energy of laser beam reduced by factor 1/e	mm
	Optical reflectivity	R	Fraction of incident light that is reflected from the surface	
	Thermal diffusivity	α	Measure of heat flow	$mm^2\ s^{-1}$
	Speed of sound	σ	Speed of sound in calculus or water	mm μs^{-1}
	Thermal diffusion time	τ_{th}	Degree of heat diffusion within optical penetration depth	μsec or msec
	Acoustic diffusion time	τ_a	Degree of acoustic wave diffusion within optical penetration depth	μsec or msec
Other	Depth	z	Depth in tissue	cm
	Laser spot size	r_0	Radius of laser spot	mm
	Pressure	P	Magnitude of stress wave or shockwave	MPa
	Temperature rise	T	Temperature increase induced by stress wave or shockwave	^oC

The laser-calculus interaction can be categorised according to the nature of the mechanism into photothermal processes and photomechanical processes (Boulnois, 1986; McKenzie, 1990; Chan et al, 2001; Berlien and Müller, 2003; Vogel and Venugopalan, 2003).

3.2 Absorption

The most important factor in the process of interaction between laser radiation and calculus is the amount of optical energy absorbed. If there is insufficient absorption then the interaction will not lead to sufficient heating and/or mechanical stresses to cause material damage to the calculus. The absorbed energy is governed by the incident laser fluence, F (J cm^{-2}), and the optical attenuation properties of the water and/or calculus.

The absorption of photons can, in principle, take place in all molecular components present. However, chromophores, in the calculi and impure water, lead to discrete and intense absorption bands at specific wavelengths. Besides electronic transitions, higher harmonics and combination modes of various vibrations may also be excited. During laser irradiation, however, thermally induced changes such as chemical decomposition or dehydration may alter the absorption properties of the calculus (Boulnois, 1986).

When laser radiation is incident on the surface of the calculus material photons undergo absorption and scattering. Generally, scattering is only significant where there is a greater diffuse reflection e.g. a pale calculus, and can be ignored for most other cases, in particular where there is very high absorption (Chan et al, 2001). Therefore, for simplicity, the depth to which the laser radiation penetrates can be assumed to be wholly dependent on the absorption properties of the material.

Beers Law gives the relationship between absorbance (A) (no units), which is a measure of the amount of absorption of light as it passes through a material, and the molar absorbtivity (ε) (L mol^{-1} cm^{-1}) the path length (b) (cm) and the molar concentration (c) (mol L^{-1}) as:

$$A = \varepsilon bc \qquad (1)$$

The optical absorption is characterized by the wavelength-dependent absorption coefficient, $\mu_a(\lambda)$ (cm^{-1}), which is the product of absorber concentration and absorption cross section. The distribution of the laser beam inside the absorbing material depends on the incident fluence, H_0 (J cm^{-2}) and the absorption coefficient, and the amount of reflection at the surface (R). According to Beer's Law, the fluence F(z) decreases exponentially with depth (z) (cm):

$$F(z) = H_0 (1 - R) \exp(-\mu_a z) \quad (2)$$

The depth at which the energy of the collimated laser beam has been reduced by the factor 1/e (i.e. to 37% of the incident laser fluence) is termed the optical penetration depth, δ (cm). This depth is a measure of the mean free path for an attenuation event and is defined as the reciprocal of the absorption coefficient:

$$\delta(\lambda) = \frac{1}{\mu_a(\lambda)} \quad (3)$$

For the Ho:YAG laser the absorption coefficient for uric acid calculus is ~ 14 cm^{-1}, therefore, using equation (3) gives an optical penetration depth in the calculus material of ~ 70 μm. In comparison, for water the penetration depth at the holmium laser wavelength is ~ 400 μm (Chan et al, 2001).

The Nd:YAG laser radiation at 1064 nm has an optical penetration depth in water of ~ 8 mm. However, the short pulse duration of the Q-switched laser (nanoseconds) gives rise to non-linear dynamics and this considerably increases the absorption coefficient.

The optical penetration depth, together with the area of the incident laser beam (spot size) determines the irradiated volume. If the laser pulse has sufficient energy then it will raise the temperature of the target volume resulting in material ablation. Typically, for pulsed lasers ablation is the outcome of more than one mechanism and is a combination of photothermal and photomechanical processes (Schmidt-Kloiber, 1991).

3.3 Photothermal Processes

Direct absorption of photons within the irradiated volume by means of excitation of electrons and molecules to higher energy levels leads to an increase in kinetic energy of

the molecular species within a confinement where a local thermal equilibrium exists. An increase of kinetic energy at the microscopic level is interpreted as a temperature rise in the laser-irradiated spot within the material (Welch, 1984).

In laser lithotripsy where the calculus is immersed in liquid, the thermal processes may result in vaporization of water and calculus material. Due to the small spot size and short optical penetration depth the heating is initially highly localized, but will dissipate into surrounding regions by the process of heat diffusion. The time taken for heat within the irradiated volume to diffuse by thermal conduction into the surroundings depends on the temperature gradient. This is the characteristic thermal diffusion time, τ_{th}, which is a function of the laser spot radius, r_0, and the optical penetration depth (McKenzie, 1990). There are two conditions of interest:

$$\tau_{th} = \delta^2 / 4\alpha \text{ when } r_0 \geq \delta \quad (4)$$

$$\tau_{th} = r_0^2 / 4\alpha \text{ when } r_0 < \delta \quad (5)$$

where α is the thermal diffusivity ($mm^2\ s^{-1}$) and r_0 the laser spot radius (mm). For the case of the Ho:YAG laser with fibre delivery ($r_0 \sim 600$ μm) in water ($\delta \sim 400$ μm) the spot size and optical penetration depth are comparable. Using equation (4) and taking $\alpha = 0.15\ mm^2\ s^{-1}$ for water at 37 ^oC (Duck, 1990) then the thermal diffusion time for the Ho:YAG laser-water interaction is 267 msec. In contrast, for the interaction between the laser and calculus material taking the quoted diffusivity of the calculus as $0.5\ mm^2\ s^{-1}$ and the penetration depth 0.1 mm (Duck, 1990) then $\tau_{th} = 5$ msec. Thus, the time taken for the initial deposited laser energy to move beyond the laser affected zone is significantly longer in water than in calculus material. For the Nd:YAG laser in water, assuming a focussed spot size of diameter ~ 0.15 mm (i.e. less than the optical penetration depth), the thermal diffusion time is 38 ms. Thus, for Q-switched operation ($\tau_p \sim 6$ nsec) the interaction is likewise thermally confined.

The relationship between the thermal relaxation time and the duration of the laser pulse influences the confinement of the thermal energy. In the case of the Ho:YAG laser the pulse duration is of the order of several hundred microseconds (in this study the pulse duration ranged from 120 – 800 μs), which is shorter than the thermal relaxation times calculated above for both water and calculus material. Therefore, during the Ho:YAG

laser- water/calculus interaction the heat is retained within the irradiated region during the time of the laser pulse. This condition is termed "thermal confinement" or local thermal equilibrium i.e. $\tau_p << \tau_{th}$. The localisation of deposited energy would be expected to lead to efficient thermal ablation processes (Welch et al, 2004).

During the period of thermal confinement the local temperature is increased in proportion to the rate of photon absorption. Heating commences at the onset of the laser pulse and the temperature rises until the processes of ablation, vaporisation, and melting occur. Hence the temperature rise is a function of the absorption coefficient (Chan et al, 2001) and the temperature profile with depth is given as:

$$\Delta T(z) = \frac{\mu_a(\lambda) H_0}{\rho c_p} \exp(-\mu_a(\lambda) z) \qquad (6)$$

Where ΔT is the temperature increase (^oC), ρ is the material density (kg m^{-3}), c_p is the material specific heat capacity at constant pressure (J kg^{-1} ^oC). A temperature rise ≥ 100 ^oC causes vaporisation of water, whereas higher temperatures may lead to chemical decomposition in the irradiated volume of the calculus. Table 3.2 gives the critical breakdown temperature for some common types of urinary calculi (Teichman et al, 1998a; Glickman et al, 1999b).

Table 3.2: Critical breakdown temperatures for selected calculi

Calculus composition	Breakdown temperature (^oC)
Struvite	100
Brushite	109
Whewellite	206
Cystine	264
Uric acid	360

3.4 Photomechanical processes

Photomechanical interactions are the result of very rapid heating in a localised volume causing thermoelastic expansion, or vaporization of water leading to pressurised steam (Teng et al, 1987a; Vogel et al, 1989; Jiang et al, 1991a). Rapid localised heating is usually attributable to very short duration laser pulses, whereas the vaporization of

water may be driven by a high absorption at the laser wavelength, as is the case for the Ho:YAG laser.

Laser-induced temperature increase on a short timescale generates impulsive mechanical excitation. The conversion of a fraction of the laser energy into mechanical energy creates stress waves in the form of acoustic and shock waves. Acoustic waves propagate at the speed of sound; σ = 1.5 mm μs^{-1} for water at 37 ^{o}C (Duck, 1990), whereas shock waves are supersonic. For the optimisation of the mechanical effect the laser pulse duration has to be shorter than the time it takes for the stress wave to propagate out of the zone of absorbed photons, referred to as the acoustic diffusion time, τ_a. Analogous to the thermal confinement criteria, where mechanical energy is retained within the irradiated region during the time of the laser pulse, the condition is termed "stress confinement" and its criterion is given by (Jansen et al, 1996):

$$\tau_p < \tau_a = \frac{\delta}{\sigma} \tag{7}$$

Where τ_p is the laser pulse duration (μs) and σ is the speed of sound in the target material (mm μs^{-1}). Calculus fragmentation by shock waves is called laser induced shockwave lithotripsy, or LISL (Schmidt-Kloiber et al, 1985). For the case of the Q-switched Nd:YAG laser radiation in water ($\delta \sim 8$ mm; σ = 1.5 mm μs^{-1}) it has a stress confinement time of ~ 5 μs which is considerably longer than the laser pulse duration (~ 6 ns). Therefore, with sufficient pulse energy the Q-switched Nd:YAG would be expected to generate strong shock waves in water with efficient conversion of optical energy into mechanical energy (Vogel et al, 1999). In contrast, for the Ho:YAG laser in water the stress confinement time is ~ 0.3 μs and therefore pulses of several hundred microsecond duration are not stress confined.

Stress confinement also requires thermal confinement, and therefore the change in pressure can be derived from the change in temperature given in equation (6):

$$\Delta P = \sigma^2 \rho \beta \Delta T \tag{8}$$

Where β is the volumetric thermal expansion coefficient (K^{-1}). This implies that the pressure profile is dependent on the temperature profile, and therefore the absorption coefficient and the laser fluence will determine the magnitude of the generated pressure pulse within the heated volume. However, this relationship only applies to stresses resulting from the fractional change in volume following thermal expansion and these are likely to be insignificant compared to pressures arising from vaporisation (phase change) processes.

3.5 Thermoelastic expansion

In the case where the laser beam vaporises a path through the water to directly irradiate the calculus, such as may occur with the Ho:YAG laser, the direct absorption of the laser energy on the calculus surface causes sudden thermoelastic expansion of the heated material (Welch et al, 2004). This expansion generates a stress wave with a magnitude proportional to the absorbed energy (and hence dependent on the absorption coefficient and the laser fluence, as described in the previous section). The stress wave propagates out of the heated volume as a compressive wave, both into the calculus and also outwards towards the surface. The half of the stress wave that travels to the surface is reflected back at the boundary because of the step change in acoustic properties between water and the calculus material. The acoustic impedance of calculus material is greater than that of the surrounding water, and therefore the reflected wave undergoes a phase inversion from a compressive wave to a tensile wave. This tensile wave follows the compressive wave travelling into the calculus material, forming a bipolar wave. Hence there is a sharp pressure gradient between the compressive and rarefractive regions which may overcome the mechanical strength of the calculus material causing fragments to be removed. This process is known as spallation (Chan et al, 2001).

3.6 Microexplosion

As with thermoelastic expansion, where the laser wavelength is strongly absorbed by water and the beam may directly irradiate the calculus (as is the case for the Ho:YAG laser) the rapid vaporization of interstitial water in the calculus material gives rise to laser induced micro-explosions (Marjaron et al, 1999). Calculi are porous and comprise of about 10 % water, thus when irradiated with laser radiation that is strongly absorbed

by water, steam is generated in the pores. The pressure of the expanding steam may be sufficient to rupture the surface of the calculus, ejecting fragments and causing internal fractures.

3.7 Shockwave-induced ablation

Intense shockwaves may be produced during the collapse of vaporized bubbles, a process known as cavitation (Vogel and Venugopalan, 2003). If the laser light is strongly absorbed by water, steam is created which expands under pressure to form a bubble. The mechanical energy stored in the bubble is released when it becomes unstable and collapses, generating a pressure gradient. A second rebound bubble may form and undergo collapse, releasing pressure and generating a further shockwave. Calculi may be fragmented by this process (Rink et al, 1995; Sperrin, 2000).

The magnitude of the pressure wave depends on the maximum size of the cavitation bubble and also its shape (Lo et al, 1990). Short pulsed lasers induce spherical bubbles that collapse at one point, producing strong resultant acoustic pressures. For long pulsed lasers, the vapour bubbles are elongated in the direction of the beam path, and rather parts the water (the "Moses effect") for direct deposition of the remaining portion of the laser pulse on the calculus surface (Chan et al, 1999).

Water vapour within the calculus material may be superheated, creating high pressure in localised regions. Therefore, even without stress confinement superheating may produce photomechanical effects. However, as the vapour bubble generated by long pulsed lasers will tend to collapse asynchronously at multiple centres, the resulting acoustic pressures would be expected to be weaker (Jansen et al, 1996).

3.8 Plasma-mediated processes

At very high laser irradiance (of the order of GW cm^{-2}) such as that produced by the Q-switched Nd:YAG laser, optical breakdown occurs (Laurent et al, 1991; Noack and Vogel, 1999). The material i.e. water or calculus, becomes ionised and the ionised molecules and electrons are ejected. The resulting hot ion and electron cloud is called plasma and this behaves as a nonlinear absorber of the laser light, inducing a sharp

increase in the absorption coefficient. Hence, laser wavelengths that are not strongly absorbed by water, such as 1064 nm (Nd:YAG), can be highly absorbed if the irradiance is sufficiently high to permit plasma formation. When the laser pulse has sufficient energy to create plasma at the start of the pulse then the remaining portion of the laser energy is absorbed by the plasma causing it to expand. The plasma collapses at the end of the laser pulse, a process that can induce shockwaves (Jiang et al, 1991b). The growth phase of the plasma may also generate a stress wave. If the plasma is initiated in water then the intense heating may cause a cavitation, causing a further stress wave (Rink et al, 1995). Thus, generally speaking, plasma generation is a desired effect in laser lithotripsy as it improves the coupling of laser energy to the target calculus (Vogel et al, 1996; Helfmann and Müller, 2001).

Laser induced plasma formation can occur as a result of two principal mechanisms. Firstly, multiple photons can be simultaneously absorbed to exceed the ionisation threshold of the medium, a process known as multi-photon ionisation (MPI). Secondly, the electric field associated with the laser photon can be sufficient to exceed the binding energy of the electrons in the medium's atoms, a process known as field ionisation (FI).

Multi-photon ionisation has been studied by a number of workers and the probability of MPI occurring is known to be a power function of the number of photons required to exceed the ionisation threshold. Field ionisation has also been studied extensively. The probability of field ionisation depends critically upon the tunnelling time of the outer electrons of the atom. The tunnelling time must be shorter than the time during which the electric vector of laser photon reverses.

Multi-photon ionisation and field ionisation can be competing mechanisms. In both cases, the intensity and the wavelength (photon energy) are critical parameters. Keldysh (1965) provided a theoretical analysis of the probability of one mechanism dominating and, assigning this to a FI mediated process, the letter γ. Both situations have a threshold laser intensity, and the mechanism which dominates is identified by the value γ, defined by:

$$\gamma = \frac{\omega(2m_e E_i)^{1/2}}{eF} \tag{9}$$

where ω (= hc / 2πλ) is the laser frequency, m_e the electronic mass, E_i the first ionisation potential, e the electronic charge and F the laser electric field. If $\gamma << 1$ field ionisation is dominant, and if $\gamma >> 1$ then multi-photon ionisation is dominant.

The probability of field ionisation actually occurring in an oscillating electric field was also addressed by Keldesh (1965). The width of the potential barrier preventing ionisation is reduced as the laser electric field is increased. The time taken by an electron to cross this barrier is given as:

$$t = \frac{(2m_e E_i)^{1/2}}{eF} \tag{10}$$

corresponding to a tunnelling rate of:

$$\omega_k = \frac{eF}{(2m_e E_i)^{1/2}} \tag{11}$$

The consequence of this relationship is that if the laser field oscillates at a higher frequency than ω_k then the electric field will reverse before escape can occur, and the electron will remain trapped.

With the Ho:YAG laser, the onset of shock-wave formation occurs at around 0.5 J per pulse (refer to 5.11.2). For a 600 μm fibre diameter and assuming a top hat profile, this corresponds to an intensity of ~ 4 x 10^9 W m^{-2}. At the highest laser pulse energy of 3 J and pulse duration of 420 μs the intensity is ~ 3 x 10^{10} W m^{-2}.

The probability of multi-photon ionisation depends critically upon the number of photons necessary to reach the ionisation threshold of water. Assuming an approximation by using the ionisation potential of hydrogen of 13eV, there are 23 Ho:YAG photons necessary to satisfy the ionisation condition (each Ho:YAG photon has an energy ~ 0.58 eV). The photon flux necessary to deliver this number of photons within the lifetime of the elevated state is ~10^{30} Wm^{-2}, a value 20 orders of magnitude in excess of that used clinically.

Using the Keldysh model, the value for γ is estimated to be 0.11 which indicates a primarily field ionisation mechanism, however the photon electric field reverses in a time of 3.5×10^{-15} s which is shorter than the tunnelling time of the outermost electron, hence FI is also highly unlikely. Thus, from this analysis the Ho:YAG laser does not appear to be capable of achieving plasma formation in water.

Chapter 4
Materials and Methods

The research was aimed at the investigation of the laser-calculus interaction from both the therapeutic and diagnostic perspectives of laser lithotripsy. With that aim in mind, the present study was confined to the investigation of three key parameters relating to optical properties, mechanical action, and plasma formation. The first key parameter was the material analysis and derivation of optical absorption properties of a selection of calculi using spectroscopic instrumentation. A total of 13 calculi, recovered from surgical procedures, were analysed. These included both urinary and biliary stones. The second parameter was the laser-induced shockwaves in water generated during the interaction process. This gave an indication of the ability of the particular laser to impart energy for the mechanical destruction of calculi. Two laser systems were employed in the experiments. One was a commercial variable-pulse holmium (Ho:YAG) laser, used for urological applications, and the other was a general purpose Q-switched Nd:YAG laser. The shockwave pressures were recorded using a needle hydrophone. The third parameter in the research was the spectral intensity of the laser generated plasma, which was analysed to obtain an indication of plasma threshold and temperature, and also to analyse optical emission lines of the elements to determine elemental composition of calculus material by the Laser induced breakdown spectroscopy (LIBS) technique.

4.1 Calculi samples

Specimens of human calculi used for the experimental work were provided by the Pathology laboratory and the Department of Urology at the Great Western Hospital, Swindon. The samples included urinary stone types of calcium, magnesium, uric acid and cystine, as well as three samples of biliary stones, and are shown in the photographs in Figures 4.1 – 4.13.

Obtaining samples proved to be difficult, in particular large, complete stones. The extensive use and success of minimally invasive surgical techniques has resulted in open surgery rarely being carried out, and therefore the retrieval of complete stones is much less common. Furthermore, stones are fragmented in situ and not routinely

recovered from the patient, as the fine particles can be left in the patient to be passed naturally in the urine, and therefore fragments are not commonly available either.

The samples obtained were a selection of complete stones from an archive and collections of fragments retrieved following lithotripsy. Fragmented samples placed limitations on some of the experiments undertaken, for example where the individual pieces were too small. It was, however, possible to carry out a number of experimental studies. Samples were numbered as identification tags and their types and general physical characteristics are presented in Table 4.1.

Table 4.1: Type and identification tags of calculi samples used in the experimental work

Sample	Calculus Type	Comments
1	Urinary	Assortment of light brown crystalline fragments, 3 – 8 mm in size
2	Urinary	Assortment of brown crystalline fragments, 3 – 8 mm in size
3	Urinary	Half of a large off-white stone, cut face revealing banded structure, ~7 cm
4	Urinary	Whole smooth yellow stone, ~ 2 cm
5	Urinary	Whole grey-green stone, ~ 3cm
6	Urinary	Single fragment, brown and crystalline, ~ 8 mm
7	Urinary	Light brown crystalline fragments, several mm
8	Urinary	Dark brown crystalline fragments, ~ 5 mm
9	Urinary	Off-white smooth non-crystalline fragments, 2 – 10 mm
10	Urinary	Large (~ 6 cm) lobed stone, amorphous off-white core / stained brown surface
11	Biliary	Whole smooth stones, mottled green-brown, 1 – 2 cm
12	Biliary	Fragments and whole stones, yellow outer / dark red-brown core, 3 – 10 mm
13	Biliary	Whole yellow stone, textured surface, ~ 3.5 cm

Before use, the received samples were washed with deionised water to ensure all traces of urine, blood, or any other biological or chemical contamination was removed. The calculi were then dried in a vacuum oven, and stored in sealed containers prior to experiments.

The following are descriptions of the samples as presented in the photographs:

Sample 1

Figure 4.1: The photograph shows a collection of fragments of urinary calculus identified as Sample 1. FT-IR analysis (see section 5.1.1) revealed the composition to be of cystine, which is a relatively uncommon type. Such stones are the result of a hereditary condition.

This comprised a number of calculus fragments retrieved following a laser lithotripsy procedure. The calculus material was brown in colour and had a crystalline appearance. The fragments ranged in size up to a maximum of 8 mm in diameter, with irregular shapes and sharp edges. The jagged edges suggested that the calculus had been broken up by mechanical forces i.e. that laser-induced shockwaves had played a role in the fragmentation process. From the number of pieces it can be assumed that the original whole stone was of the order 1 – 2 cm diameter, or perhaps greater (some fragments may not have been recovered during the procedure).

Sample 2

Figure 4.2: Sample 2, as with the previous specimen (Sample 1), was identified from FT-IR spectroscopy as a cystine calculus (refer to results in 5.1.1). Stones of this type are both rare and hereditary, and it is quite possible that the patients were related particularly as the samples were obtained from the same clinic.

This specimen was of similar appearance to Sample 1, in particular the size and shape of the fragments, which from the scale in the photograph can be seen to up to 8 mm in size. From the amount of stone pieces it would also appear that the original stone was of similar size, and therefore probably required a similar number of holmium laser pulses to achieve fragmentation. The main difference is the apparent increased level of pigmentation, indicated by the darker coloration. The crystalline nature of the internal structure can also be seen in the image, and in the absence of any obvious thermal damage on the exposed faces it seems reasonable to conclude that the calculus was effectively shattered by the laser action.

Sample 3

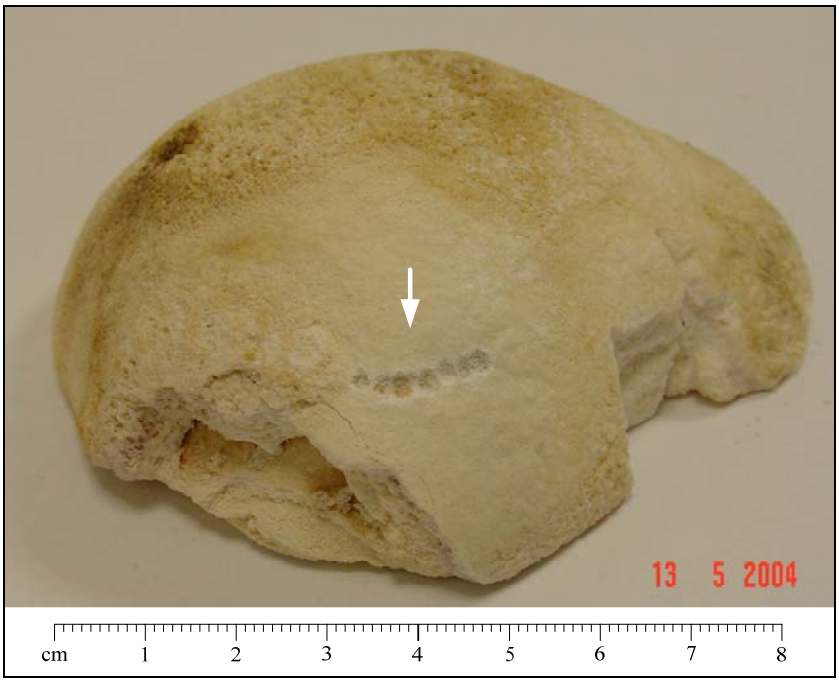

Figure 4.3: Sample 3 (pictured above and below) was of considerable size and presumably retrieved by open surgery. Although of unknown origin, FT-IR analysis revealed the composition to be of struvite (magnesium ammonium phosphate hexahydrate) indicating that the individual suffered from a urinary tract infection. The arrow indicates craters caused by laser damage during experiments.

This was the largest of the samples investigated and reported in this thesis. As shown in the photograph (right), the dimension of the cross-section is approximately 60 - 70 mm. It was comprised of an off-white chalky material, and had a rounded, although uneven surface, some areas of which had a brownish colouration. The specimen had been previously cut, revealing a concentric layered structure around a central core. The core itself was missing.

Sample 4

Figure 4.4: The photograph shows an intact specimen of a brushite calculus (calcium hydrate phosphate dihydrate). The crater seen at the front of the stone was caused by Nd:YAG laser irradiation during experiments described in a later section (see Appendix C for further details).

This sample, like the previous specimen, had been removed by open surgery hence it was in its original form, taking on the appearance of a smooth yellow-cream pebble. Its size along the axial extent was estimated to be ~ 22 mm. The scratches that can be seen on the surface are due to removal of fragments for FT-IR analysis, and in removing material it was noted that the calculus was of a hard composition in comparison to other samples. The pit seen at the front was induced by a series of Nd:YAG laser pulses during experimental work. From the small size of the crater (~ 1 mm) it is evident that the specimen would require a considerable number of laser shots to reduce it to a passable size. It is quite likely that this stone had to be surgically removed as it may have been unbreakable by lithotripsy technology available at the time.

Sample 5

Figure 4.5: Photograph showing Sample 5. A further example of a cystine calculus (see 5.1.1), in this case extracted from the patient by open surgery rather than laser treatment. The charred pit seen on the upper side of the stone was ablated by Ho:YAG laser radiation during experiments (see Appendix C for further details).

This calculus was oval shaped with smooth appearance and green surface colouration. Where the green outer layer had been removed a grey form was exposed, which is interesting as the other two cystine calculi (Samples 1 and 2) were distinctly brown in colour. The dark pit that can be seen on the top of the stone is, as with other samples, due to laser induced damage during experiments and this is discussed further in Appendix C.

Sample 6

Figure 4.6: Sample 6 is a remnant of a larger calculus composed of wedellite (calcium oxalate dihydrate). COD stones are often resistant to traditional lithotripsy techniques on account of their hardness, although in this case the Ho:YAG laser has achieved fragmentation.

The photograph of this remnant of a laser-ablated calculus clearly shows a crystalline structure that is associated with calcium oxalate compositions. Jagged edges are also seen resulting from the fracture process. The physical size of this fragment represents the upper limit for extraction by basket technique, and would be too large to be passed spontaneously. Fragments left behind in the urinary tract following lithotripsy that are too large to be passed by the individual are known to act as seeds for further calculus formation and so are important to completely remove during the procedure.

Sample 7

Figure 4.7: As with some of the other specimens, only relatively small fragments were available, as shown in the photograph comprising Sample 7. The remnants were determined to be fragments of a larger calculus of whewellite composition (calcium oxalate monohydrate).

Sample 7 was a collection of post-treatment stone debris, of which most of the material was too small for use in the experiments. However, the largest of the fragments are shown above and measured ~ 5 mm in diameter, which was sufficient for laser induced breakdown spectroscopy. The calculus fragments were light brown and crystalline, and similar in appearance to other samples despite their being of different compositions e.g. Samples 1, 2 and 6.

Sample 8

Figure 4.8: Sample 8 was found to be pieces of an original calculus composed of whewellite (calcium oxalate monohydrate). This type of composition is by far the most common in the stone forming population.

These are a further collection of dark brown fragments retrieved following laser lithotripsy. As with the previous sample, the sharp and irregular features are considered to be indicative of the action of the laser-induced fragmentation process, in particular mechanical effects. The photograph reveals that although the calculus appears to have some crystalline structure, it also appears to be an irregular agglomeration of crystalline components. This suggests that the architecture is a result of various growth phases, possibly under different chemical conditions, and that the calculus would therefore be expected to have lines of weakness. This raises the possibility that this calculus has been fragmented by exploiting the inherent weakness in its structure, such as by shockwave action.

Sample 9

Figure 4.9: Sample 9 comprised fragmented components of uric acid calculi removed from a patient.

This sample comprised a large number of cream colour fragments of smooth non-crystalline appearance. It was not known if the pieces were from the fracture of a single calculus or from several stones, although the similarity of the fragments suggested a common composition. The larger components of around 5 to 10 mm in size were suitable for experimental work, although were found to be friable and easily disintegrated particularly when submerged in water and exposed to laser-induced shockwaves. The blackened areas seen on two of the fragments are a result of direct laser irradiation (see Appendix C).

Sample 10

Figure 4.10: Photograph showing a large specimen of a urinary calculus. FT-IR analysis identified the composition to be of struvite (magnesium ammonium phosphate hexahydrate), suggesting the likely cause to be urine infection.

This sample, as can be seen in Figure 4.10, was a large calculus with an overall size of approximately 50 mm. When removing a portion for analysis it was found to have a chalky consistency and was easily scratched. Its surface was stained a yellow-brown colour, presumably from the urine environment in which it was formed. Parts of the surface appeared to have regions resembling crystalline deposits, whereas the underlying bulk material appeared to be amorphous, unlike some of the other samples. The history of the specimen was unknown, although such a large calculus would certainly have been removed by surgical operation which was common before the advent of minimally invasive techniques in the early 1980's. The shape was particularly interesting as it indicated growth into lobes, presumably an indication of its origin within the urinary system, possibly where the kidney ducts into the upper ureter.

Sample 11

Figure 4.11: Photograph showing Sample 11, a collection stones formed in the gall bladder as opposed to the urinary system. FT-IR analysis identified the presence of bile salts and cholesterol deposits (see 5.1.1).

This was a collection of gallstones that form in the gall bladder, part of the digestive tract. Gallstones precipitate under different chemical conditions to urinary stones, in particular in the presence of fatty deposits which are not found in urine. Their appearance, as can be seen in Figure 4.11, was different to the samples 1 – 10. The composition was pigmented, having a green-brown coloration, and appearing darker in the core material. The surface had a grey-green residue possibly from the bile liquid. The smooth forms of the calculi are probably due to their growth being influenced by surrounding structures, including the presence of other gallstones. The history of these particular samples was unknown although it can be assumed that they were removed by endoscopic techniques as is commonly practiced. Lasers can be used to break up larger specimens so that they are more easily extracted.

Sample 12

Figure 4.12: Sample 12 comprising deposits of gallstones having a distinct yellow appearance. This was later confirmed as cholesterol, bilirubin and calcium phosphate composition.

This was another collection of gallstones but with an obvious yellow appearance compared to previous suggesting a mostly fatty composition. The stones were smaller than sample 11, only up to 10 mm in size, but likewise of smooth appearance. It could be seen from the broken components that these had very different core and outer compositions. The core could be seen to be of a dark red-brown substance which presumably was the initial precipitation, which was apparently later coated by an off-white / yellow deposit.

Sample 13

Figure 4.13: Sample 13, a particularly large specimen of a gallstone, was identified by the hospital laboratory as a cholesterol deposit. FT-IR analysis of the surface layers (see 5.1.1) also revealed the presence of bilirubin.

This was another biliary stone, believed to be an unusual specimen on account of its size. Measuring approximately ~ 35 mm in diameter, it was considerably larger than the other samples of gallstone. The yellow colour suggested a fatty / cholesterol composition, as with Sample 12. The rough surface texture suggested it may have a crystalline form although this was possibly a surface deposit rather than an indication of its inner structure. It may be that the core material was similar to the red-brown substance seen in the previous sample, although this was not investigated.

4.2 Material analysis: FT-IR spectroscopy

Although the samples were supplied by the hospital with an indication of their composition from laboratory analysis using a commercial wet chemistry kit (Merckognost, Merc, Germany), chemical testing is often inaccurate and imprecise due to poor performance of such analysis systems (Ooi, 1998; Kasidas et al, 2004). For many stone compositions chemical techniques can only indicate the presence of individual ions and radicals rather than a specific compound. For example, chemical procedures cannot distinguish between the monohydrate and dihydrate forms of calcium oxalate (Ochmanski et al, 1999). X-ray diffraction is a suitable technique for quantification of crystalline calculi, but it cannot adequately detect amorphous substances such as carbonate apatite. Fourier transform infrared (FT-IR) spectroscopy is, however, a standard technique for analyses of bio fluids and solid biosamples, and has been routinely applied to the analysis of calculi (Vergauwe et al, 1994; Carmona et al, 1997; Estepa and Daudon, 1997; Paluszkiewicz et al, 1997). It is a reliable, specific and rapid technique, and has reasonable sensitivity. For this reason, the samples were subject to spectroscopic analysis using FT-IR and absorption spectroscopes to obtain accurate information on their composition.

In FT-IR spectroscopy samples are exposed to infrared radiation and a fraction of the IR radiation is absorbed at wavelengths that are specific to the molecular excitation states of covalently bonded atoms. Each molecule has its own specific absorption spectrum, and the IR spectra are represented as a plot of transmittance across the infrared band. To establish an identity of the compounds present in the sample a comparison needs to be made against spectra of pure laboratory compounds, or with reference spectra libraries and databases of molecular species verses excitation band.

Fourier transform infrared spectroscopy records the relative absorption properties of the sample over a range of wavenumbers (cm^{-1}), a descriptor which is related to frequency and inversely related to wavelength (μm) i.e. wavelength (μm) = 10,000 / wavenumber (cm^{-1}). The corresponding range of wavelengths recorded by the FT-IR scan corresponds to the mid to far infrared region. High absorption bands can therefore be identified in terms of their corresponding wavelengths. In addition to identifying

composition, this information can be used to give an indication of laser wavelengths which will be strongly absorbed by the material leading to efficient calculus destruction. Absorption properties in the UV-Visible-NIR region are investigated in a later section (section 4.6) for the purposes of identifying other laser wavelengths as a basis for further work.

FT-IR measurements were carried out using the Bruker Vector 22 spectrometer (Bruker Spectrospin, Germany). OPUS software was used to control the instrument and to acquire and manipulate the spectra. The spectrometer has a wavenumber range of 4000 – 400 cm^{-1} (2.5 – 25 μm) and was set to average 16 scans with a resolution of 1 cm^{-1}.

The technique involves the manufacture of a transparent disc which contains a quantity of the sample under investigation. The system is a single beam spectrometer and therefore a background scan using a blank potassium bromide (KBr) disc formed from 55 mg dry spectroscopic grade KBr was taken. The background measurement enabled the subtraction of signal variation due to calibration errors from system components and also, for example, the effects arising from atmospheric water vapour and CO_2 absorption.

Samples were carefully prepared for subsequent FT-IR analysis, avoiding contamination by other substances. All masses were measured using a digital balance having an accuracy of ± 0.1 mg, although for this purpose such accuracy was not absolutely necessary.

A portion of calculus material was pulverised to a fine powder in an agate mortar and pestle. A small portion of the material weighing approximately 10 mg was then ground and mixed thoroughly with 300 mg of dried potassium bromide. From this mixture, approximately 55 mg was transferred into a mould (die). The powder was distributed evenly within the die by first rotating the plunger, and the assembly was placed in a press. A load of 10 tonnes was applied for 3 – 4 minutes to form a transparent KBr disc of 13 mm in diameter. The die was disassembled and the disc carefully removed and

placed in a sample holder. Imperfect KBr discs, for example damaged (e.g. with cracks) or uneven sample distribution (e.g. seen as white spots) were discarded.

The FT-IR spectra were recorded immediately after preparation to avoid or minimize degradation by atmospheric vapour. Three independent discs were produced and subjected to separate FT-IR measurements to reduce the influence of variability in sample concentration and non-homogenous distribution of sample particles in the potassium bromide.

As an identification aid, a set of reference spectra were also recorded. Calcium oxalate dihydrate, calcium oxalate monohydrate, calcium hydrogen phosphate dihydrate, magnesium ammonium phosphate dihydrate, uric acid and cystine, were obtained as powders from commercial chemical suppliers (Fluke, and Analar). KBr discs comprising the pure compounds were pressed and scanned and their FT-IR spectra were used for comparison against those obtained for the samples.

Spectral absorption peaks of the calculi were identified using Opus software, and data files were imported to Excel. Identification was made by comparison with the reference spectra, published spectra, and by means of standard decision tree identification for calculi (Carmona et al, 1997; Estepa and Daudon, 1997).

4.3 Laser devices: characteristics and preliminary measurements

Two laser systems were used for experiments on laser interaction with water /calculi. Results obtained using a Q-switched neodymium YAG laser (Nd:YAG) based at the research laboratory at the Cranfield University (Centre for Applied Laser Spectoscopy) were compared to those obtained using a clinical variable pulse duration holmium YAG laser (Ho:YAG) based at the Great Western hospital (Swindon). The following are descriptions of the lasers and also of the preliminary measurements that were carried out to characterize the laser sources.

4.3.1 Nd:YAG Laser

The neodymium YAG laser source was a Litron-200 Nano Series Q-switched Nd:YAG laser (Litron Optical, UK). The laser is designed for scientific application and has full trigger control including Q-switch synchronization. The laser pulse energy was continuously adjustable via the high-voltage control of the flashlamp (range up to 1000V). A photograph of the laser system is shown in Figure 4.14.

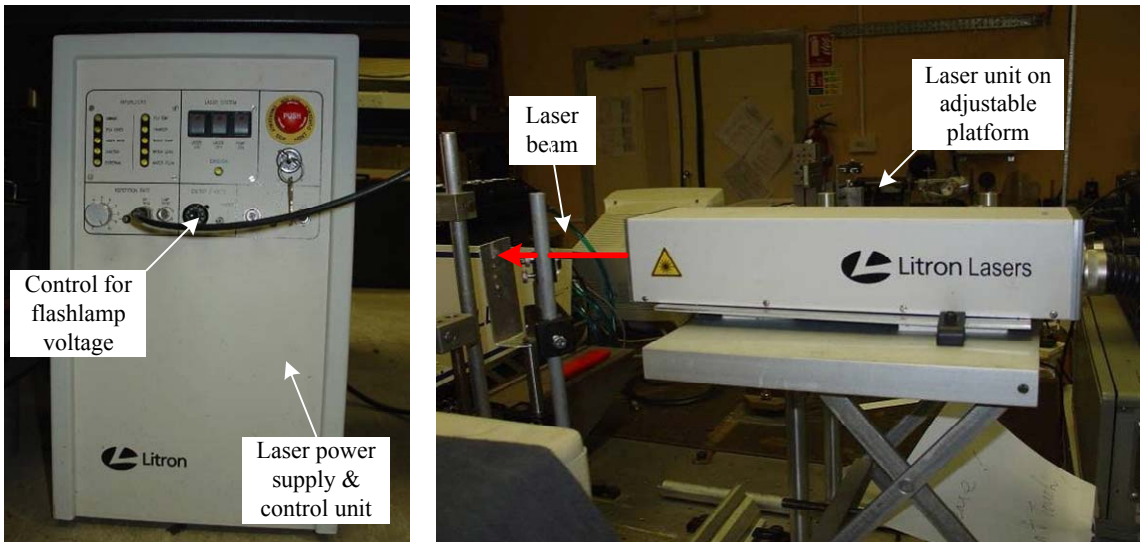

Figure 4.14: Nd:YAG laser system used for the experiments

The Nd:YAG laser was operated at its fundamental mode having a wavelength of 1064 nm, and had a pulse duration of ~ 6 ns (FWHM). The maximum pulse repetition rate was variable from single pulse up to 20 Hz. Details of other specifications are presented in Appendix A.

The combination of nanosecond pulse duration and small focal spot created very high peak irradiance at the laser focus. Assuming a diffraction limited minimum spot size according to the equation, $r = 1.22\lambda f / D$ (where r is the diffraction limited spot radius, f is the focal length of the focusing lens, λ is the wavelength of the laser, and D is the beam diameter at the lens), the peak pulse irradiance was of the order $\sim 10^{13}$ W cm^{-2} for a lens of focal length 25 mm and a beam diameter of 5 mm.

The Nd:YAG laser was mounted on an optical bench and the beam directed via optical components to either a setup for underwater experiments for pressure measurements, or to a sample platform for plasma spectroscopy measurements. For the generation of laser-induced pressures in water, the laser beam was guided by means of optical prisms to a 25 mm focal length lens (f#1). The lens was mounted at the distal end of a purpose-made periscope assembly as shown in Figure 4.15. Beam alignment was by manipulation of the prisms, two of which were mounted on fully adjustable platforms. The transmitted power was maximized by monitoring the laser power at the lens using a laser power meter whilst fine tuning the optical alignment.

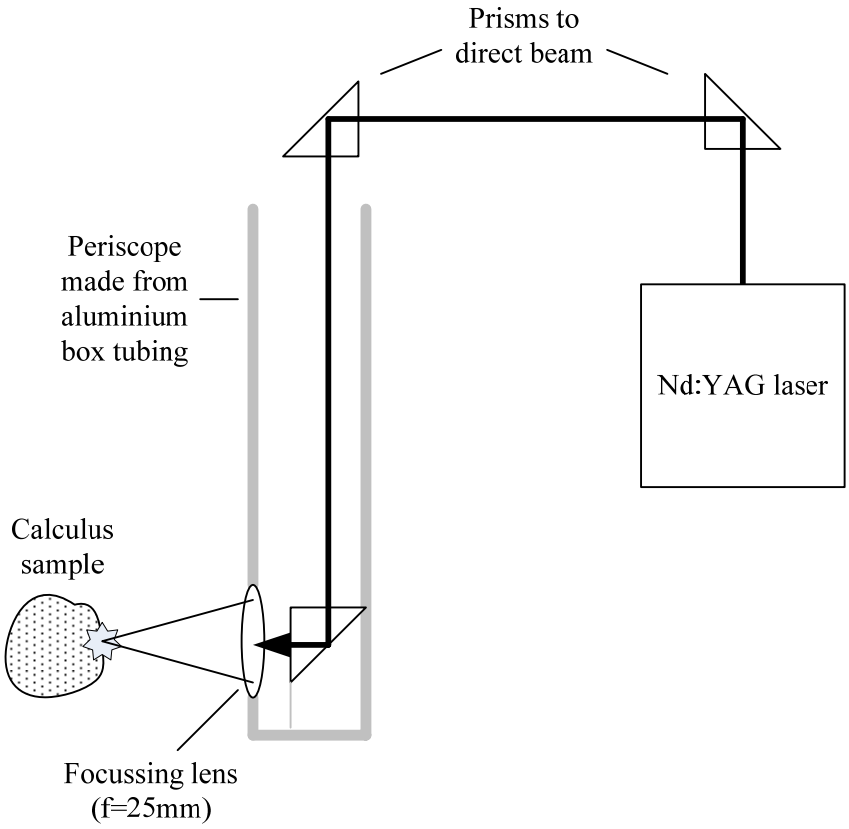

Figure 4.15: Schematic of the Nd:YAG laser beam delivery system (periscope) used for the water tank experiments

Laser burn patterns were obtained using photographic paper held at the focal point to confirm that the beam was tightly focused. From these burn patterns the spot size was estimated using a microscope to be approximately 0.1 – 0.2 mm, which is larger than

predicted using the diffraction limit formula. Therefore, the calculated irradiance using the measured spot size was of the order ~ 90 GW cm^{-2} for a pulse energy of ~ 90 mJ, a factor of ~ 10^4 lower than the theoretical maximum.

The periscope arrangement was used as a convenient method of delivering the laser beam into the bulk of the water in a water tank. The lower part of the periscope was sealed to prevent ingress of water. A fibre optic delivery would have been a suitable alternative but was not available. However, optical fibres may suffer damage at the high peak powers with this laser and this would have affected the output consistency required for the experiments.

The laser beam power/ pulse energy output at the lens was determined using a calibrated laser power meter with thermopile detector (Ophir Nova with F150 detector, Ophir). Care was taken to avoid placing the thermopile too close to the beam focus to avoid possible damage as well as an inaccurate measurement. A direct correlation between the voltage setting on the laser and the actual laser energy delivered to the target was then available.

4.3.2 Ho:YAG Laser

The Ho:YAG laser used for this research was a commercial medical laser type BLM 1000 varioPulse (WaveLight Laser Technologie AG, Germany). The laser is used at the hospital for stone removal and also tissue coagulation/cutting in urological applications. Depending on the procedure, the operator achieves the desired effect by selection of the appropriate laser pulse energy, pulse duration, and pulse repetition rate, within the available range. Three fibre sizes were available; the thinner fibres (200 μm and 320 μm) are used where a high degree of flexibility is required such as stone clearance in the upper urinary tract, thicker fibres (600 μm) allow maximum available laser output without damage to the fibre. A low power red laser beam was co-aligned with the invisible Ho:YAG beam to enable visual guidance. The laser is shown overleaf in the photograph in Figure 4.16.

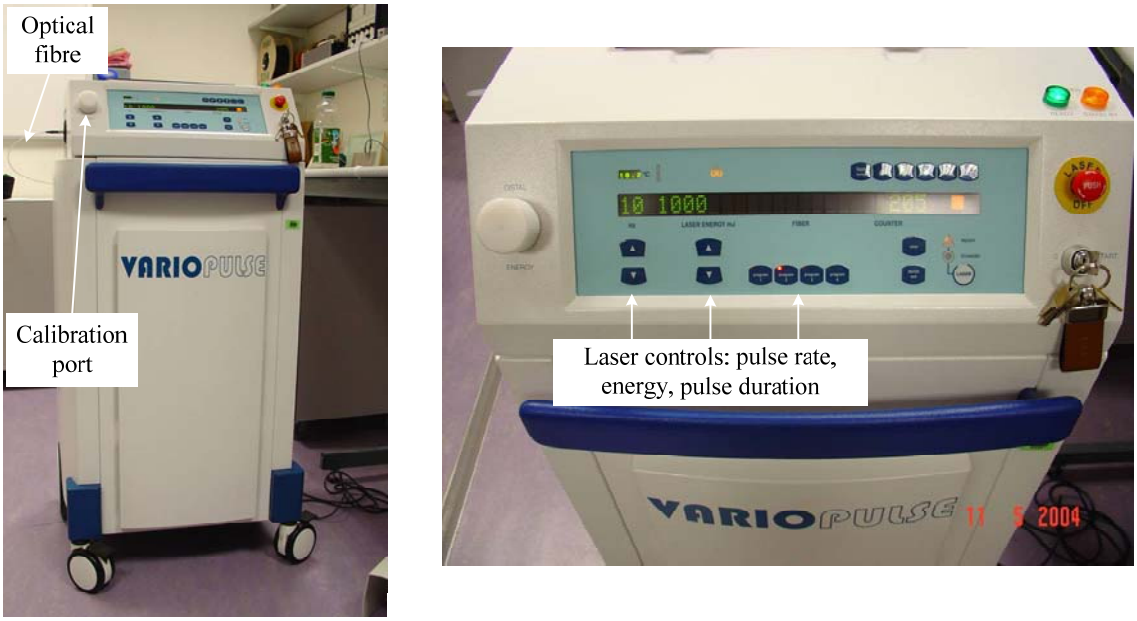

Figure 4.16: Ho:YAG laser system used for the experiments

The output of the Ho:YAG laser had a wavelength of 2.12 µm (2100 nm) and was operated at a pulse repetition rate of up to a maximum of 20 Hz. The pulse duration was varied in the range 120 – 800 µs (FWHM) and the energy from 0.2 J – 3 J.

The maximum laser pulse energy available depended on the chosen pulse duration and the laser pulse repetition rate. These parameters are determined by the operation of the laser flash lamps and also on the ability of the laser system to remove the heat build up from the Ho:YAG crystal and maintain stability.

The peak irradiance levels at the fibre tip were also dependent on the fibre diameter. A 600 µm anhydrous silica optical fibre of length 3 m was used for the experiments, giving a peak irradiance of ~ 3 MW cm^{-2}. The irradiance can be increased by a factor of ~ 10 when using the 200 µm fibre compared to the 600 µm fibre.

Although the laser was equipped with a built-in power monitoring system and also an external fibre calibration port, as with the Nd:YAG laser the output was verified by means of a calibrated laser power meter, as shown in Figure 4.17.

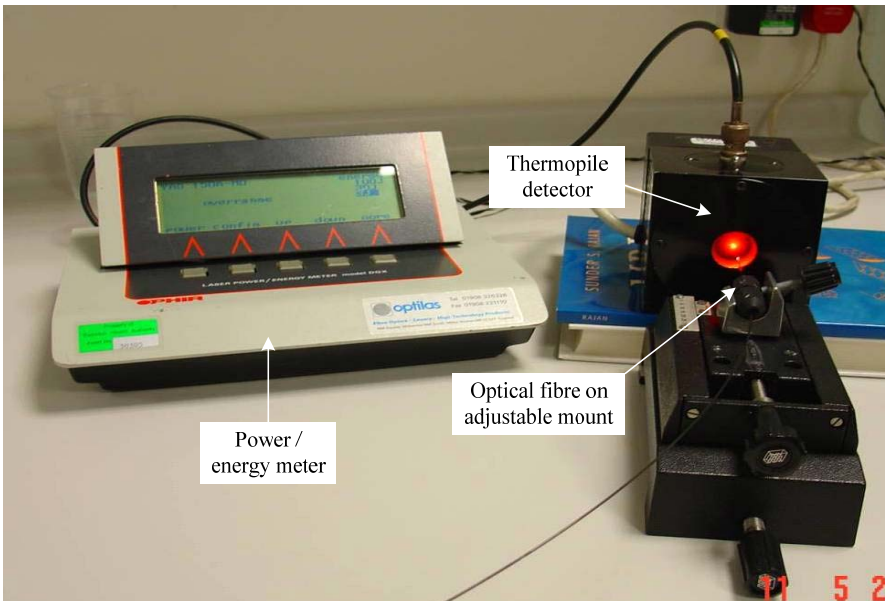

Figure 4.17: Output calibration of the Ho:YAG laser system using a laser power meter

Pulse energy was measured across the range to confirm both the accuracy of the laser setting and also to establish the pulse to pulse variation. A frequent calibration check was found to be necessary as the fibre tip was susceptible to damage particularly when in contact with the calculus, reducing output by 20 – 50% depending on the pulse energy and number of shots fired. Also, the fibre was recleaved every ~ 1000 laser pulses or when the shape of the aiming beam was non-circular upon inspection (Figure 4.18).

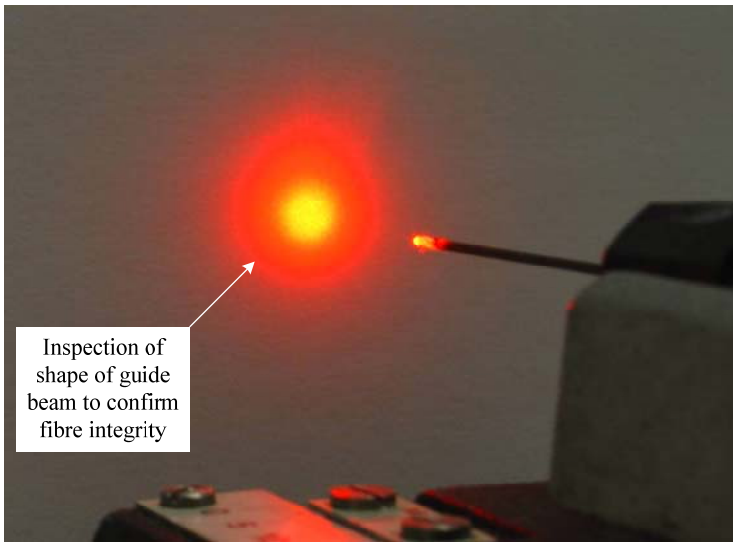

Ho:YAG laser burn pattern on photographic paper

Figure 4.18: Beam check for uniformity and circular shape

The fibre damage was thought to be a result of mechanical forces created by the shockwave action leading to crack formation in the silica. Optical fibres are brittle and are known to be prone to damage during clinical use (Spore et al, 1999; Knudsen et al, 2005). Also, thermal effects and ejection of fragments from the calculus at high speed in the vicinity of the fibre tip may also have contributed to the observed fibre damage.

Laser pulse duration was also measured across the range to confirm the pulse characteristics. Pulse waveforms were captured using a photodiode (BXP65) connected to a digital scope (PicoScope ADC 200). The digital data were then transferred to a computer for retrospective processing and analysis.

Thus, a comprehensive set of measurements of power, energy, and pulse duration were taken to determine the output characteristics of the laser system.

4.4 Laser-induced shockwaves: pressure measurements

Laser energy delivered to a target calculus in a liquid environment induces pressure transients on account of photomechanical (and photothermal) effects. The relationship between the laser parameters, in particular the variable pulse duration of the holmium laser, and the generated pressure pulse was investigated using the experimental setup described in this section. The results obtained with the Nd:YAG laser (a laser with parameters typical of a 'LISL' system) were compared to those using a clinical variable pulse duration Ho:YAG laser. As far as practicable, the apparatus and experimental setup were the same for each laser. Where different measurement equipment or a different arrangement of apparatus was used this is indicated, and results explained taking into consideration such differences.

Shockwave recordings were made using a calibrated needle hydrophone with a polyvinylidene fluoride (PVdF) active element, a photograph of one of the models used is shown in Figure 4.19. The small sensor area at the tip of the needle probe made it possible to carry out more precise spatially localized measurements of the pressure amplitude compared to the use of a large area membrane hydrophone detector, as used by other investigators. The small element also enabled measurements to be made very

close to the laser focus / fibre tip. Although needle hydrophones are less sensitive than membrane types, a built-in pre-amplifier gave the hydrophone that was used good signal-to-noise characteristics and sensitivity, as well as lowering its susceptibility to electromagnetic interference that may arise from the laser device and high electric field strength at the focus (particularly with the Q-switched pulses from the Nd:YAG laser).

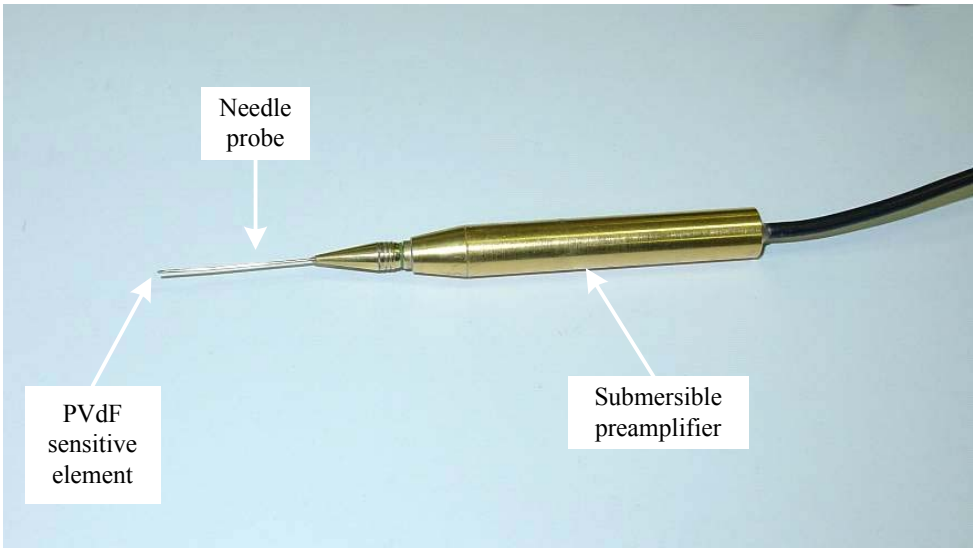

Figure 4.19: Needle hydrophone used for the measurement of shockwave pressures

The hydrophone specifications were slightly different for the investigations with each laser due to different models used in these experiments. For the series of experiments with the Nd:YAG laser, a needle hydrophone comprising a 0.2 mm diameter element (HP Series, Precision Acoustics Ltd, UK) was available and used. Pressure sensitivity (defined as mV MPa^{-1}) was quoted on the calibration certificate as ranging from 75 – 130 mV MPa^{-1} for the frequency range 1 – 20 MHz. The hydrophone system used for the experiments using the Ho:YAG laser is described later. The hydrophone was coupled to the external measuring equipment via a 28 ± 1V DC power supply module.

Laser-induced pressure pulses were recorded on a digitizing oscilloscope (Agilent 5000 series, model DSO5054A) which had a specification of 4 GSa s^{-1} digitizing rate, 500 MHz bandwidth, and input impedance of 50 Ω. A PC based transient recorder (EG&G 9845) was also used for a series of experiments with a specification of 200 MSa s^{-1}

digitizing rate, 100 MHz bandwidth, and input impedance of 50 Ω. A trigger pulse to initiate data recording was taken from the laser Q-switch signal output.

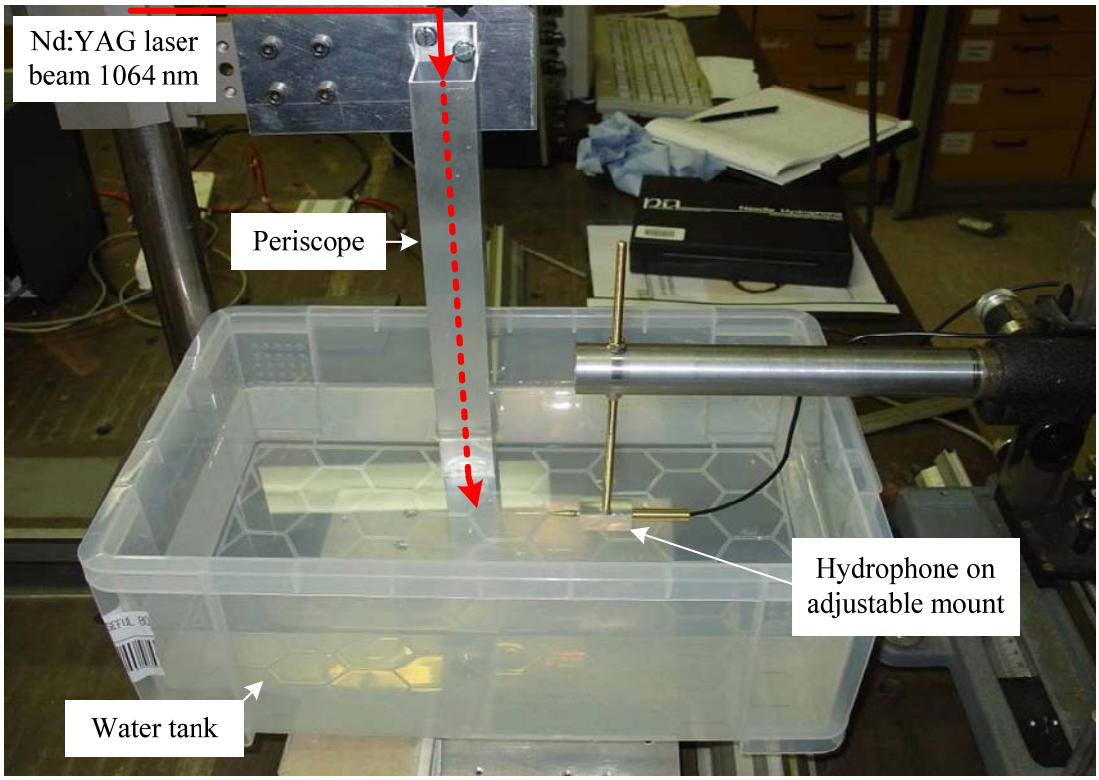

Figure 4.20: Basic setup for the measurement of Nd:YAG laser-induced shockwave pressures

A photograph of the experimental jig for the preliminary shockwave measurements with the Nd:YAG laser is shown in Figure 4.20. The laser was set for fixed pulse energy and a pulse frequency (~ 30 mJ, 10 Hz). The hydrophone was kept in the same fixed position relative to the origin of the laser plasma, maintaining a separation of ~ 3 mm from the tip (sensor element). Pressure measurements were averaged over ~ 125 measurements to ensure good signal averaging.

A cross calibration was carried out between the digital oscilloscope and the PC transient recorder. An assumption was made that the higher specification digitizing oscilloscope was more accurate and could be used as a reference. Using a correction factor, measured signal amplitudes (in mV) could then be calibrated for the PC based system. Measured

voltages were converted into units of pressure (in MPa) using the quoted sensitivity in absolute units (mV MPa^{-1}).

Calibration of the hydrophone was necessary to enable the shockwave pressure to be determined from the measured voltage amplitude. The input impedance of the measurement equipment was matched to the impedance of the hydrophone to ensure that the true signal amplitude was recorded. Prior to measurements being taken the hydrophone was immersed in water for a period of at least 30 minutes to ensure that its sensitivity, which increases as water is absorbed by the PVdF sensor, had stabilized.

The calibrated sensitivity spectrum for the 0.2 mm hydrophone system is shown in Figure 4.21. From this it can be seen that it is important to know the frequency of the shockwave so that the appropriate sensitivity could be used to derive pressure values.

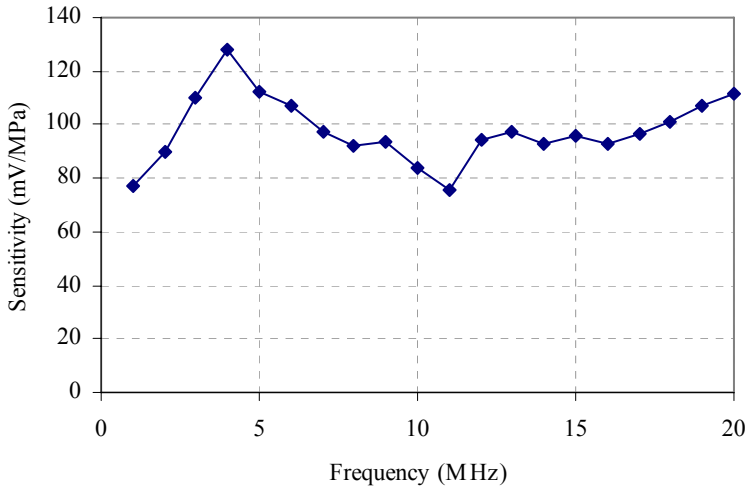

Figure 4.21: Frequency response of the 0.2 mm hydrophone

The frequency components of the shockwave were determined using a mathematical function on the oscilloscope. A Fourier Transform function calculation was applied to an averaged single-period waveform to derive the frequency components.

For the shockwave measurements with the Ho:YAG laser, a similar needle hydrophone but with a smaller PVdF sensitive area of dimensions ~ 0.12 mm x 0.15 mm (Precision Acoustics Ltd, UK) was used. The quoted sensitivity of the hydrophone system was 20

mV MPa^{-1}, which compared to the (max) 130 mV MPa^{-1} for the HP series hydrophone used previously, was less sensitive on account of the smaller sensor area. Output from the hydrophone was connected to a digital oscilloscope (Le Croy 7550) operating at 100 MHz and with an input impedance of 1 MΩ.

For the Nd:YAG laser a trigger pulse to initiate the recording of the pressure transient was taken from the electrical signal which activated the opening of the laser Q-switch. However, a similar approach was not possible with the Ho:YAG laser and an alternative method of providing a trigger signal was needed. Preliminary investigations using the rising edge of the pulse recorded by the hydrophone as a trigger proved to be problematic owing to poor signal-to-noise ratio, and therefore detecting the optical output of the laser was considered the best approach. However, the holmium laser beam as it emerged from the optical fibre was fully absorbed by the water, so instead the scattered flashlamp light emanating from the laser system with the holmium beam was detected. Using a fast photodiode (BPX65, RS Components, UK) having a rise time of approx 3.5 ns, a reliable trigger signal was achieved. An assumption was made that the onset and duration of the flashlamp was approximately coincident with the laser radiation output.

The photodiode was mounted behind a collecting lens (focal length 25 mm, f#1) and positioned on the beam axis outside of the water tank. The tank was made of a semi transparent plastic which allowed the scattered flashlamp light to pass through and be detected by the photodiode.

The tip of the hydrophone was positioned with reference to the point where the laser beam was assumed to interact with the water/calculus, defined as the ‘emission centre’. This point was taken to be where the Nd:YAG laser beam was brought to a focus by the lens, and for the Ho:YAG laser as the end face of the optical fibre (Figure 4.22).

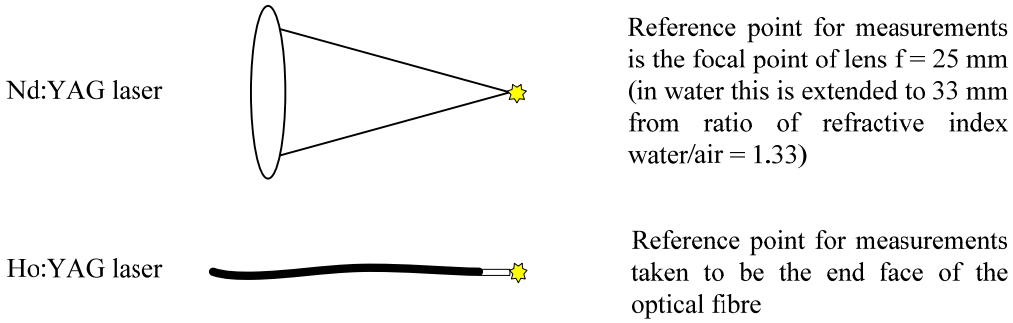

Figure 4.22: The definition of the 'emission centre' as a reference point for measurements

The hydrophone was mounted on a fully adjustable travelling stage with a 0.1 mm scale and lowered into a tank filled with degassed and deionised water at room temperature. The laser delivery system (i.e. the periscope or the optical fibre) was in a fixed position within the tank, at least 100 mm from the edges and immersed to a depth of not less than 40 mm to avoid problems arising from acoustic reflections. The schematic layouts for each laser type are shown in Figures 4.23 and 4.24.

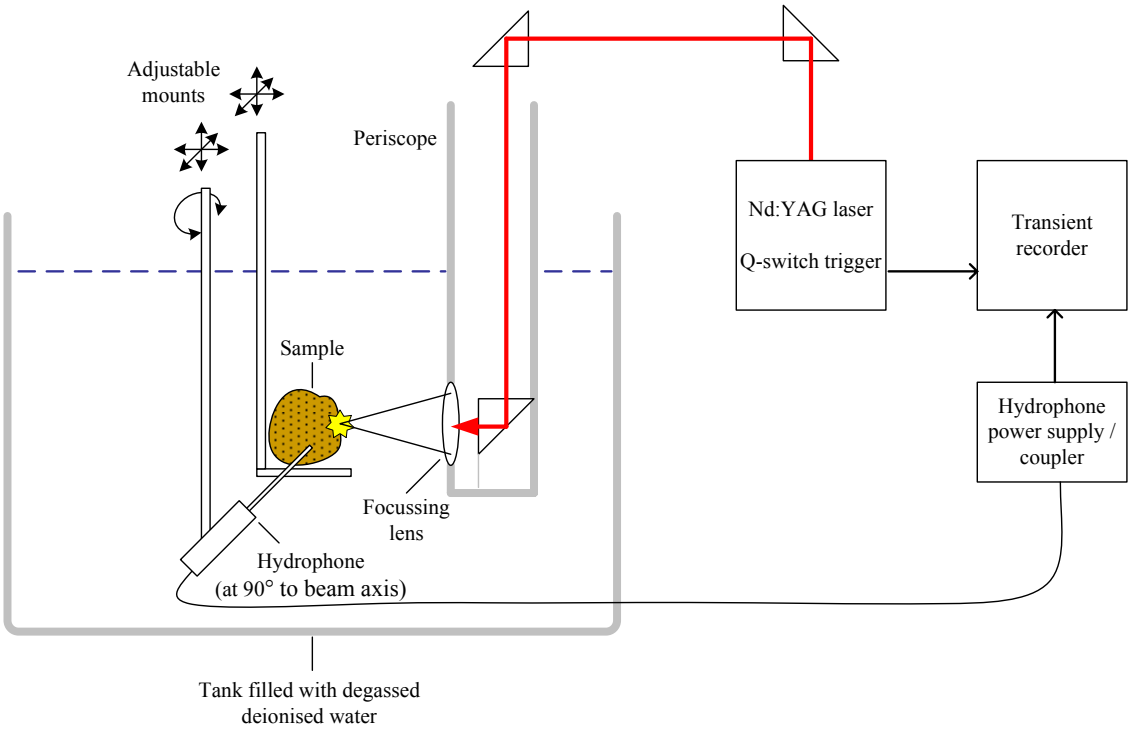

Figure 4.23: Schematic of the setup for the measurement of shockwaves initiated by the Nd:YAG laser

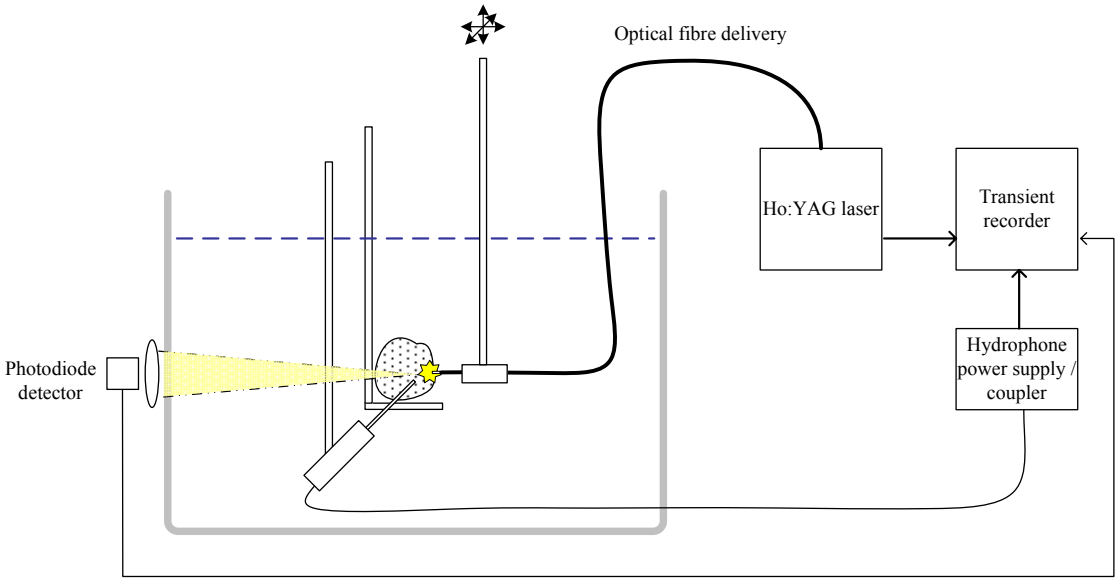

Figure 4.24: Schematic of the setup for the measurement of shockwaves initiated by the Ho:YAG laser using fibre-optic for beam delivery

In practical terms, after initially aligning the hydrophone tip with the emission centre, the probe was retracted a known distance from this position. The hydrophone was therefore kept out of the laser beam path to avoid damage to the sensitive element. Using the scale on the stage, the separation between the hydrophone's active element and the emission centre could be measured to an accuracy of better than ± 0.5 mm.

A calculus sample was presented on a tray which was attached to a vertical stand connected to a second travelling stage. The stage could be adjusted with 3 degrees of freedom to achieve an accurate alignment, and to vary the position of the calculus to emission centre separation between 0 – 40 mm.

Using this arrangement, adjustments of the travelling stages permitted accurate measurements of laser-calculus and laser-hydrophone separations. For later experiments, a modification to the hydrophone mount was made to allow accurate rotation of the hydrophone tip about a fixed point (the emission centre). For these measurements a turntable with a scale marked in 1° intervals was utilised, which permitted the hydrophone tip to be positioned at various angles around the fibre tip / beam focus to study the angular variation of the shockwave amplitude.

Generated pressure pulses were measured for the evaluation and analysis of the dependence of shockwave intensity on various laser parameters and experimental conditions. This was carried out to provide a complete characterisation of the acoustic field so that peak pressures could be determined close to the emission centre for optimum laser parameters i.e. the clinically realistic location of the calculus at ~ 1 mm from the fibre tip. For each laser the effects on the pressure transient due to the incident laser pulse energy, laser pulse duration, and pulse repetition rate were investigated. Furthermore, the effect of the proximity of the calculus to the site of laser interaction was also investigated to determine if there is a difference in the magnitude of the pressure pulse between 'free firing' into water and the laser directly impinging on the calculus.

For all pressure measurements the transient recorders were set up to average over approximately 100 laser shots to ensure good statistics. For the Nd:YAG laser it was found that the pulse to pulse repeatability of the pressure recording was within a few percent and therefore uncertainties in the average values of 100 pulses were low. However, for the Ho:YAG laser recorded pressure amplitudes were considerably more variable and occasionally no pressure pulse was detected at all. Therefore, compared to the Nd:YAG laser the averaged pressure values for the Ho:YAG laser have a greater measurement uncertainties i.e. standard deviation but this is a result of the laser-water/calculus interaction process and not the instrument uncertainty.

Environmental factors were also investigated that may influence the shockwave formation and peak pressure. Adding salts into the water has been reported to lead to greater pressure amplitudes for certain laser parameters (Reichel et al, 1991, 1992) but has not been investigated for the Ho:YAG laser, in particular the variable pulse duration Ho:YAG. Therefore, the effect of adding salts into water on the peak amplitude of the shockwave was evaluated in a side by side comparison between the two laser systems. Deionised water was used as a standard reference solution and the effect of adding sodium chloride (NaCl) and iron chloride (Fe_2Cl_3) on the shockwave parameters were studied. The basis for this investigation was to introduce free ions into solution in order to facilitate optical breakdown and thus enabling plasma formation at reduced laser

pulse energies. Sodium chloride dissociates into Na^+ ions, whereas iron chloride liberates Fe^{3+} ions which would be expected to have a greater influence on the optical breakdown threshold as the plasma requires charged particles to initiate the process. If plasma was formed more readily then it would be reasonable to expect an effect on the generated pressure. On the other hand, if the shockwaves were not dependent on plasma formation, the effect would not be seen.

Across the range of output parameters a series of pressure measurements were conducted at identical laser settings for the different solutions: deionised water and standard solutions (by weight) of 0.9 % NaCl and 1 % Fe_2Cl_3. The solutions were made up from laboratory grade chemicals (Fluke, Analar), weighed using a digital balance to an accuracy of ± 0.1 mg, and dissolved in deionised water. A range of other solution strengths were also included in the investigation. The standard solutions used in the experiments were 0.9 % NaCl @ 9 g L^{-1} (25.7 mmol L^{-1}) and 1 % Fe_2Cl_3 @ 10 g L^{-1} (37 mmol L^{-1}). Deionised water was used as a reference.

In clinical lithotripsy although the calculus is naturally submerged in urine, during the procedure the site is continuously irrigated with sterile water (to aid clearance of debris and improve visualisation). Therefore, the choice of using deionised water as the standard solution for experiments was considered to be representative of the clinical situation.

The solution of 0.9 % sodium chloride (i.e. 9g NaCl in 1 litre of water) corresponded to physiological saline which is biocompatible and therefore was considered to be a potential alternative irrigation fluid. The Fe_2Cl_3 solution strength of 1 % is not necessarily physiologically compatible but was included in the experiments for comparison against NaCl. The inclusion of stronger solutions of NaCl (5 %) and Fe_2Cl_3 (2.5 %) in the study was to identify whether any observed effect on the shockwave pressure was influenced by the concentration.

4.5 Laser-induced plasma: threshold and temperature

The laser-calculus interaction may, under the right conditions, generate plasma, a hot ionised gas formed from the ablation of matter (see section 3.8). The formation of plasma is an important parameter in the context of this research as a plasma would be expected to contribute to fragmentation action on calculi through high temperature ablation and the creation of mechanical stress waves. Furthermore, optical emissions from plasma can be analysed to identify the elements present in the ablated surface material of the calculus, and this is described in the next section (see 4.6). The following describes the experimental procedures used in the investigation of conditions necessary for plasma formation, i.e. plasma thresholds, and the properties of the plasma including its temporal history and peak temperature.

Plasma emission from the laser-calculus and laser-water interaction site was observed in a darkened room using a microscope. The microscope was equipped with a travelling stage to enable accurate measurement of the plasma volume, to an accuracy of ± 0.05 mm. A digital camera (Cybershot, Sony) set to a long exposure time (2 s) was used to record digital images for further analysis.

For the Nd:YAG laser, a spectrometer was also used to confirm plasma formation; detection of optical emission over a broad continuum confirms the presence of plasma. Plasma light emission over time in relation to the duration of the laser pulse was investigated, and the spectral plasma envelope (i.e. Bremsstrahlung radiation) was recorded in order to determine the plasma temperature using Wein's displacement formula (see section 3.9).

A spectrometer (SPEX 270M) having a 1200 g mm^{-1} diffraction grating allowing a spectral range of 0 – 1100 nm and spectral dispersion of 3.1 nm mm^{-1} was used. The spectrometer unit was coupled to a 1024 element intensified photodiode array detector (EG&G 1420), controlled by an optical multichannel analyser / pc (EG&G, OMA), and set up to cover a range of ~ 200 nm. The spectral scan was set to 350 – 550 nm for the first acquisition and 550 – 750 nm for the second. The detector was set to 8 elements per pixel, with each pixel equivalent to ~ 2 nm. The laser was run at 10 Hz pulse

repetition rate and each acquisition was an average spectrum of 10 scans. A portion of the laser pulse was reflected from an aluminium plate and detected by a photodiode to provide the trigger for the gating control unit of the multichannel analyser. A second photodiode detected the plasma flash and the signal was recorded to a digital oscilloscope together with the laser pulse signal. The light emission from the sample/water was coupled to the spectrometer by a 600 µm silica optical fibre held in a fixed position at a distance of ~ 1 cm from the beam focus, and at 90° to the beam axis. The setup is shown schematically in Figure 4.25.

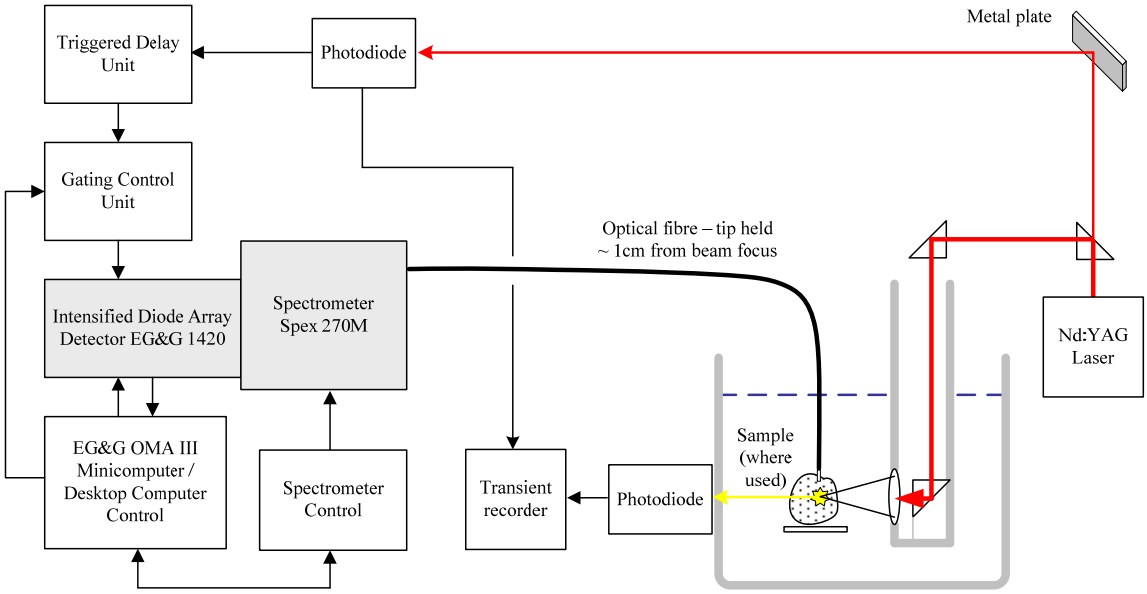

Figure 4.25: Schematic of the plasma detection experiments with the Nd:YAG laser

A set of spectral scans from 350 – 550 nm and 550 – 750 nm, along with the temporal plasma emission and laser pulse signals, were recorded for laser interaction with water and various calculi samples. Laser pulse energy was varied to achieve a good signal and also to observe the effect of pulse energy on the plasma emission.

For the Ho:YAG laser experiments, a spectrometer was not available and an alternative technique was used to detect plasma. Temporal optical emission signals were captured using a photodiode (BXP65, RS Components) and transient recorder (PicoScope ADC 200) for a range of laser pulse energies delivered to the calculus surface. It was expected

that the light intensity signal would be seen to increase significantly above any background signal once the threshold for plasma formation had been exceeded and plasma emission occured. Preliminary experiments were carried out to capture the light emission from an aluminium target during Ho:YAG irradiation, as shown in the photograph in Figure 4.26.

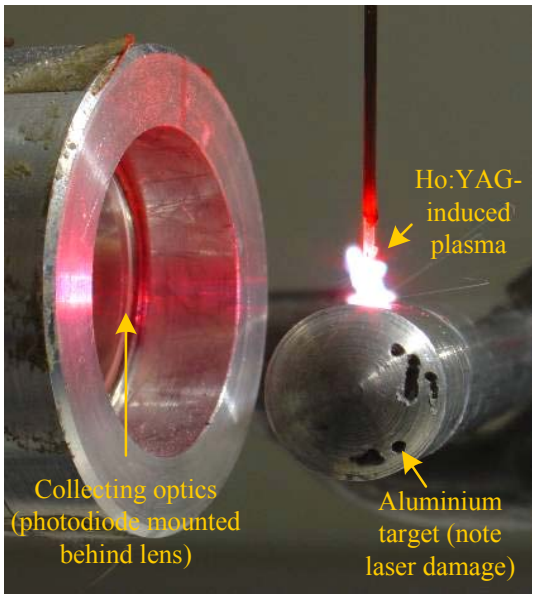

Figure 4.26: Photograph showing the preliminary setup for plasma detection experiments with the Ho:YAG laser. The holes seen on the end of the aluminium rod are a result of holmium laser ablation. The interaction, presumed to be a plasma, was accompanied by a loud 'crack' and ejection of hot metal. The image was captured with an exposure time of 2 seconds.

The laser emission, however, contained a significant contribution from scattered light presumed to be from the laser flashlamp, which was transmitted with the laser pulse. The intensity of the scattered light was found to increase with laser pulse energy, which would be expected as the output of the flashlamp is directly related to the laser output. Subtraction of the scattered light from the detected optical signal to reveal the plasma component proved to be problematic, however, as the intensity of the scattered light varied significantly from pulse to pulse. In particular, as the target became pitted by the laser beam the signal was found to be unreliable. To provide a level of confidence, the presence of plasma was, therefore, correlated with visual observations.

The Ho:YAG laser beam was fired at a number of calculi samples in air and in water. For each sample, the laser was initially set to the lowest available pulse energy (200 mJ) and incrementally increased whilst observing the interaction and capturing the light signal from the emission centre. When it appeared that a plasma was formed the energy

setting was noted, and from the known laser spot size (i.e. fibre diameter) the threshold irradiance was determined. Plots of intensity versus time, and estimated threshold irradiances, were thus obtained for the experiments with the holmium laser.

4.6 Laser-induced breakdown spectroscopy (LIBS) of calculi

Further spectroscopy measurements were carried out on plasma emission from samples to investigate characteristic line emissions to analyse and identify elemental constituents of urinary calculi i.e. laser induced breakdown spectroscopy. The aim of this work was to investigate the potential for the LIBS technique to provide in situ diagnostic information on calculi samples as in many cases the fragmented stones are normally lost.

For this study, a setup similar to that described in the previous section was employed and is shown schematically in Figure 4.27.

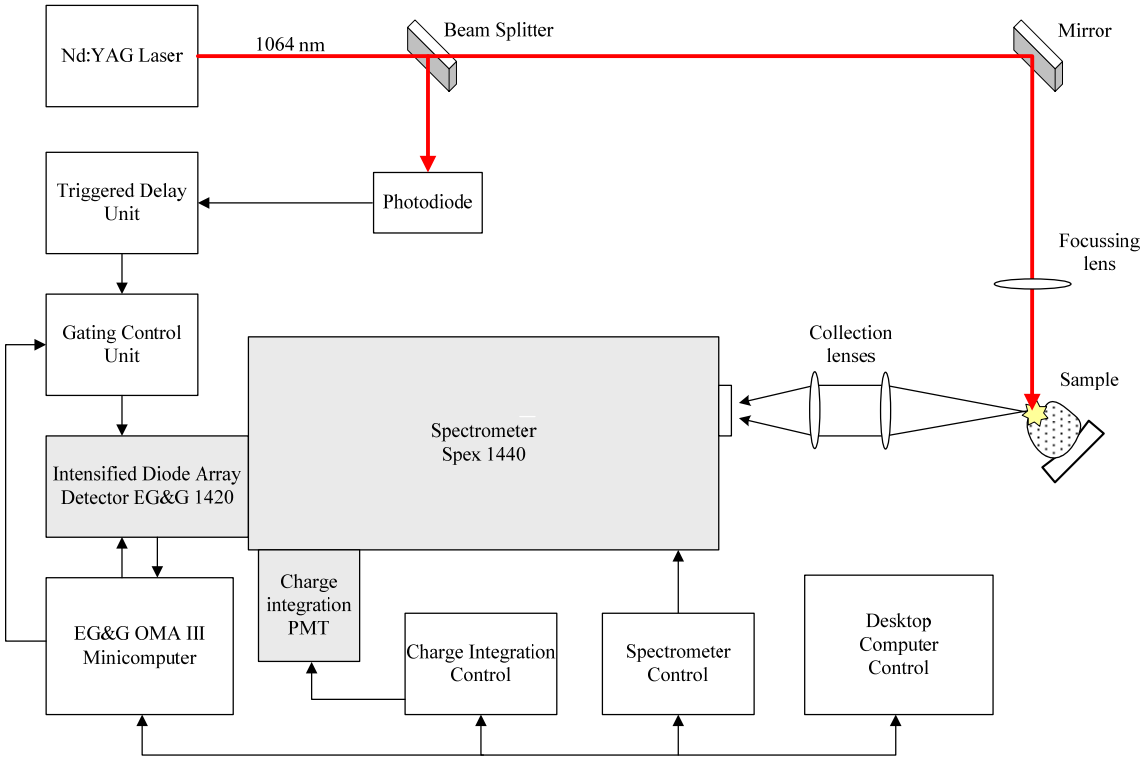

Figure 4.27: Schematic of apparatus for laser induced breakdown spectroscopy for elemental analysis

The apparatus was used to obtain spectra across the range 300 – 700 nm as an overview of emission lines but without highest resolution, and to then look more closely at specific peaks to determine the intensities of characteristic emission lines in order to estimate the concentration of elements such as calcium (Ca), magnesium (Mg), sodium (Na), strontium (Sr), potassium (K) and lead (Pb). The elements identified were then compared to those found using a second spectroscopy system, a high resolution commercial LIBS instrument, which is described later.

The setup comprised the Q-switched Nd:YAG laser as the excitation source, an optical system to transmit the laser radiation to the sample and collect plasma light for transmission to the spectrograph, a monochromator/spectrograph and choice of two detection systems, and a computer and associated software to perform data acquisition and data analysis.

For the capture of the broad spectrum (300 – 700 nm) the detector used was an intensified diode array (EG&G Model 1420) as described in the previous section, coupled to a multichannel analyser (EG&G OMA III), achieving a resolution of 0.2 nm. A gate delay of 4 μs and gate width of 20 μs gave optimal signal to noise ratio. The spectrometer slit width was fixed at 100 μm to avoid saturation of the detector.

For the capture of specific peaks the detection system used was a photomultiplier/ gated charge integrator which allowed for improved signal to noise compared to the intensified diode array detector, thereby enabling a more accurate determination of the emission wavelength and the corresponding line intensity. The spectrometer was set to a spectral width of 7 nm corresponding to a resolution of ~ 0.01 nm, with the centre wavelength being set to the principal emission line of the element of interest. Due to the abundance of calcium and magnesium in the samples it was necessary to avoid signal saturation by selecting a wavelength for these elements of lower intensity than their principal lines. In addition the slit width was adjusted from 100 μm to 25 μm. For the target elements emission intensities at the following wavelengths were recorded: 457.9 nm, 458.1 nm, 458.6 nm (Ca); 407.5 nm (Mg); 589.0 nm, 589.6 nm (Na); 460.7 nm (Sr); 404.4 nm, 404.7 nm (K); and 405.8 nm (Pb).

Samples were mounted on a metal plate using Blu-Tack® adhesive, as shown in Figure 4.28, which was presented to the focus of the laser beam by means of a 25 mm focal length lens (Figure 4.29). The laser pulse energy and pulse repetition rate were maintained at 25 mJ and 20 Hz, respectively for this experiment. The sample holder was micro-adjustable to allow manipulation and control of the area under ablation. With certain samples the composition material was rapidly ablated and it was necessary to continually adjust the position of the focus on the sample to avoid drilling a hole and maintain plasma emission.

Figure 4.28: Photograph showing an example of samples prepared for LIBS experiments.

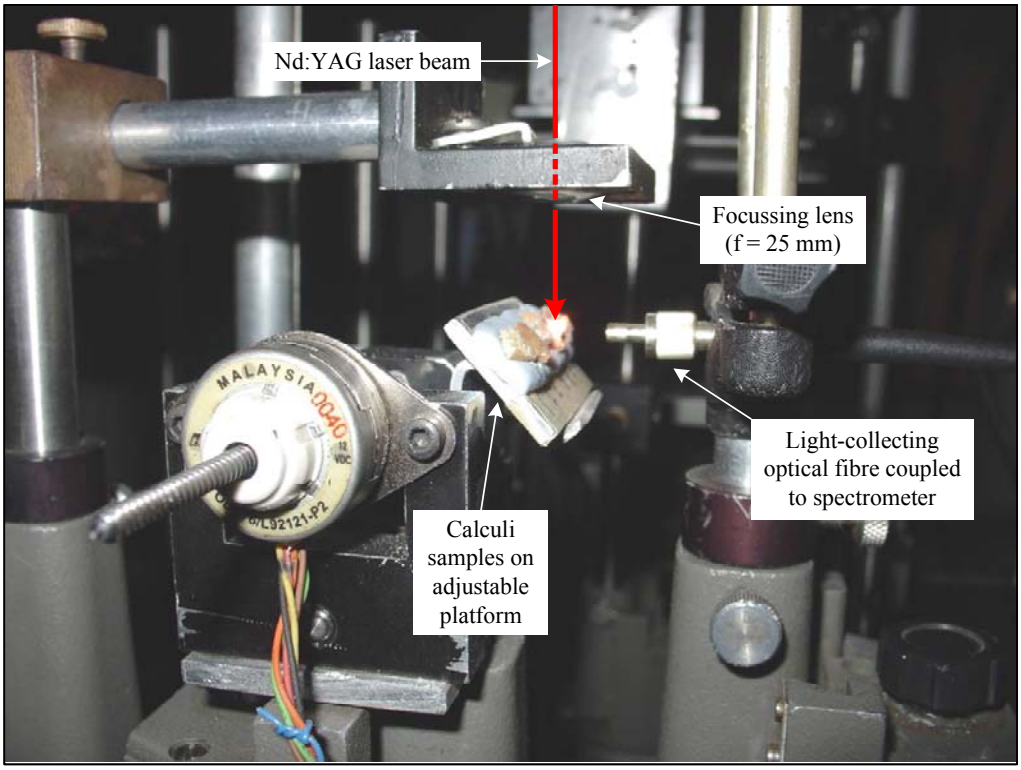

Figure 4.29: Sample presentation and light collection arrangement

The spectral dispersion was achieved by a high-resolution (maximum ~10 cm^{-1}) f/7.8 double monochromator (SPEX 1404). The spectral purity was quoted to be < 10^{-14} at wavelength > 0.5 nm from a set wavelength, and spectral coverage extended from UV to near IR wavelengths. The plasma source was imaged onto the entrance slit of the monochromator with a collecting lens of 50 mm diameter and a focusing lens (f = 200 mm) giving an f# nearly matching that of the monochromator to achieve optimum collection of light.

Temporal scans of the emission from the plasma on the samples were recorded using a digital oscilloscope (Digiscope-HP5, Hewlett Packard, USA). The bandwidth of the instrument was 500 MHz, thus enabling it to faithfully reproduce signals with a rise time of ≥ 2 ns.

The gated charge integrator electronic system (EG&G Model 4420) allowed detection of signals from the plasma through a time gate of width, variable between 2 ns to 2 ms and after a time delay from the laser pulse, variable from 50 ns to 2 ms. The photomultiplier (Electron Tube - 9214B) has a rise time of 2 ns and a spectral window for good response of 300 – 600 nm. The photomultiplier tube dark current is quoted to be 1 nA (200 counts s^{-1}).

Although relatively low laser power was required to generate plasma on the calculus surface, the tightly focused laser pulses bored into the stone material creating a pit. Thus during collection of the LIBS spectra, plasma signal from both the surface and the underlying material was included. Also, as the pit at the ablation site became more pronounced the material was no longer in the exact focus and so weaker plasma was generated, thus requiring the repositioning of the sample several times during signal collection. This offered the added advantage of averaging the signal emanating from a larger area of the sample.

The concentrations of the elements were derived from calibration data obtained for pure sample powder of compounds of known elemental concentration (see Appendix D for further details).

The LIBS studies using a high resolution system were carried out with an echelle spectrograph (Aryelle) as shown in Figure 4.30. The instrument incorporated a two dimensional detector and echelle grating to achieve very high spectral resolution and broad band efficiency, by diffraction of light in a multitude of high interference orders. A prism separates the echelle orders and achieves a resolution of 0.004 nm enabling the identification of characteristic lines with greater certainty compared to the OMA system. In addition, the optical detection system is cooled to around -65 °C to minimise detector noise, thereby achieving a higher spectral signal to noise ratio. As with the OMA instrument, the gate delay was adjusted to avoid signal saturation from bremsstrahlung emission and varied between ~ 24 – 32 μs with an optimised setting of 23.9 μs. Gate width was adjusted between 5 s and 20 s and found to give best results at a setting of 20 s owing to the increased number of emission lines resolved. During this exposure time a signal average of 400 laser shots were obtained (laser set to 20 Hz and 25 mJ). The spectrometer was calibrated against the emission from a mercury lamp before use to ensure the system was set to give reliable spectral measurements. Once set up, the spectra were obtained for a number of urinary calculi across the spectral range ~ 190 – 430 nm.

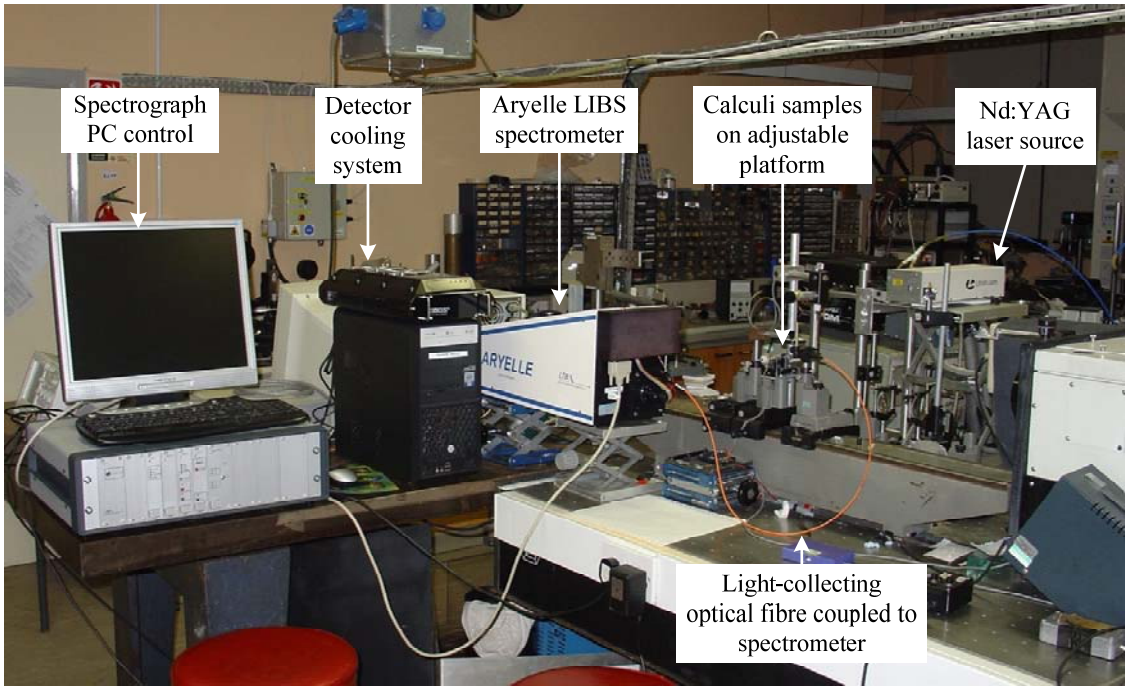

Figure 4.30: Apparatus for high resolution LIBS experiments

The atomic emission spectra obtained with the OMA and Aryelle instruments were compared against characteristic lines of elements obtained from a software database (Optical Emission Lines of the Elements, John Wiley & Sons, 2000). The database search was based on a number of elements potentially present in urinary stones as reported in the literature (Lin et al, 1987; Pougnet et al, 1988; Galassini et al, 1989; Al-Kofahi and Hallak, 1996; Golavanova et al, 2003; Chaudhri et al, 2007; Singh et al, 2008) and included the metal elements Ca, Mg, K, Na, Pb, Fe, Cr, Sr, Cu, Mn, Zn and Al. Parameters for the search were set to a plasma temperature of 6500 K and first order atomic ionisation.

The Aryelle system was also potentially able to detect light organic elements as well as metals, and the search was widened to include elements such as O, P, H, N, S and C. The software on this system (Sophie for Aryelle) was utilised to identify peaks by comparison to the National Institute for Standards and Technology (NIST) database of emission lines, and assigned presence of elements to peaks where agreement was within the pixel resolution (± 0.004 nm). However, this was not relied upon and for each significant peak identified the identification was compared to the software database used as a reference for identification of elements with the OMA system.

Thus, LIBS spectra were obtained for a selection of samples of urinary calculi and specific peaks investigated. The concentrations of the key metal elements present were estimated. A comparison was made with results obtained with a high resolution echelle spectrometer. The next section presents experimental work that may potentially indicate areas for further work regarding other laser wavelengths that may offer promise in the fragmentation of calculi.

4.7 Optical absorption in the UV-Vis-NIR: basis for further work

In section 4.2, FT-IR spectroscopy was described for material analysis and also for the matching of absorption bands to laser wavelengths that would be expected to lead to efficient fragmentation. In this section, absorption properties of selected calculi the in UV-Vis-NIR region are investigated. There are a number of lasers available with emission in the range 250 – 850 nm (see Figure 4.31) and this set of experiments may

point to specific wavelengths where there is greater absorption in this region and thus highlight lasers for further investigation in lithotripsy application.

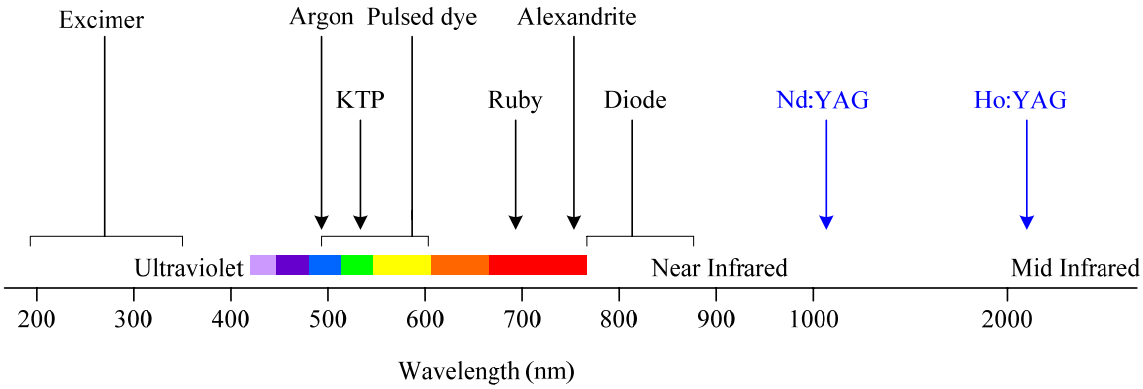

Figure 4.31: Common lasers with an emission in the range 250 – 850 nm. For comparison the Nd:YAG (1064nm) and Ho:YAG (2100 nm) lasers are also shown.

Calculus material is practically opaque and therefore conventional absorption spectroscopy based on direct transmission measurement was not possible. For these samples, an estimate of how much incident light is absorbed at a particular wavelength was determined from measurements of diffuse reflection. An assumption is made that what is not diffusely reflected is absorbed i.e. $I_A(\lambda) = 1 - I_R(\lambda)$, where I_A and I_R are the fractions of absorbed and reflected intensities of light at wavelength λ incident on the calculus surface. As the sample surface was diffuse (unpolished), specular reflection can be ignored and the approximation is sufficiently accurate to give a good indication of the spectral absorption properties of the materials.

A plot of the estimated absorbed intensity versus an accurate measure of the wavelength was made, from which wavelengths of peak absorption peaks were identified. This procedure allows matching samples to available laser wavelengths for the optimum destruction of calculi.

The diffuse reflectance spectra were recorded using a commercial UV-Visible-NIR spectrophotometer (Perkin Elmer Lambda 9), as shown as a photograph in Figure 4.32. The instrument is a double-beam double-monochromator ratio recording

spectrophotometer. A 150 mm integrating sphere was incorporated into the spectrophotometer for collecting the diffuse reflection from the samples.

Figure 4.32: The Lambda 9 system used for diffuse reflectance measurements

The spectrometer has two radiation sources, a deuterium lamp for the ultraviolet region, and a tungsten-halogen lamp for the visible and near infrared regions. For diffuse reflection measurements the usable range with the integrating sphere attached was 250 nm to 850 nm.

Samples for measurement were held over an aperture on the integrating sphere where the probe beam was incident (see Figure 4.33). Spectralon material was placed over a second aperture to serve as a reference diffuse reflector (diffuse reflectance >> 99 %). A background correction for the instrument was carried out with spectralon at both sampling apertures. This allowed the system to automatically adjust for calibration errors between the two optical pathways, and therefore, record an accurate sample to reference ratio.

The beam size at each aperture was approximately 8 mm x 20 mm. Only samples of at least this size could be used for this measurement, otherwise diffuse reflectance would be underestimated leading to an overestimate of optical absorption.

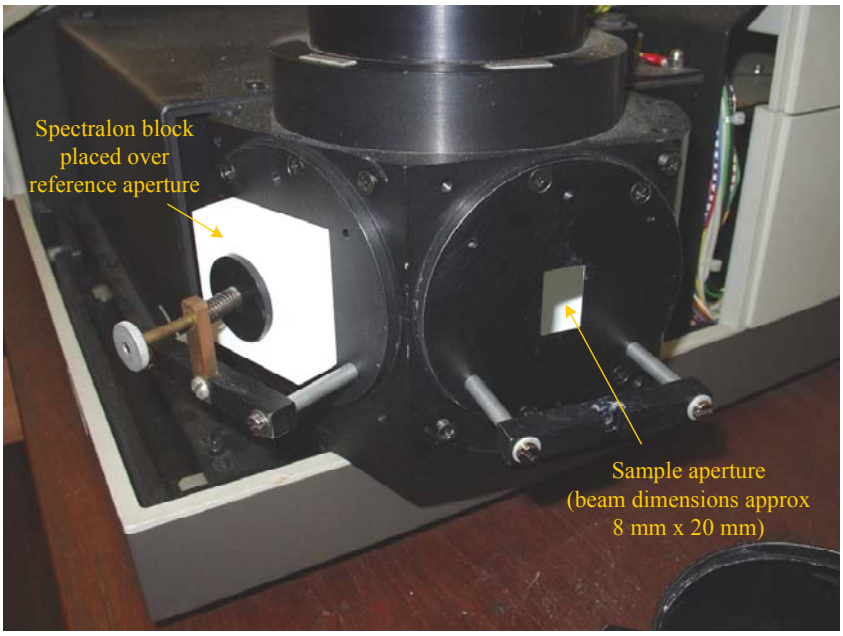

Figure 4.33: The Lambda 9 integrating sphere apertures showing the sample presentation arm

The spectrometer was adjusted to the following settings: run from 250 nm to 850 nm with a scan speed of 240 nm per minute, step size of 0.2 nm and data capture to PC in 1 nm increments. Recorded data was imported to Excel spreadsheet.

Thus, in this chapter, a technique for the analysis of calculi samples using conventional FT-IR spectroscopy has been described. Two laser systems for laser-calculus and laser-water interaction experiments were characterised and compared. The design and construction of a sample chamber for the measurements in water has been devised and evaluated. High sensitivity hydrophone devices have been used to record laser generated pressure pulses. Apparatus for the capture and analysis of plasma signals has been described for example spectroscopy instrumentation. A methodology for conducting laser induced breakdown spectroscopy as a novel technique for the analysis of urinary calculi has been described. The results of experiments using the systems outlined in this chapter are presented in the next chapter.

Chapter 5
Results and Analysis

The results and discussion of the experimental work carried out for this thesis are presented in this chapter. The first section reports the findings of the analysis of the calculus samples using FT-IR and diffuse reflectance spectroscopy. The analysis of results of this study allows a judicious choice of laser wavelength for effective stone fragmentation, although the experiments conducted in this work were limited to only two available lasers suitable for such application. The second section evaluates the laser interaction experiments; firstly with water, to produce shockwaves, and secondly with calculus material, to cause ablation. The third section covers the results of the laser induced plasma experiments, including the studies carried out on laser induced breakdown spectroscopy (LIBS) of calculi.

5.1 FT-IR spectroscopic analysis of calculi samples

The following are the results of FT-IR analysis of a selection of calculi samples, categorised in chapter 4. Test parameters and instrument specifications are included in the previous chapter. The spectra and analyses are as follows:

Sample 1 (urinary stone)

The infrared absorption spectrum obtained for sample 1 (Figure 5.1) exhibits a large number of sharp absorption lines within the 450 cm^{-1} – 1625 cm^{-1} band. The prominent lines are found at 1625 cm^{-1}, 1587 cm^{-1}, 1488 cm^{-1}, 1410 cm^{-1}, 847 cm^{-1}, 541 cm^{-1} and 453 cm^{-1} wavenumber positions. This type of absorption spectra with multiple characteristic peaks is typical of organic compounds. The major line frequencies compare closely with the reference spectrum obtained for pure cystine, and although marginally low, are within ± 5 cm^{-1} (peaks at 1622, 1582, 1483, 1406, 845, 540, 451). The general form of the spectrum is also in very good agreement with the spectrum of laboratory grade cystine (see Appendix B), showing a similar shoulder at around 3340 cm^{-1}, and steadily rising transmission from around 3000 cm^{-1} to a peak at 1785 cm^{-1}. This sample is therefore identified as being composed primarily of cystine ($C_6H_{12}N_2O_4S_2$).

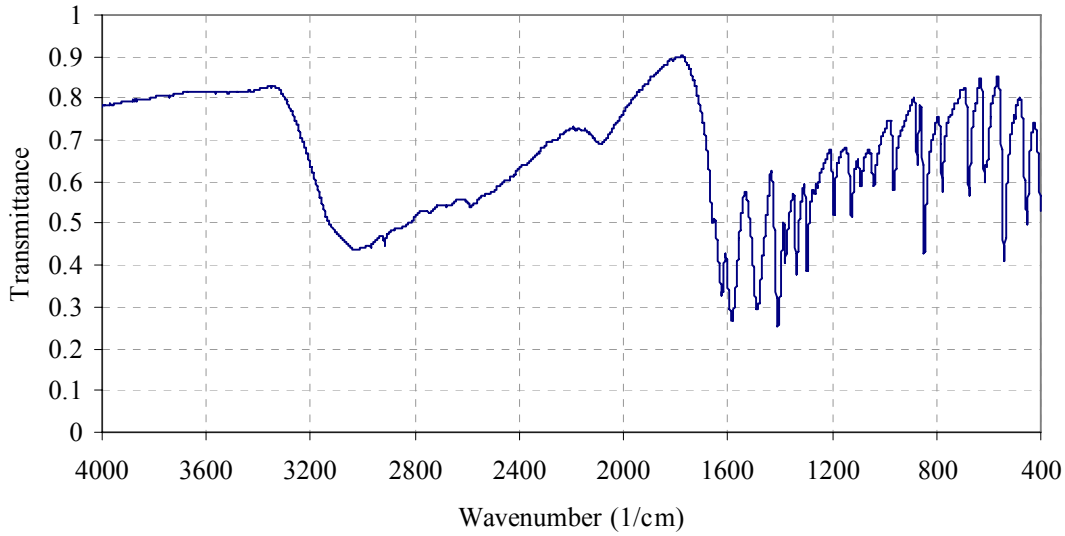

Figure 5.1: FT-IR spectrum of Sample 1 identified as cystine

A crystalline amino acid found in protein, cystine stones arise from a genetic defect in which the renal tubule is unable to reabsorb filtered cystine. The result is a very high level of cystine in the urine, which becomes supersaturated at normal pH levels resulting in spontaneous precipitation of cystine. Some patients are treated with large doses of alkali, such as calcium phosphate, which helps to maintain cystine in solution. For this reason, although the majority of cystine calculi formed in humans are pure in composition, calcium phosphate is sometimes found as a component. The indicator for calcium phosphate is a broad band at 870 cm^{-1}, however, no such band is present in this sample suggesting that the patient had not been given such treatment. Studies have also indicated other components may be found in the nuclei of cystine stones (Carmona et al, 1997), however, in this case the core was not analysed.

Clinically, cystine stones can be particularly difficult to treat, and sufferers of cystinuria generally require lifelong treatment. Shockwave treatment is largely ineffective against cystine stones on account of their hardness. This particular sample has been successfully fragmented using holmium laser lithotripsy, which suggests that the Ho:YAG laser-calculus interaction is not a purely shockwave mechanism, or that it generates greater intensity shockwaves than other lithotripsy modalities.

Sample 2 (urinary stone)

The spectrum obtained for this sample (Figure 5.2) was identified as being very similar to sample 1. Absorption bands at 1620 cm^{-1}, 1585 cm^{-1}, 1481 cm^{-1}, 1407 cm^{-1}, 847 cm^{-1}, 539 cm^{-1} and 451 cm^{-1}, compare very closely with the reference spectrum for pure cystine (see Appendix B). Again, no calcium phosphate was identified and therefore this sample also is identified as having primarily composed of cystine ($C_6H_{12}N_2O_4S_2$). This stone was also successfully removed from a patient using a holmium laser to induce fragmentation.

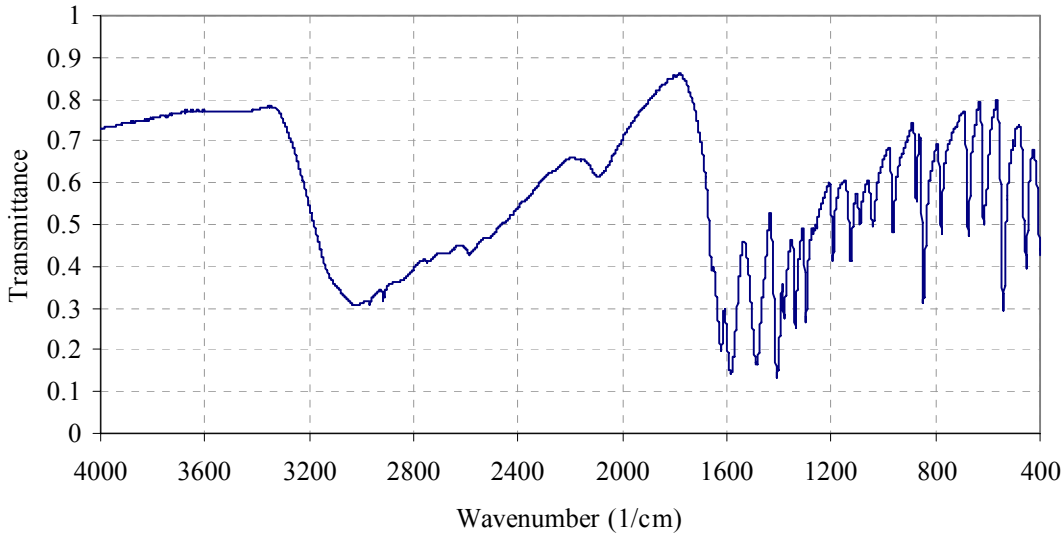

Figure 5.2: FT-IR spectrum of Sample 2 identified as cystine

Sample 3 (urinary stone)

Fewer bands are present in the FT-IR spectrum of this sample (Figure 5.3), and only one relatively strong absorption band appears. The bands consist of lines at 1650 cm^{-1} (weak), 1431 cm^{-1} (medium), 1005 cm^{-1} (strong), 746 cm^{-1} (weak) and 560 cm^{-1} (weak). Characteristic transmission maximums at both 1344 cm^{-1} and around 2035 cm^{-1} are also observed. Comparison with a reference spectra (Appendix B) revealed a close match for magnesium ammonium phosphate hexahydrate (MAPH/ struvite) was found. The composition of this sample can be identified even in mixed stones by the position of the strong band at 1005 cm^{-1} of PO_4 group vibration, which is present as the strongest band found in this sample. Characteristic weaker bands at 760 cm^{-1} and 572 cm^{-1} (N-H bond and PO_4 group respectively) are also expected, and peaks appear at approximately 750 cm^{-1} and 560 cm^{-1} and are within the ±10 cm^{-1} of the expected value. The band at 1430

cm^{-1} indicates the presence of carbonate, a minor composition of the stone, in the form of calcium phosphate carbonate (carbonate apatite). Sample 3, therefore, is considered to be composed of magnesium ammonium phosphate hexahydrate ($MgNH_4PO_4.6H_2O$) with a small amount of calcium phosphate, carbonate/ carbonate apatite ($Ca_{10}(PO_4)_6CO_3$).

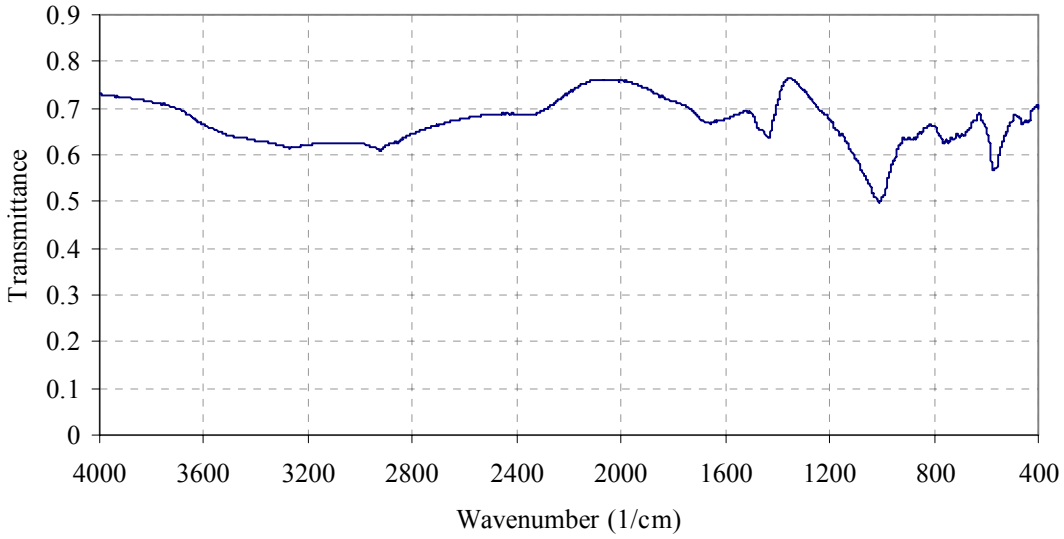

Figure 5.3: FT-IR spectrum of Sample 3 identified as magnesium ammonium phosphate hexahydrate (struvite) with minor calcium phosphate carbonate (carbonate apatite)

Calculi containing struvite are a result of urinary tract infection. Urea-cleaving bacteria produce a high concentration of ammonia in the urine, which raises the pH value to above 7.5. At this pH value, normal concentration levels of magnesium and phosphate in the urine becomes supersaturated and struvite crystals precipitate out of solution.

Sample 4 (urinary stone)

The FT-IR absorption lines for this sample are at 3537 cm^{-1}, 3483 cm^{-1}, 1647 cm^{-1}, 1132 cm^{-1}, 1059 cm^{-1}, and 527 cm^{-1} from the spectrum shown in Figure 5.4. The features of the spectrum show close similarity to the reference spectrum for calcium hydrogen phosphate dihydrate, also known as brushite, (Appendix B). Comparatively sharper lines in the range 650 – 1200 cm^{-1} can be attributed to some organic components from the spectral fingerprints. From the above analyses the sample is identified as calcium hydrogen phosphate dihydrate ($CaHPO_4.2H_2O$).

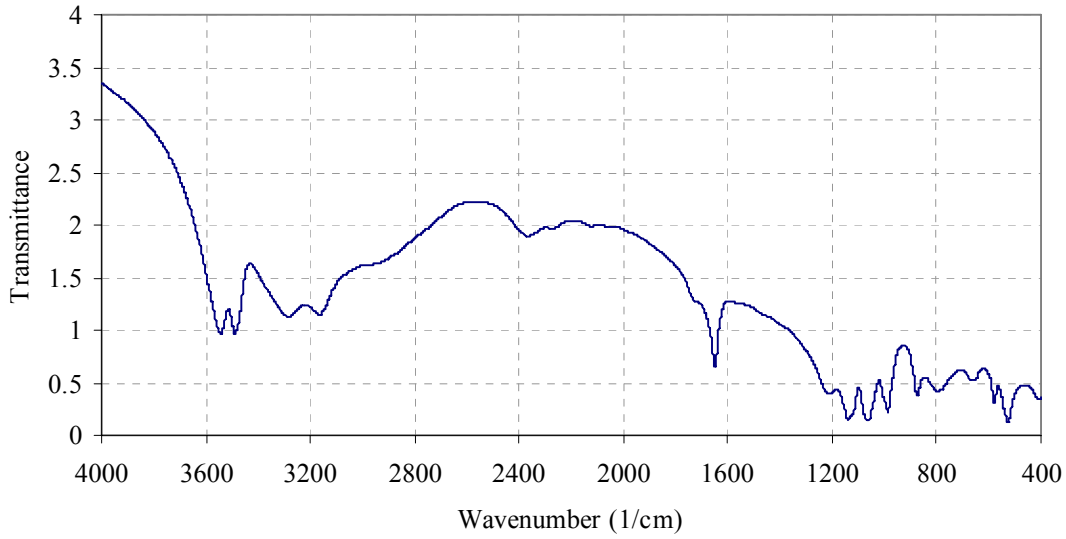

Figure 5.4: FT-IR spectrum of Sample 4 identified as calcium hydrogen phosphate dihydrate (brushite)

Sample 5 (urinary stone)

The absorption bands found at 1618 cm^{-1}, 1587 cm^{-1}, 1481 cm^{-1}, 1404 cm^{-1}, 845 cm^{-1}, 540 cm^{-1} and 451 cm^{-1} as shown in Figure 5.5 match with the spectrum of the reference cystine (Appendix B), and this sample is therefore identified as being composed of cystine ($C_6H_{12}N_2O_4S_2$).

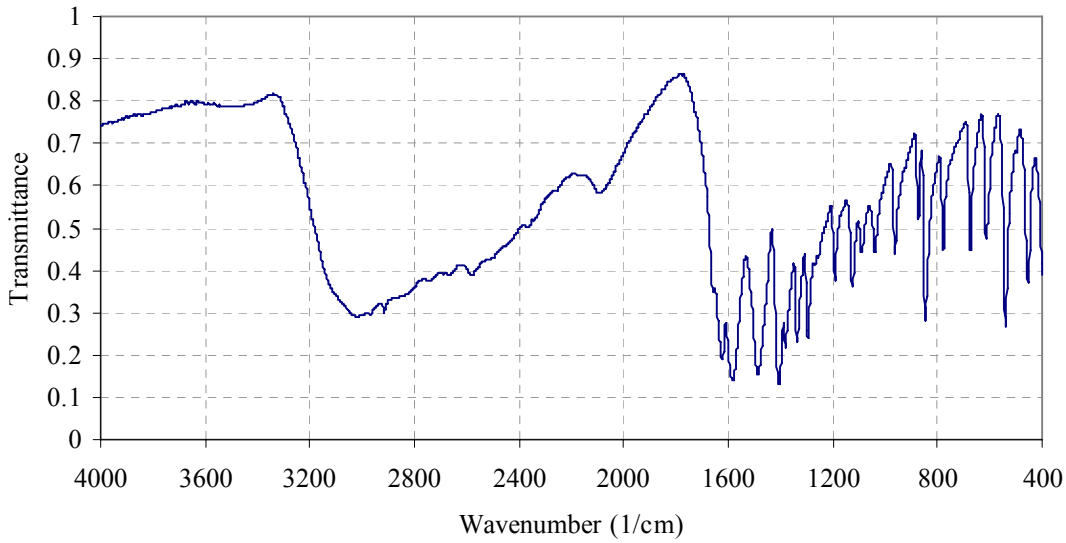

Figure 5.5: FT-IR spectrum of Sample 5 identified as cystine

Sample 6 (urinary stone)

The spectrum of this sample, as presented in Figure 5.6, shows a close similarity to reference spectra for calcium oxalate dihydrate/ weddellite (Appendix B). Therefore this (COD) should be a major component of this sample. The peak absorption bands at 1640 cm^{-1} and 1325 cm^{-1} provides a definite identification of the presence of calcium oxalate dihydrate (COD). Often, the two calcium oxalates (monohydrate and dihydrate) appear together in varying proportions, leading to confusion in identification when one component is in excess. However, inspecting for the presence of calcium oxalate monohydrate (COM) revealed that there was no apparent sharpening and increase in the intensity of the 780 cm^{-1} band, and there are no characteristic bands of COM at 3492, 3430, 3340, 3058, 952, 885, and 665 cm^{-1}. Hence, this sample is identified as pure calcium oxalate dihydrate ($CaC_2O_4.2H_2O$).

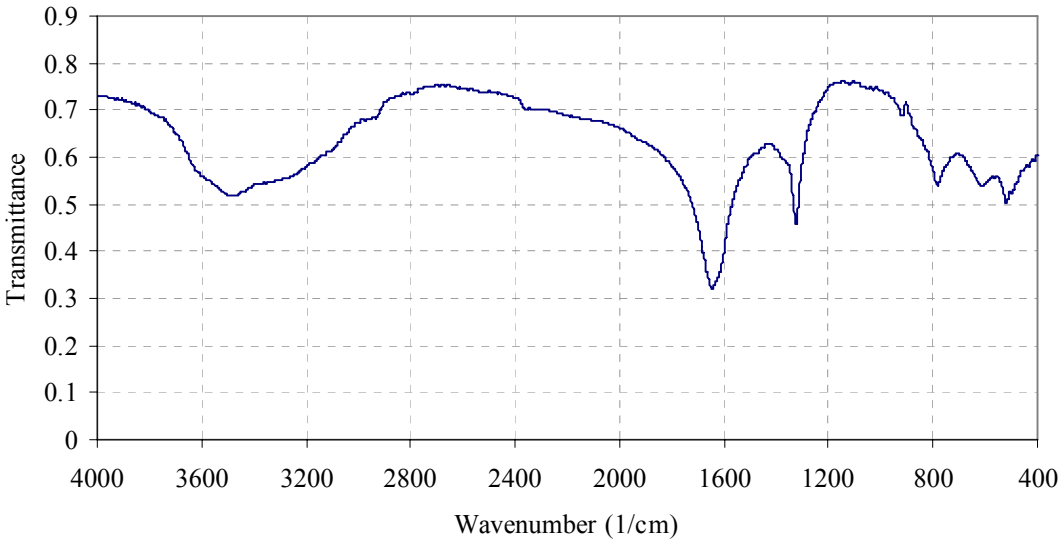

Figure 5.6: FT-IR spectrum of Sample 6 identified as calcium oxalate dihydrate (weddellite)

Calcium oxalate is the most common constituent of urinary calculi (Robertson and Peacock, 1979). Even in normal urine calcium oxalate is very close to the point of spontaneous precipitation, and because of their low solubility, once formed, they are extremely difficult to disolve. In the majority of cases no specific underlying disease is identified. Raised levels of oxalate and an increase in calcium excretion are among a number of risk factors, however, the exact mechanism of their formation is not fully understood.

Sample 7 (urinary stone)

The FT-IR spectra of the sample, shown in Figure 5.7, exhibits absorption lines at 1617 cm^{-1} (strong), 1315 cm^{-1} (strong), 779 cm^{-1} (strong) and 512 cm^{-1} (medium). The significant bands of the reference calcium oxalate monohydrate sample (Appendix B) are at 1620 cm^{-1} and 1315 cm^{-1} (C-O bond) and 780 cm^{-1} (O-H bond). This is a very good agreement and confirms the identity of the calculus sample as calcium oxalate monohydrate ($CaC_2O_4.H_2O$), also known as whewellite.

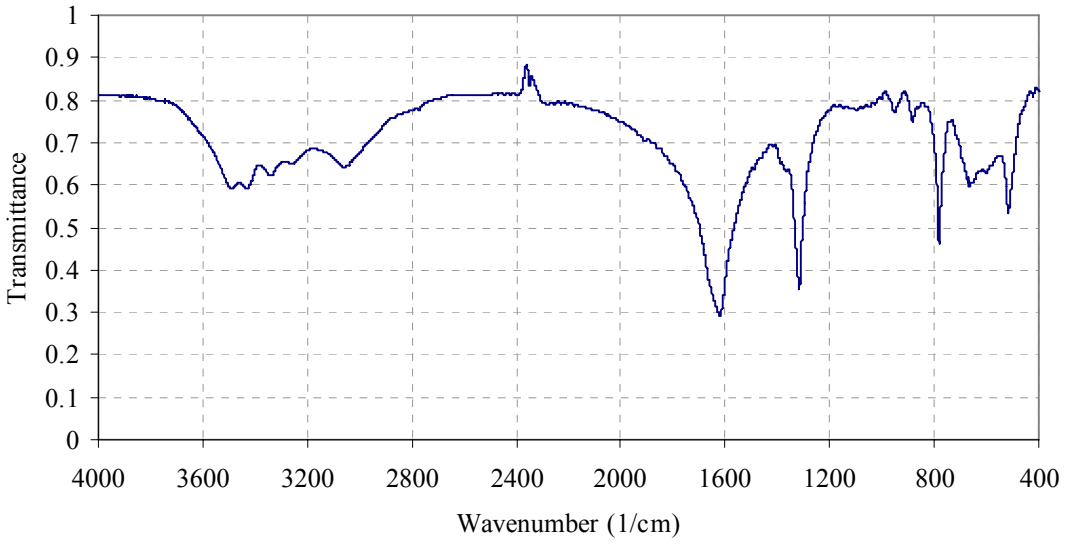

Figure 5.7: FT-IR spectrum of Sample 7 identified as calcium oxalate monohydrate (whewellite)

Sample 8 (urinary stone)

The spectrum of this sample shows absorption bands at 1616 cm^{-1} (strong), 1314 cm^{-1} (strong), 780 cm^{-1} (strong) and 511 cm^{-1} (medium) as shown in Figure 5.8. As with the previous sample this calculus is identified as being composed of calcium oxalate monohydrate ($CaC_2O_4.H_2O$).

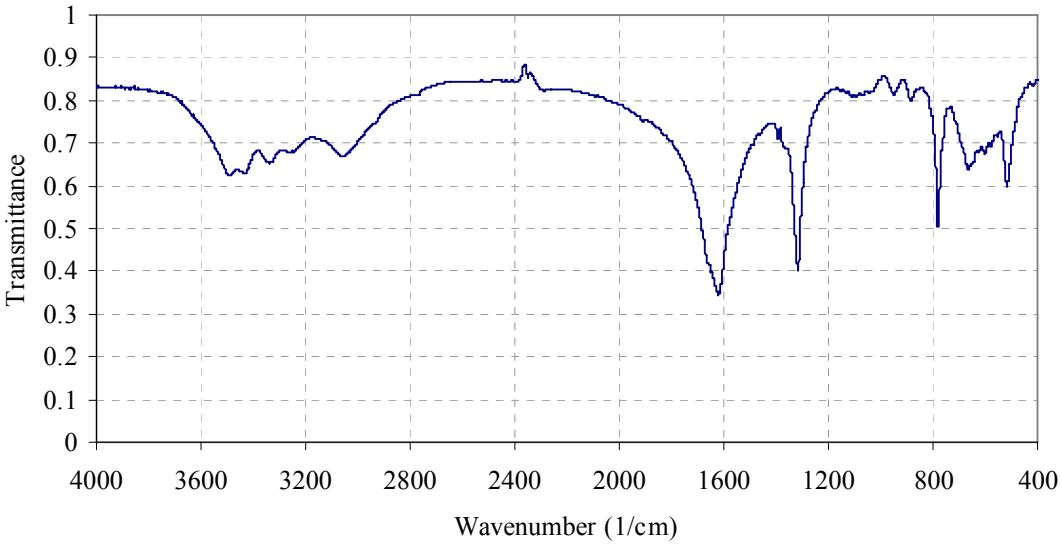

Figure 5.8: FT-IR spectrum of Sample 8 identified as calcium oxalate monohydrate (whewellite)

Sample 9 (urinary stone)

This sample has a large number of strong absorption lines within the 400 cm^{-1} – 1600 cm^{-1} band and characteristic shape, as shown in Figure 5.9, which matches well with the reference spectra for uric acid (Appendix B). The bands are identified as 2021 cm^{-1} (strong), 1585 cm^{-1} (strong), 1435 cm^{-1} (medium), 1400 cm^{-1} (medium), 1348 cm^{-1} (medium), 1308 cm^{-1} (medium), 1122 cm^{-1} (strong), 991 cm^{-1} (strong), 876 cm^{-1} (medium), 783 cm^{-1} (strong), 744 cm^{-1} (strong), 704 cm^{-1} (medium), 619 cm^{-1} (strong), 573 cm^{-1} (strong), 523 cm^{-1} (strong) and 474 cm^{-1} (strong). There are no water bands present at 3515 and 3445 cm^{-1}, which means that it is the anhydrous form of uric acid.

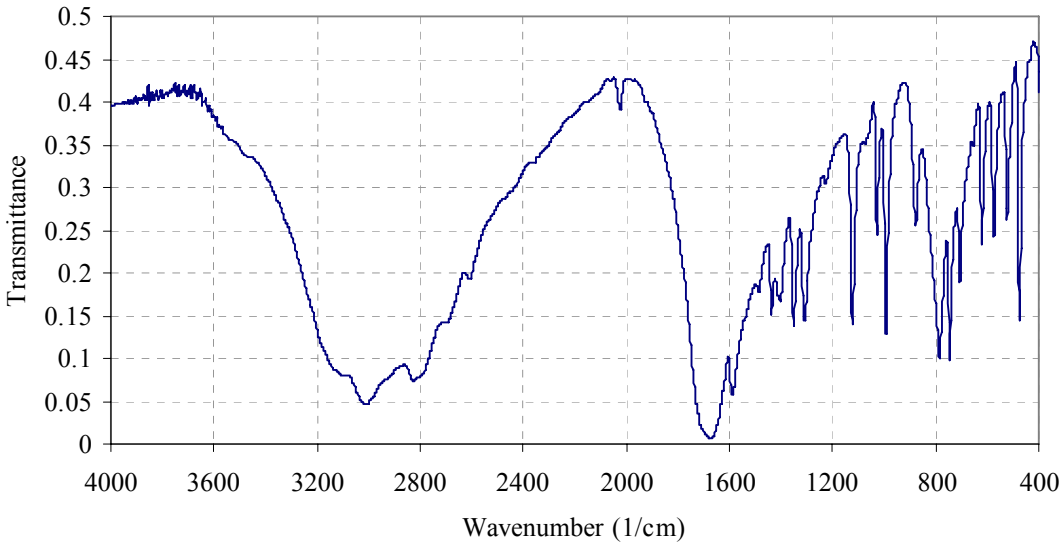

Figure 5.9: FT-IR spectrum of Sample 9 identified as uric acid

The formation of uric acid stones can largely be accounted for in terms of the biochemical conditions that favour uric acid precipitation. The most important factors are the concentration of uric acid and the pH of urine. In uric acid lithiasis, patients are found to have above normal saturation levels of uric acid, lying above the point of spontaneous precipitation of uric acid. For that reason, dehydration may be a significant contributing factor with this condition.

Sample 10 (urinary stone)

FT-IR spectrum of this sample (Figure 5.10) is very similar to sample 3, with only a few absorption peaks. The peaks are at 1650 cm^{-1} (weak and broad), 1435 cm^{-1} (weak and broad), 1018 cm^{-1} (strong), 600 cm^{-1} (medium) and 5601 cm^{-1} (medium). Comparing to a reference spectra (Appendix B) this appears to be a close match for magnesium ammonium phosphate hexahydrate (MAPH), also known as struvite. This is most likely to be caused by urinary tract infection by urea-splitting bacteria.

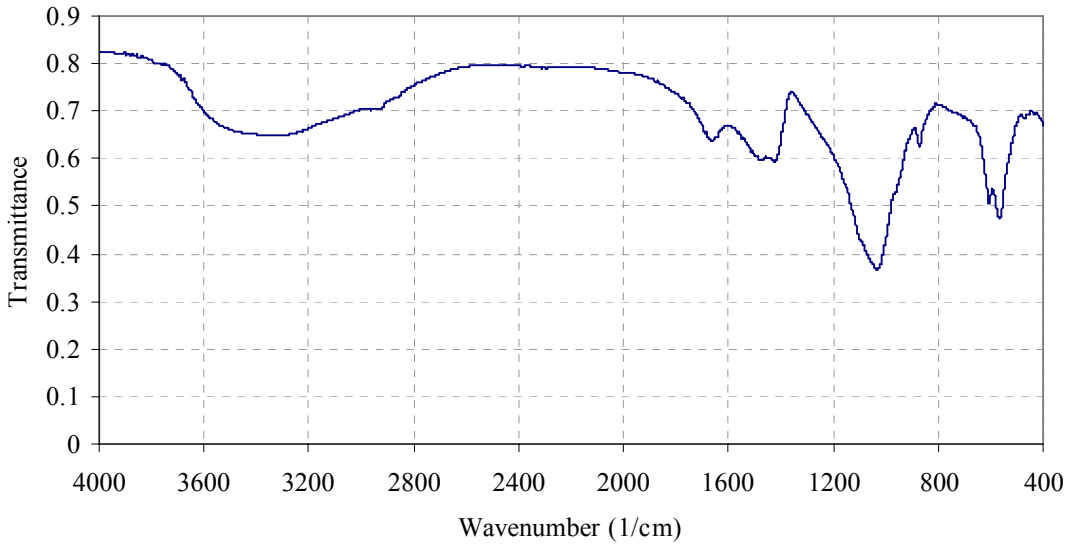

Figure 5.10: FT-IR spectrum of Sample 10 identified as magnesium ammonium phosphate hexahydrate (struvite)

Sample 11 (gallstone)

This is a sample of a gallstone which has a very different composition to stones formed in the urinary tract. The chemical environment in the gall bladder is a solution of bile salts and fat deposits. Despite their different composition and anatomical location, such stones can, however, also be treated using lasers and thus three specimens were included in this study. The FT-IR spectrum presented in Figure 5.11 shows absorption peaks at 3389 cm^{-1} (medium and broad), 2926 cm^{-1} (strong), 1462 cm^{-1} (strong), 1053 cm^{-1}(strong), and 798 cm^{-1}(weak). The strong band between 2700 and 3100 cm^{-1} indicates that cholesterol is present, and the band between 1600 cm^{-1} and 1800 cm^{-1} indicates the presence of bilirubin. Phosphate is also present as a minor component, as identified from the sharp line at 1053 cm^{-1}.

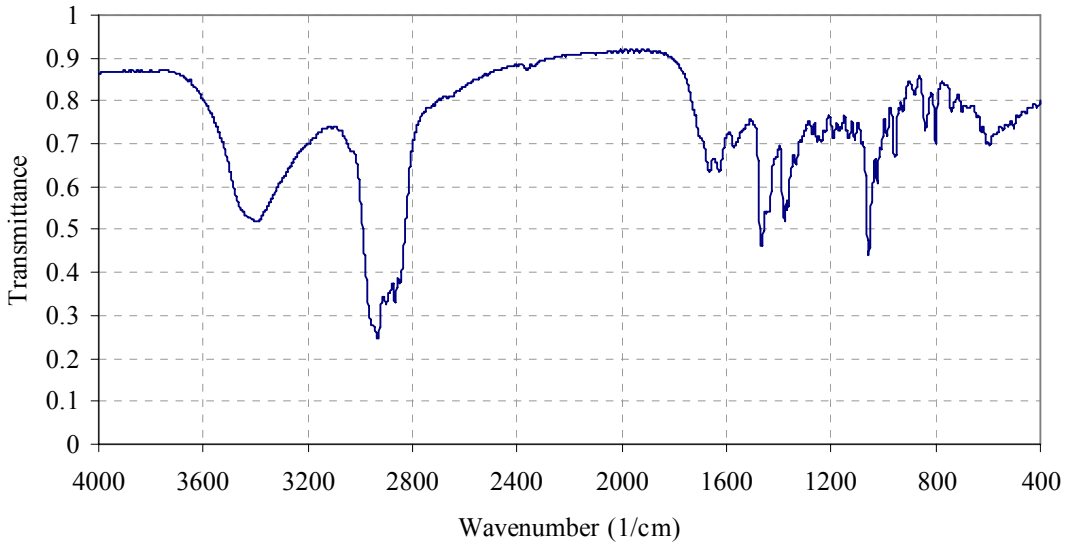

Figure 5.11: FT-IR spectrum of Sample 11 identified as cholesterol / bilirubin / phosphate

Sample 12 (gallstone)

The spectral characteristics of this sample, as shown in Figure 5.12, is similar to that of sample 11 and is also of a gallstone. The FT-IR spectrum reveals absorption bands at 3398 cm^{-1} (medium and broad), 2930 cm^{-1} (strong), 1464 cm^{-1} (strong), 1055 cm^{-1} (strong), and 798 cm^{-1} (weak). Using the same analysis as previous example is identified as comprising bilirubin, cholesterol, and a small component of phosphate.

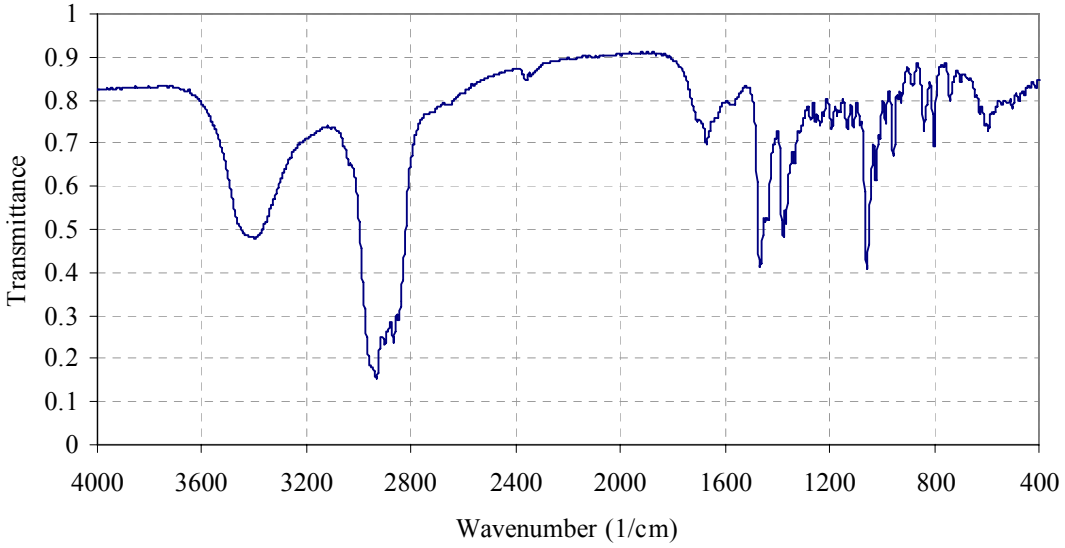

Figure 5.12: FT-IR spectrum of Sample 12 identified as cholesterol / bilirubin / phosphate

Mixed biliary calculi form when the bile, a liquid secreted in the gallbladder to break down fatty foods, becomes saturated with cholesterol or bile salts.

Sample 13 (gallstone)

This sample has fewer absorption bands in the region 500 cm^{-1} – 1600 cm^{-1}, as shown in Figure 5.13. The bilirubin and cholesterol absorption bands are identified; however, there is no indication of phosphate or carbonate present in the sample.

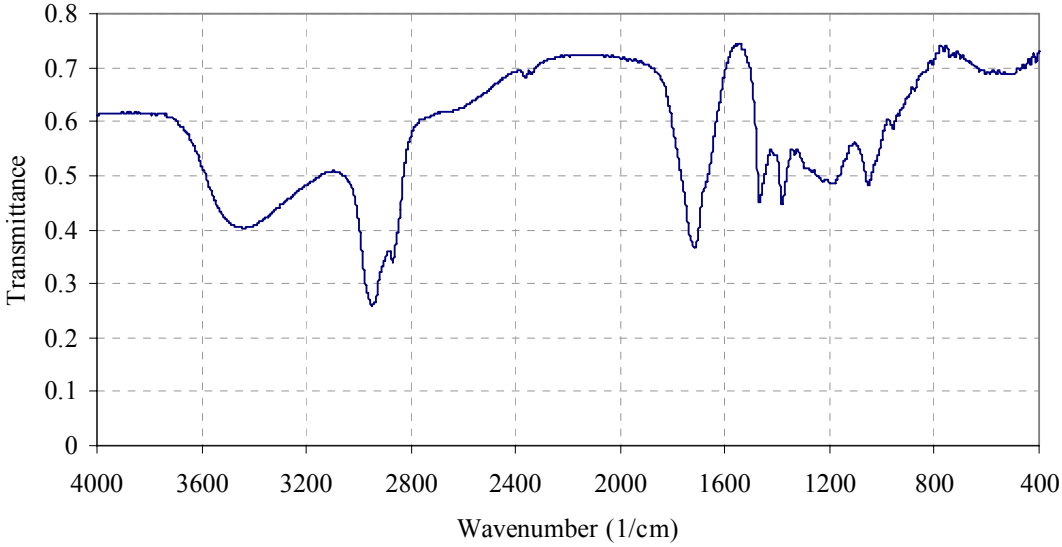

Figure 5.13: FT-IR spectrum of Sample 13 identified as cholesterol and bilirubin

The samples obtained for analysis were found to be of a range of compositions as summarized in Table 5.1. The calculi include the most common types of urinary stones which are the calcium oxalate monohydrate and dihydrate forms, and also the mixed stones arising from infection which comprise struvite and other constituents. The samples found to be of cystine composition are less common, however, it is not surprising that 3 specimens were identified as they are generally resistant to other treatment modalities hence were presented for holmium laser lithotripsy. Uric acid stones occur more frequently than cystine calculi, but are less common than calcium based compositions. Gallstones, on the other hand, are mainly found to comprise a mixture of cholesterol, bilirubin, and calcium carbonate in varying proportions

depending on the conditions at the time. The samples analysed were found to constitute all of these substances and are therefore fairly typical specimens.

Table 5.1: Summary of sample identification and their peak absorption wavelengths

Sample	Calculus composition	Strong absorption lines / wavelengths (μm)
1	Cystine	3.3, 6.3, 6.8, 7.1, 11.8, 18.6
2	Cystine	3.3, 6.3, 6.8, 7.1, 11.8, 18.6
3	Magnesium ammonium phosphate hexahydrate (struvite) / minor calcium carbonate apatite	10.0
4	Calcium hydrogen phosphate dihydrate (brushite)	4 – 12
5	Cystine	3.3, 6.3, 6.8, 7.1, 11.8, 18.6
6	Calcium oxalate dihydrate (weddellite)	6.1, 7.6
7	Calcium oxalate monohydrate (whewellite)	6.2, 7.6, 12.8
8	Calcium oxalate monohydrate (whewellite)	6.2, 7.6, 12.8
9	Uric acid	3.3, 5.9, 12.7, 13.4
10	Magnesium ammonium phosphate hexahydrate (struvite)	10
11	Cholesterol, bilirubin / minor phosphate	3.4, 6.8, 9.5
12	Cholesterol, bilirubin / minor phosphate	3.4, 6.8, 9.5
13	Cholesterol, bilirubin	3.4, 5.8

The peak wavelengths for absorption give an indication of optimal laser wavelengths for possible direct ablation of the stones, although it must be noted that the samples were dried prior to analysis and therefore the absorption properties of water are not accounted for in the spectra. The erbium laser (Er:YAG) at 2.94 μm, and also the carbon dioxide laser (CO_2) at 10.6 μm have wavelengths that would appear to be strongly absorbed by a number of these calculi compositions, and are also highly absorbed by water. Er:YAG and CO_2 are both relatively common types of medical laser and might be potential candidates for use in effective fragmentation of calculi based on this data. However, at these wavelengths there is a lack of suitable fibre optic material for the delivery of the beam to the stone for lithotripsy. The free electron laser can also

generate wavelengths in the far infrared that may potentially be tuned precisely to these absorption peaks, although currently this type of laser is not commercially available, and beam delivery will also be a problem.

Common to all calculi that exist in the body is that they are impregnated with water (Welch et al, 2004). For this reason, the use of a laser that is strongly absorbed by water is advantageous as it will be well absorbed by all types of calculi and therefore leading to fragmentation. The alternative is to have a laser with output characteristics that initiate a strong mechanical action from its interaction mechanism that will break up the concrements by shockwaves. This can arise from short pulse duration where the conditions for stress confinement are met, or potentially from wavelengths that are very strongly absorbed generating highly localized vaporization leading to acoustic transients.

For those calculi that are composed of especially hard compositions such as cystine and calcium oxalate types, where laser-generated shockwaves may not have sufficient energy to cause destruction a laser wavelength tuned to water absorption may act on the calculus by direct ablation. The ideal would be to have a choice between direct ablation and shockwave generation, or a combination of both actions. The holmium laser at 2.12 μm is strongly absorbed by water and has been reported to generate shockwaves during the interaction. The combined effect of the holmium laser may explain the high success rate in fragmenting calculi.

In conclusion, a number of absorption bands exist in the infrared region and these may indicate potential optimal laser wavelengths for efficient calculus destruction. The specific peak absorption bands depend on the composition but are generally found at around 3.3 μm, 6.2 μm, 7 μm, 10 μm, 12 μm, 13 μm and 19 μm. These findings are broadly in line with Chan et al (2000b), however, it was noted that ablation efficiency was not only dependent on optical absorption properties but also dependent on thermal properties and in particular laser pulse duration.

5.2 Calibration of the laser source

The laser sources used for the experimental work, a Q-switched Nd:YAG laser (λ = 1064 nm, pulse duration ~ 6 ns, max pulse energy ~ 200 mJ) and a variable pulsed Ho:YAG laser (λ = 2.12 μm, pulse duration 120 – 800 μs, max pulse energy ~ 3 J) were set up and calibrated for output delivered to the target. The results are given in the following sections.

5.2.1 Nd:YAG laser

The results of the preliminary calibration measurements of the Nd:YAG laser output are shown in Table 5.2. All measurements and errors were derived from 10 consecutive laser pulses. The beam transmission through the prisms and lens arrangement was measured using a calibrated laser power meter at the distal end of the optics and compared to the power measurements made at the laser aperture. Transmission was approximately 40 – 50%, which could be improved with antireflection optics. However, despite these high losses the pulsed energy available was sufficient, as it is the high irradiance achieved through focusing and high peak power resulting from short pulse duration that are crucial.

Table 5.2: Nd:YAG laser output measurements and pulse energy at the target

Voltage setting (V)	Cavity output (mJ)	Energy at target (mJ)	Transmittance of beam delivery system
575	15.1 ± 0.6	8.7 ± 0.4	0.57 ± 0.03
590	26.0 ± 0.7	12.6 ± 0.6	0.48 ± 0.02
600	31.8 ± 0.5	16.1 ± 0.6	0.51 ± 0.02
650	62.4 ± 1.1	31.7 ± 0.4	0.51 ± 0.01
700	87.8 ± 1.4	42.7 ± 0.4	0.49 ± 0.01
750	112.3 ± 0.8	53.9 ± 0.6	0.48 ± 0.01
800	135.4 ± 0.8	62.8 ± 0.6	0.46 ± 0.01
850	158.2 ± 0.9	71.5 ± 0.3	0.45 ± 0.01
900	178.5 ± 0.9	75.9 ± 1.3	0.42 ± 0.01
925	187.4 ± 0.7	80.7 ± 0.7	0.43 ± 0.01
950	195.3 ± 0.8	83.9 ± 0.7	0.43 ± 0.01
1000	204.8 ± 0.8	87.3 ± 0.6	0.43 ± 0.01

The laser pulse energy measured independently, as recorded above, was plotted against the voltage setting on the laser power supply, as shown in Figure 5.14. A straight line is drawn for the data points, however, the calibration appears to deviate from linearity.

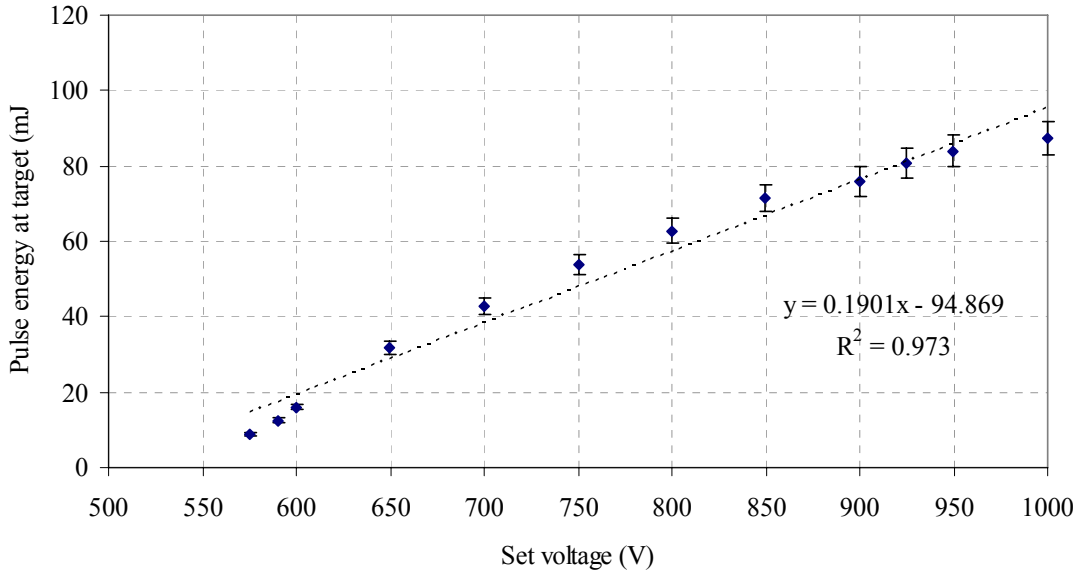

Figures 5.14: Relationship of laser output with voltage setting for the Nd:YAG laser

The deviation from linearity reveals that the conversion of electrical energy into flashlamp output, which in turn leads to laser output from the Nd:YAG crystal, is a non-linear process i.e. a saturation effect occurs. For the purposes of the experiments a lookup table of pulse energy with set laser voltage was used.

5.2.2 Ho:YAG laser

The holmium laser output as measured using a calibrated power meter was found to be in good agreement with the setting on the laser console, as shown in Table 5.3. Pulse to pulse energy consistency was determined for a series of 10 pulses and found to be within ± 5 %. However, over a sequence of 1200 shots (2 J, 10 Hz, 2 minutes) fired at a submerged calculus it was evident there was some damage to the end face of the fibre. This was not surprising as the fibre was in close contact with the calculus during the experiments and laser-generated mechanical and thermal effects would have occurred in the vicinity of the fibre tip. Fibre damage with the Ho:YAG laser has been reported by Spore et al (1999), who found that the degree of damage varied with calculus type

suggesting it arises from ejected fragments. Therefore, as a rationale for the experimental work the output was measured after several hundred pulses to check for possible fibre damage. If the output was reduced by more than 10% the fibre was cleaved to remove the damaged tip.

Table 5.3: Ho:YAG laser output measurements

Energy setting (J)	No. of shots averaged	Measured pulse energy (mJ)	Variation (%)	Comments
1.0	10	0.95 ± 0.05	5	Fibre cleaved and polished before measurements
2.0	10	1.91± 0.07	5	
3.0	10	2.90 ± 0.13	3	
2.0	1200	1.62 ± 0.10	19	Measured after firing 1200 shots at calculus in water

As with the pulse energy, the pulse duration was measured over a range of set pulse lengths to verify the correct operation of the laser pulse controller (200 mJ, 5 Hz, 100 shots), as shown in Table 5.4. All pulse durations were found to be within ± 10%.

Table 5.4: Ho:YAG laser pulse duration measurements

Pulse duration setting (µs)	Measured pulse duration (µs)	Difference (µs)
140	152 ± 15	12
200	215 ± 21	15
300	318 ± 26	18
400	408 ± 25	8
500	496 ± 24	4
600	580 ± 27	20
700	690 ± 26	10
800	785 ± 22	15

Strictly speaking, what was measured is the duration of the flashlamp. The laser pulse can be reasonably expected to be of similar duration, although pulse structure may be different. Solid-state lasers such as the Ho:YAG typically have a spike structure in the pulse arising from the spontaneous emission process (Berlien and Müller, 2003).

The temporal flashlamp pulse waveforms recorded for set laser pulse energy are shown in Figure 5.15. It can be seen that, as expected, as the pulse duration decreases the flashlamp intensity increases proportionally to deliver the same total optical energy to the laser crystal. The laser output, therefore, remains the same, in this case at 400 mJ.

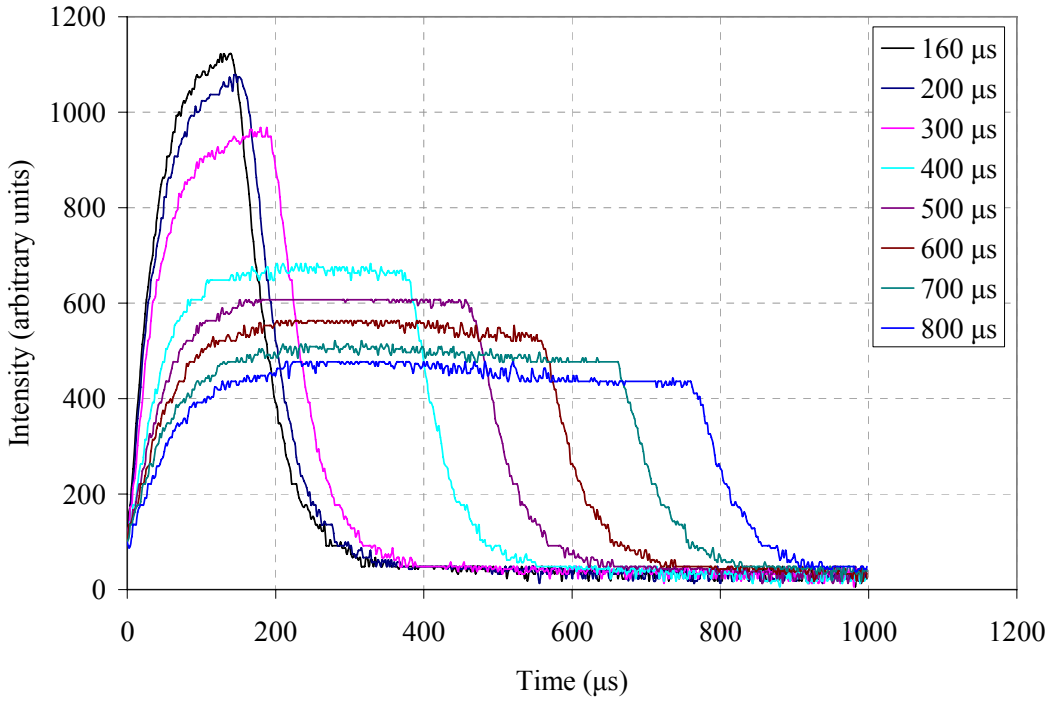

Figure 5.15: Temporal histories of the Ho:YAG laser flash lamp pulse with laser pulse time setting as a parameter

In summary, the Q-switched Nd:YAG laser (1064 nm, 6 ns, 8 – 87 mJ at target, up to ~ 82 GW cm^{-2} at emission centre i.e. focal point) and the Ho:YAG laser sources (2.12 µm, 120 – 800 µs, 200 mJ – 3 J at target, up to 3 MW cm^{-2} at emission centre i.e. fibre tip) were set up and calibrated for the experiments.

The output has been characterised and found to be consistent on a pulse to pulse basis. In the next section, the lasers are used in the investigation of the interaction with calculi and water.

5.3 Direct laser interaction with calculi

In this section, the action of the laser beam incident directly on the calculus is investigated, in particular for evidence of plasma formation on calculus material. The studies were conducted by capturing images of the interaction using a digital camera, for the Nd:YAG laser recording spectral emissions using standard spectroscopes, and for the Ho:YAG laser the temporal light signal was detected using a photodiode and recorded to a digital oscilloscope.

5.3.1 Nd:YAG laser

The Q-switched Nd:YAG laser pulses were tightly focussed onto the surface of various calculi samples, and in all cases there was obvious evidence of plasma formation. An audible "crack" was heard and, as shown in Figure 5.16, a bright bluish-white flash was observed. Even at the lowest laser energy setting (~ 10 mJ, estimated irradiance of ~ 10 GW cm^{-2}) plasma was formed.

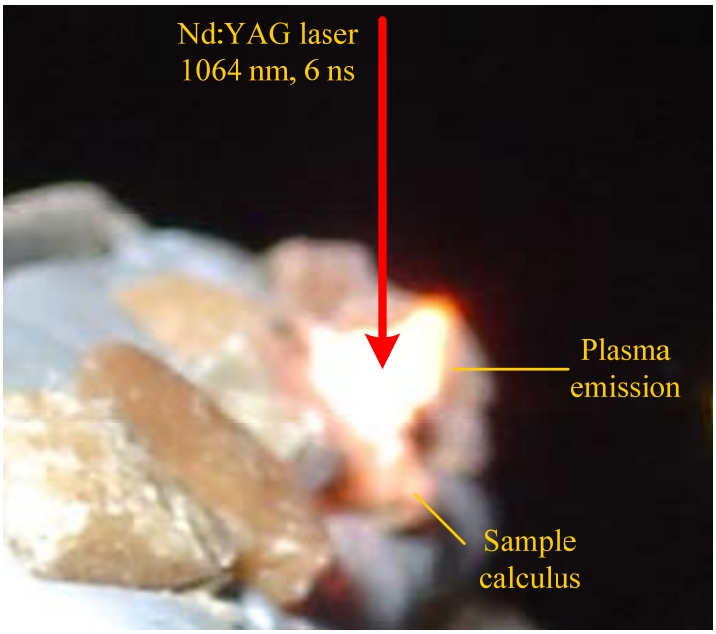

Figure 5.16: Photograph of Q-switched Nd:YAG laser action on a urinary calculus in air (Sample 6: COD). The plasma emission can be clearly seen. The calculus composition is calcium oxalate dihydrate.

The plasma signals were recorded using a spectrometer (SPEX 270M) coupled to an intensified photodiode array detector (EG&G 1420) controlled by an optical multichannel analyser (EG&G OMA), as described in 4.5.1. An example of the resulting spectral envelope for the plasma emission is shown in Figure 5.17, in this case for the sample as described above (Sample 6: calcium oxalate dihydrate).

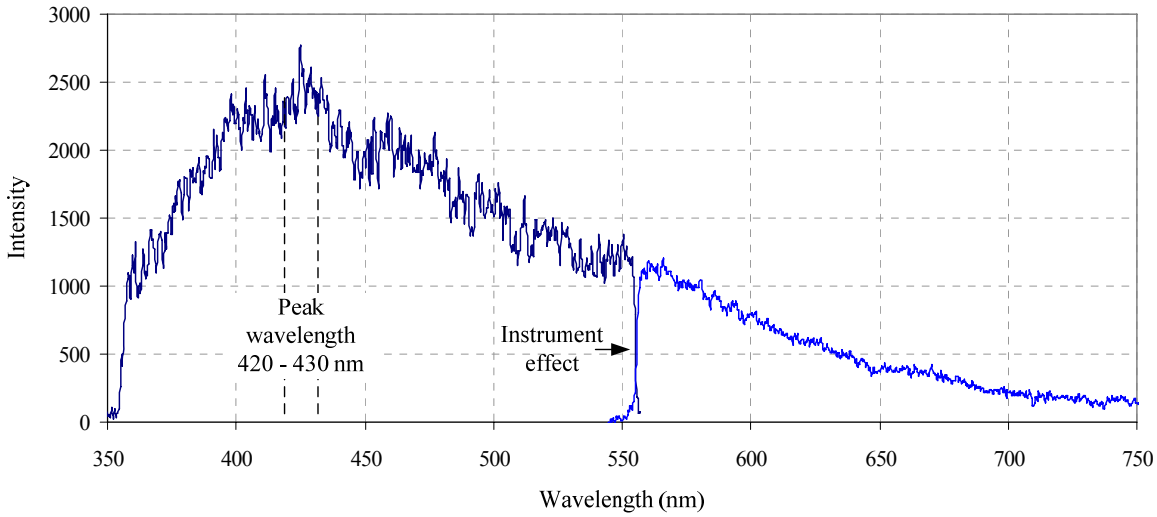

Figure 5.17: Spectrum of plasma envelope for Nd:YAG laser action with calcium oxalate dihydrate calculus (Sample 6: COD)

The peak wavelength taken from the graph, ~ 425 ± 5 nm, can be used to determine the plasma temperature. Using Wein's displacement formula, $T = b/\lambda_{max}$ where b = 2.897768 x10 $^{-3}$ m.K, the estimated temperature of the plasma is 6820 K. The results for the samples investigated are given in Table 5.5, and it can be seen that the estimated plasma temperatures are very similar. For all the samples the spectra were obtained with the same experimental set up i.e. fixed laser output.

Table 5.5: Estimated temperature of Nd:YAG laser-induced plasma on various calculi

Sample identification	Peak wavelength emission (nm)	Calculated plasma temperature (K)
(1) cystine	425 ± 5	6820 ± 80
(2) cystine	422 ± 5	6870 ± 80
(3) struvite	434 ± 5	6680 ± 80
(4) brushite	432 ± 5	6710 ± 80
(5) cystine	423 ± 5	6850 ± 80
(6) COD	425 ± 5	6820 ± 80
(7) COM	426 ± 5	6800 ± 80
(8) COM	426 ± 5	6800 ± 80
(9) uric acid	420 ± 5	6900 ± 80
(10) struvite	425 ± 5	6820 ± 80

5.3.2 Ho:YAG laser

The holmium laser was used to directly irradiate a selection of calculi samples, both in air and in water environments. During the interaction process a sharp "click" was heard, becoming more pronounced at higher laser energy, and a simultaneous bright light was observed. Digital photography, using a long exposure time (2 s), was used to capture images of the laser-calculus interaction. Figure 5.18 shows the bright light emitted from the irradiated zone, possibly a plasma formation. The calculus in this image is composed of, as identified from previous (5.1.1), magnesium ammonium phosphate hexahydrate/ calcium carbonate apatite (sample 3).

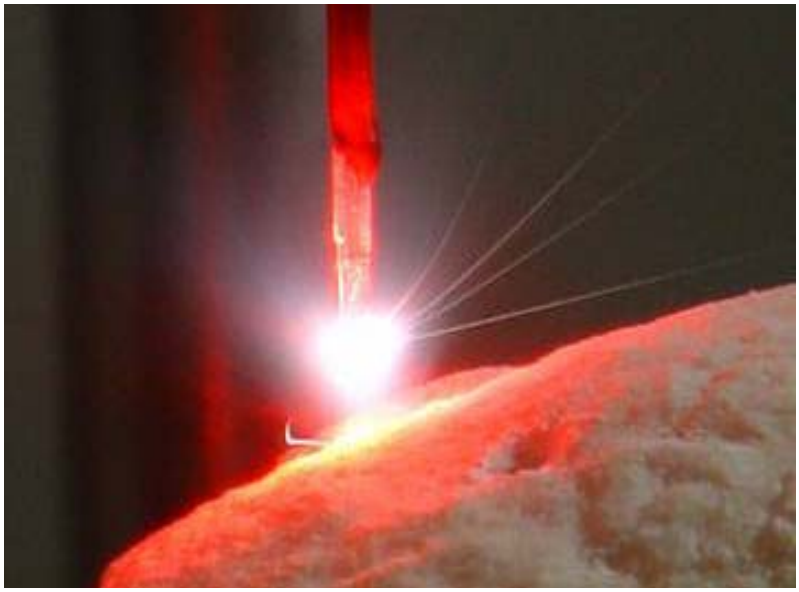

Figure 5.18: Photograph of pulsed holmium laser action on a urinary calculus in air. The calculus shown is mainly composed of magnesium ammonium phosphate dihydrate (Sample 3).

The recorded temporal signal of light emission for this calculus is shown in Figure 5.19. It was observed that for a Ho:YAG laser pulse of energy 800 mJ the "plasma" light intensity detected increased considerably from that detected at 600 mJ. This again would appear to suggest to the formation of a plasma, with an estimated threshold laser power density of around 0.8 MW cm^{-2} based on a fibre diameter of 600 μm.

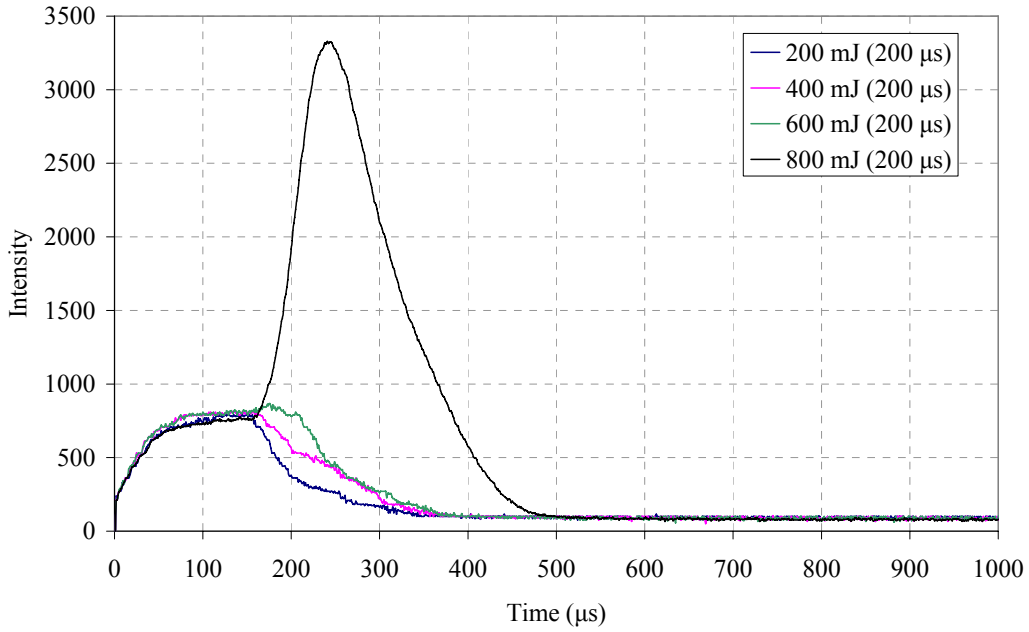

Figure 5.19: Temporal signal of "light emission" during Ho:YAG interaction with a urinary calculus (Sample 3: struvite)

An alternative possibility for the observed bright flash is that it is reflected flashlamp light, as discussed in 5.2.2. In this case, the laser pulse energy may have been sufficient to eject a plume of particles from the calculus surface which then are illuminated in the flashlamp light. The photograph has captured the motion of particles of calculus material ejected at a high speed and recorded them as streaks of light, which lends support to this theory. Hence, it is not possible to be certain if the emission is caused by a plasma formation.

Another photographic image of a calculus undergoing Ho:YAG laser ablation is shown in Figure 5.20. In this case, the bright light emitted extends beyond the region between the fibre tip and the calculus and therefore it is unlikely to be scattered flashlamp light. However from the size and shape of the light region it would appear to have too great a volume to be a plasma. Therefore, the light appears to have been generated by a thermal interaction with the calculus material i.e. ignition. The melting point of uric acid is ~ 360 ^{o}C and this temperature would be reached with sufficient laser energy.

Figure 5.20: Photograph capturing the thermal interaction of pulsed holmium laser on a uric acid calculus in air (Sample 3).

The captured light signal, shown in Figure 5.21, appears to confirm that there is a steady light generation with increasing laser pulse energy. The indication is that a sufficient temperature was reached during the laser pulse to ignite calculus fragments. The interaction appears to have been violent, as the motion tracks seen in the image indicate that fragments were ejected at a high speed. A chemical smell that accompanied the interaction event suggested that chemical decomposition processes had taken place. Chemical analysis of the laser-affected area on the calculus would be required to confirm the presence of decomposition products, however, this extent of the work was not a part of the remit of this thesis.

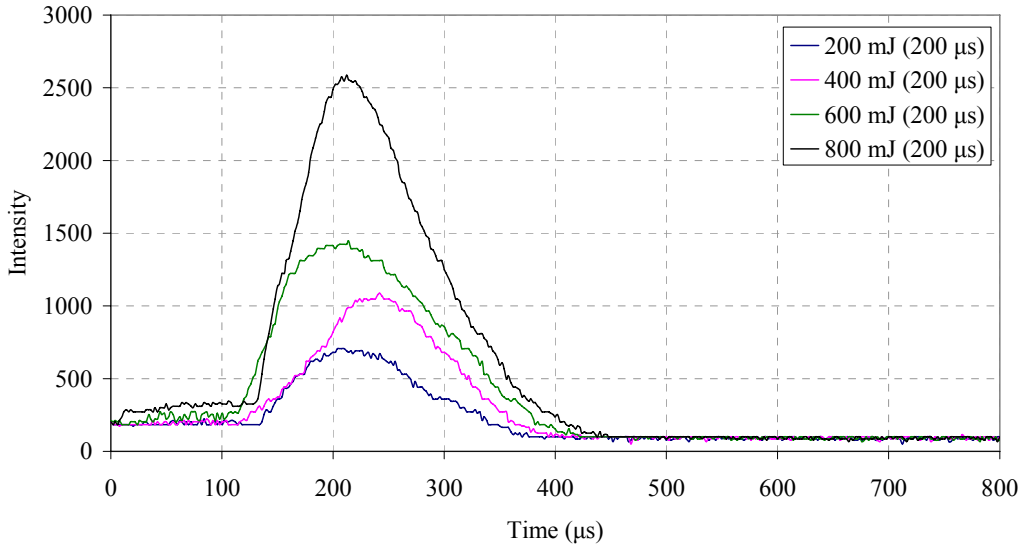

Figure 5.21: Temporal signal of "light emission" during Ho:YAG interaction with uric acid calculus (sample 9)

A further example of Ho:YAG laser-calculus interaction is shown in Figure 5.22, in this case a gallstone composed of cholesterol (Sample 13). The effect of the laser appears to melt the calculus material in the beam path. There does not appear to be any indication in the photograph of ejection of material.

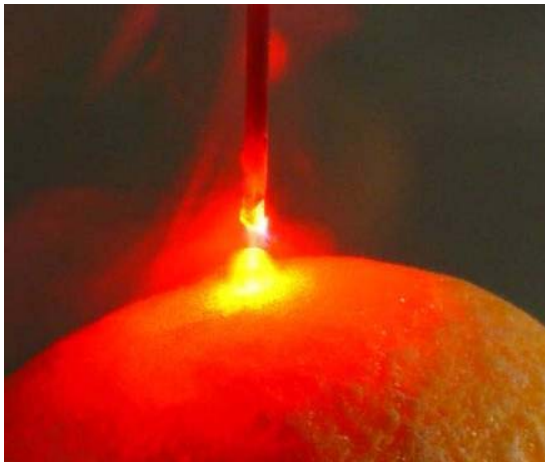

Figure 5.22: Photograph showing melting of cholesterol stone during holmium laser irradiation in air (Sample 13). Cholesterol has a melting point of ~ 150 ^{o}C.

The observations of the laser-calculus interaction have provided further indications as to the nature of the physical processes. The Nd:YAG laser has been shown to generate a plasma on calculus material, as expected given the high laser irradiance, whereas the Ho:YAG laser did not appear to create optical breakdown although it did generate thermal effects. In the next section the laser interaction with water would be investigated, as the calculi in the real-world situation would be immersed in a liquid environment during laser lithotripsy.

5.4 Laser interaction in a water environment

As with the laser-calculus experiments described above, the laser-water interaction was investigated with a similar setup of apparatus. For the Nd:YAG laser a spectroscope was available to study the plasma signals, and for the Ho:YAG laser optical emissions were investigated using digital photography.

5.4.1 Nd:YAG laser

Focussing the Nd:YAG laser into water was found to consistently form a plasma, which was expected. The plasma formation was found to have a threshold at a laser pulse energy of ~ 10 mJ, which corresponded to an irradiance at the focal spot of an estimated

~ 9 GW cm^{-2}. At this irradiance, for a series of 100 laser pulses the plasma was observed an estimated 50 % of the time. When there was no plasma, the accompanying audible "click" was not heard, suggesting that the generation of a pressure pulse is dependent on the formation of a plasma. This was later confirmed with pressure measurements using a hydrophone (see 5.9.1), where the threshold for pressure pulse formation was around a laser pulse energy of 10 mJ.

The temporal signals of the laser pulse and plasma emission were captured and an example is shown in Figure 5.23. From this recording it is seen that there is a delay between the laser pulse and the onset of the plasma emission. This is due to the initial portion of the laser pulse being required to initiate the plasma formation i.e. for the conversion of optical energy into the heating of target material to liberate electrons and ions to start the process of plasma formation. The length of the delay gives an indication of the energy required for the process of plasma formation, as shown on the graph.

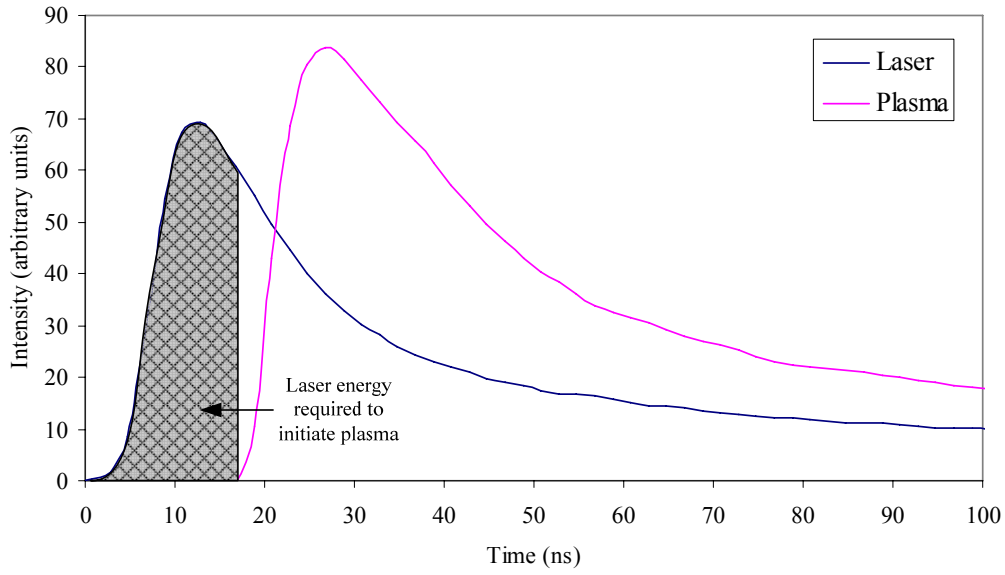

Figure 5.23: Temporal signal of Nd:YAG laser pulse and plasma emission in water

The temporal signals of the Nd:YAG laser pulse and the plasma emission were captured for a range of laser pulse energies. The pulse energies required to initiate a plasma were determined as described above, and the breakdown thresholds calculated for an estimated 0.15 mm laser spot diameter. The results are presented in Table 5.6.

Table 5.6: Estimated Nd:YAG laser energy required for plasma onset in water

Laser pulse energy (mJ)	Delay before plasma onset (ns)	Estimated laser energy to initiate plasma (mJ)	Estimated laser energy to plasma peak (mJ)	Estimated optical breakdown threshold (J cm^{-2})	Estimated optical breakdown threshold (GW cm^{-2})
16.1	10	6.2	8	35	3.5
42.7	16	9	12.8	51	3.2
62.8	8	9.3	10.8	53	6.6
75.9	8	9.4	13.8	53	6.7
87.3	14	13.9	21.7	79	5.6

The results show that the estimated laser pulse energy required to initiate plasma formation, found to be in the range 6.2 mJ – 13.9 mJ and with a mean of 9.6 mJ, is in close agreement with the previously observed plasma threshold of around 10 mJ. The data shows an apparent increase in the threshold energy as the laser pulse energy was increased, this may be due to broadening of the laser beam at higher output which would result in a reduction in the irradiance and hence more energy would be required to initiate an optical breakdown. However, the trend is most likely due to uncertainties in estimating the fraction of laser energy for plasma initiation from the graph owing to the long pulse tail and an arbitrary cut-off level.

The optical breakdown irradiance threshold was found to be of the order 5.1 ± 1.5 GW cm^{-2} for the Nd:YAG laser in deionised water. The threshold fluence for plasma onset was estimated to be 54 ± 14 J cm^{-2}. These figures are estimates, an accurate determination requires a more accurate measurement of the laser spot size.

The effect of increasing the laser pulse energy on the plasma intensity was also investigated, and the results are shown in the graph in Figure 5.24. Plasma intensity was determined from the height of the optical signal as recorded using a photodiode. As expected, the plasma intensity increases with laser pulse energy. The dependence was found to be non-linear, that is, there appeared to be a saturation effect where at higher laser energies the plasma volume was apparently not linearly increasing in size with

laser pulse energy. This effect may be attributable to plasma shielding which is described in a later section (see Figure 5.52).

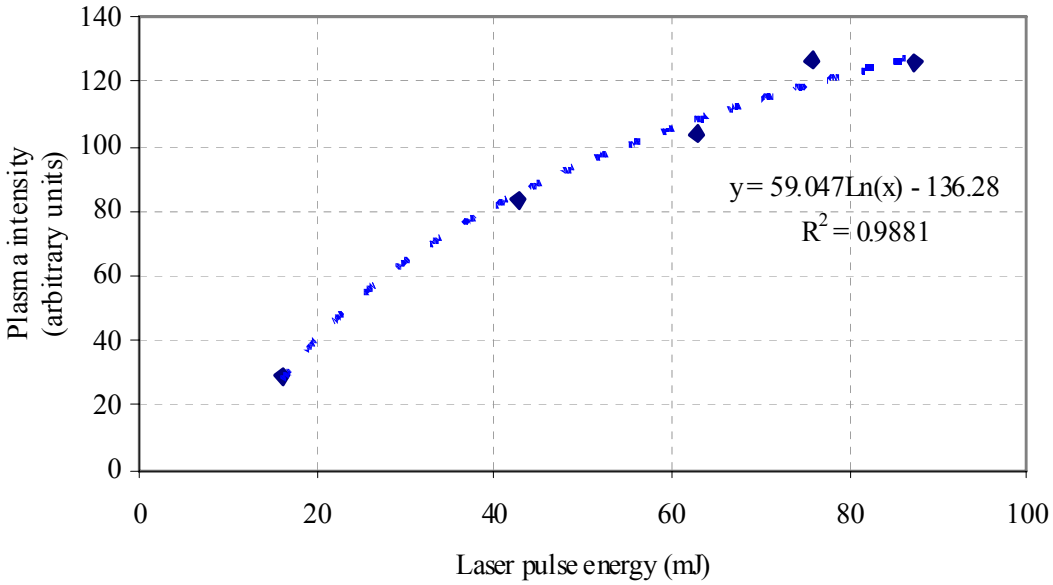

Figure 5.24: Dependence of plasma intensity in water with Nd:YAG laser pulse energy

A spectral envelope for the plasma emission was recorded using the setup as previously described, and the results are shown in Figure 5.25. The plasma temperature was estimated from the peak wavelength using Wein's displacement formula.

Figure 5.25: Spectrum of plasma envelope for Nd:YAG laser action in water (laser ~ 43 mJ, 6 ns, average of 20 scans)

The plasma temperature for Nd:YAG laser irradiation in water was estimated to be ~ 6590 K. The generation of such a high temperatures in the focal volume would account for laser-induced mechanical effects. The results show that a plasma was a significant effect with this laser and that the plasma increased with laser energy and attained a very high temperature. Such high temperatures will lead to water vaporisation, and possibly direct calculus ablation if the plasma is in close proximity to the calculus surface. Plasma expansion and vaporised steam expansion will be driven by the interaction leading to significant pressure pulses. These Nd:YAG laser-induced pressures were investigated in later experiments.

The interaction of the Nd:YAG laser on calculi in a water environment was investigated. A selection of samples were placed in a water tank and exposed to focused laser pulses and the plasma signals, both temporal and spectral, were recorded. An example of the results obtained for the temporal laser vs plasma signals is presented below in Figure 5.26.

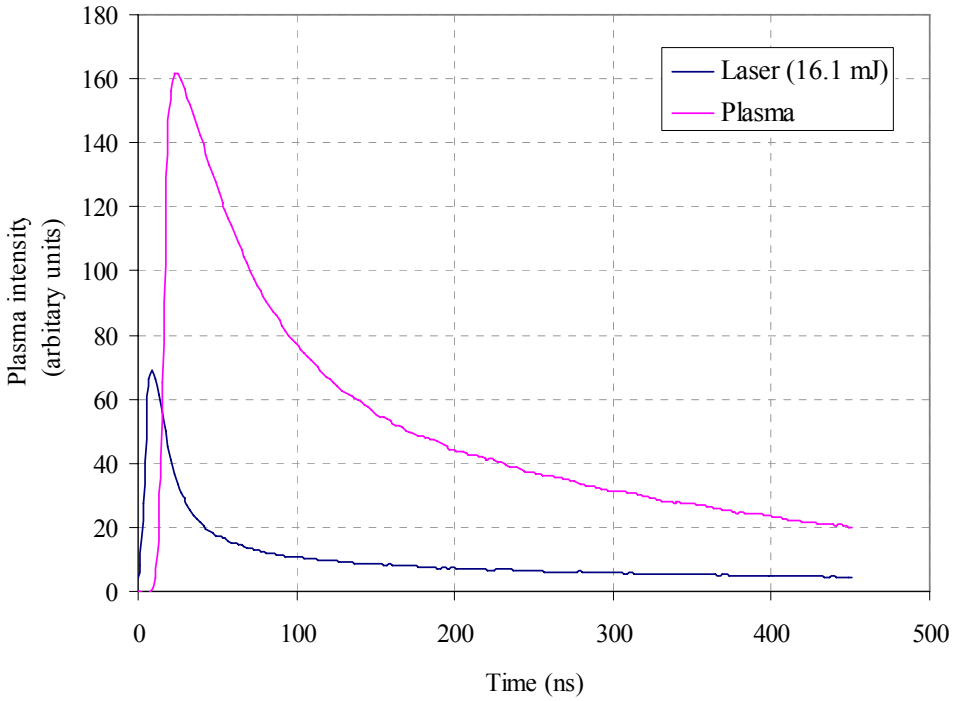

Figure 5.26: Temporal signal of Nd:YAG laser pulse and plasma emission on calculus in water (Sample 3: struvite, laser ~ 16 mJ, 6 ns)

The estimated delay times for a range of laser pulse energies from the start of the laser pulse to the onset of the plasma emission were found to be more or less identical to the times determined for the direct laser interaction with water (see Table 5.7). The implication of this result is that the energy required to initiate plasma on the calculus would also be expected to be similar to that determined for water. However, the threshold irradiance determined from the graph is slightly higher for plasma formation on calculus material, 7.7 ± 3.3 GW cm^{-2} compared to 5.1 ± 1.5 GW cm^{-2}, and the optical breakdown threshold for the struvite calculus was found to be 80 ± 24 J cm^{-2} compared to 54 ± 14 J cm^{-2} for water. The differences are possibly due to the uncertainties in estimating the area under the curve on the graph.

Table 5.7: Estimated Nd:YAG laser energy required for plasma onset on calculus in water (Sample 3: struvite, laser focal spot estimated as 0.15 mm)

Laser pulse energy (mJ)	Delay before plasma onset (ns)	Estimated laser energy to initiate plasma (mJ)	Estimated laser energy to plasma peak (mJ)	Estimated optical breakdown threshold (J cm^{-2})	Estimated optical breakdown threshold (GW cm^{-2})
16.1	10	5.7	11.3	32	3.2
42.7	16	15.2	30.4	86	5.4
62.8	8	17.1	47.3	97	12.1
75.9	8	15.4	37.6	87	10.9
87.3	14	17	41.5	96	6.9

The plasma duration was found to increase with higher laser pulse energies (Figure 5.26. At 16 mJ laser energy the plasma signal FWHM was of the order ~ 40 ns, this increased to 240 ns for ~ 62.8 mJ laser pulse, and to ~ 480 ns for laser pulse energy of ~ 87 mJ. The laser pulse duration in all cases was ~ 6 ns.

The considerable afterglow of the plasma may have been due to emission from heated calculus material. The data suggests that material was heated to a significant temperature, again this indicates thermal interaction on calculus material.

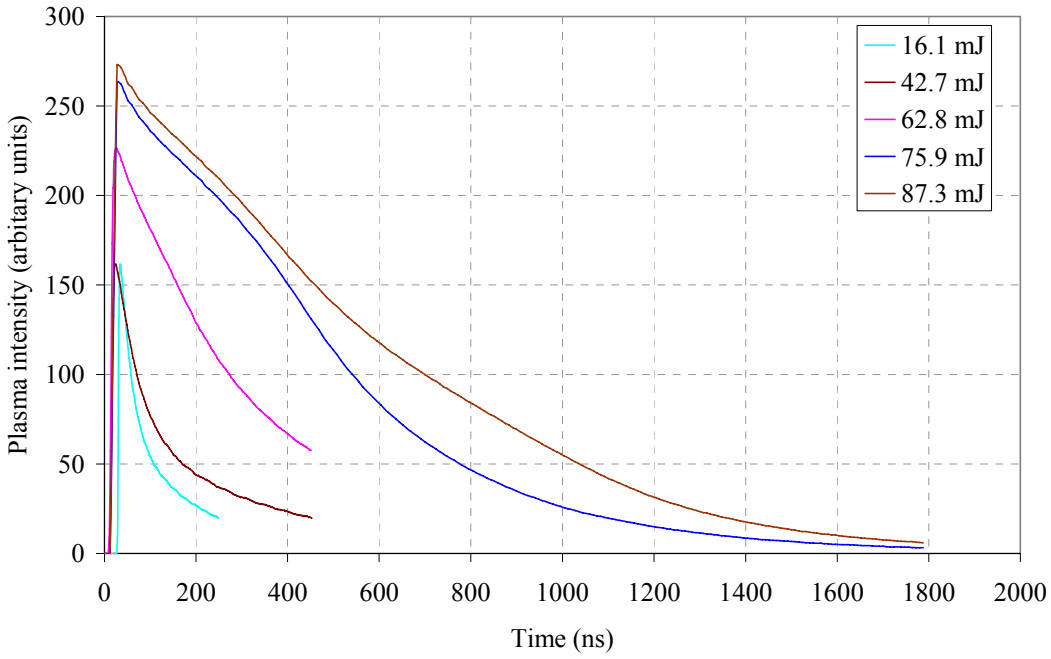

Figure 5.27: Plasma duration following Nd:YAG laser excitation on calculus in water (Sample 3: struvite)

The plasma spectrum of the same calculus (Sample 3: struvite) was investigated to determine the peak plasma temperature. The spectrum obtained for a laser pulse energy of ~ 25 mJ is shown in Figure 5.28. The peak temperature was calculated using the same formula as previous, and was found to be 6540 K.

As with the above findings for the plasma threshold energies, this result is very similar to that obtained for water (6590 K). The estimated temperature for a plasma formed in water was slightly higher than that for the calculus because the laser pulse energy was higher, 43 mJ compared to 25 mJ. However, the results indicate that the Nd:YAG laser achieves optical breakdown on calculus material at a similar threshold to in water, and produces equivalent peak temperatures.

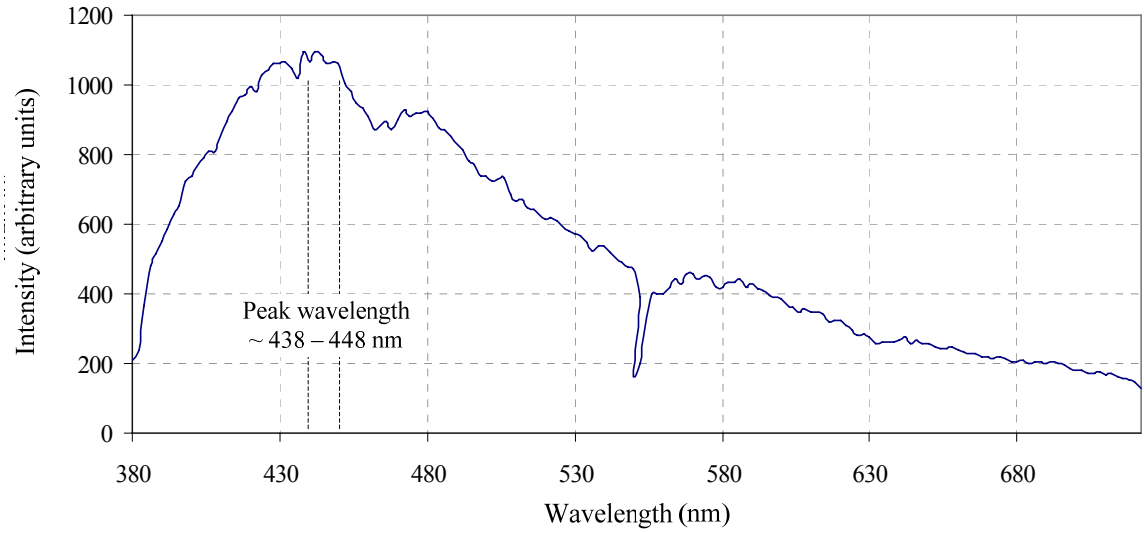

Figure 5.28: Plasma duration following Nd:YAG laser excitation on calculus in water (Sample 3: struvite)

In summary, it was found that the Q-switched Nd:YAG laser is efficient at generating an optical breakdown both in water and on calculi. The plasma generates high ablative temperatures, and also mechanical effects. The plasma appeared to be necessary for the production of shockwaves. In the next section the Ho:YAG laser was fired in water and at calculi placed in a water tank.

5.4.2 Ho:YAG laser

The interaction of the Ho:YAG laser with water was observed and recorded on digital camera (Figure 5.29). A bright flash was seen when the laser was fired, accompanied by a loud click, presumably originating from the generation of an acoustic transient. A cloud of small bubbles were visible around the fibre tip.

The bubbles were propelled away from the fibre tip when the following laser pulse was fired, giving a clear indication that the interaction generated a mechanical impulse. The motion tracks captured in the long exposure photograph are also indicative of the fact that the interaction caused significant disturbance in the water. The length of the light streaks, illuminated by the red light of the aiming beam, indicated micro-bubble displacement of several millimetres during the 1 second exposure time.

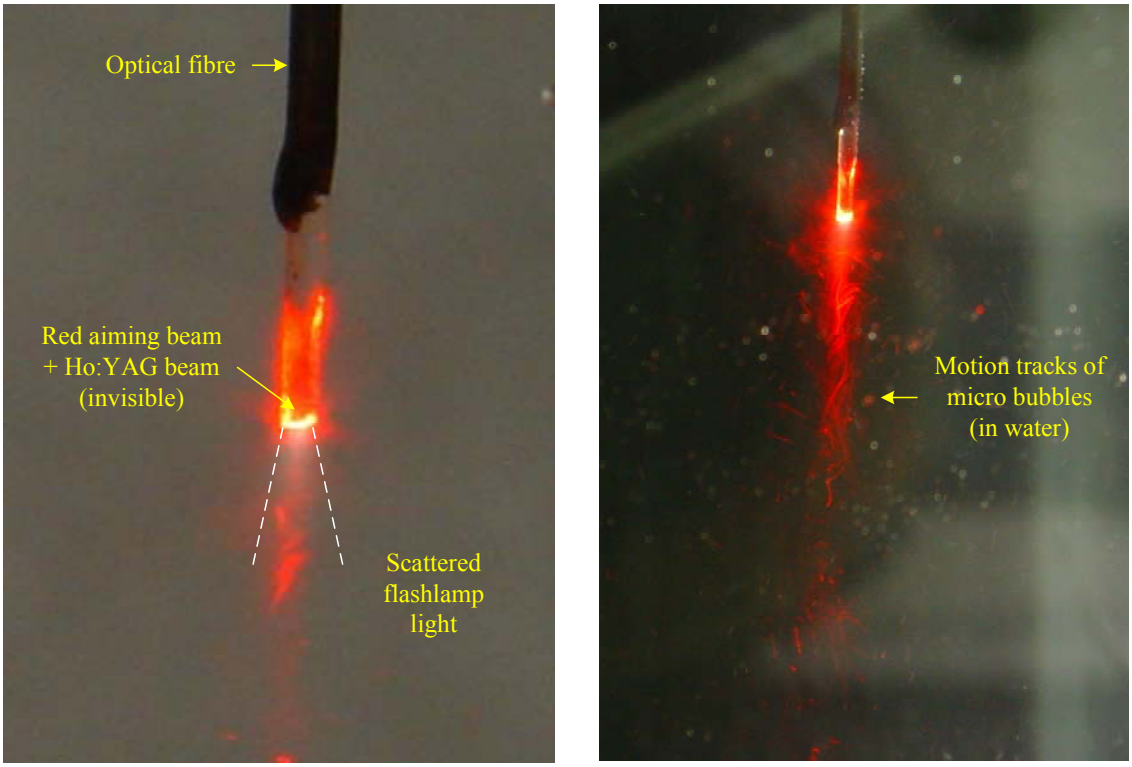

Figure 5.29: Photographic images of the Ho:YAG laser-interaction with water

There was, however, no photographic evidence of plasma formation in water with the Ho:YAG laser. A plasma emission would be indicated if light was generated in front of the fibre tip. Compared to the Nd:YAG laser, which generated a bright white-violet plasma at the emission centre, the bright flash with the Ho:YAG laser appeared to be scattered light from the laser flash lamp. The light appeared to be emerging from the fibre tip and scattered, possibly by water vapour (steam) micro bubbles in the water.

Calculi samples were placed in a water tank and irradiated with holmium laser energy. A photograph of the Ho:YAG laser interaction on a sample urinary calculus (Sample 3: struvite) is shown in Figure 5.30 and the temporal light emission results are shown in Figure 5.31. From the image and captured light signal it would appear that no plasma is evident. This is as expected since no plasma was identified with the same sample in air where there is no absorption of the laser beam by water. The light signal has the same waveform as recorded from the flashlamp output (Figure 5.17) and therefore it is confirmed as scattered flashlamp light, and not plasma emission.

Figure 5.30: Photograph of Ho:YAG laser action on a urinary calculus in water. The calculus shown is mainly composed of struvite (Sample 3).

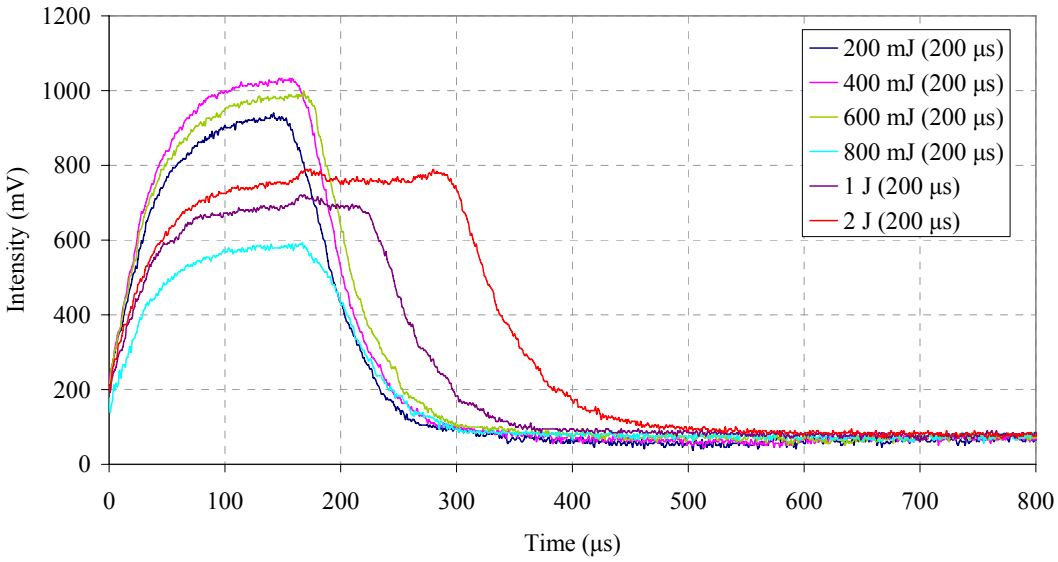

Figure 5.31: Temporal signal of "light emission" during Ho:YAG interaction with a urinary calculus in water (Sample 3: struvite)

The photographic evidence gave a clue as to the shockwave effects in water. The (red) aiming beam light allowed for better visualisation of the motion tracks and it was seen that there was water or plume movement even at some considerable distance from the emission centre (> 2 cm). The motion was at 90° to the calculus surface and apparently not radial from the emission centre. This suggested possible jet formation which would occur following the collapse of the steam bubble towards the calculus surface, as has been reported by other investigators (Van Swol et al, 1998).

In summary, the laser interaction with water was found to generate steam bubbles and a mechanical impulse. In the case of the Nd:YAG laser a plasma has been confirmed, however, there was no conclusive evidence for a plasma with the Ho:YAG laser. In the following the photomechanical effects of the interaction process of the focussed laser beam with water will be evaluated. The dependence of the laser-generated pressure pulse on the laser parameters will be presented.

5.5 Calibration of the hydrophone

Accurate measurements of the shockwave pressures for the Nd:YAG laser required initial calibration of the hydrophone and transient recorder system. Measurements taken with the 0.2 mm hydrophone connected to the Agilent digitising oscilloscope were compared with those obtained with the data capture card and associated software installed in the PC of the transient recorder. Measurements were averaged over a minimum of 100 laser pulses and corrected for the hydrophone offset. The results are shown in Table 5.8.

Table 5.8: Cross calibration of the hydrophone / transient recorder systems

Set parameters (arbitrary)	Transient amplitude with PC recorder (mV)	Transient amplitude with digitizing oscilloscope (mV)	Ratio
Laser ~30 mJ, 10 Hz, average of 100 laser pulses Hydrophone ~5mm separation Deionised water	341.5 (uncorrected) 330.0 (corrected)	1018.4	3.09

From this it can be seen that all measurements recorded with the PC system would require a correction factor of 3.09 to account for differences in the scaling of the signal.

It was also necessary to determine the approximate frequency of the shockwave waveform in order to apply the appropriate correction factor to the signal amplitude from the frequency response data provided with the hydrophone. A trace of the waveform of the Nd:YAG laser-induced shockwave is shown in Figure 5.35.

A Fourier Transform computation on an averaged pressure pulse waveform produced the frequency spectrum shown in Figure 5.32. The peak in the frequency spectrum of the shockwave occured at around 4.5 MHz. From this it was indicated that the appropriate hydrophone sensitivity value to use for the experiments was 120 mV MPa^{-1} (see Figure 4.13) for the conversion of measurements in mV to pressure in MPa.

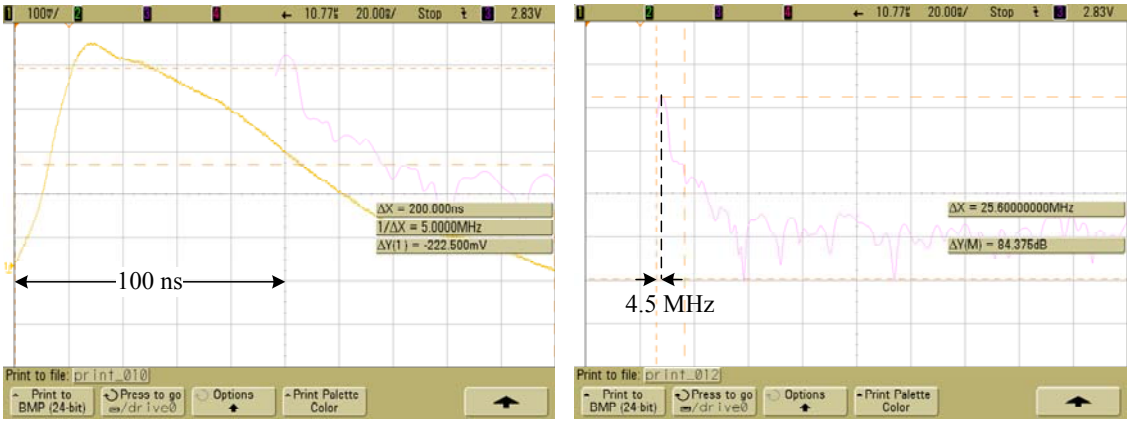

Figure 5.32: Pressure pulse temporal waveform (left) and corresponding Fourier Transform indicating the frequency components (right)

Frequency response data was not available for the hydrophone used for the Ho:YAG pressure measurements. The quoted sensitivity of 20 mV MPa^{-1} was applied to all readings. However, from the data provided with the 0.2 mm hydrophone it was apparent that these devices did not have a flat frequency response. Therefore, this was considered to be a potential source of error in the data obtained with the Ho:YAG laser and this hydrophone.

5.6 Pressure pulse waveforms

Pressure waveforms were recorded to investigate the relationship between the pressure amplitude in water and specific laser parameters. The leading edge of the laser pulse was used as a trigger for the capture of the recording. Generally speaking, the laser pulse (from either the Nd:YAG or the Ho:YAG lasers) provided a convenient trigger as it rose sharply and could be easily detected. A typical recording of the laser pulse and resultant acoustic signals for the Ho:YAG laser is shown in Figure 5.33. The laser pulse / pressure transient recording for the Nd:YAG laser was similar.

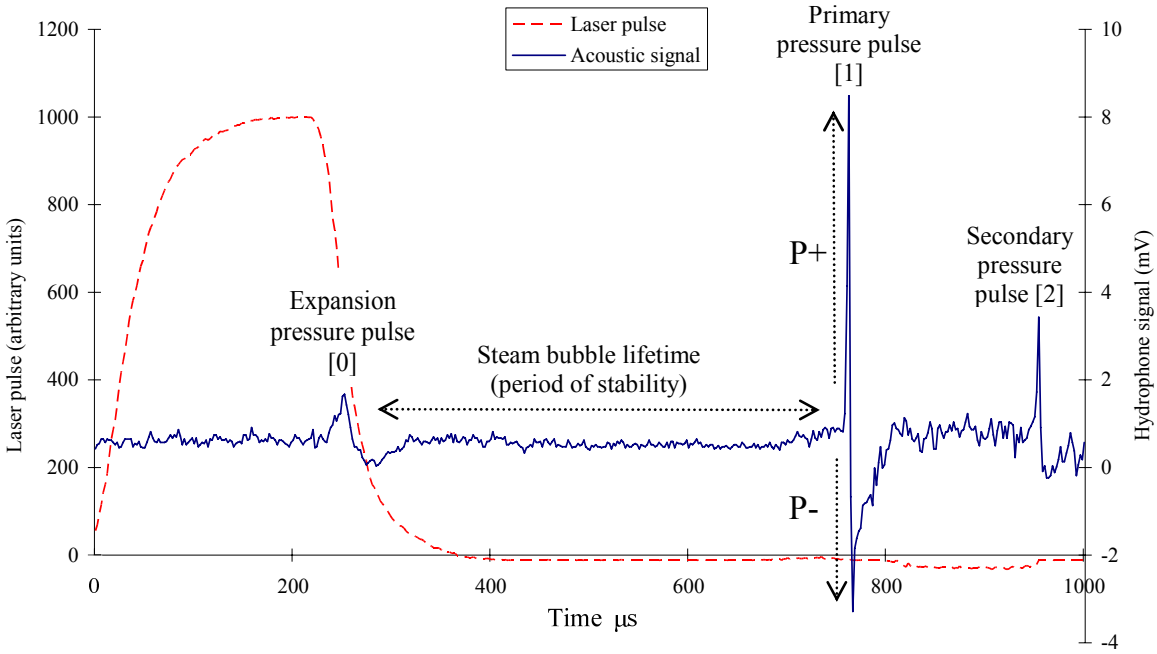

Figure 5.33: A typical recording of the Ho:YAG laser pulse and the induced pressure pulses [0-1-2] in water

In the example shown (Figure 5.35), which is for a Ho:YAG laser pulse, it can be seen that the laser pulse has a duration of approximately 250 µs, tailing off to zero after ~ 400 µs (following the pulse the recorded signal is shown as negative, this was due to drift in the circuit). The laser pulse generated three acoustic signals [0], [1] and [2]. The first acoustic signal [0] is a weak pressure transient detected as the laser pulse terminates. The primary acoustic signal [1], is detected several hundred microseconds after the end of the laser pulse and is a significantly stronger transient than the other signals detected. Finally, a delayed (secondary) acoustic signal [2], which is less than half the amplitude of the primary pulse [1], was detected around 200 µs later.

The initial pressure transient that is coincident with the end of the laser pulse is likely to be due to expansion effects and the creation of a steam bubble. The optical energy of the laser pulse is absorbed in the irradiated volume generating heat which reaches a maximum temperature at the end of the laser pulse. The heating of material (i.e. water) will lead to volume expansion, particularly if boiling occurs and steam is generated, and the expansion of water into steam is the likely explanation for this pressure transient.

Laser pulses that initiate a plasma may also generate a pressure transient as the plasma expands. These processes are illustrated in Figure 5.34.

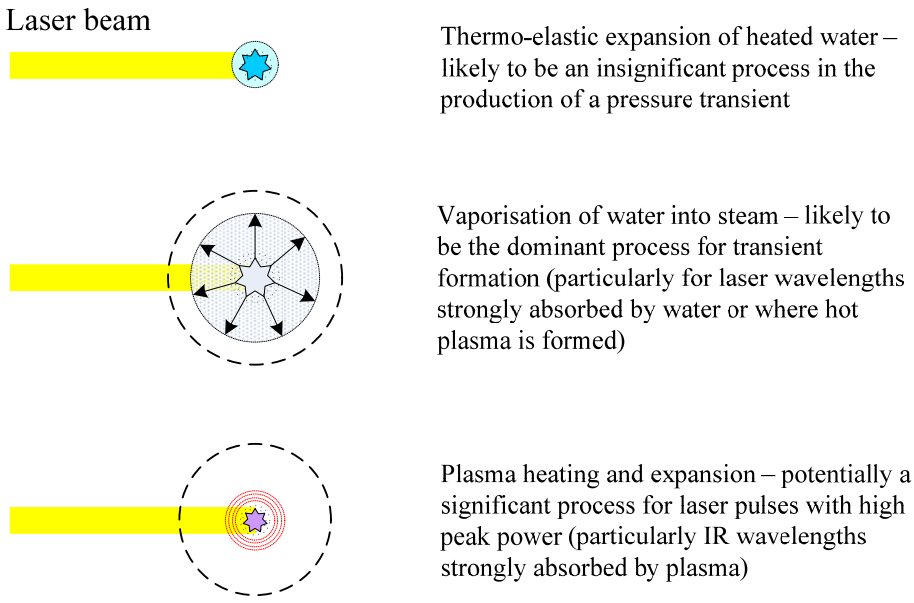

Figure 5.34: Schematic illustration of physical processes of laser-induced pressure pulses

The primary pressure pulse [1] had the greatest pressure amplitude and is therefore of importance in laser lithotripsy as it will impart the greatest mechanical action on the calculus. The pressure rises sharply as a crest of the positive wave and imparts compressive forces on the calculus. The pressure then falls sharply in the opposite direction (negative), in this case producing a rarefaction or negative pressure cycle. The negative pressure amplitude is lower in magnitude than the peak positive pressure, however, it may be more significant as a negative pressure induces tensile stresses which have a more damaging effect on brittle materials such as calculi (Vogel, 1997). The time taken for the peak negative to return to ambient pressure is much longer than that for the positive cycle of the pulse, probably due to a damping effect (Brujan and Vogel, 2006). The origin of this pressure transient is likely to be the collapse of a steam filled bubble, a process known as cavitation and reported by a number of investigators (e.g. Rink et al, 1995).

There is a time delay between the laser pulse and the primary laser-induced pressure pulse. This delay is partly due to the time it takes for the shockwave to travel from the emission centre to the hydrophone element, which depends on the speed of the shockwave and the distance. The time delay will also be dependent on the lifetime of effects arising from cavitation, i.e. the stability of the vapour bubble before it collapses. The more stable the bubble the longer is the delay before the bubble releases its pressure, which gives rise to delays in the detection of the transient.

The secondary pressure transient [2] that is seen in this example has a similar waveform to the primary pressure pulse, but lower in amplitude. A rapidly rising positive pressure is followed by a sharply falling, but much weaker, negative component. This pulse is likely to be a rebound shockwave from the collapse of the steam bubble.

The primary pressure transients [1] were investigated further. Averaged hydrophone signals of these transients were recorded for the Nd:YAG and Ho:YAG lasers, as shown in Figures 5.35 and 5.37. The pressures were generated under similar conditions i.e. laser beam fired into deionised water, and were measured at various distances and orientations from the emission centre. The pressure waveforms were found to be similar in shape and of comparable amplitudes, however, some interesting differences were observed and evaluated in the following sections.

5.6.1 Nd:YAG laser

The pressure pulse generated in water by the focussed nanosecond-pulsed Q-switched Nd:YAG laser has a peak amplitude of the order of MPa, and a duration of around 100 ns (FWHM). The pressure rises from ambient to a maximum value at around 60 ns, it then takes a further 160 ns to return to zero (ambient pressure). The transient is a positive pressure cycle i.e. a compressive wave is generated, and there appears to be no significant negative component in the transient waveform, as can be seen from the example pressure pulse waveform in Figure 5.38.

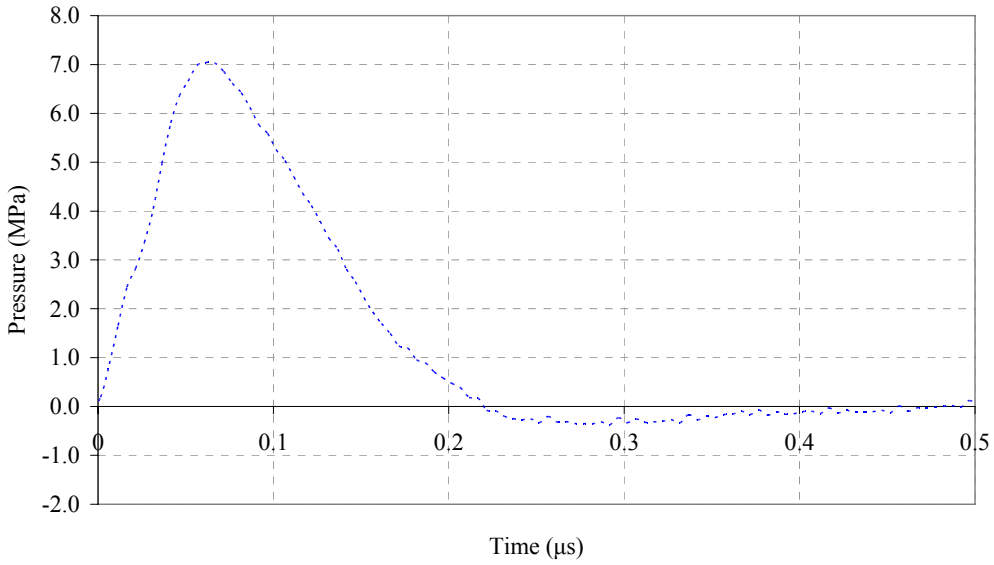

Figure 5.35: An averaged pressure pulse waveform in water for Q-switched Nd:YAG laser excitation (laser pulse 16 mJ, 6 ns, measured at 5 mm, n = 100)

The onset of the pressure pulse was found to occur within a few microseconds of the termination of the laser pulse. This time delay varied linearly with increasing distance between the hydrophone element and the emission centre, and within the range 4 – 20 microseconds. The delay time is highly reproducible, that is, the generation of the pressure transient was found to occur at a very precise time after the termination of the laser pulse.

Measurements of the delay time were taken at various distances to estimate the speed of the shockwave. The emission centre to hydrophone separation was moved in 1 mm intervals from a distance of 2 mm up to 20 mm whilst maintaining laser parameters. The laser settings were fixed at a pulse energy of ~ 60 mJ and repetition rate 5 Hz.

The results indicate that the time taken for the arrival of the pressure transient is proportional to the distance over the range of distances investigated, as shown in Figure 5.38. This means that the speed of the wavefront was constant across this range, that is, it was not decelerating due to attenuation. From the linear relationship it is straightforward to determine the speed. Calculation of the speed reveals that the pressure wave propagates at 1473 ± 20 ms^{-1} which is in good agreement with the published speed of sound in water (1497 ms^{-1} at 25 °C).

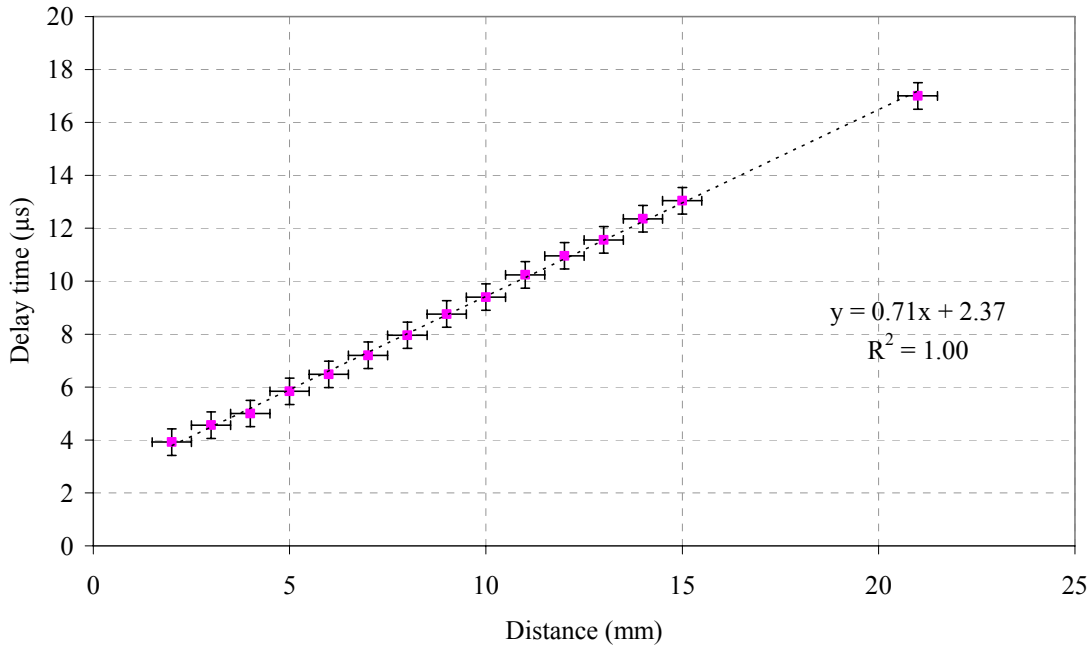

Figure 5.36: Dependence of delay time of Nd:YAG laser-induced pressure pulse with distance from the emission centre (n = 100)

The pressure transient, therefore, is not supersonic, and hence not strictly speaking a "shockwave". It is possible that the pressure wave may have an initial speed exceeding the speed of sound in water but slows down rapidly such that at the distances measured it is moving at normal speed. Measurements at very close range would be needed to investigate this further. However, due to the risk of damage to the hydrophone this was not carried out. Repeating these measurements at 20 Hz revealed that the speed of propagation of the pressure front remained unchanged and therefore had no dependence on laser pulse repetition rate.

A significant pressure transient was also seen with the Nd:YAG laser, coincident with the laser pulse ([0] as referred to in Figure 5.36). This pulse would correspond to pressures generated during rapid thermo-expansion or vaporisation processes, such as expansion of heated material, steam generation, or expansion of the plasma volume. However, it was observed that the pressure pulse was still detected even when the laser beam was blocked in its path (the laser was fired but the beam path was deliberately blocked). This suggested that the pulse was not due to the laser-water interaction but in fact was arising from electrical interference generated by electrical emissions from the

laser unit. This is plausible as the laser operates at high voltage and has rapid electrical switching (e.g. Q-switch operation). Cables in the pressure detection circuit may have coupled with the electromagnetic emissions. Therefore, for the Nd:YAG laser, this signal was considered to be an artefact and was ignored.

5.6.2 Ho:YAG laser

Waveforms were also captured for the Ho:YAG laser. In comparison to the Nd:YAG laser, the pressure transient was of a significantly longer duration and also included a negative pressure component, as can be seen in Figure 5.40.

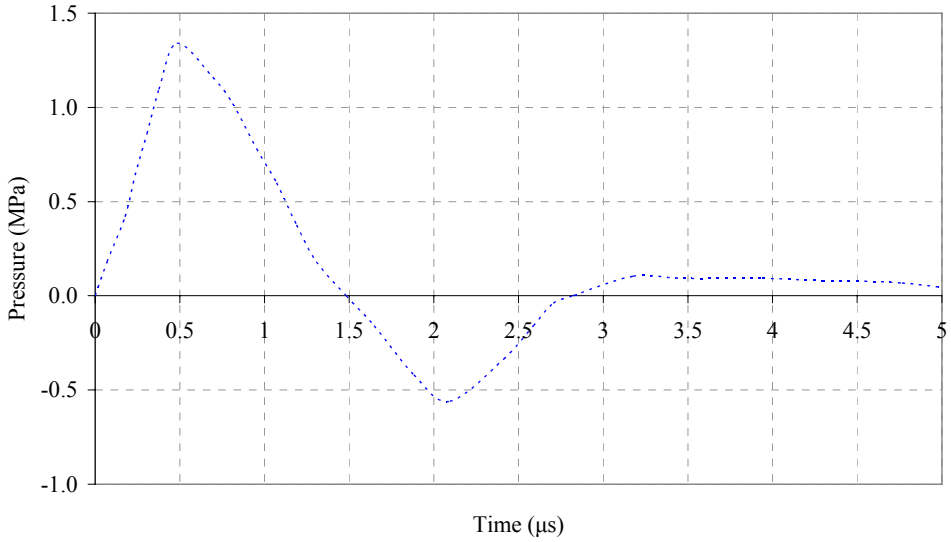

Figure 5.37: An averaged pressure pulse waveform in water for Ho:YAG laser excitation (laser pulse 1 J, 300 µs, measured at 5 mm, n = 100)

The maximum value of the positive pressure is less than that produced by the Nd:YAG laser, by a factor of ~ 6 (of the order of a few MPa). However, the positive pressure pulse duration is of the order of 1 µs, compared to ~ 0.1 µs for the Nd:YAG. The rise time of around ~ 500 ns in this case is in contrast to 60 ns for the case of the Nd:YAG laser. The negative cycle has a peak value of around one third or less of the positive cycle. The duration and rise time of this part of the waveform is similar to the positive cycle.

A significant difference was also seen in the delay time between the end of the laser pulse and the detection of the pressure transient. Compared to the Nd:YAG laser, where

the delay time was found to be a few microseconds, the delay time with the Ho:YAG laser measured several hundred microseconds. Also, the arrival of this pressure pulse did not occur at a precise time after the laser pulse. Pulse to pulse there was some variation in the time the pressure pulse was detected, by a few tens of microseconds. For this reason it was found that recording an average pressure waveform for the Ho:YAG using the laser pulse as a trigger was not possible, and therefore the rising edge of the pressure transient was used as a trigger instead.

The variation in arrival time of the shockwave (±10's of μs) to a set distance from the emission centre made it more difficult to determine the propagation velocity. Ideally, two hydrophones would be used to detect the passing of the shockwave at different but known distances from the emission centre, and the time between the two detected signals could then be used to calculate the velocity. However, this setup was not used due to non-availability of a matched pair of hydrophones.

5.7 Lifetime of the laser-induced steam bubble

5.7.1 Nd:YAG laser

From the determination of the speed of the pressure front, it is apparent from Figure 5.36 that there is a period of time (~ 2.37 μs) that is not accounted for by the propagation time of the pressure transient. One explanation for this is that it is the outcome of a systematic error in the measurement of distance (at 1473 ms^{-1} a time period of around 2.4 μs equates to ~ 3.5 mm). However, care was taken to set up and measure the hydrophone to emission centre separation accurately and so this is unlikely. Therefore, this can be attributed to the time period during which a steam bubble exists prior to its collapse and subsequent generation of a pressure transient.

The total time between the onset of the laser pulse and the detection of the pressure pulse is assumed to be the lifetime of the steam bubble (Figure 5.38). The trigger for the recording was taken from the trailing edge of the Q-switch signal (t = 0). Emission of the laser pulse occurs ~ 0.2 μs after the Q-switch is opened, and the Q-switch trigger signal has a duration of ~ 12.5 μs. Therefore, accounting for the 2.4 μs identified from

the graph shown in Figure 5.36, the lifetime of the steam bubble is calculated to be in the domain of 14.7 ± 0.5 μs.

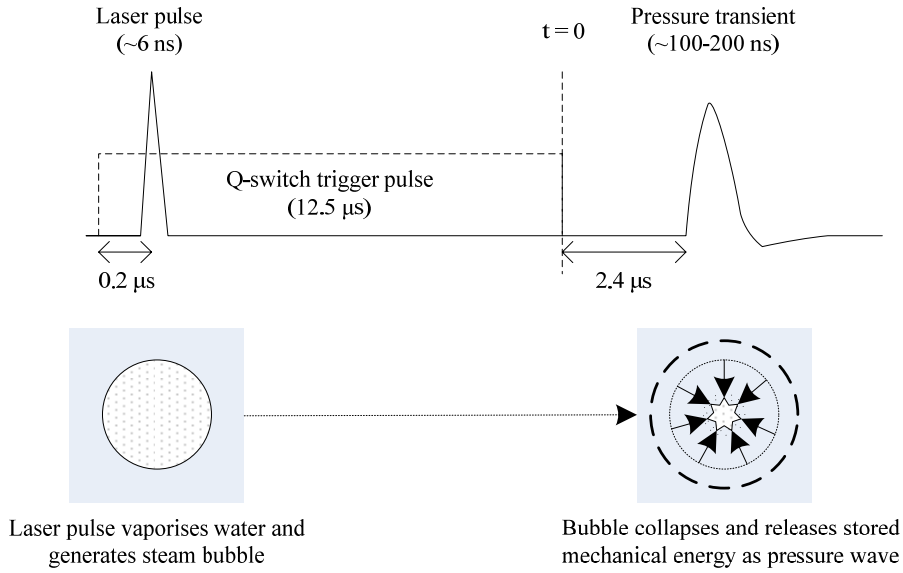

Figure 5.38: Sequence of events from Nd:YAG laser emission to detection of pressure pulse in water

The effect of increasing the laser energy on the lifetime of the vapour bubble was investigated. It was found that increasing the laser pulse energy over the range, 12 mJ – 87 mJ had little effect on the stability of the bubble, as shown in the plot in Figure 5.39 of the steam bubble lifetime versus the laser pulse energy.

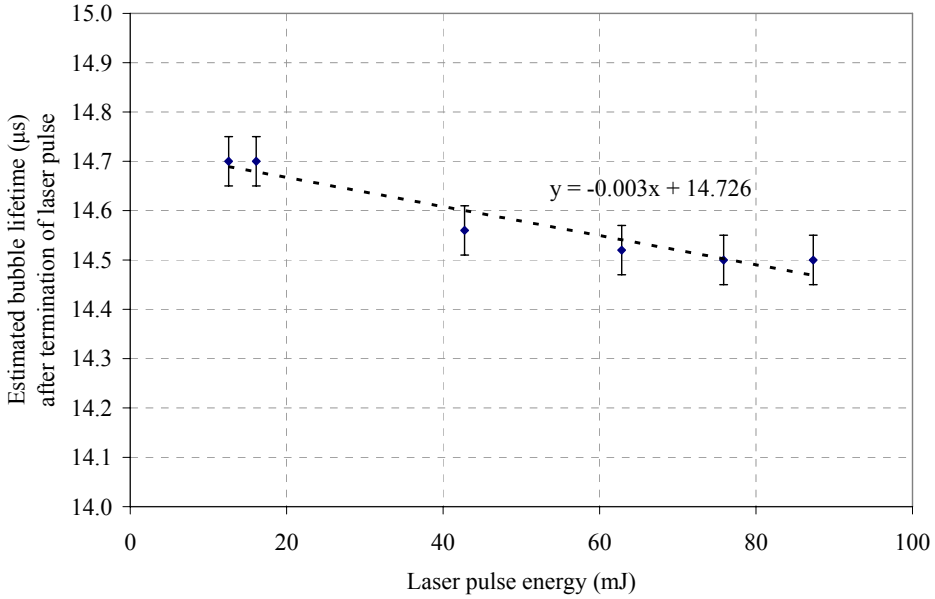

Figure 5.39: Estimated lifetime of Nd:YAG laser-induced steam bubble with laser pulse energy

From the graph it is seen that there is a slight trend towards a shorter lifetime at higher laser energies, but only by a few percent, which could be experimental error. If bubble stability, and therefore its lifetime, is largely determined by its shape, then the results suggest that the bubble is of the similar shape regardless of the input laser energy. This is plausible as the short-duration laser pulses (~ 6 nanoseconds) generates a highly localized interaction with stress and thermal confinement and therefore the possible creation of a spherical shaped steam bubble as reported by Rink et al (1995).

5.7.2 Ho:YAG laser

The lifetime of the Ho:YAG-generated vapour bubble was also estimated as in the previous section. An assumption was made that the pressure wave generated by the Ho:YAG laser propagates at a similar speed to that generated by the Nd:YAG laser. This assumption may be justified considering that the Nd:YAG laser induces an interaction event that is effectively far more "explosive" i.e. in a shorter timescale and with a steeper pressure gradient, and yet the speed of the shockwave propagates at the speed of sound in water, and not faster. The delay time, as measured from the start of the laser pulse to the arrival of the Ho:YAG-induced shockwave, for a range of hydrophone to emission centre distances are given in Table 5.9. The data is based on an average of 10 pulses (1 J, 420 μs, measured at 90°).

Table 5.9: Estimated lifetime of Ho:YAG laser-induced steam bubble

Hydrophone to emission centre separation (mm)	Measured time delay (start of laser pulse to start of pressure pulse) (μs)	Calculated steam bubble lifetime (μs)
3 ± 0.5	780 ± 20	358 ± 30
4 ± 0.5	780 ± 20	357 ± 30
5 ± 0.5	786 ± 20	363 ± 30
6 ± 0.5	788 ± 20	364 ± 30
7 ± 0.5	788 ± 20	363 ± 30
8 ± 0.5	788 ± 20	363 ± 30
9 ± 0.5	791 ± 20	365 ± 30
10 ± 0.5	798 ± 20	371 ± 30

The variations in delay times were found not to be linear and hence reveal that there is variability in bubble lifetime over this time period. The estimated uncertainty in the values for the measured time delay is ± 20 μs, and therefore taking an average of the values in the table the steam bubble lifetime is estimated to be ~ 363 ± 30 μs. This is in contrast to the bubble lifetime with the Nd:YAG laser which was estimated to be ~ 14.3 ± 0.5 μs.

The effect of bubble stability (lifetime) was investigated further. It was found that the time delay before a pressure transient is detected and the duration of the Ho:YAG laser pulse has an inverse relationship across the range 200 – 800 μs, as shown in Figure 5.40. Essentially, the steam bubble would appear to exist for a longer period (by up to several hundred μs) when generated by laser pulse durations that are shorter e.g. 200 μs. The relationship is similar for both the primary pressure transient and also the secondary (rebound) pressure pulse (refer to Figure 5.36).

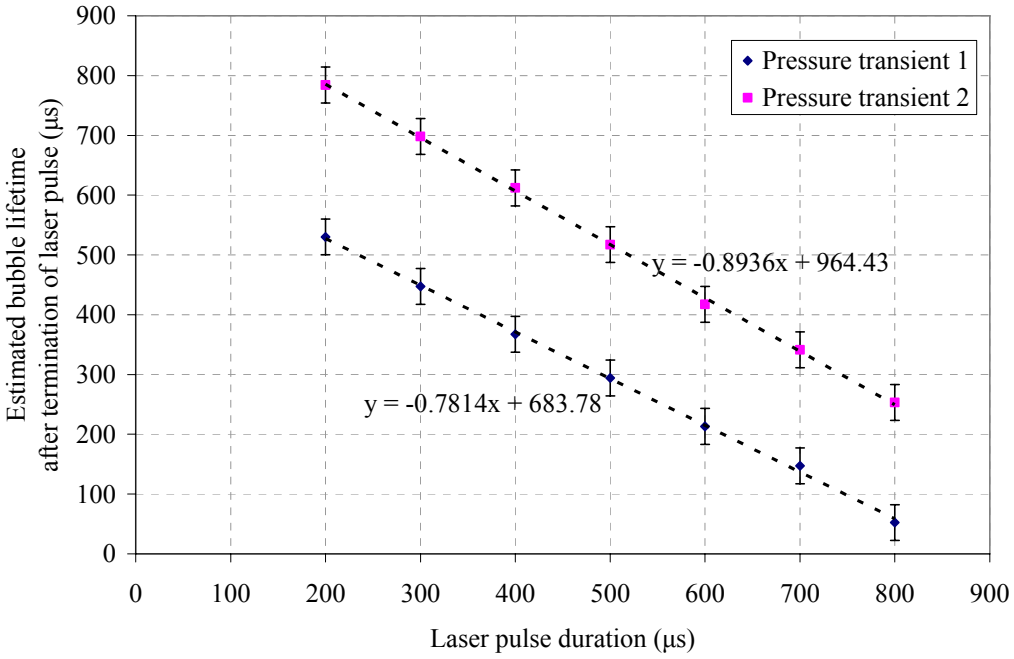

Figure 5.40: Variation of lifetime of Ho:YAG laser-induced steam bubble with pulse duration

The greater stability is again likely to be linked to the bubble dynamics and in particular the bubble shape. As previously described, shorter duration laser pulses have been reported to generate steam bubbles that are more spherical in shape, compared to longer

duration laser pulses that generate elongated bubbles (Figure 5.41). The difference in shape arises because of the extended duration of the vaporisation process at the distal end of the bubble i.e. the laser continues to vaporize the far side of the steam void, distorting the shape of the final bubble. Distorted bubbles have uneven stresses and have been shown to collapse at multiple centres because of instability (Chan et al, 2001).

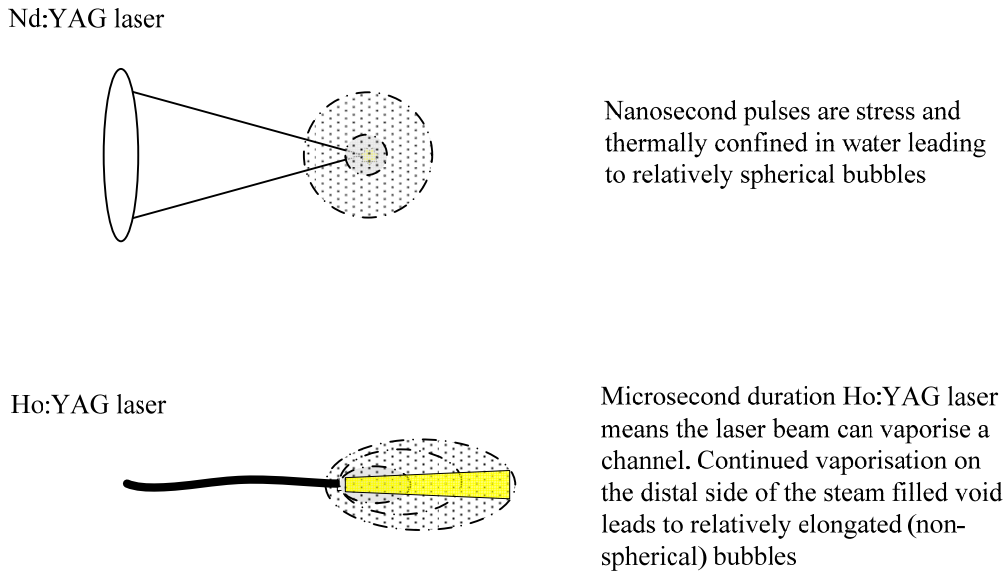

Figure 5.41: Steam bubble shape with laser pulse duration

The relationship between Ho:YAG laser pulse energy and bubble lifetime was also investigated and the results are shown in Figure 5.42. It was found that for a fixed laser pulse duration (420 μs) the time delay between the laser pulse and the detection of the pressure pulse increased, suggesting the bubble was in existence for a longer time when more laser energy was delivered. This is in contrast to the Nd:YAG laser where no significant effect on stability with laser energy was seen.

From the graph it can be seen that a laser pulse energy of 400 mJ apparently generated a bubble with a duration of ~ 200 μs, whereas a 3 J pulse generated a bubble that lasted for up to 3 times longer (~ 600 μs). A possible explanation for this observation is that the increase in laser energy generates an increase in steam which raises the internal pressure of the bubble. This increases the surface tension within the boundary wall which is expected to be a more stable configuration.

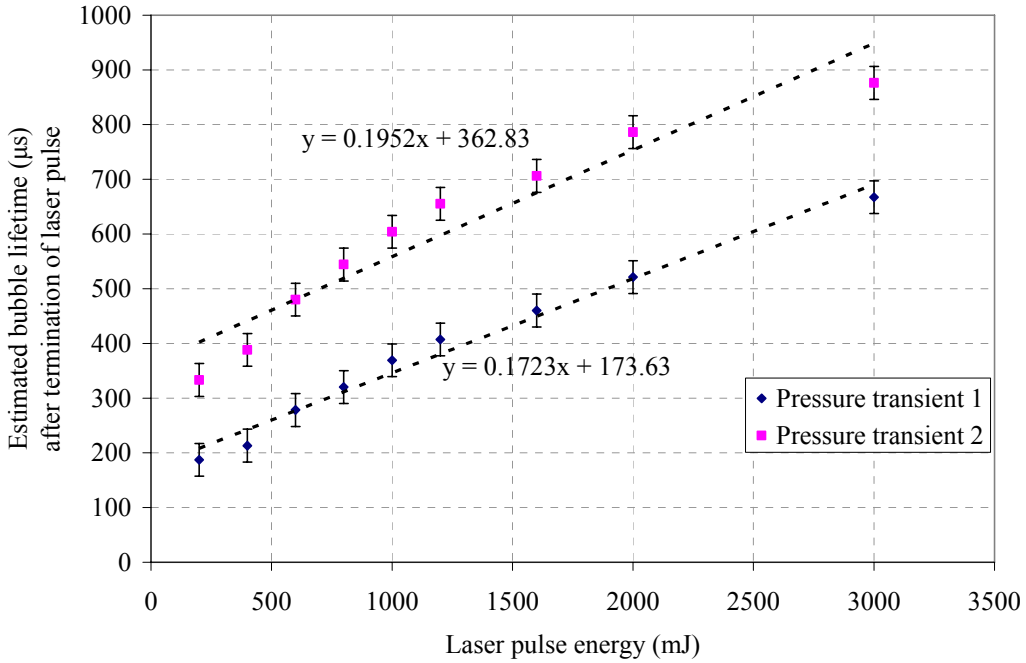

Figure 5.42: Estimated lifetime of Ho:YAG laser-induced steam bubble with laser pulse energy

The data has revealed that there is a relationship between the lifetime of the steam bubble and the magnitude of the pressures generated. In particular, laser parameters that create larger, more stable, and more spherical bubbles are particularly important, as greater mechanical action would result. The next stage is to measure the amplitude of the pressure transient and investigate the dependence on the laser parameters, and these are studied in the following sections.

5.8 Effect of the calculus on the pressure amplitude in water

Prior to conducting a set of experiments to measure the magnitude of the laser induced pressures in water for a range of laser parameters, it was necessary to determine the effect of the calculus on the pressure values. There is the possibility that the presence of the calculus has a significant effect on the peak pressure as the surface of the calculus may influence the bubble dynamics. If that was the case then the pressures recorded for firing the laser free into water (often referred to as “free cavitation”) may not accurately reflect the pressures experienced by the calculus. For this reason a set of measurements was carried out to investigate how the pressure amplitude varies as the calculus is brought towards the emission centre. The results are shown in Table 5.10.

Table 5.10: Variation of pressure with calculus to emission centre separation (Nd:YAG laser 32 mJ, 6 ns, 5 Hz)

Distance calculus to emission centre (mm)	Pressure (MPa)
0 ± 0.5	2.4 ± 0.2
1 ± 0.5	4.0 ± 0.2
2 ± 0.5	3.9 ± 0.2
3 ± 0.5	4.0 ± 0.2
20 ± 0.5	4.2 ± 0.2

The data shows that when the calculus surface was coincident with the emission centre, there was an apparent reduction in the pressure generated. This is expected as ejected fragments of calculus material and generation of bubbles may perturb the liquid environment and this might affect the propagation of the pressure pulse. It may also be that the interaction and bubble dynamics are confined by the physical boundary presented by the calculus surface, and this may have a similar effect on the pressure amplitude. However, there is also a possibility that this effect may not be real but instead a shielding effect of the calculus i.e. the calculus partially obscures the line of sight between the hydrophone and the origin of the pressure wave.

Measurements made with the calculus at various distances from the laser focus indicate that down to ~ 1 mm proximity the generated pressure is not significantly altered by its presence. Pressure recordings taken with the calculus at a distance of ~ 1 mm from the emission centre were comparable with the pressure recording at ~ 20 mm (assumed to be equivalent to the situation of having no calculus present), 4.0 ± 0.2 MPa and 4.2 ± 0.2 MPa respectively. As the generated pressure does not appear to be significantly altered by the presence of the calculus, pressure measurements taken free in water can be assumed to be valid for estimating the pressure imparted to the calculus. Also, a 1 mm gap between the calculus and the emission centre is a reasonable assumption for lithotripsy, where the optical fibre is positioned close to the calculus but is not maintained in direct contact. Thus, the laser-induced pressures for a range of laser parameters investigated in the following experiments are recorded with the laser 'free firing' into water.

5.9 Angular variation of the pressure amplitude

The pressures generated from the collapse of bubbles are difficult to measure at close range because of the potential for damage to the hydrophone element. At close proximity to the emission centre, there is potential for a direct laser strike on the PVdF element, and also the pressure damage threshold (> 20 MPa) may be exceeded. This was proven during a set of preliminary measurements at < 3 mm distance from the Ho:YAG fibre tip. In this a permanent damage to the element occurred and the hydrophone had to be replaced. From this it was concluded that measurements with the hydrophone in the beam path would need to be taken at a distance > 10 mm. However, measurements at close range would be possible at an angle to the laser beam. With knowledge of the angular variation in amplitude the data can be corrected to reveal the on-axis pressures.

With the hydrophone mounted on a rotating platform marked with a scale in 0.1° increments, a set of pressure measurements for a range of angles was obtained. The hydrophone element was rotated about a fixed distance from the emission centre, as shown in Figure 5.43. The 0° orientation was defined as when the hydrophone was in line with the direction of the laser beam. Measurements were taken either side of this position i.e. ± 90° of the emission centre.

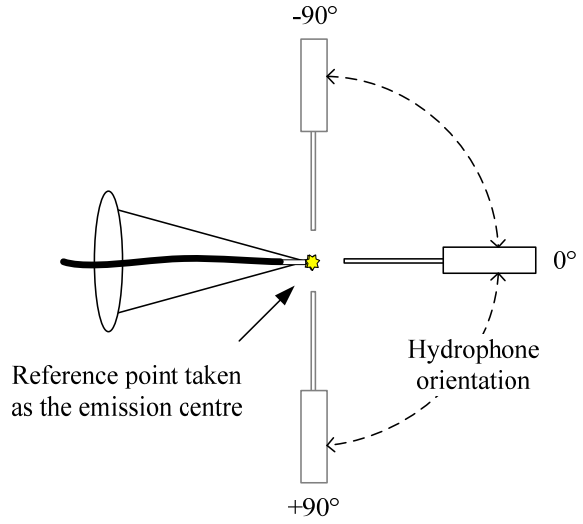

Figure 5.43: Schematic of the experimental setup for the measurements of angular variation of the pressure pulse

5.9.1 Nd:YAG laser

The angular dependence of the pressure amplitude recorded for the Nd:YAG laser is shown in Figure 5.44. In addition to measurements across the range of angles, the laser

pulse energy was also varied. The results show that for all laser pulse energies the pressure recorded at ± 90° (lateral position) was significantly higher than the pressure recorded approximately on-axis (~ 10° i.e. forward position) with the laser beam. At low laser pulse energies (~16 mJ) the ratio of forward to lateral pressures is approximately 1:3, whereas for higher pulse energies (> ~ 43 mJ) the ratio increases to approximately 1:10. The forward pressure was found to be fairly constant and independent of laser pulse energy whereas the lateral pressure increased steadily with increasing laser pulse energy. From 10° through to ~ 45° the pressure pulse increases only slightly from ~ 0.6 MPa to ~ 1 MPa. However, between 45° and 90° the magnitude of pressure pulses increased sharply, from ~ 1 MPa up to ~ 10 MPa for higher laser pulse energies (e.g. 87.3 mJ).

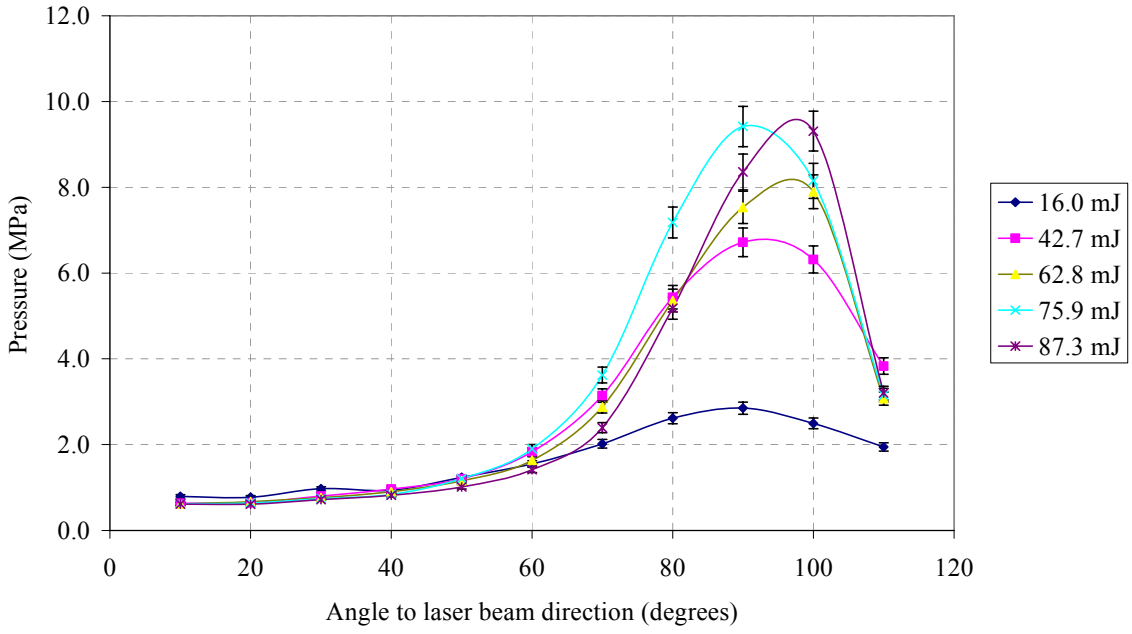

Figure 5.44: Angular variation of Nd:YAG laser-induced pressure pulse with laser pulse energy as a parameter (n = 100)

These measurements indicate that a calculus placed adjacent to the laser beam focus would experience a greater pressure when it is placed at an angle of 90° with respect to the direction of the laser beam than if it were directly in the beam path (i.e. 0°). This result was unexpected. As the process of generating the steam bubble is initiated by a plasma, the plasma itself was investigated. Closer inspection of the shape of the laser-

induced plasma was conducted in an attempt to reveal why the forward pressure was considerably lower in magnitude than the lateral pressures with a setup as illustrated in Figure 5.45.

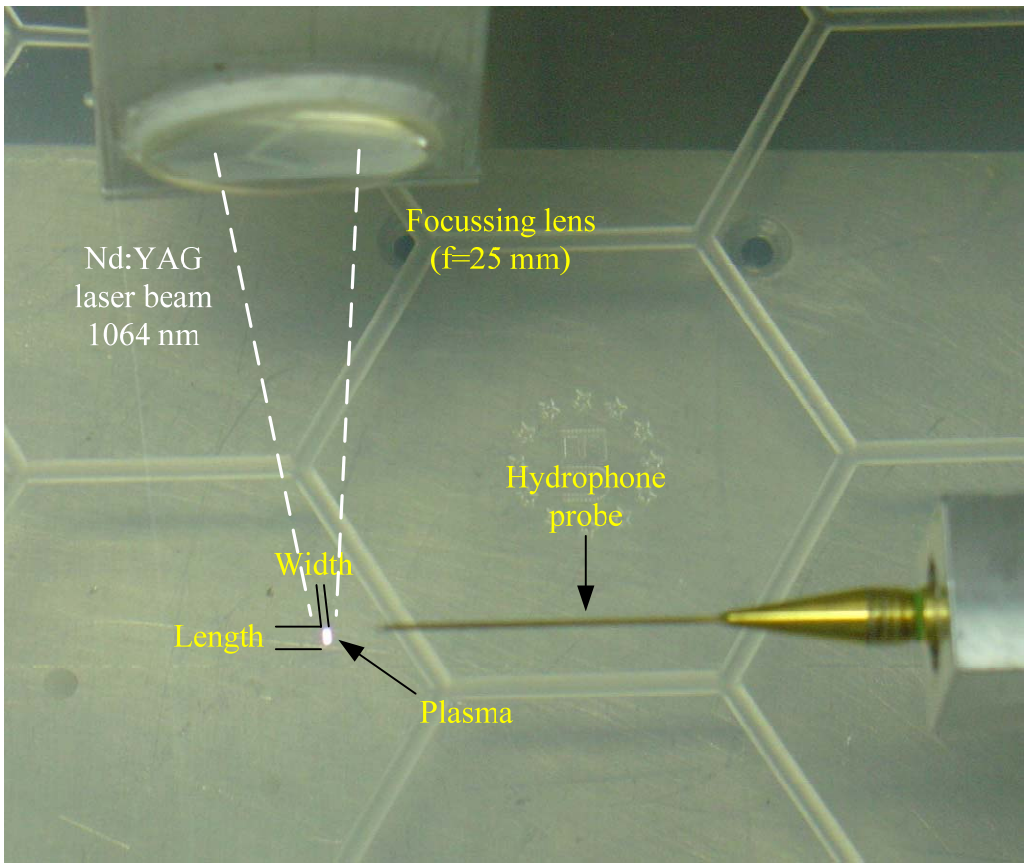

Figure 5.45: Nd:YAG laser-induced plasma in water

The dimensions of the plasma were measured using a travelling microscope with a scale to an accuracy of ± 0.05 mm. The laser was set to 10 Hz to enable better visualisation of the intense blue-white flash. Laser pulse energy was varied across the range available. It was found that the plasma formed at the beam focus had a lateral dimension (width) of approximately 0.15 ± 0.05 mm, and that this dimension did not change when the laser pulse energy was varied. The length of the plasma, however, did increase with increasing laser energy, from 1.8 ± 0.5 mm at ~ 16 mJ to 4.0 ± 1.0 mm at ~ 87 mJ. Across this range of pulse energies the relationship between the dimension of the plasma length and laser pulse energy was found to be linear with a slope of ~ 0.013 mm mJ^{-1}, as shown in Figure 5.46.

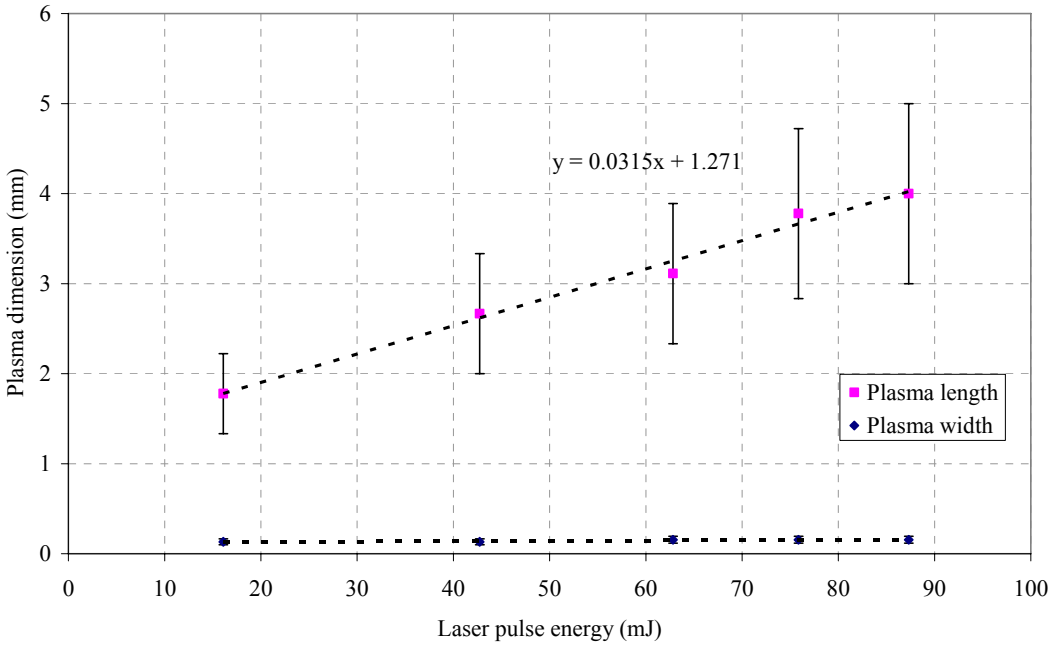

Figure 5.46: Variation of dimensions of the Nd:YAG laser-generated plasma in water with laser pulse energy (n = 10)

The increase in plasma size with laser pulse energy is to be expected. The focused beam forms a region of high irradiance and plasma occurs within the volume and where the optical breakdown threshold of water is exceeded. An increase in the laser pulse energy increases the irradiance proportionately and therefore extends the zone in which optical breakdown can take place and plasma can be formed, as illustrated in Figure 5.47. Due to plasma being an efficient absorber of infrared radiation, an effect known as "plasma shielding" (Puliafito and Steinert, 1984) prevents it growing in the forward direction of the laser beam, instead it increases its dimensions towards the laser source. The effect of plasma shielding was noted during observations. Nd:YAG laser-induced plasma occurs in the focal volume where high irradiance exceeds the optical breakdown threshold of water, at a value of around 5 GW cm^{-2} (see 5.4.1). Plasma length was seen to increase with laser energy, expending along the direction of the beam axis. The length of the plasma varied significantly from pulse to pulse as shown by the error bars on the graph, and the uncertainty was estimated from a series of 10 measurements.

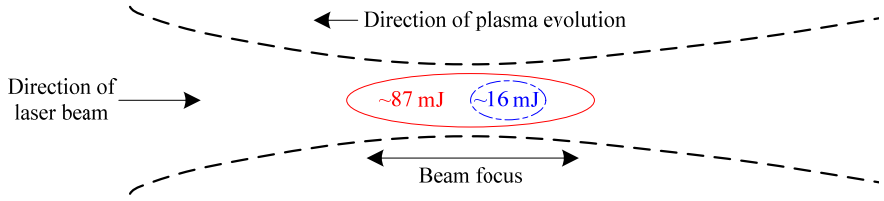

Figure 5.47: Schematic representation of the direction of plasma formation with respect to the direction of the laser beam

From these observations it is evident that the plasma dimensions influence the magnitude of the pressure wave. Across the width of the laser beam the plasma is at its narrowest and pressures of ~ 10 MPa were recorded laterally from the beam direction. The generation of these high pressures may be a result of the sharp temperature gradient at the edge of the plasma. In the forward direction the extended plasma leads to reduced pressures being generated, possibly a result of a reduction in the temperature gradient along the beam axis. There may also be an effect regarding the bubble dimensions in this direction, whereby the extended plasma volume leads to a distorted bubble shape.

The indications are that if pressure waves are desirable in the fragmentation of calculi then the beam must be tightly focused to minimize the plasma volume and thereby maximize the pressure amplitude. In practice, as the fibre tip would be held very close to the calculus (e.g. ~ 1 mm) this would restrict the plasma length in the beam direction. Therefore, the high pressures recorded across the beam are also likely to be encountered in the forward direction and thus imparted on the calculus. These measurements, therefore, are considered to be valid in the estimation of peak pressures experienced by the calculus.

5.9.2 Ho:YAG laser

For a fixed laser pulse energy and pulse duration the pressure pulse generated by the Ho:YAG laser exhibited a more or less non-directional radial variation of amplitude compared to that of the Q-switched Nd:YAG laser. Measured pressure amplitudes recorded at 10° intervals from ± 90° about the direction of the fibre tip were found to have a variation of less than 20 %, which is insignificant given the variation in the

pressure amplitude on a pulse to pulse basis of approximately ± 20%. The result was the same when the pulse energy was varied in the range 200 mJ – 2 J.

The difference between the properties of the pressure pulses for the two lasers may be due to the variation in the type of delivery system, or a difference in the laser-water interaction process for two different wavelengths and pulse durations. The observations noted in 5.4.2 suggest that holmium laser-induced pressure transients do not involve plasma formation and therefore can be assumed to arise from direct vaporization of water by the beam energy. Direct vaporization will take place immediately in front of the fibre tip. The steam bubble will originate in this region and the collapse centre will be located in front of the fibre tip, hence wavefronts will emanate from this point. The wavelength of holmium laser radiation is strongly absorbed by water and the high pulse energy leads to the creation of steam bubbles. However the event takes place in only a few hundred microseconds and therefore the steam bubble is not captured in the photographs taken. The micro bubbles seen are likely to be the remnants of collapsed steam bubbles. High speed photography would be required to investigate this further.

5.10 Variation of pressure amplitude with distance

Pressure measurements conducted at a distance do not reveal the peak pressure that would be experienced by a calculus in close proximity to the emission centre i.e. at the fibre tip or beam focus. In clinical practice, the urologist advances the optical fibre to more or less be in contact with the calculus. However, during the course of lithotripsy the gap between the fibre and calculus may increase as the surface of the calculus becomes ablated. Also, stone retropulsion may result from the pressures pushing the stone away from the fibre tip (Kang et al, 2006). There is also the possibility of fibre damage arising from the pressures and high temperatures created (Knudsen et al, 2005). A reasonable estimate would be to assume a ~ 1 mm gap and to extrapolate measured pressures to this location. For this to be possible it is necessary to record pressure amplitudes at various distances so that the relationship between pressure and distance can be determined.

5.10.1 Nd:YAG laser

The measured pressures at various distances for the Nd:YAG laser fired into deionised water is shown in Figure 5.48a. The hydrophone was positioned laterally (at 90°) to the beam direction. As expected, the pressure amplitude falls off with distance as the acoustic energy becomes distributed over a larger surface area. Attenuation losses arising from absorption in water will also contribute to a reduction in pressure with increasing distance. Scattering from micro bubbles and calculus debris will cause reflection and energy losses. The pressure recorded at 3 mm was the closest measurement to the emission centre and revealed a pressure amplitude of ~ 11 MPa for a laser pulse energy of ~ 32 mJ. The value of the pressure at 1 mm would be expected to be greater than this, however, the value depends on the relationship with distance.

Theoretically, a spherically divergent wave from a point source has an r^{-1} dependence for amplitude as a function of distance. However, this model is simplistic and the complexities that influence the laser generated pressure waves such as the possibility of a distorted steam bubble (i.e. non-spherical), thermal effects, the presence of micro bubbles, and the influence of the proximity of the fibre and calculus (i.e. presence of solid boundaries) make it difficult to predict the propagation dynamics (Sperrin, 2000).

From the measurements recorded with the Nd:YAG laser, pressure versus distance can be modelled as an exponential relationship. Using the formulae indicated on the graph (Figure 5.48a), the extrapolated pressure at 1 mm for a 32 mJ laser pulse is predicted as ~ 12.9 MPa. The 'R' value (which represents the quality of fit using regression, values closest to 1 indicating the best fit) indicates that the exponential relationship accurately fits the data. This finding can be explained by an exponential attenuation of the acoustic energy as it travels through the water.

The exponential relationship derived from the plot in Figure 5.48a implies a pressure amplitude falloff with distance that is less steep than r^{-1} i.e. r^{-n} where $n < 1$. Plotting the data on a logarithmic scale, as shown in Figure 5.48b, the slope gives an indication of the value of n.

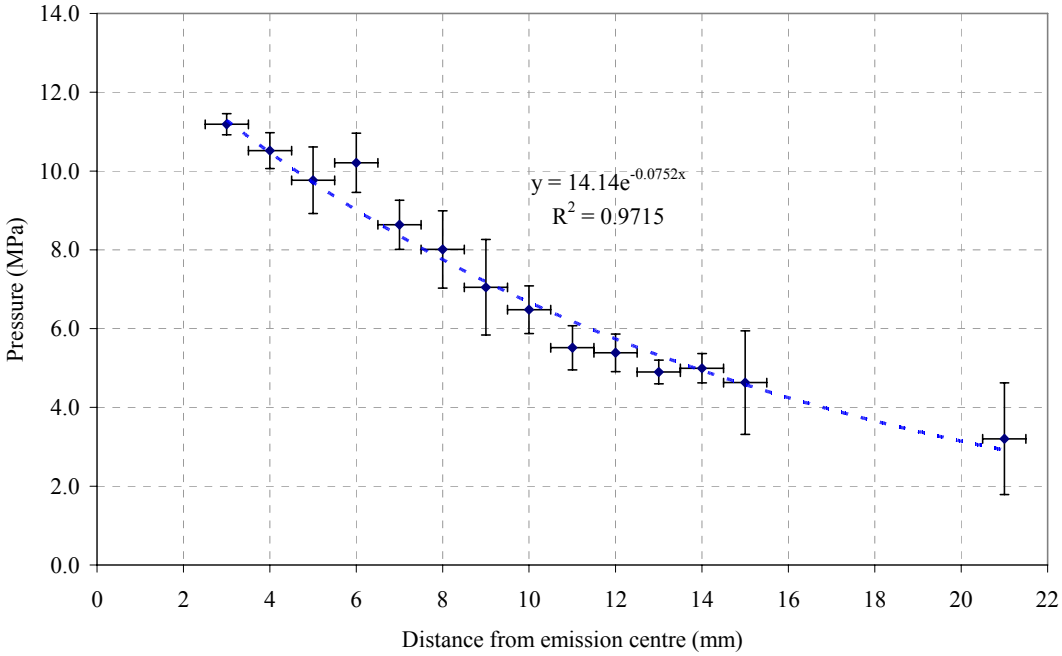

Figure 5.48a: Plot of pressure amplitude versus distance from the emission centre (focal spot) for Nd:YAG laser excitation (laser 32 mJ, 6 ns, n = 100)

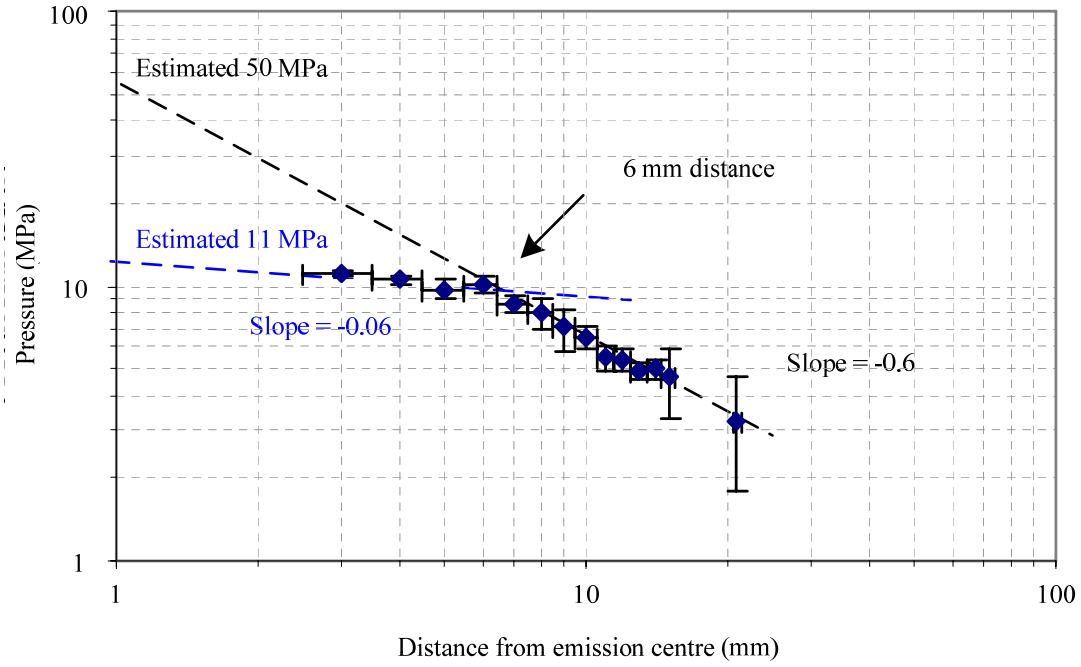

Figures 5.48b: Log-log plot of pressure amplitude versus distance from the emission centre (focal spot) for Nd:YAG laser excitation (laser 32 mJ, 6 ns, n = 100)

It is found that pressure pulse amplitudes fall off with a $r^{-0.06}$ relationship for distances within ~ 6 mm, and for distances ~ 6 mm – 21 mm the relationship with distance is $r^{-0.6}$. This suggests that the pressure amplitude falls off gradually at close range then falls off more rapidly beyond a certain range, in this case around ~ 6 mm from the emission centre. This can be explained by the presence of near and far field effects in the acoustic field.

The peak pressure estimated at 1 mm can be combined with the formulae for radial dependence that has been determined for the 0° orientation. The relationship of pressure with pulse energy and pulse duration, as well as the effect of pulse repetition rate and the propagating medium, will be determined in a later section.

5.10.2 Ho:YAG laser

The results for the intensity versus distance measurements with the Ho:YAG laser can be seen in Figure 5.49a.

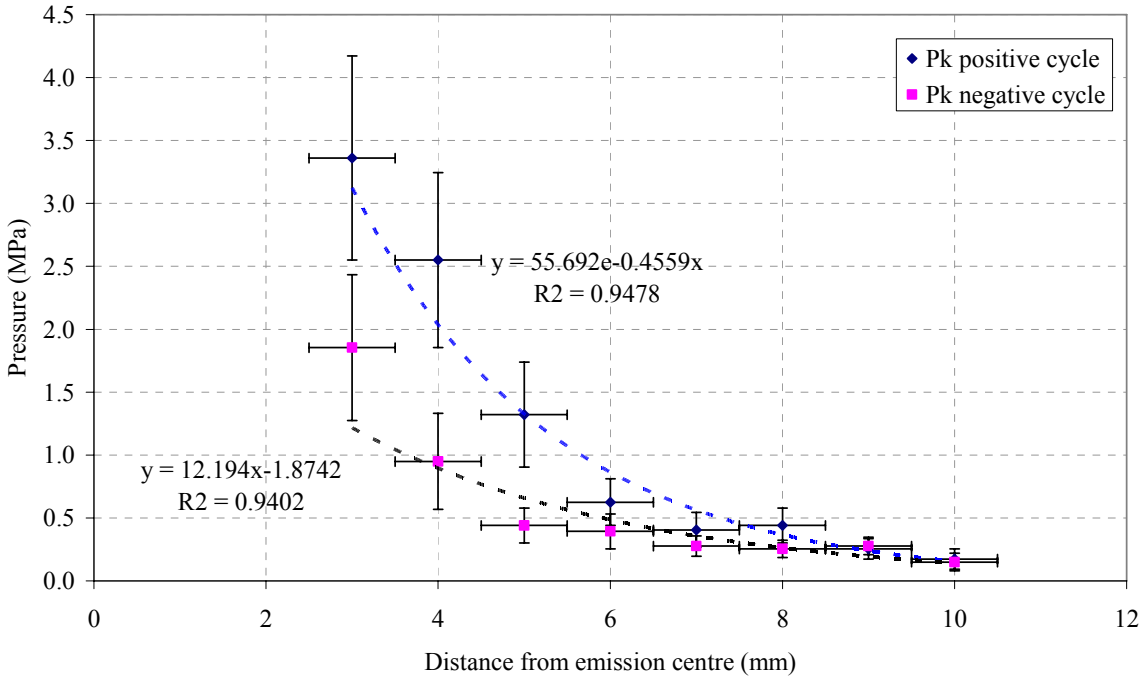

Figure 5.49a: Plot of pressure amplitude versus distance from the emission centre (1 mm from the fibre tip) for Ho:YAG laser excitation (laser 1 J, 300 µs, n = 100)

In contrast to the Nd:YAG laser, the pressure generated by the Ho:YAG laser in water was found to be lower in amplitude and falls off more rapidly with distance. It was therefore difficult to measure pressures beyond 10 mm as the transients were too weak. It was also noted that the variation in pressure amplitudes on a pulse to pulse basis was significantly greater with the Ho:YAG compared to that for the Nd:YAG laser, and this is reflected in the larger uncertainties (and error bars on the graph). The reason for this variation was believed to be due to perturbations in the water affecting bubble formation and unstable bubble collapse. The data is considered reliable as all pressure measurements were taken as an average of at least 100 pulse recordings, and the error bars represent the standard deviation of the measurements.

The data suggests that although the pressure at 3 mm from the laser fibre is weaker for the Ho:YAG laser than at 3 mm from the Nd:YAG laser focus. The steeper fall off with distance in this case points to the prediction of significantly higher pressures at close range. Using the formulae derived for the best fit trendlines, the predicted pressure at 1 mm distance are + 35.3 MPa and - 12.2 MPa for the positive and negative cycles respectively, which are greater than those predicted for the Nd:YAG laser. This trend is closer to r^{-2} than r^{-1}, and therefore investigators who have estimated pressures using the r^{-1} dependency may have underestimated the peak pressure at the emission centre for the Ho:YAG laser.

However, plotting the same data on a log-log scale (Figure 5.49b) shows that pressure with distance does fit well with a power relationship that is close to r^{-1}; the positive pressure fall-off with distance can modelled as a $r^{-0.80}$ trend and the negative pressure as a $r^{-0.75}$ dependency. Using these values the predicted pressure at 1 mm distance for the laser parameters of pulse energy 1 J and pulse duration 300 μs is + 50 MPa and - 25 MPa for the positive and negative cycles respectively.

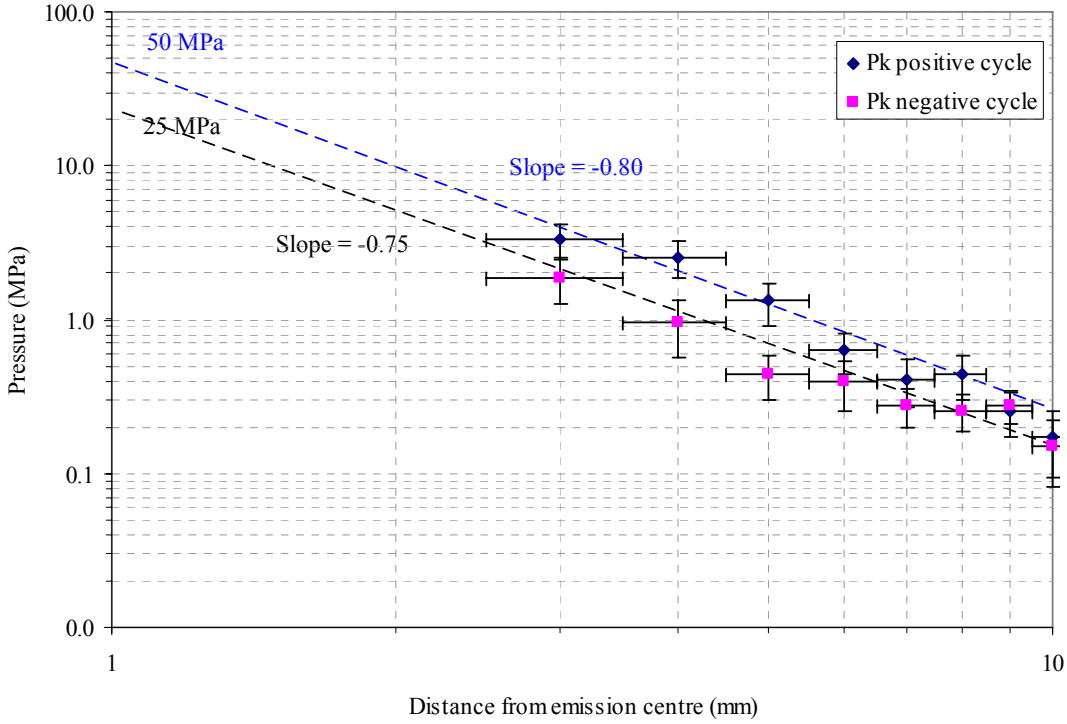

Figure 5.49b Logarithmic plot of amplitude of pressure pulse versus distance from the emission centre (1 mm from the fibre tip) for the Ho:YAG laser (laser 1 J, 300 µs, n = 100)

The stronger dependence on the pressure amplitude with distance for the Ho:YAG laser suggests that the attenuation losses are significantly higher for the pressure wave compared to the losses for the pressure wave generated by the Nd:YAG laser. This may be linked to differences in the interaction process, such as the presence of micro bubbles or ejected particles of calculus material in the path of the pressure wave. The Ho:YAG laser pulse has a higher energy and is very strongly absorbed by water and so it is possible that there may be an increased quantity of steam bubbles and calculus debris present and these will lead to an increase in the attenuation of the acoustic energy.

Another possibility is that the pressure wave generated by the Ho:YAG laser is more strongly absorbed by water than the Nd:YAG laser. Generally, higher frequency acoustic waves suffer greater attenuation in water. There may be higher frequency components in the pressure waveform generated by the Ho:YAG laser compared to the Nd:YAG laser. However, as the Ho:YAG pressure pulse has a considerably longer

period of around 3 μs (compared to 0.3 μs for the Nd:YAG), this suggests that the frequency is actually lower rather than higher. Increased attenuation experienced by the Ho:YAG pressure wave may also explain the origin of the negative pressure component (tensile tail) that is not seen in the Nd:YAG waveform.

The indication from these results is that to impart the maximum laser-generated pressure the calculus must be close to the emission centre i.e. a gap of ~ 1 mm between the tip of the optical fibre and the surface of the calculus. However, at such close proximity there is also the possibility for the laser beam to vaporize a channel across the 1 mm gap and directly induce thermal damage to the calculus surface. Therefore, the action of the Ho:YAG laser will be a combination of pressure waves (mechanical action) and direct ablation (thermal action).

Calculi that are of friable material will be particularly susceptible to the pressure waves and may breakup from the action of the impulse. Hard calculi will be less affected by the pressure transient or even not at all, but will be disintegrated as a result of the direct ablation action (Schmidt-Kloiber, 1991).

5.11 Variation of pressure amplitude with laser pulse energy

For a given hydrophone to emission centre separation it would be expected that the peak shockwave intensity increases with laser pulse energy. This was investigated by recording pressure versus pulse energy at a distance of 25 mm for the Nd:YAG laser, and at 5 mm for the Ho:YAG laser. The greater distance for the Nd:YAG laser was required because of the substantial pressures generated at high pulse energy which at 5 mm saturated the transient recorder and also were liable to damage the hydrophone.

5.11.1 Nd:YAG laser

For the focussed Nd:YAG laser, the pressure amplitude in water was measured for a set of pulse energies. The energy was varied by changing the high voltage setting of the power supply unit of the laser. This was pre-calibrated and the laser energy values were read directly from the instrument dial. As expected, and shown in the graph in Figure 5.50a, the pressure increased with laser pulse energy as predicted. The measured

pressure increased from approximately 1 MPa at ~ 13 mJ of laser energy to 9 MPa at ~ 90 mJ of laser energy i.e. an increase in pressure by a factor of ~10 for a similar 10-fold increase in laser pulse energy. The trend, however, was not linear across this range of pulse energies.

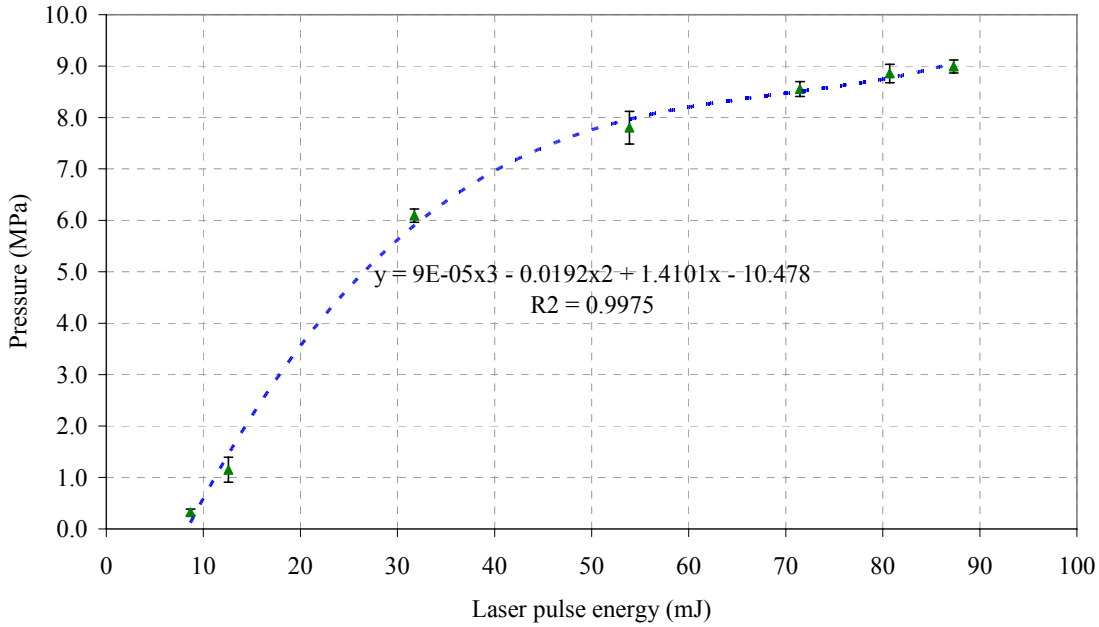

Figure 5.50a: Variation of Nd:YAG laser-induced pressure pulse with laser energy (laser 6 ns, 5 Hz, measured at 25 mm, n = 100)

The data plot shows an initial approximately linear pressure rise with pulse energy which then falls off to a less steep gradient. At the higher energies the reduced rate of increase of pressure suggests a saturation effect with regards to pressure generation. More laser pulse energy does not appear to be proportionately as effective at generating greater pressures as would be expected from a linear relationship i.e. larger steam bubbles.

A possible explanation is that the larger steam bubbles formed with the higher energy laser pulses are less stable and collapse before they have reached their maximum size. However, although the previous measurement on bubble lifetime showed a trend towards slightly shorter lifetimes at higher pulse energies, the relationship was found to be linear which suggests this is not the case.

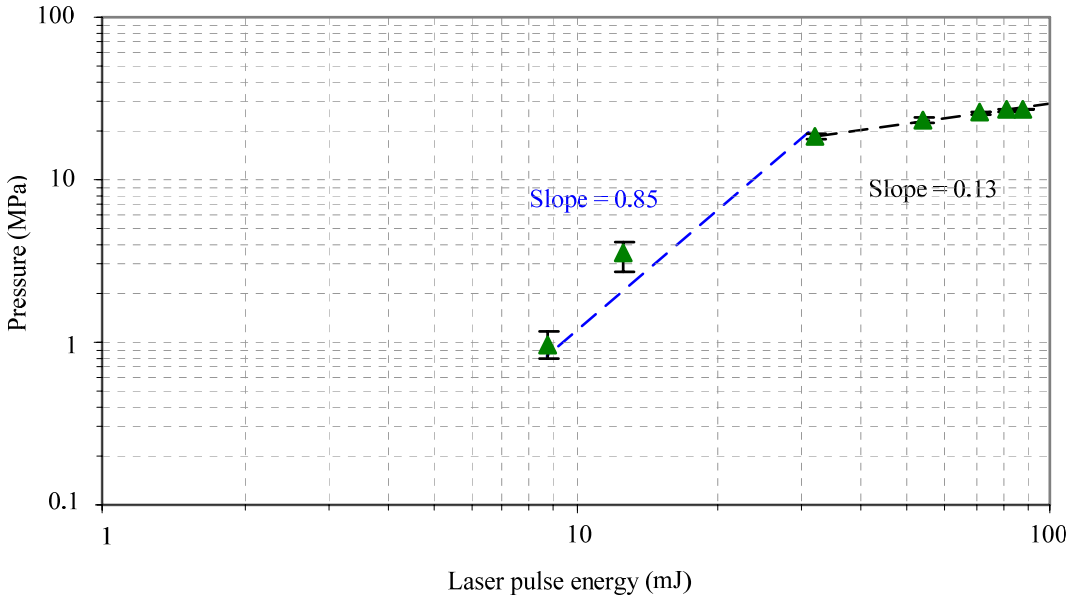

Figure 5.50b: Logarithmic plot of variation of Nd:YAG laser-induced pressure pulse with laser energy (laser 6 ns, 5 Hz, measured at 25 mm, n = 100)

At pulse energies above ~ 50 mJ the increase in pressure for each 10 mJ increment is approximately 0.04 MPa. Thus it would require a pulse energy of greater than 1 J to increase the pressure by approximately 1 MPa. This is a rather small gain for a substantial increase in laser pulse energy, and suggests that increasing pulse energy is not an efficient way of generating greater pressures with the Nd:YAG laser. This is therefore a limiting factor.

A measure of the efficiency of the Nd:YAG laser energy in generating "pressure" was taken as the ratio of the pressure amplitude to the laser energy i.e. MPa per J. The optimum laser pulse energy value was in the region below saturation. In this case, a 32 mJ laser pulse was approximately at the limit of the region of proportionality, and gave a pressure pulse of ~ 6.1 ± 0.1 MPa.

Using the pressure vs distance relationship derived in 5.10.1 the pressure at 1 mm was estimated to be ~ 11 MPa which gave laser energy to pressure "efficiency" measure of ~ 340 MPa J^{-1}. The pulse to pulse variation in the pressure pulses was < 5 %, indicating a reliable shockwave formation process.

5.11.2 Ho:YAG laser

The pressure dependence on laser pulse energy for the Ho:YAG is shown in Figure 5.51. It was found to have a different trend to that for the Nd:YAG laser, although the error bars make an accurate determination of trend less certain (the error bars are derived from the standard deviation of ~ 100 measured pulses). The rise in pressure does not show a well-defined plateau effect at higher laser pulse energies. The dependence, as expected, is in conformity with the trend that it is approximately linear with laser pulse energy, in comparison linear at the lower end of the energy scale (10 mJ – 45 mJ) for the Nd:YAG laser excitation.

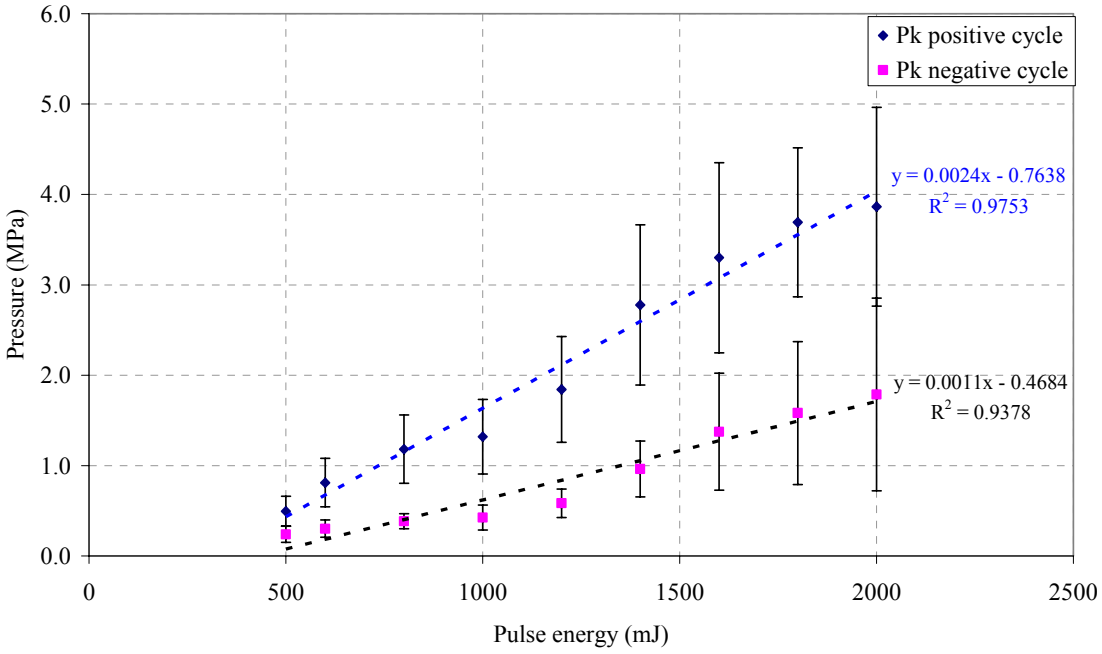

Figure 5.51: Variation of Ho:YAG laser-induced pressure pulse with laser energy (laser 10 Hz, 300 µs, measured at 5 mm, n = 100)

Across the range of pulse energies investigated, the peak positive pressures increased by a factor of 7, which is a comparable increase to that with the Nd:YAG. The peak negative pressures also showed a trend of increasing with laser pulse energy, but at a lesser rate of increase. Therefore, the waveform of the pulse would appear to be changing at higher laser energies in that the ratio of peak positive to peak negative pressures is increasing.

The difference between the Ho:YAG and the Nd:YAG pressure versus laser pulse energy trends are, as indicated with other parameters, likely to be a result of different interaction mechanisms and bubble dynamics. The indication is that to achieve the maximum mechanical destructive power with the Ho:YAG laser, the laser pulse energy should be set to a high value.

For example, a laser pulse energy of around 1.6 J gave a pressure amplitude of 3.3 ± 1.0 MPa. Correcting this value to 1 mm distance using the relationship given in 5.10.2 and the ratio of pressures for 1 J to 1.6 J shown in Figure 5.53 gives a predicted pressure of 125 MPa and therefore an estimated "efficiency" measure of ~ 78 MPa J^{-1}.

Compared to the Nd:YAG laser which gave a value of ~ 340 MPa J^{-1}, the Ho:YAG laser is significantly less efficient at converting the laser pulse energy to shockwave pressure. Furthermore, the greater variability in pressure values with the Ho:YAG laser of ~ ± > 25% suggests the shockwave formation process is also less reliable, suggesting the Nd:YAG to be a better choice in that respect.

5.12 Variation of pressure amplitude with laser pulse duration

The laser pulse duration could be varied on the Ho:YAG laser and the effect of changing this parameter on the recorded pressures was investigated. The Nd:YAG laser had a fixed pulse duration and therefore was not used for this experiment.

Data on the pressure amplitudes for various laser pulse durations (but with the same pulse energy) were recorded and plotted in Figure 5.52. It is seen from the graph that pressure increases with laser pulses of shorter duration. Across the range of pulse durations investigated (160 μs to 800 μs) the peak pressures increased by a factor of 15. Thus there is a strong dependence of laser-induced pressure pulse on the pulse duration of the laser.

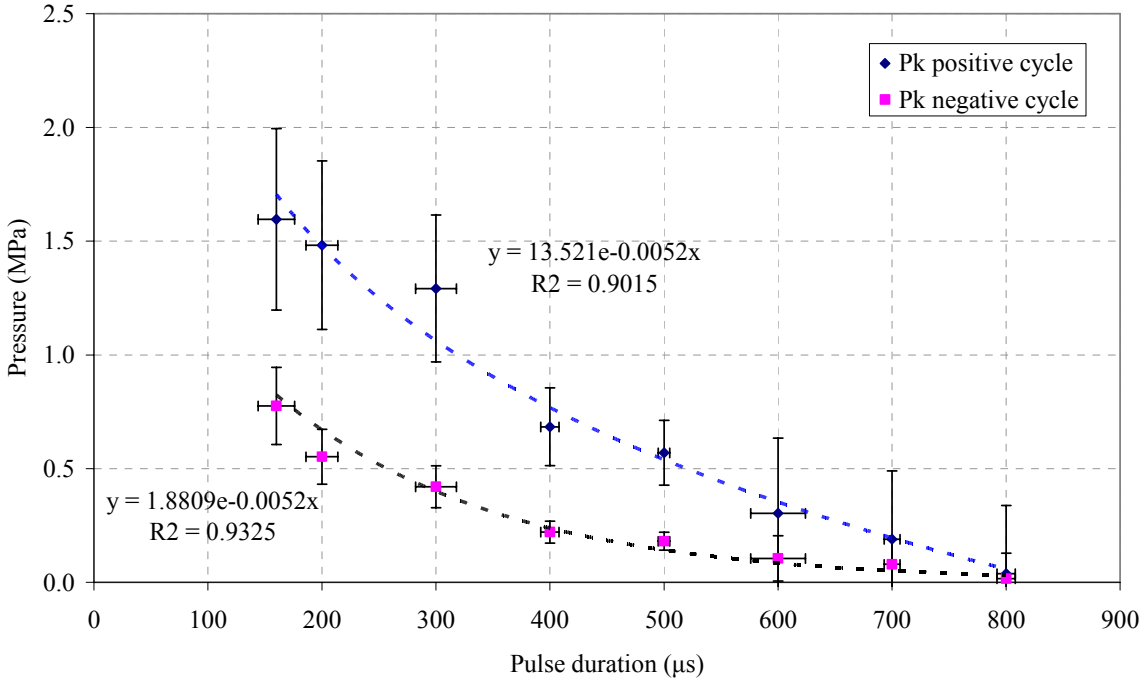

Figure 5.52: Ho:YAG laser-induced pressure pulse with laser pulse duration (laser 1 J, 10 Hz, measured at 5 mm, n = 100)

The effect of pulse duration on pressure is, as with other parameters, likely to be linked to the bubble dynamics. In addition to the effect of the laser pulse vaporising the far side of the steam bubble (which has been described previously) the bubble size and shape may also be linked to the confinement of the laser energy. With longer pulse duration there is more time available for conduction of the heat energy into the surroundings. Therefore, some laser energy is lost and there is less energy for the vaporization of the steam bubble, and the resulting pressure would therefore be lower. However, from the discussion in 3.3 this is not likely to be significant as the thermal diffusion time for the Ho:YAG laser is ~ 267 m sec, although there may still be local thermal effects.

The relationship derived from the data suggests that extrapolating to shorter pulse durations, for example in the region 1 – 10 µs, the peak pressures achieved are considerably higher. Using the formula for the best fit trendlines gives a peak positive pressure of ~ 13 MPa at 10 µs compared to ~ 1.5 MPa at ~ 150 µs i.e. an increase of approximately a factor of ~ 10. Peak negative pressures are similarly predicted to increase by a factor of ~ 10.

Extrapolation of this trend may not be accurate, however, as the bubble shape and dynamics will be changing as the pulse duration becomes shorter. The laser energy is thermally confined owing to the high absorption coefficient of water, and at sufficiently short pulse duration the mechanical energy becomes stress confined, and these situations would be expected to generate high acoustic pressures.

5.13 Variation of pressure amplitude with laser pulse frequency

The pulse repetition rate is an important parameter when considering the time taken to disintegrate a calculus, and it is also likely to have an effect on the dynamics of the pressure wave propagation. The effect of varying this parameter on the resulting pressure amplitude was investigated for both lasers.

5.13.1 Nd:YAG laser

The results for the effect of pressure with variations in pulse repetition rate across the range 1 – 20 Hz is shown in Figure 5.53. It was found that increasing the pulse repetition rate reduced the peak pressure, by up to 10 %. The effect was most significant for the highest laser pulse energy of ~ 87 mJ.

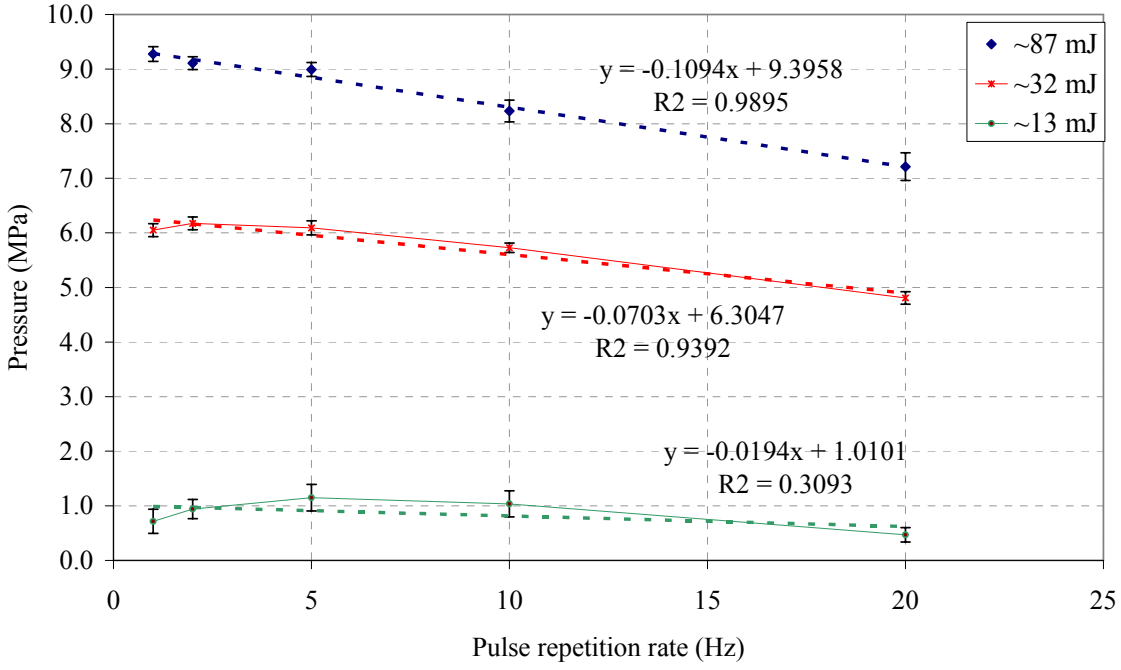

Figure 5.53: Nd:YAG laser-induced pressure pulse with pulse repetition rate (laser 6 ns, measured at 25 mm, n = 100)

The decrease in peak pressure with pulse frequency was also apparent for a pulse energy of 32 mJ, but insignificant at ~ 13 mJ which was the lowest laser energy investigated. Overall, the reduction in laser-induced pressure with pulse rate for the Nd:YAG laser is relatively small, and so in practice the benefits of speed i.e. operating the laser at the highest pulse rate, may outweigh the marginal decrease in peak pressure.

The decrease in pressure may be due to several possibilities. The first possibility is that the increased average power of the laser beam into the irradiated volume will cause a greater temperature rise and this may have an effect on bubble formation and dynamics. Another effect is that the time interval between laser pulses may be too short to allow fragments and micro bubbles from the previous shock to disperse out of the propagation volume. The presence of debris and micro bubbles will lead to acoustic attenuation as described previously. The reduction in pressure with pulse repetition rate becomes more significant with greater laser pulse energy, which is consistent with the effect being due to micro bubbles, calculus fragments, and possibly thermal effects, as these are all enhanced at higher laser pulse energy.

5.13.2 Ho:YAG laser

For the holmium laser there was no observed effect seen on the peak pressure with the variation of the pulse repetition rate. The same trend may be present but is masked by the large uncertainties which arise from the spread in pressure values recorded at any given laser setting from the inconsistency of the pressure pulse.

5.14 Effect of metal ions on pressure amplitude (plasma seeding)

The possibility of altering the properties of the liquid (i.e. water) to enhance the peak pressure was investigated. Where the pressure wave production is a plasma mediated process the introduction of free ions into solution may permit a reduction in optical breakdown threshold. If that is possible, plasma may be initiated at lower laser energy and therefore more laser energy is available for generating a steam bubble, and thus pressures would be expected to increase. The effect of spiking the water with different metal ions was investigated for both the laser wavelengths and described as follows.

5.14.1 Nd:YAG laser

Deionised water was spiked with the addition of NaCl and Fe_2Cl_3 separately at different concentrations. Concentration levels used were 0.9 %, 5 % and 10 % of NaCl and 1 %, and 2.5 % of Fe_2Cl_3. Solutions, thus produced, were tested for laser-induced pressure pulse generation. The results for the Nd:YAG laser are shown in Figure 5.54. It was found that relative to deionised water it was possible to raise the peak pressure generated for a given laser pulse energy by adding iron chloride or sodium chloride.

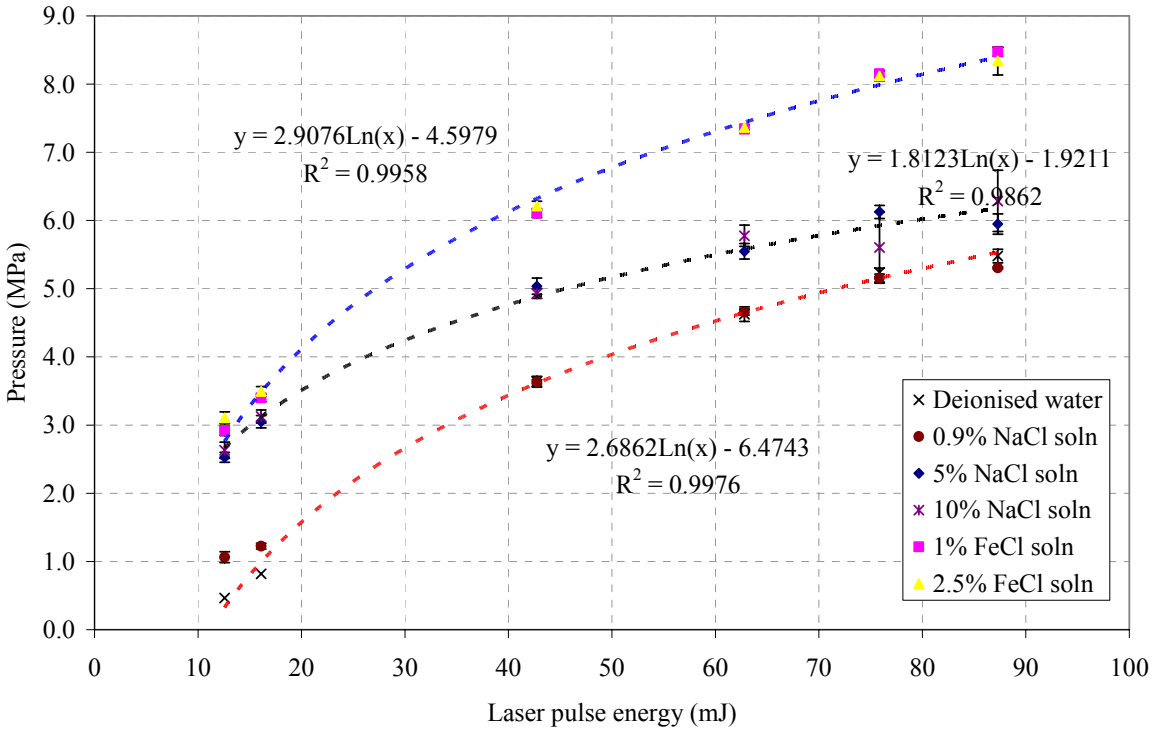

Figure 5.54: Effect of adding salts on Nd:YAG laser-induced pressure pulse (n = 100)

Sodium chloride solution showed an ability to increase the pressure but only in high concentrations. Physiological saline, which has a concentration of 0.9 % sodium chloride by weight, showed relatively little enhancement over deionised water. Concentrated solutions of 5 % and 10 % NaCl increased peak pressures by at least 1 MPa, with the greatest increase seen at lower laser pulse energy.

At the lowest laser energy investigated, which corresponded to the threshold for breakdown in deionised water, the pressure was increased from ~ 0.5 MPa to

approximately 2.5 MPa with 5 % NaCl. At the top end of the range, a laser pulse energy of around ~ 90 mJ generated a peak pressure of 6 MPa with 5 % NaCl compared to ~ 5.5 MPa in deionised water.

These substantial gains in pressure with added NaCl are confirmation that the pressures are generated as a result of an optical breakdown process and plasma formation. However, the concentration of NaCl required to enhance pressures is significantly greater than the concentration of saline solution used for medical purposes. For this reason, 5 % and 10 % solutions are unlikely to be suitable for lithotripsy purposes.

The greatest enhancement in pressure was exhibited by the addition of Fe^{3+} into solution. Concentrations of 1 % and 2.5 % Fe_2Cl_3 were used for these experiments. For a laser pulse of ~ 90 mJ the pressure was increased by a factor of nearly 2. Across the range of laser pulse energies tested there was pressure enhancement at all energies. There was no significant difference between the pressures generated with 1 % and 2 % Fe_2Cl_3 solutions, suggesting that it might be possible to reduce the concentration further and still maintain the enhancement in pressure. Reichel et al (1991) reported an effect at 0.02 mmol L^{-1}, which is equivalent to a 0.03 % solution. There may also be the possibility that Fe_2Cl_3 solution in low concentrations may be physiologically compatible.

Similar to the effect of sodium chloride solution, the greatest effect with the addition of Fe_2Cl_3 was seen at the lowest laser pulse energy. Again, this is likely to be at or near the breakdown threshold for deionised water, hence the substantial gain in pressure at this energy.

5.14.2 Ho:YAG laser

In contrast to the findings with the Nd:YAG laser, adding sodium chloride or iron chloride into solution did not provide any improvement in the shockwave pressures generated with the holmium laser. A range of solution strengths were investigated and the data on the amplitudes of the pressure pulse against the concentration of the metal ions (NaCl and Fe_2Cl_3) are plotted in Figure 5.57. In both the cases the resulting

pressures were less than the equivalent pressures in deionised water with the experimental laser. Again, the error bars are significant and it is not possible to say with certainty that the effect is present at all.

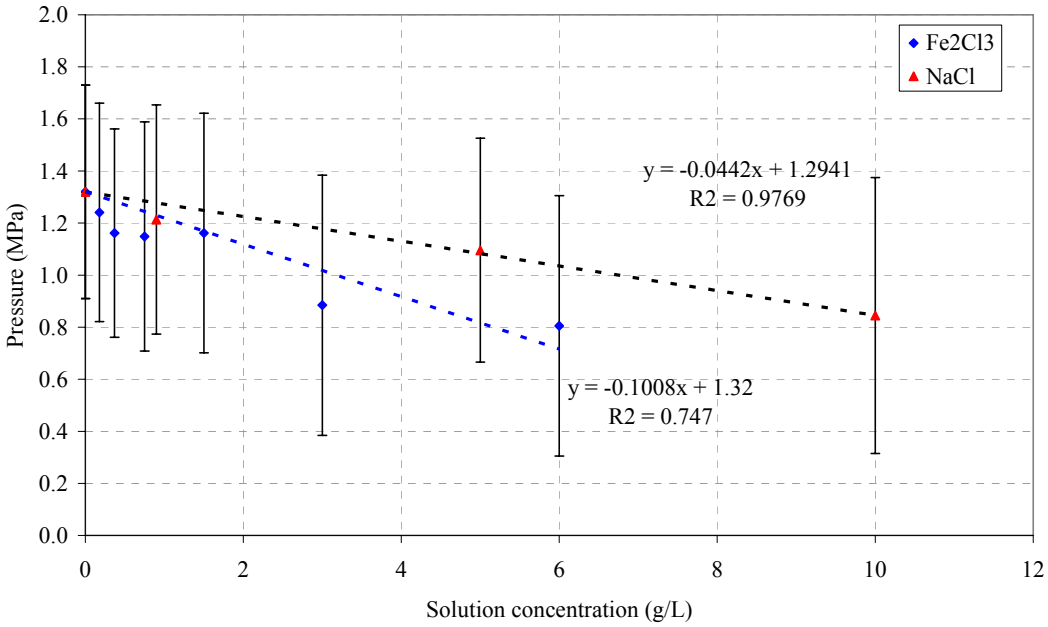

Figure 5.55: Effect of adding salts on Ho:YAG laser-induced pressure pulse (laser 1 J, 300 μs, n = 100)

A possible explanation for this is that the fibre appeared to be more susceptible to damage in these solutions i.e. the solution has a corrosive effect, thereby reducing the output laser energy, which would indicate a lower pressure. To avoid this effect on the measurements the fibre end was re-polished on a frequent basis to avoid the energy falling by more than 20 %. These observations are consistent with there being no plasma formed with the Ho:YAG laser.

The preceding work has revealed that the laser interaction processes are different for the Nd:YAG and Ho:YAG lasers. In both cases significant thermal effects were apparent and pressure pulses detected, however, the interaction process with the Q-switched Nd:YAG laser was plasma mediated. Plasma was evident in water and also on calculus material, whereas, for the holmium laser there was little evidence of a plasma formation even at the highest available laser output or with the introduction of free ions into solution. The Nd:YAG laser, therefore, could potentially be used for laser induced

breakdown spectroscopy of calculi samples. This was investigated in the following section.

5.15 Elemental analysis by LIBS

Focussing the high peak power Q-switched Nd:YAG laser onto calculus samples creates a plasma once optical breakdown has been exceeded. From previous experiments it was found that this could be achieved with laser settings of 25 mJ and 20 Hz. The optical emission from the plasma could then be analysed to identify the elements present, a technique known as laser induced breakdown spectroscopy (LIBS).

The optical emission from laser induced plasma on solid material contains an intense Bremsstrahlung emission superimposed with weaker characteristic emission lines at specific wavelengths from atomic excitations of the elements. These characteristic emissions follow the Bremsstrahlung radiation by a few microseconds delay. Therefore a gating method with a proper gate delay and gate width allows the excited atomic emission in the plasma environment to be detected without receiving or with little plasma Bremsstrahlung emission as a background.

From preliminary measurements it was found that a gate width of ~ 20 μs and a gate delay of ~ 3 μs with respect to the Bremsstrahlung emission were optimal parameters and were used to detect the signals of the atomic emission lines of the calculus samples. Throughout the LIBS measurements the Nd:YAG laser output was fixed and the samples were placed with the beam focussed tightly onto the surface via a 25 mm focal length lens.

The LIBS spectra of a selection of the urinary calculi samples were measured and analysed for elemental identification and for comparison of their concentrations. From a detailed analysis and comparison of the data with those obtained from the software database (Optical Emission Lines of the Elements, John Wiley & Sons, 2000) the elements identified in these samples included calcium (Ca), magnesium (Mg), strontium (Sr), sodium (Na), potassium (K), lead (Pb), chromium (Cr), copper (Cu), iron (Fe), manganese (Mn), aluminium (Al), zinc (Zn) and other trace elements.

The following are the LIBS results in three sections; preliminary broad spectral scans over the range 300 – 700 nm for the purpose of an overview of the emission peaks present and possible elements to investigate further. Secondly, LIBS investigation of specific peaks with high resolution and high sensitivity detector setting to home in on characteristic lines to confirm the presence of certain metals and to quantitatively estimate their concentrations in the analysed volume of the sample; and thirdly, results are presented from LIBS measurements using a high resolution broad scan system.

5.15.1 LIBS spectra of calculi samples

The following are the results of the LIBS measurements on selected calculi for the wavelength range 300 – 700 nm. These spectra were recorded using the OMA spectrograph to obtain an overview of the emission lines present across a broad range, in particular to include the strongest emission lines of the major metal elements such as calcium and magnesium. In order to measure across a wide range of wavelengths the instrument resolution and sensitivity was traded off against spectral range.

Sample 3

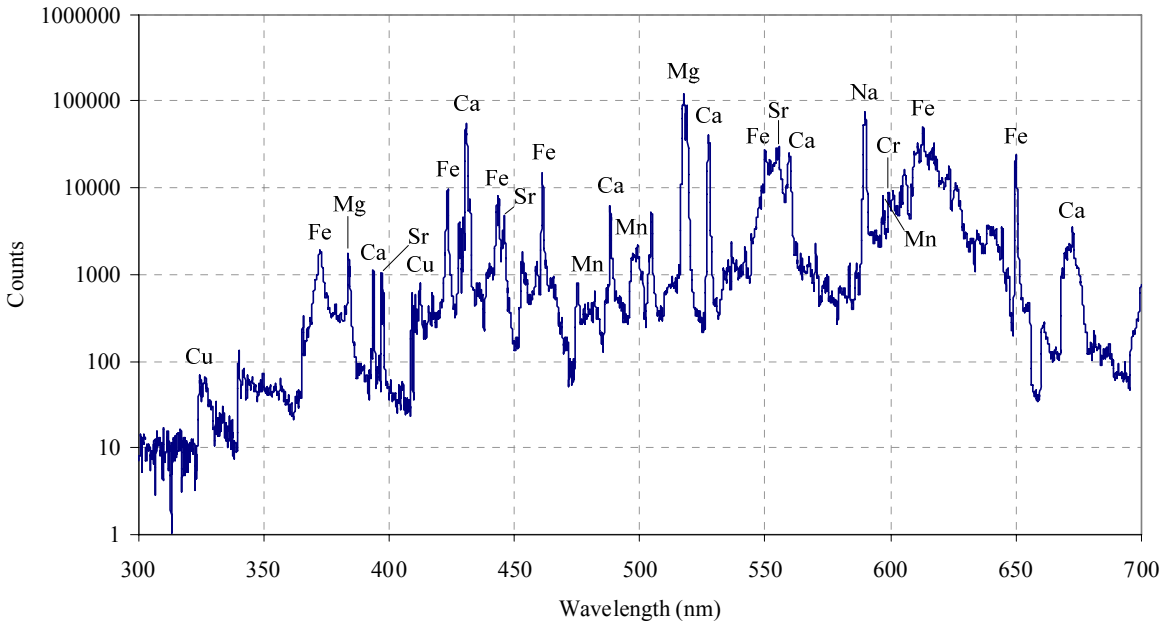

Figure 5.56: LIBS spectrum of a sample of magnesium ammonium hydrogen phosphate with calcium carbonate apatite

Figure 5.56 shows the LIBS spectrum obtained for sample 3, a composition of magnesium ammonium hydrogen phosphate (struvite) with calcium carbonate apatite. A number of peaks were found and by comparison with the reference database the following elements and their corresponding emission lines were identified: Mg at 383.8 nm, 517.26 nm and 518.36 nm, Ca at 393.5 nm, 394.0 nm, 430.77 nm, 487.8 nm, 527.0 nm, 559.8 nm and 672.6 nm, Na at 588.99 nm and 589.59 nm, Fe at 372.3 nm, 372.8 nm, 423.3 nm, 443.5 nm, 461.1 nm, 613.7 nm and 649.89 nm, Sr at 396.9 nm and 453.1 nm, Mn at 475.4 nm, 482.4 nm, 498.7 nm, 596.4 nm and 554.0 nm. Cr at 599.4 nm, and Cu at 324.8 nm and 412.3 nm.

Sample 4

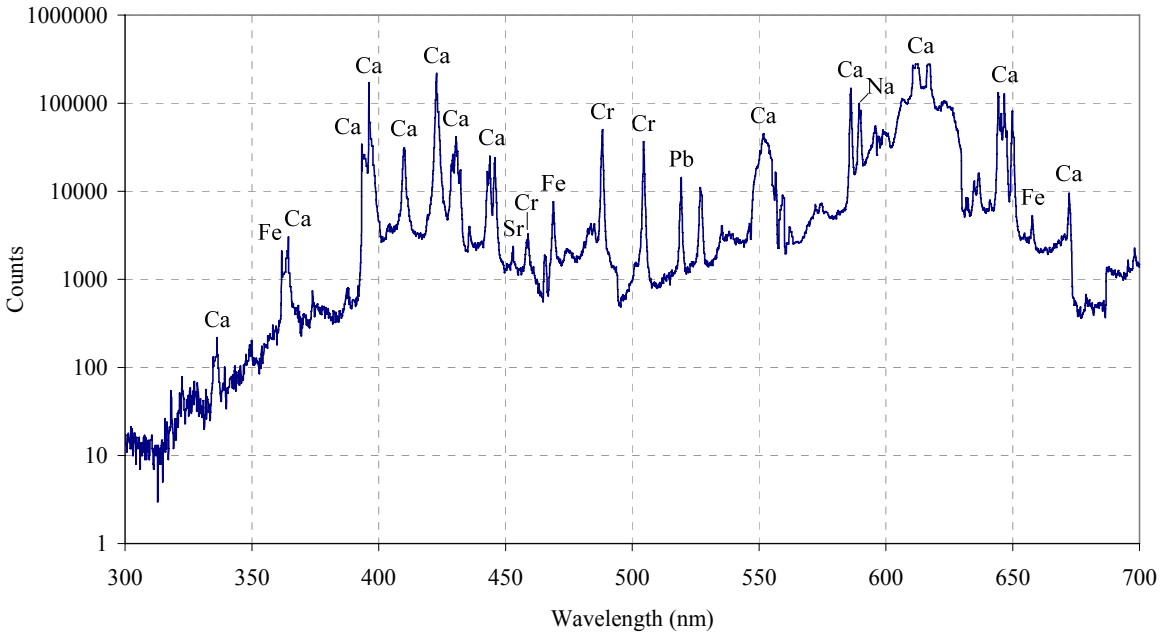

Figure 5.57: LIBS spectrum of a sample of calcium hydrogen phosphate dihydrate (brushite)

The LIBS spectrum shown in Figure 5.57 was obtained for sample 4, a composition of calcium hydrogen phosphate dihydrate (brushite). The strongest emission lines were identified as: Ca at 336.19 nm, 364.44 nm, 392.346 nm, 395.94 nm, 395.88 nm, 410.85 nm, 422.67 nm, 430.25 nm, 443.5 nm, 445.5 nm, 551.298 nm, 586.11 nm, 612.22 nm, 616.2 nm, 643.9 nm, 64.25 nm, 649.378 nm and 657.3 nm, Fe at 361.877 nm, 468.86 nm and 657.5 nm, Sr at 453.13 nm, Cr at 488.7 nm and 504.288 nm and possibly Pb at 520.14 nm.

Sample 5

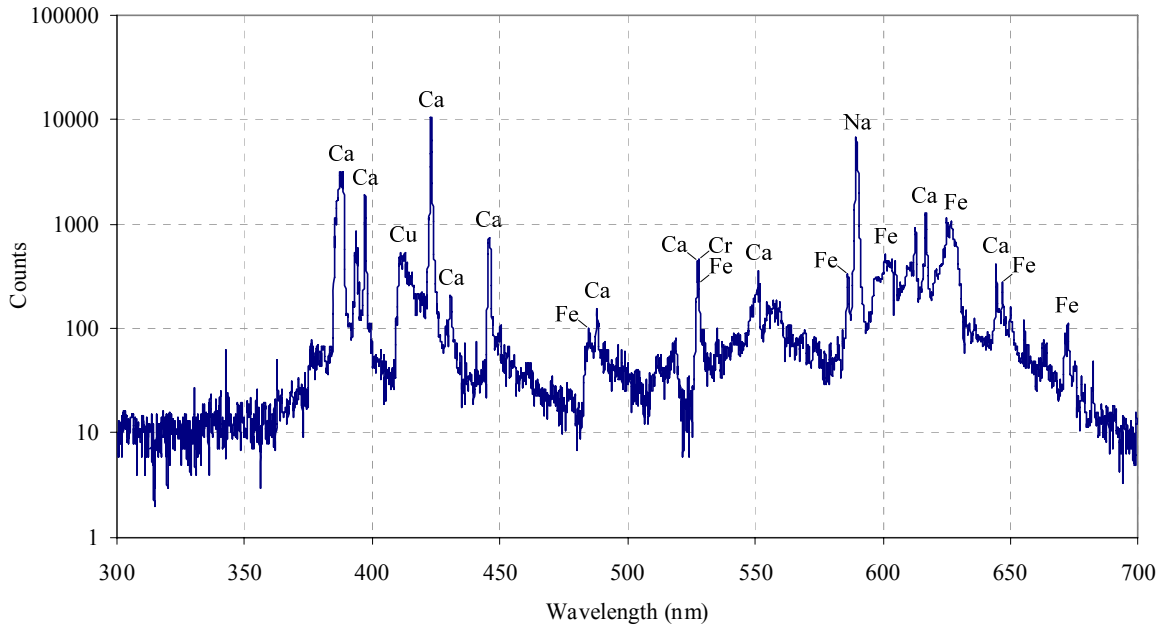

Figure 5.58: LIBS spectrum of a sample of cystine

Figure 5.58 shows the results for LIBS analysis of sample 5, which was previously determined to be a pure cystine calculus. The main peaks are identified as: Ca at 388.4 nm, 393.6 nm, 423.0 nm, 430.6 nm, 445.8 nm, 488.0 nm, 527.4 nm, 616.8 nm and 644.4 nm, Cr at 528.0 nm, Cu at 411.2 nm, Fe at 484.8 nm, 528.2 nm, 586.2 nm, 601 nm, 625 nm and 672.4 nm, and Na at 589.6 nm.

Sample 6

The LIBS spectrum for the sample of calcium oxalate dihydrate (COD) shows strong presence of calcium, as expected, and shown in Figure 5.59. Other metals identified include Mg, Cr, Fe, Na and possibly Pb. The main peaks are identified as Ca at 335.2 nm, 336.4 nm, 393.6 nm, 397.2 nm, 410.2 nm, 423.2 nm, 430.6 nm, 527 nm, 558.6 nm, 559.4 nm, 645.6 nm and 672.4 nm, Cr at 380.4, 488.2 nm and 599.6 nm, Mg at 383.8 nm, Fe at 410.2 nm, 448.8 nm, 479.0 nm and 657.8 nm. A peak that possibly corresponds to lead was identified at 506.6 nm.

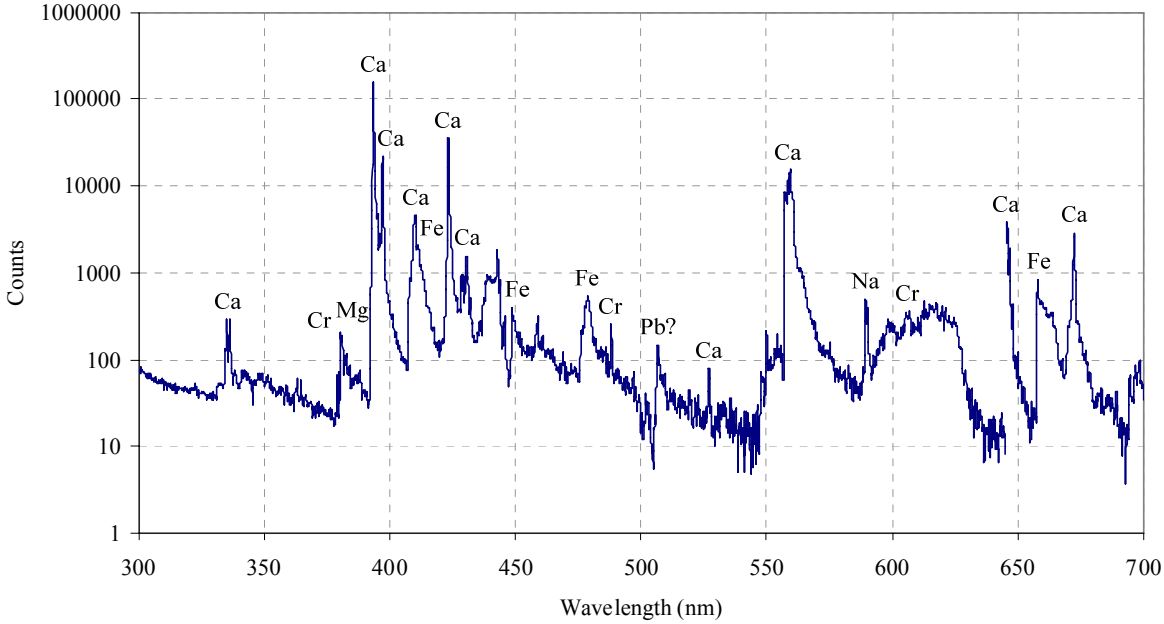

Figure 5.59: LIBS spectrum of a sample of calcium oxalate dihydrate

Sample 8

The LIBS spectrum for a calculus composed of COM is shown below, in Figure 5.60.

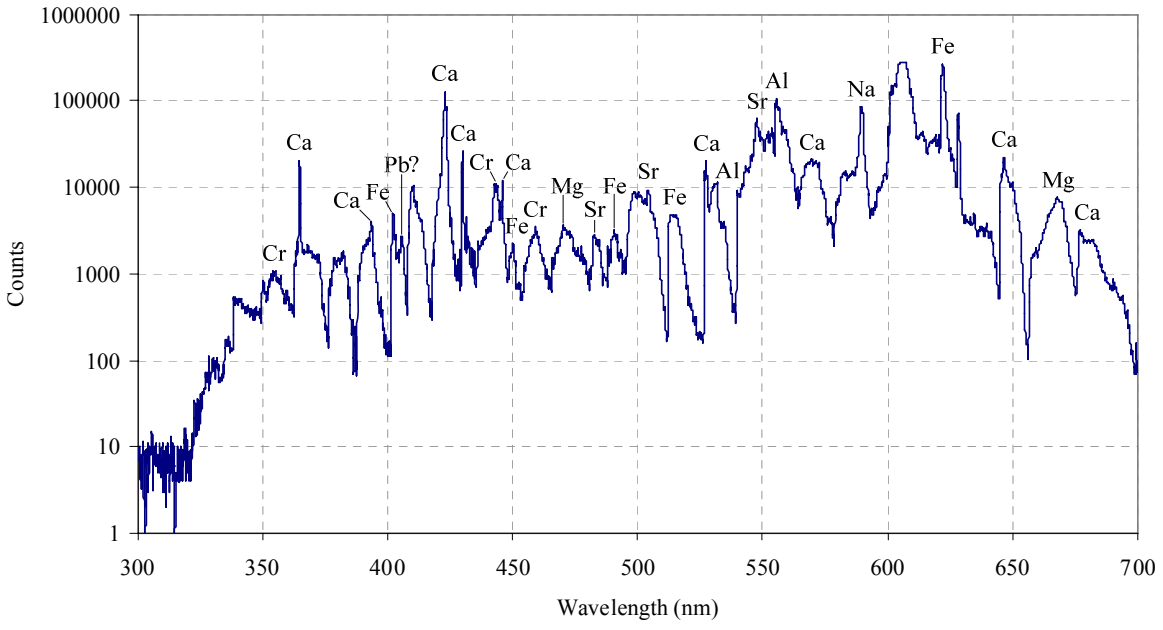

Figure 5.60: LIBS spectrum of a sample of calcium oxalate monohydrate

The metal elements are identified from the following peaks: Ca at 364.8 nm, 393.8 nm, 423.2 nm, 430.2 nm, 445.8 nm, 527.4 nm and 571.64 nm, Cr at 335.4 nm, 444.0 nm and 459.0 nm, Fe at 402.2 nm, 448.8 nm, 490.8 nm, 499.0 nm, 515.2 nm, 606.6 nm, 622.2

nm, 628.2 nm, 646.6 nm and 677.8 nm, Mg at 470.4 nm and 667.8 nm, Sr at 482.2 nm, 504.2 nm and 547.8 nm, Al at 532.0 nm and 535.8 nm, Na at 590.0 nm, and lead at 405.8 nm.

Sample 9

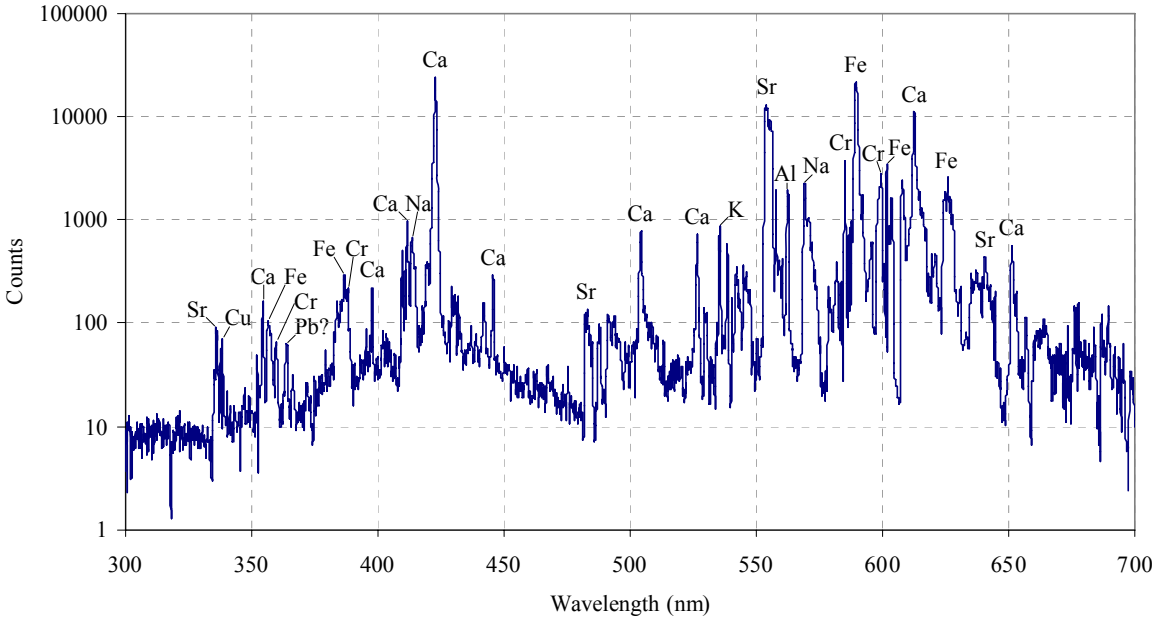

Figure 5.61: LIBS spectrum of a sample of uric acid calculus

For sample 9, a uric acid composition, the peaks were found to correspond to the following elements: Ca at 354.8 nm, 398 nm, 410.4 nm, 411.8 nm, 423.0 nm, 445.8 nm, 504.4 nm, 526.6 nm, 612.6 nm and 651.2 nm; Cu at 338.8 nm; Sr at 336.6 nm, 483.2 nm, 554.4 nm and 640.6 nm; Fe at 356.8 nm, 384.2 nm, 388.6 nm, 589.4 nm, 601.8 nm and 626.0 nm; Pb at 364.0 nm, Na at 569.2 nm; K at 536.0 nm; Al at 526.6 nm; Cr at 359.8 nm, 387.0 nm and 599.4 nm

Sample 10

The LIBS spectrum for a calculus composed of magnesium ammonium phosphate hexahydrate (struvite) is shown in Figure 5.65. Elements identified: Ca at 363.0 nm, 390.2 nm, 393.8 nm, 397.4 nm, 410.4 nm, 423.0 nm, 430.6 nm, 443.8 nm, 505.6 nm, 527.4 nm, 535.4 nm, 610.2 nm, 577.0 nm, 586.4 nm, 532.0 nm, 560.8 nm, 650.0 nm and 669.2 nm; Cr at 367.1 nm, 488.2 nm, 543.4 nm, 602.6 nm and 644.2 nm; Cu at 384.4

nm and 459.2 nm; Fe at 349.2 nm, 429.2 nm, 446 nm, 468.8 nm, 510.8 nm, 512.8 nm, 617.4 nm, 623.8 nm and 635.0 nm; K at 403.4 nm; Mg at 519.4 nm; Na at 569.2 nm and 589.4 nm; Sr at 365.4 nm and 453.2 nm.

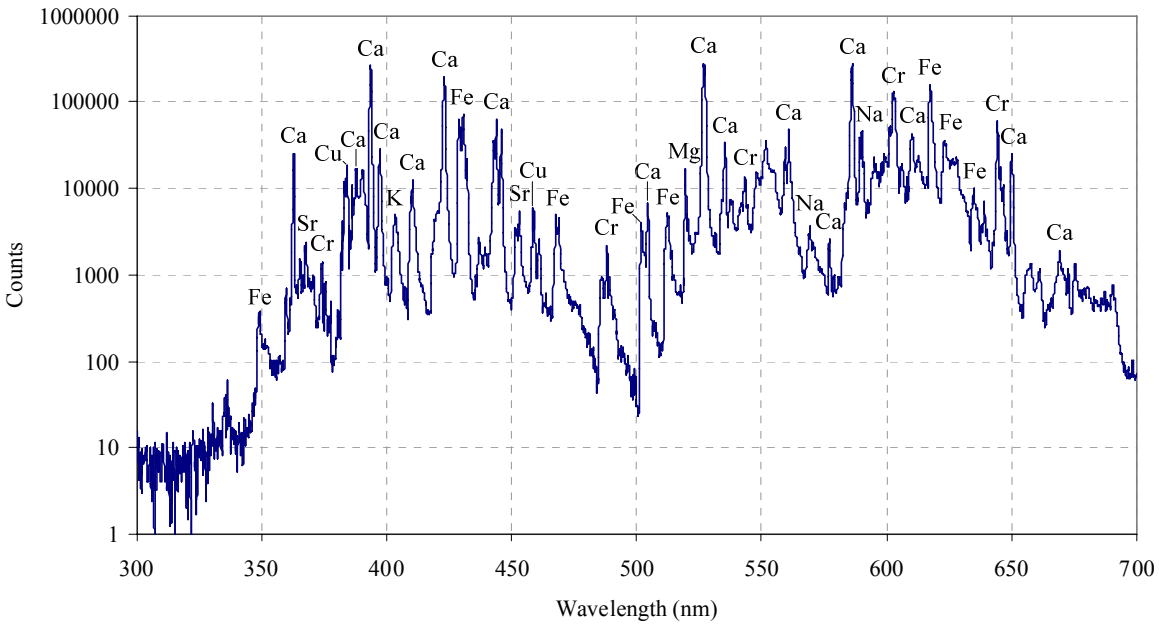

Figure 5.62: LIBS spectrum of a sample of magnesium ammonium phosphate hexahydrate (struvite)

The results show that the elements Ca, Mg, Na, Fe, Sr, Cr, Mn, Cu, Pb and Al have potentially been identified in the collection of calculus samples. Also the spectra appear to have differences in the intensities and peaks present.

The identification of calcium in the calcium type stones such as calcium oxalate monohydrate and dihydrate, and calcium hydrogen phosphate dihydrate is expected, however, calcium was found in all stone types including cystine and uric acid. The relative abundance of the element approximated from the signal intensities was in accordance with the calcium stones having the strongest calcium signal (~ 100,000 counts) and uric acid and cystine having slightly weaker signals (but in excess of 10,000 counts). The presence of calcium in all compositions suggests that calcium is readily incorporated in the stone matrix, and also that it is important in stone formation.

Magnesium was found, as expected, in the magnesium ammonium phosphate hexahydrate (struvite) stones in conformance with the chemical formula ($MgNH_4PO_4.6H_2O$). However, magnesium was possibly also identified in a calcium oxalate stone (sample 8) although the peak is not sharp and this may be a contribution from another element such as iron or chromium, as these metals were identified as possibly abundant in all of the samples measured.

Sodium was also identified in some of the samples and this may be due to its presence in urine, or if the calculus had at some stage been immersed in saline solution. The identification of copper, manganese and strontium is less certain, however, as the peaks are relatively weak and there is a significant level of noise in the data for all spectra. A possible emission line attributable to Pb was found in more than one sample, but this could be confused with calcium or iron peaks which are close to this particular wavelength. Furthermore, the resolution of the spectrograph was ~ 0.2 nm which is not ideal for identification and therefore makes it a more difficult task to confirm elements that are present in low concentration. For this reason some of the main peaks were analysed more accurately with optimised instrument parameters and this is reported in the next section.

5.15.2 Analysis of specific peaks

Further to acquiring spectra across a broad range of wavelengths, the spectrometer was set up to zoom in on a very narrow range of wavelengths in order to detect specific peaks. The purpose of this was to confirm the presence of certain elements that were identified in the previous set of experiments but with some uncertainty, and also to determine the elemental concentration.

As described in section 4.6, a photomultiplier/ gated charge integrator was used which allowed for high resolution (~ 0.01 nm) interrogation of the optical emission lines compared to the intensified diode array used in the previous experiments. The centre wavelength was set to a strong emission line of the element of interest, and an integrated signal of spectral width ± 4 nm was accumulated to obtain an intensity of around 100,000 counts. The laser output was optimised to generate a strong plasma

signal but without saturating the detector or causing excessive drilling action on the calculus surface. 25 mJ pulses at 20 Hz were found to be a reasonable compromise and gave consistent results on all calculi samples.

Calcium (457.9/ 458.1/ 458.6 nm)

Calcium had been shown to be present in all samples investigated in the previous section but had not been quantified in terms of elemental concentration. Therefore, an accurate determination of calcium intensity at a specific line emission, compared to that of a suitable reference sample exposed to the same laser ablation, would allow for a calibrated estimate of concentration (see Appendix D for further details).

Figure 5.65 shows the LIBS spectrum obtained for the calcium analysis of selected calculi. Strong Ca atomic lines at 457.9 nm, 458.1 nm and 458.6 nm were detected and having different signal strengths, for example, in Samples 4, 6 and 9. Sample 4, a calcium hydrogen phosphate dihydrate calculus (brushite) calculus, shows the strongest signal strength among these samples. Sample 6 is calcium oxalate dihydrate calculus and also shows a strong signal arising from the calcium rich composition, albeit a weaker signal than Sample 4. Sample 9 is composed of uric acid and has the weakest calcium signal which can be explained by the lack of calcium in the chemical form of pure uric acid.

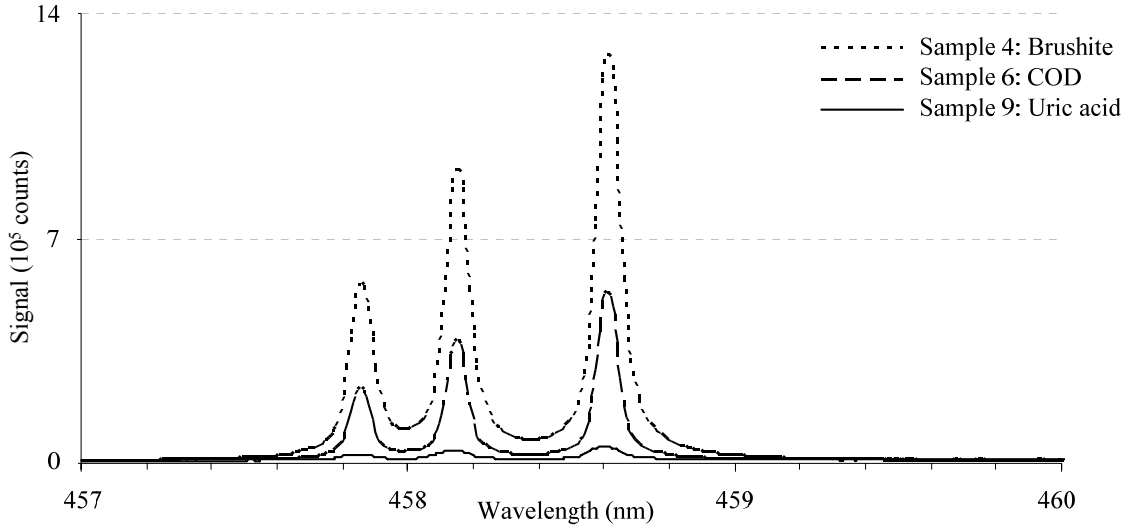

Figure 5.63: Calcium atomic emission lines of selected calculi samples at lines 457.9 nm, 458.1 nm and 458.6 nm

Sodium (589/ 589.6 nm)

Strong Na atomic lines at 589 nm and 589.6 nm were detected, as shown in Figure 5.66, for Samples 4 (calcium hydrogen phosphate dihydrate), 5 (cystine) and 10 (magnesium ammonium phosphate dihydrate).

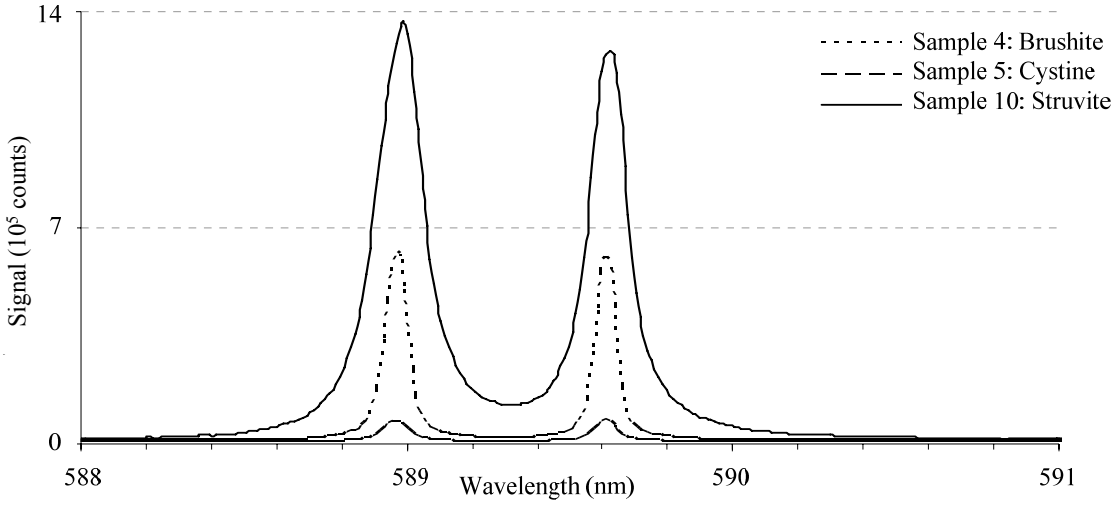

Figure 5.64: Sodium atomic emission lines of selected calculi samples at 589 nm and 589.6 nm

Magnesium (407.5 nm)

With relatively weaker signal strengths, the emission from Mg at 407.5 nm in different samples as shown in Figure 5.67.

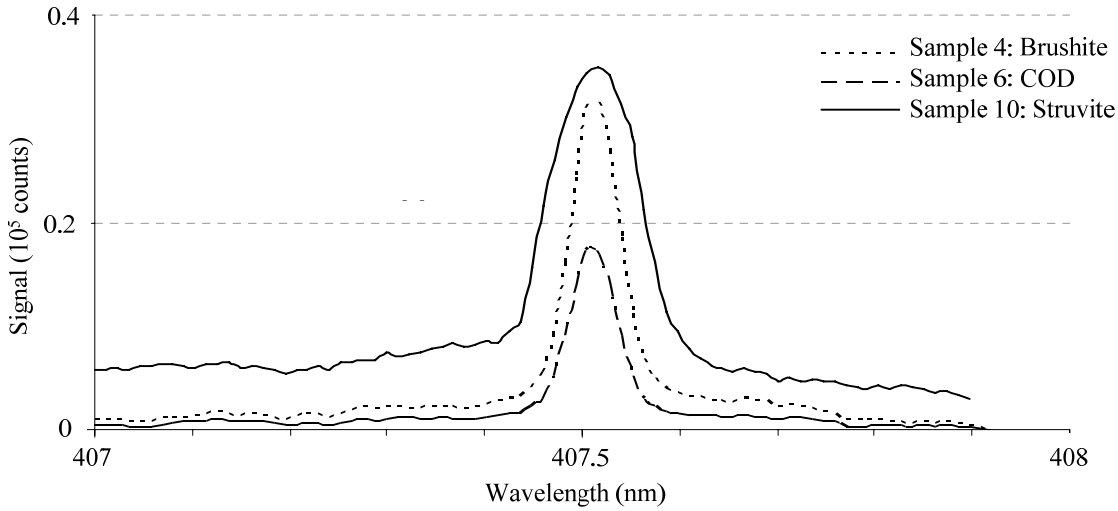

Figure 5.65: Magnesium atomic emission line of selected calculi samples at 407.5 nm

Strontium (460.7 nm)

Relatively weaker signals were observed at 460.7 nm from Samples 3, 4 and 10, indicating presence of strontium (Sr).

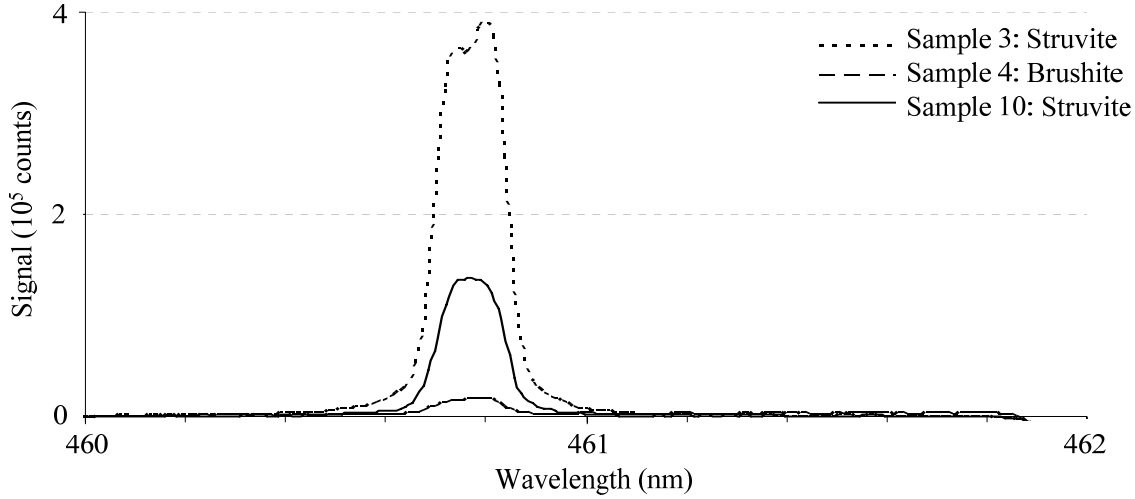

Figure 5.66: Strontium atomic emission line of selected calculi samples at 460.7 nm

Potassium (404.4/ 404.7 nm)

Relatively weaker signals were observed at 404.4 nm and 404.7 nm from Samples 3, 7 and 9, indicating presence of potassium (K) and an emission line from Samples 4 and 6 at 405.8 nm indicating the presence of lead (Pb), as shown in Figures 5.69 and 5.70 respectively.

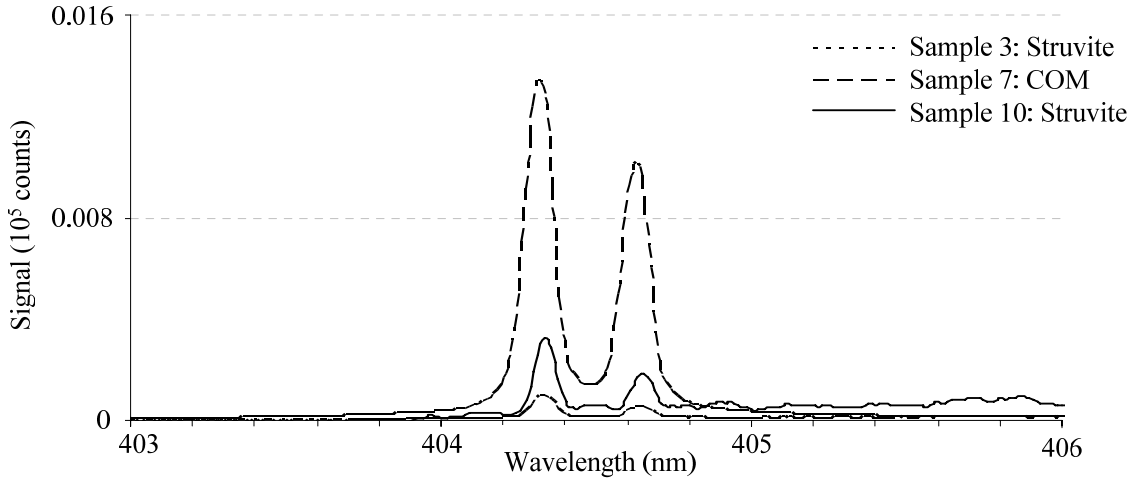

Figure 5.67: Potassium atomic emission lines of selected calculi samples at 404.4 nm and 404.7 nm

Lead (405.8 nm)

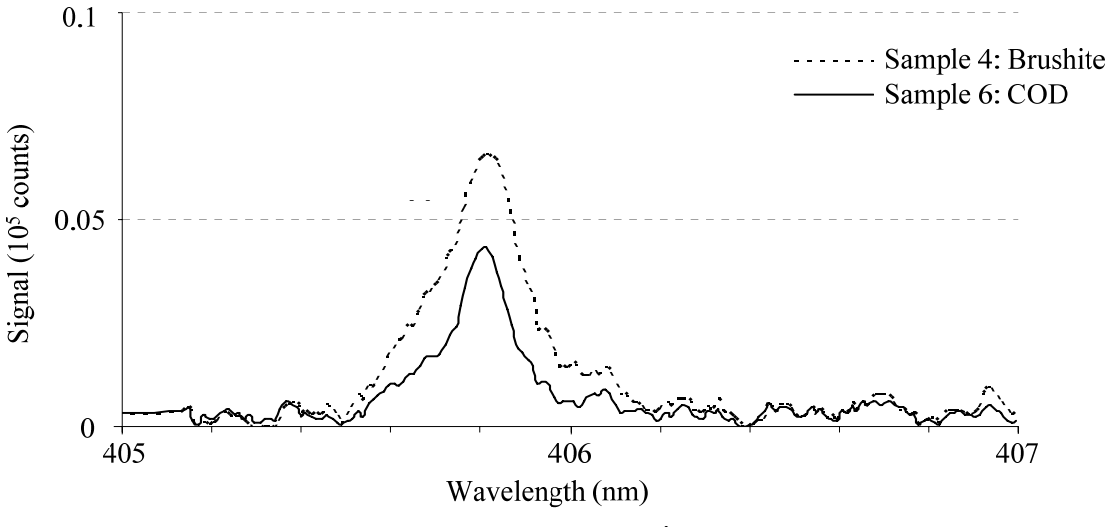

Figure 5.68: Lead atomic emission line of selected calculi samples at 405.8 nm

The concentrations of these metals in the urinary stone samples were indicated by the signal intensities of the atomic lines. Assuming linear calibrations for each element at its detected emission wavelengths, their elemental concentrations in all the samples were estimated as orders of magnitudes and listed in Table 5.11. At low values of the concentration, the above assumption of linearity with concentration is most likely to be valid. However, at higher concentrations, the signal intensities are expected to be non-linear and likely to saturate at some values of concentration of the species.

The relatively high concentrations of calcium present in all the samples correspond to their major constitute and the present estimation for Ca and Mg may have large error. However, such error due to saturation is expected to be negligible for other elements and the error due to monitoring methods is estimated to be less than 10 %.

Table 5.11: Elemental concentrations of the urinary stone samples measured with laser induced plasma spectroscopic techniques

Sample	Ca (%)	Mg (%)	Na (ppm)	Sr (ppm)	K (ppm)	Pb (ppm)
Struvite (3)	12	1	239	310	31	ND
Brushite (4)	36	7	596	14	ND	392
Cystine (5)	0.03	0.4	53	6	ND	ND
COD (6)	15	4	453	3	ND	224
COM (7)	10	2	320	9	460	ND
Uric acid (9)	0.3	ND	942	1	ND	ND
Struvite (10)	5	8	1218	107	117	ND

* ND: Not detected

Struvite (Sample 10) shows strong emission of magnesium line (407.5 nm) and therefore a relatively high concentration in agreement with its FT-IR identification of magnesium ammonium phosphate hexahydrate ($MgNH_4PO_4.6H_2O$) with a small amount of calcium carbonate apatite ($Ca_{10}(PO_4)_6CO_3$. However, high concentration of Mg in the brushite calculus (Sample 4) does not agree with the chemical composition identified as calcium hydrate phosphate dihydrate ($CaHPO_4.2H_2O$). From the results, it is observed that the samples of brushite and calcium oxalate dihydrate having significant amount of lead (Samples 4 and 6 respectively) contained relatively higher concentration of calcium. Although the chemical analysis of the samples did not indicate the presence of sodium in any of the samples, using LIBS to analyse the same samples has identified sodium in all of them. It is possible that the wet chemistry testing may have introduced sodium contamination.

5.15.2 Comparison with high resolution (Aryelle) system

LIBS spectra were obtained using a high resolution (± 0.004 nm) spectrograph having a broad spectral range of ~ 200 nm. Hence this system had the benefits of both sets of apparatus described above in that it was able to capture the whole range at high resolution and with a minimal number of laser pulses. This had the advantage of minimising the effect of the laser drilling a hole into the sample during data acquisition. The LIBS spectra are presented on the following pages.

Sample 1

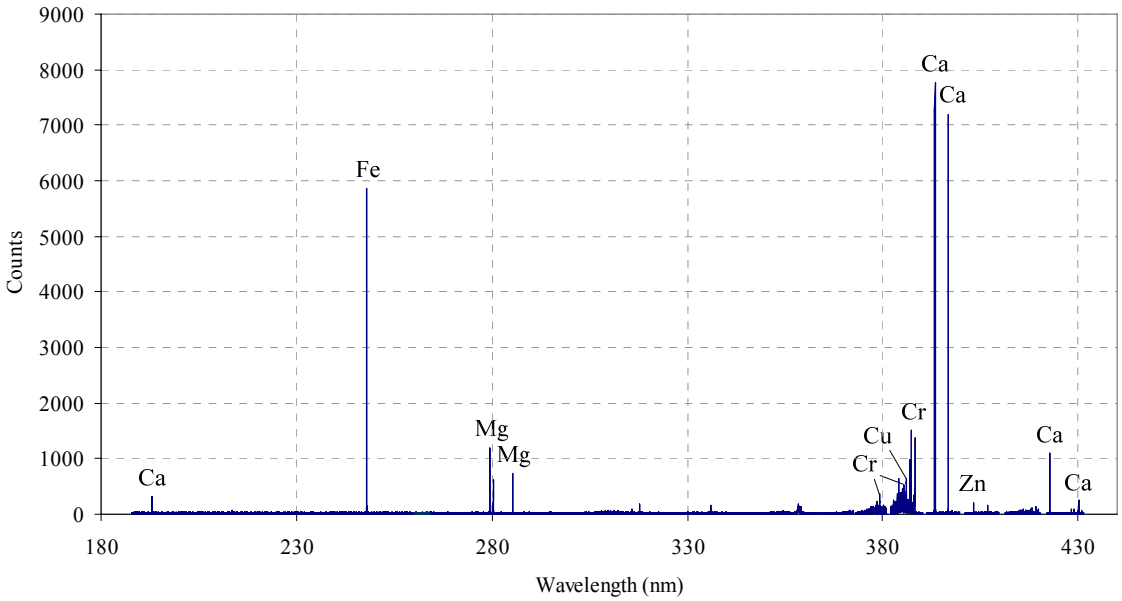

Figure 5.69: LIBS spectra for cystine calculus (Sample 1)

Sample 2

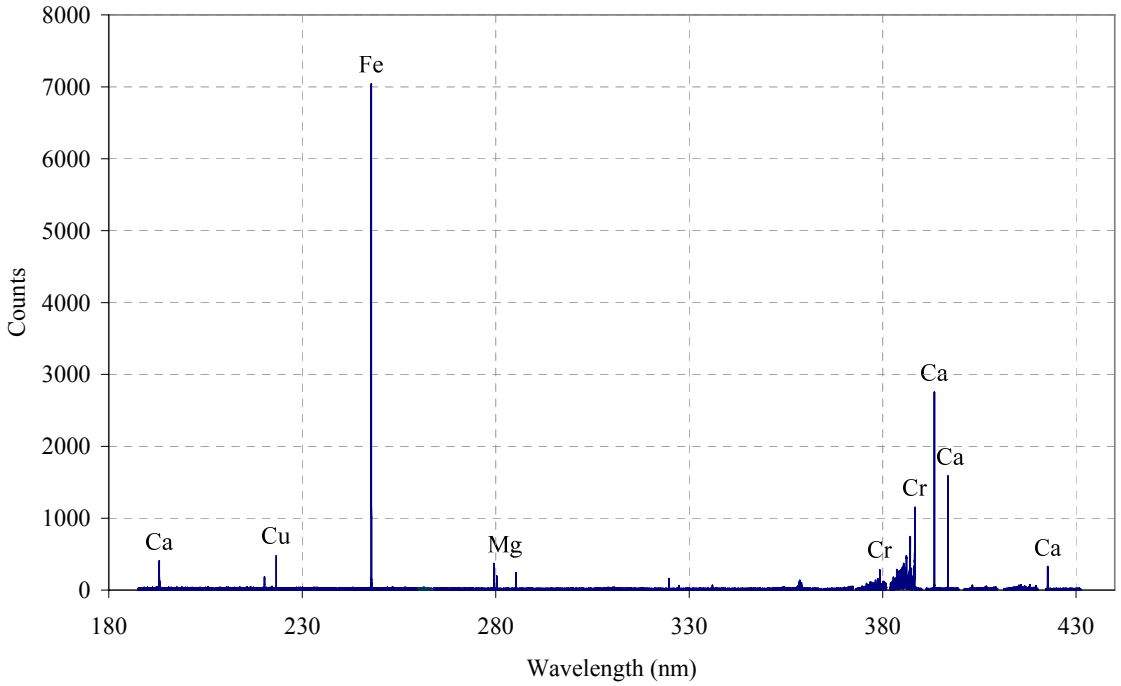

Figure 5.70: LIBS spectra for cystine calculus (Sample 2)

Sample 3

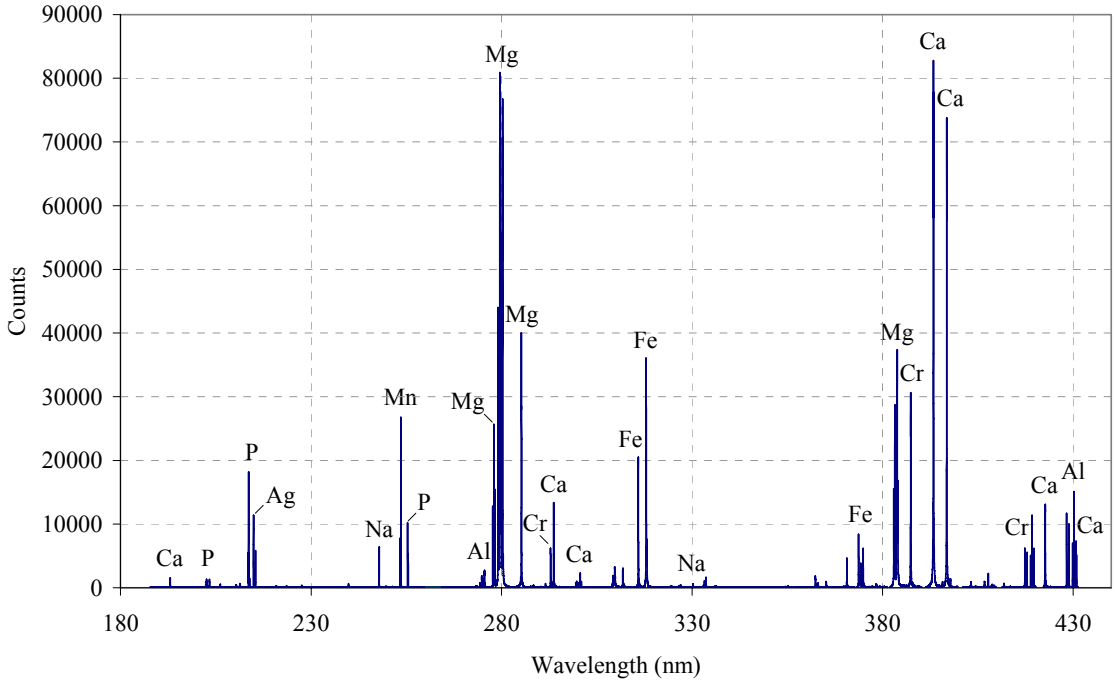

Figure 5.71: LIBS spectra for magnesium ammonium hydrogen phosphate with calcium carbonate apatite calculus (Sample 3)

Sample 4

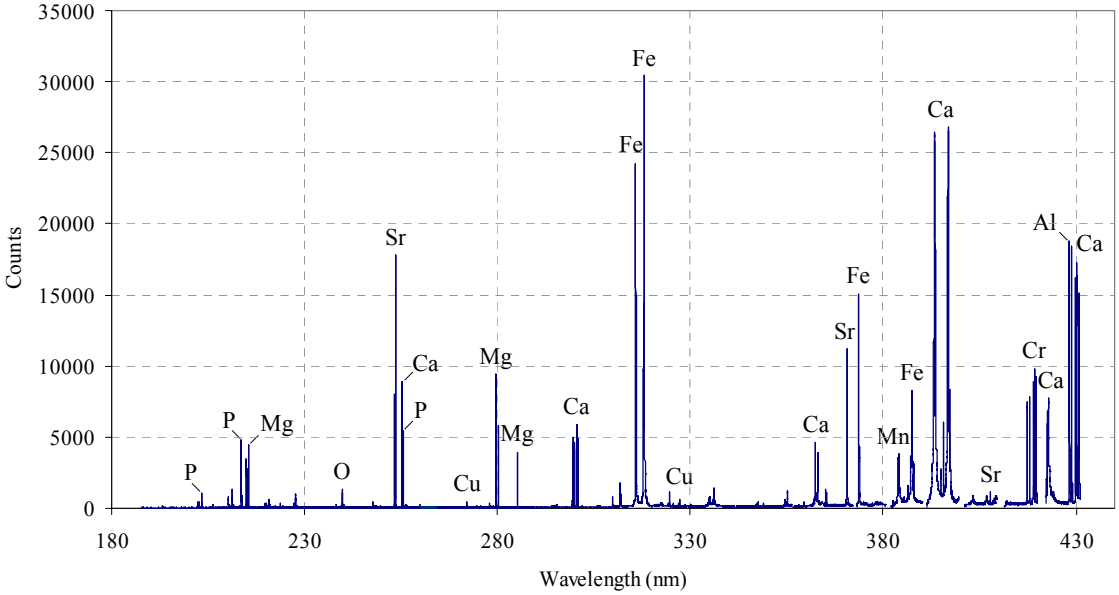

Figure 5.72: LIBS spectra for calcium hydrogen phosphate dihydrate calculus (Sample 4)

Sample 5

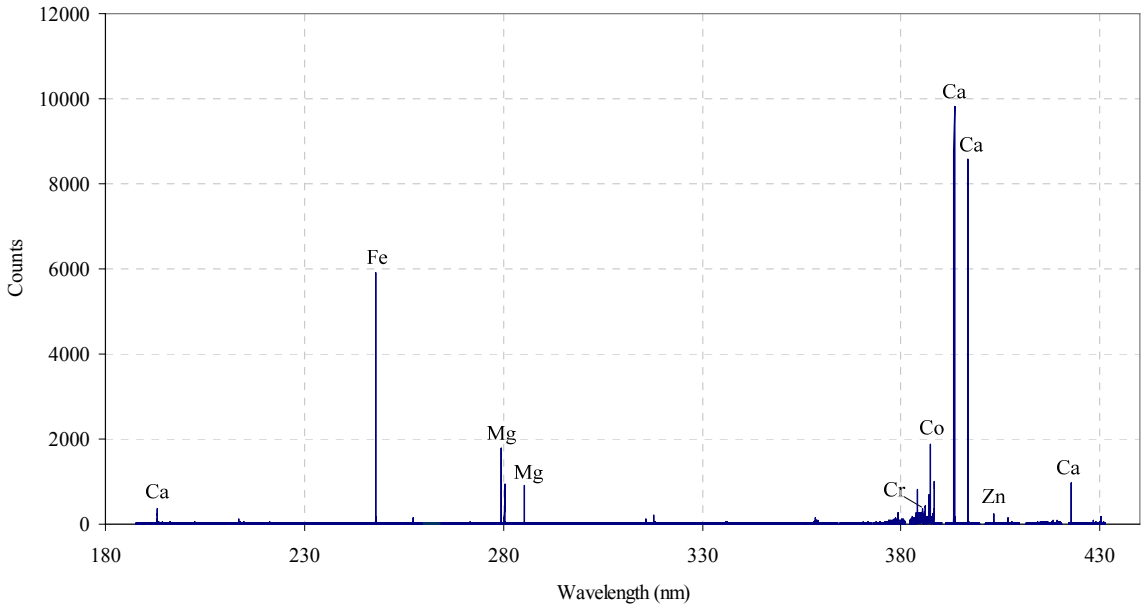

Figure 5.73: LIBS spectra for cystine calculus (Sample 5)

Sample 6

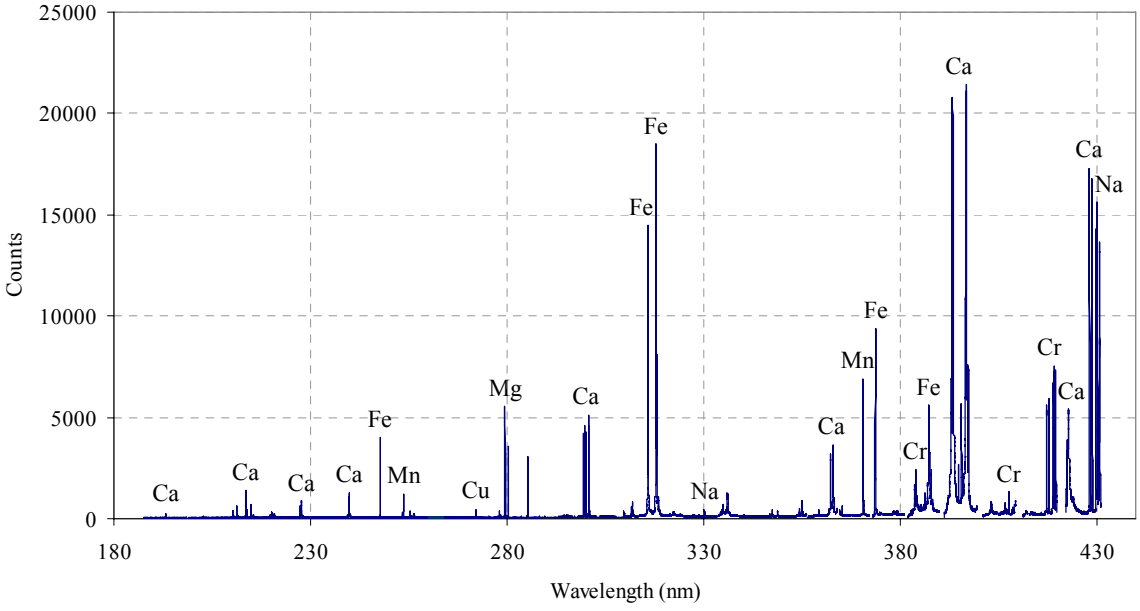

Figure 5.74: LIBS spectra for calcium oxalate dihydrate calculus (Sample 6)

Sample 7

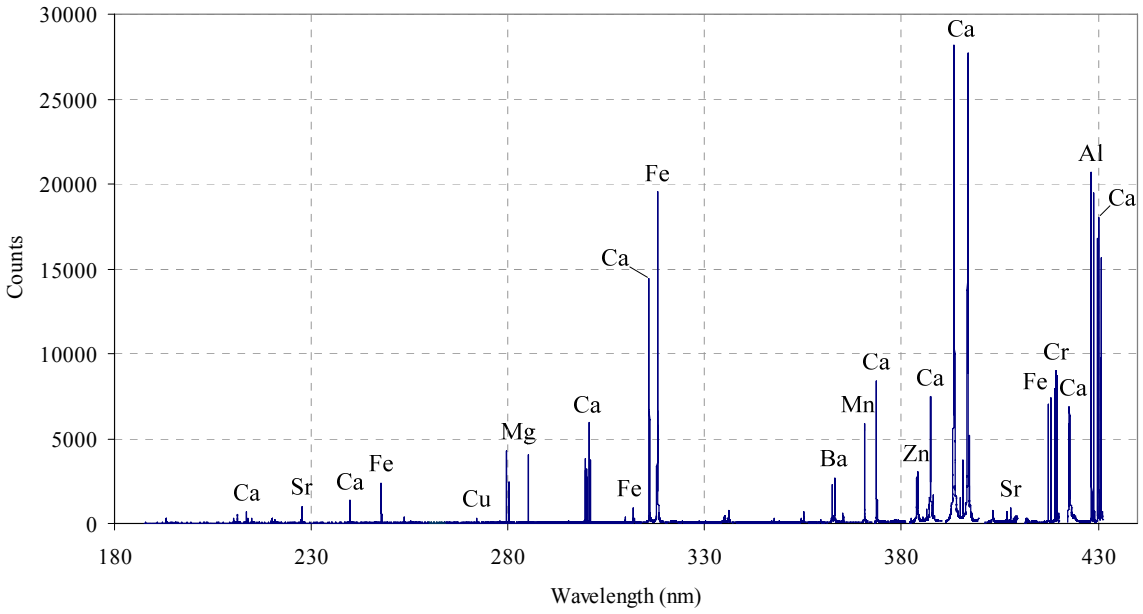

Figure 5.75: LIBS spectra for calcium oxalate monohydrate calculus (Sample 7)

Sample 8

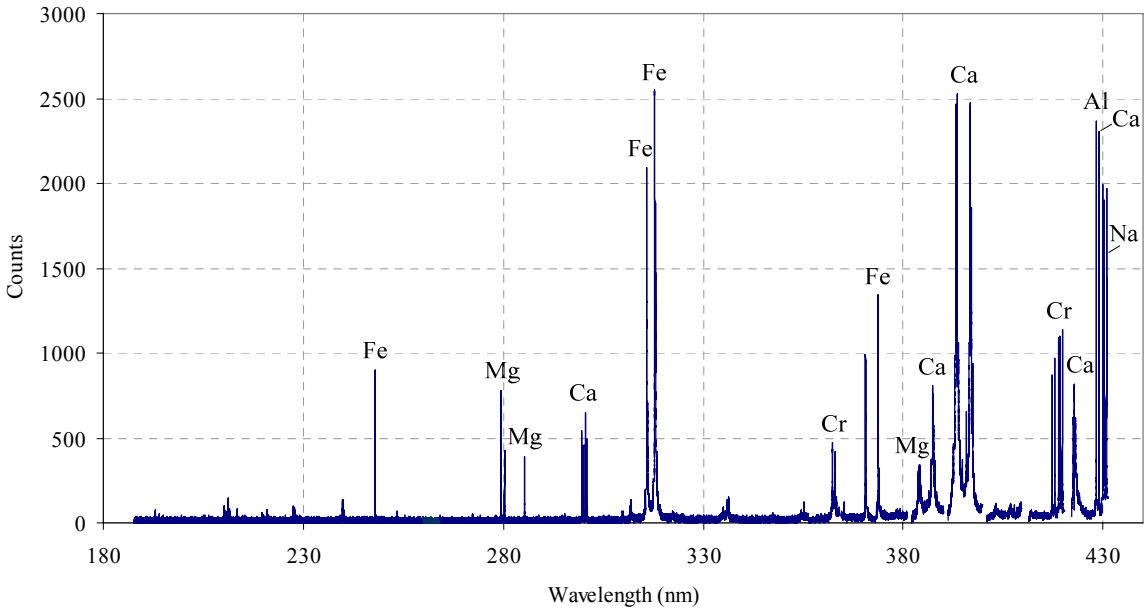

Figure 5.76: LIBS spectra for calcium oxalate monohydrate calculus (Sample 8)

Sample 9

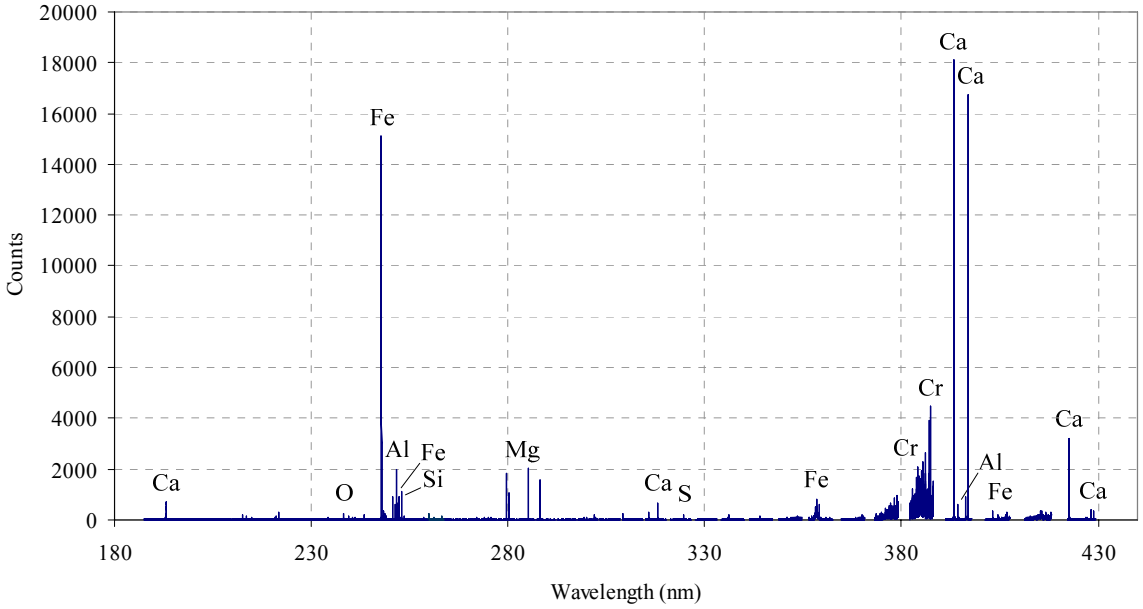

Figure 5.77: LIBS spectra for uric acid calculus (Sample 9)

Sample 10

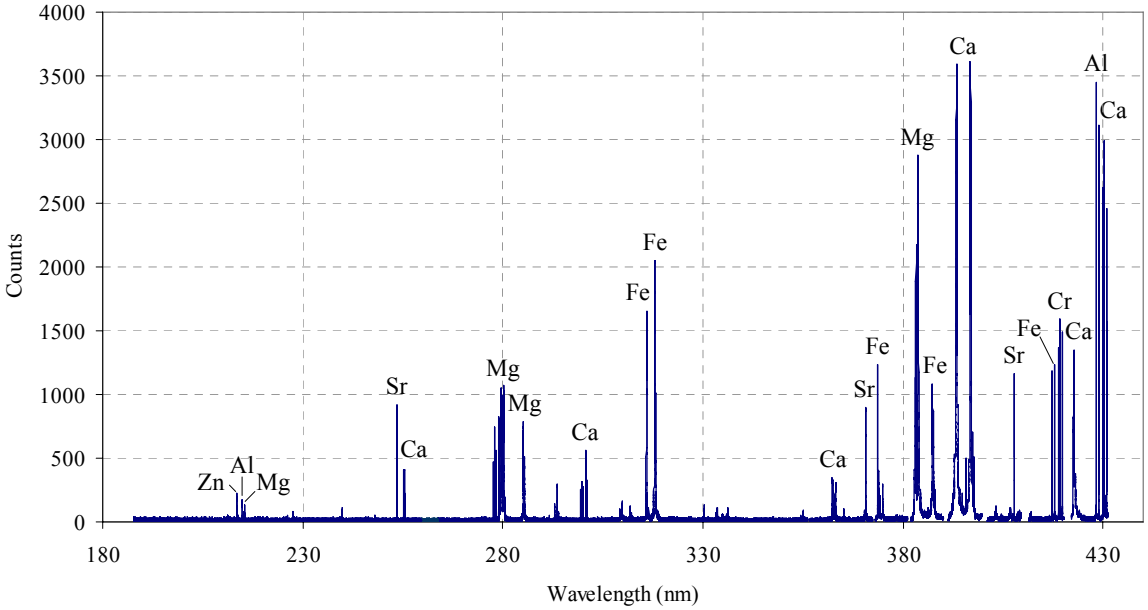

Figure 5.78: LIBS spectra for magnesium ammonium phosphate hexahydrate calculus (Sample 10)

The elements found with the Aryelle LIBS are listed in Table 5.12. The system has confirmed the detection of a number of metals initially suspected, but were not confirmed due to resolution or sensitivity limitations.

Table 5.12: Elements identified with the Aryelle LIBS system

Sample no.	Elements identified with Aryelle
Cystine (1)	Ba, C, Ca, Co, Cr, Cu, Fe, Mg, O, Zn
Cystine (2)	Be, Ca, Cu, Co, Cr, Fe, Mg, O, S
MAPH (3)	Ag, Al, Ca, Co, Cr, Fe, K, Mg, Mn, P, Sr
Brushite (4)	Al, As, Au, Ca, Cr, Cu, Fe, Mg, Mn, O, P, Sr
Cystine (5)	Be, Ca, Co, Cr, Cu, Mg, Zn, O, S,
COD (6)	Ca, Cr, Cu, Fe, Mg, Mn, Na, O, P
COM (7)	Al, Ba, Ca, Cr, Cu, Fe, Mg, Mn, P, Sr, Zn
COM (8)	Al, Ca, Cr, Fe, Mg, Na, Sr
Uric acid (9)	Al, Au, Ba, Bi, C, Ca, Co, Cr, Cu, Fe, Mg, O, Pb, S, Si
MAPH (10)	Al, Ba, Ca, Cr, Fe, Mg, Zn, S

The ratio of the intensity of calcium (at 393.4 nm) to magnesium (at 275.5 nm) and iron (at 247.86 nm) are shown in Table 5.13.

Table 5.13: Ratios of intensities of Mg and Fe with respect to Ca in samples

Sample no.	Ca (393.4 nm)	Ca relative to max	Mg/Ca (275.5 nm)	Fe/Ca (247.86 nm)
Cystine (1)	7758	0.10	0.15	0.76
Cystine (2)	2756	0.03	0.12	2.55
MAPH (3)	81610	1.00	0.99	0.07
Brushite (4)	26477	0.32	0.36	0.00
Cystine (5)	9829	0.12	0.18	0.60
COD (6)	20667	0.25	0.27	0.17
COM (7)	27433	0.34	0.13	0.08
COM (8)	2527	0.03	0.31	0.28
Uric acid (9)	18104	0.22	0.10	0.81
MAPH (10)	3481	0.04	0.28	0.00

Laser induced plasma spectroscopy has been used successfully for the elemental analysis of urinary stones. The technique offers the possibility of accurate measurements of trace elements in such stones without the need for any elaborate sample preparation. However, for quantitative measurements the system needs to be calibrated for each elemental species. It is also possible that the technique may be used for in vitro diagnosis for choosing appropriate laser parameters in laser lithotripsy. Further research on the dependence of signal strengths of the atomic lines on laser wavelength and pulse width will allow optimization of laser parameter for the design and development of a cost-effective portable laser lithotripter incorporating LIBS system.

5.16 Optical absorption in the UV-Vis-NIR: basis for further work

UV-Vis-NIR spectroscopy

Spectral absorption as a percentage was estimated from the diffuse reflectance to obtain spectra of the samples (see chapter 4). The results of the measurements are shown in Figures 5.79 and 5.80. The data represents an averaging over the sampled area of the target, which was comparatively large in the scheme of measurement. The measurements were restricted to the large size samples only.

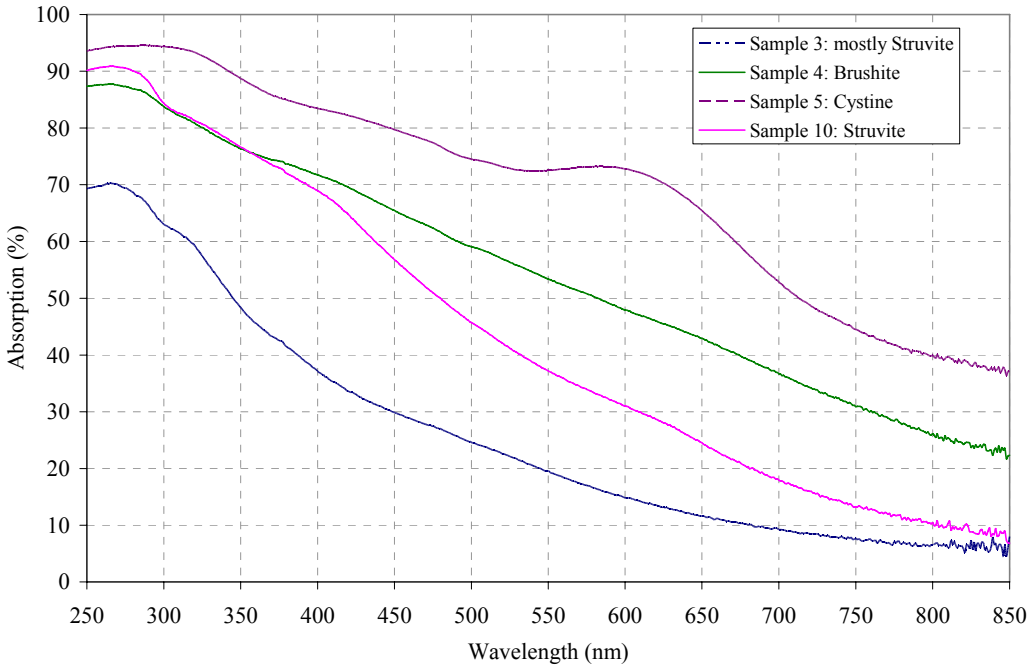

Figure 5.79: UV-Vis-NIR optical absorption properties of several urinary calculi

All the samples tested in this experiment exhibited a strong absorption in the ultraviolet end of the spectrum up to ~ 250 nm. For example, 70 – 95 % absorption are noted at 250 nm for a few samples. In general it appears that blue light is more strongly absorbed than the visible or near infrared radiation.

The general trend appears to be that optical absorption gradually decreases over the wavelength band of 250 – 850 nm, by a factor of 9 to 2 depending upon the type of sample. This difference is attributed to differences in their surface morphology and pigmentation. The sample of cystine, which was dark green-grey in color, shows the strongest absorption, whereas the pale off-white struvite samples exhibits the weakest absorption in the UV-Visible spectral range. This, however, is expected as pale calculi are more reflective.

The absorption (reflection) spectra for the biliary calculi samples, as shown in Figure 5.80, exhibit a strong absorption in the ultraviolet region. The dark green-brown gallstone (Sample 11) absorbs strongly in the UV-Vis spectrum. The yellow cholesterol stone on the other hand absorbs far less radiation at wavelengths above approximately 500 nm, falling to ~ 20% absorption at around 600 nm. Again, as with the urinary calculi, the absorption appears to increase for more heavily pigmented compositions.

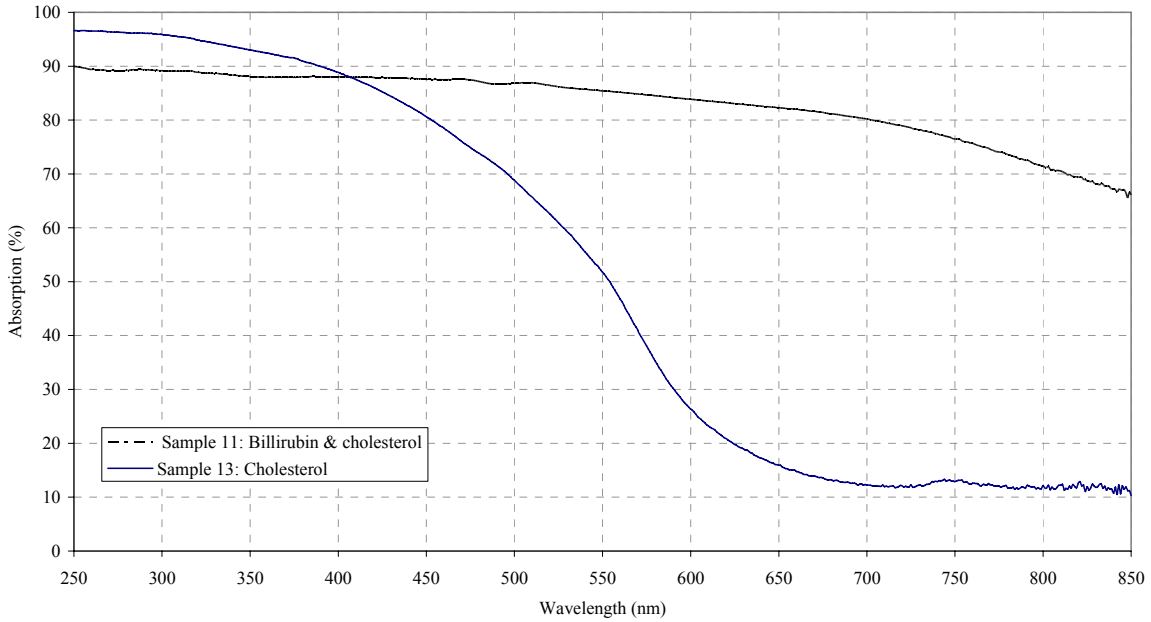

Figure 5.80: UV-Vis-NIR optical absorption properties of 2 types of biliary calculi

The results of diffuse reflectance measurements suggest that a laser emitting in the ultraviolet would more efficiently impart its energy to calculus material, and would therefore be a good choice for laser lithotripsy. In the visible region, lasers such as the pulsed dye laser operating at 504 nm, are reasonably well absorbed by calculi which underlines why the laser has been a popular laser for lithotripsy. Laser beam in the red-NIR region is much less absorbed by calculi and therefore would have to have higher pulse energy to compensate. This underlines why lasers such as the ruby (694 nm), alexandrite (755 nm) and diode are not as good a choice for stone fragmentation.

In this chapter, the results of the analysis of calculi has revealed the samples to be of a range of compositions including common calcium oxalate types, mixed compositions containing calcium and magnesium, and less common varieties including cystine and uric acid. Using laser induced breakdown spectroscopy the presence of certain metals has been confirmed including calcium, magnesium, sodium, strontium, potassium and lead, either as major or trace constituents.

The interaction of the Q-switched Nd:YAG laser with calculi and water has been revealed the process to be plasma mediated, and the dependence of the pressure pulses on the plasma has been shown to be related to the plasma dimensions and the laser pulse energy. For this laser the plasma temperature has been estimated to be ~ 6500 K or higher, both in water and on the surface of the calculus. The holmium laser generated pressure pulses in water comparable to the Nd:YAG laser but requiring higher pulse energy and therefore with less efficiency, also the amplitude of the pulses showed greater variability. The nature of the pressure pulses with the Ho:YAG and Nd:YAG lasers were found to be different in that the holmium laser generated a negative pressure component as well as a positive pressure, whereas the Nd:YAG laser was only effective in generating positive pressure pulses. The dependence of the pressure pulse with distance was found to be greater with the Ho:YAG laser, and from the derived relationships based on the pressure measurements recorded the predicted pressure at 1 mm distance from the emission centre is ~ 12 MPa with the Nd:YAG laser system used for the experiments, and ~ 50 MPa with the Ho:YAG laser system. In the next chapter

the results and conclusions will be discussed further and indications for further research will be identified.

Chapter 6
Discussion and Conclusions

The research was aimed at the investigation of the laser-calculus interaction with the aim of making a contribution to advances in the application of laser technology for the treatment of urinary calculi in humans, from both the therapeutic aspect in identifying optimum parameters and also from the diagnostic perspective in the application of laser-induced breakdown spectroscopy (LIBS). In particular, the novel aspects of this research are the investigation of the interaction dynamics with the variable pulse duration Ho:YAG laser and how the laser parameters influence shockwave pressures (and potentially plasma formation), and how this laser compares to a shockwave laser operating in the nanosecond domain. The use of a needle hydrophone has enabled better experimental technique in evaluating the pressure at close range to the source. Furthermore the prospect of using LIBS for the material analysis of human calculi has been investigated and work in this area has been published (Fang et al, 2005).

The experimental work has identified the dependence of the plasma and the shockwave characteristics on laser parameters for two laser systems, the microsecond pulsed Ho:YAG ($\lambda = 2.12$ μm) and the nanosecond pulsed Q-switched Nd:YAG ($\lambda = 1064$ nm) lasers. With this knowledge it was possible to identify lasers with parameters most effective for use in in-vivo fragmentation of the calculi. Additionally, the potential application of the laser for the purposes of laser induced breakdown spectroscopy was demonstrated. In this chapter a general discussion of the findings of this research, the conclusions that can be drawn, and the areas for further work, are presented in orders of heading in which the results were reported in the previous chapter.

6.1 Absorption experiments

The urinary calculi samples used in the experiments were identified from their FT-IR spectra. These were found to consist of an assortment of compounds such as calcium oxalate monohydrate, calcium oxalate dihydrate, magnesium ammonium phosphate hexahydrate (struvite), calcium hydrogen phosphate dihydrate (brushite), uric acid and cystine types etc. One sample was found to contain a small amount of calcium

carbonate apatite. Samples of biliary calculi were found to be of different composition to those formed in the urinary tract due to the different chemical environment in which they are formed i.e. the gall bladder, comprising a mixture of cholesterol and bilirubin, and in some cases calcium phosphate.

All stone types can, and often are, treated by laser although the use of a laser is more common in the fragmentation of urinary stones, particularly where other treatment modalities have failed. The success and efficiency of the laser as a lithotripsy device depends upon the choice of laser type and its output beam parameters. Direct laser irradiation of calculi will lead to interaction and possible destruction but for this process to occur there must be absorption at the particular laser wavelength. The calculi samples were found to have strong absorption in the ultraviolet region, moderate absorption across the visible region, and less in the red and near infrared region. The urinary stones were typically pale in color and therefore the reduced absorption in the visible region was not unsurprising. In contrast, the gallstone samples were darker in color and showed a better absorption than urinary stones across the UV-Vis-NIR wavelength range. In the far infrared a number of absorption bands specific to the composition type were found. Water also has a number of absorption peaks in the far infrared.

The indication from the above findings are that an ultraviolet laser e.g. an excimer laser, would potentially be a good choice for lithotripsy as its energy will be highly absorbed by the calculus surface leading to action on the bulk material. There are several excimer lasers commercially available, although they are typically high-cost devices and as such have not become a viable option for lithotripsy application.

Similarly, in the visible region, particularly at blue-green wavelengths, the calculi samples showed good absorption and this matches well to the wavelengths corresponding to the pulsed coumarin-dye laser (504 nm) and the KTP laser (532 nm), and also the CW argon-ion laser (488 nm – 514 nm). Of these, unlike the microsecond-pulsed dye laser (PDL) and the Q-switched KTP laser, the argon-ion laser does not generate high peak power pulses. The average power levels available from an argon-ion laser may be sufficient to cause burning of the calculi, but is not capable of creating a

shock for fragmentation. In contrast, the pulsed dye laser has become a popular and successful laser lithotripter, and more recently the KTP laser has emerged as a potential alternative system.

A number of the absorption bands of the calculi that were identified in the far infrared correspond to existing lasers. The carbon dioxide laser (10.6 μm) and the erbium laser (2.94 μm) are the main choices, although the lack of a suitable optical fibre delivery system currently precludes their use for lithotripsy. The free electron laser has been reported as promising as it can be tuned to the peak absorption wavelengths, however, this laser is not yet available as a commercial lasertripter for similar reasons of lack of a delivery system, cost and complexity.

The alternative is to use a laser with output parameters that are largely independent of the calculus absorption properties in the interaction process. The Q-switched Nd:YAG laser is, by far, the most efficient laser system (in terms of generating peak laser power) and may be used to effectively generate a plasma at the beam focus; the plasma then becomes an efficient absorber of the laser radiation at the incident wavelength. This means that the laser energy is coupled to the surrounding medium and therefore to the calculus through the transfer of heat from the plasma volume and also through mechanical action of generated pressure pulses. The holmium laser is also less dependent on absorption of its wavelength by the calculus as it is highly absorbed by water. The laser energy converts water to steam and this expansion results in pressure pulses, and also the potential vaporization of a channel through to the calculus surface where it can impart direct ablation of the calculus material – the "Moses Effect". Both of these lasers were shown to generate substantial thermal effects and pressure waves in the course of the laser-calculus interaction.

6.2 Plasma experiments

The focussed Q-switched Nd:YAG laser was able to reliably generate a plasma on calculus material, in bulk water, and on the surface of a calculus immersed in water. Plasma was generated at a relatively low laser energy of ~ 10 mJ, corresponding to an estimated irradiance of ~ 9 GW cm^{-2} at the focal point, which is in good agreement with

Vogel et al (1996) using a similar setup. In air, the plasma temperature on the calculus was estimated at 6700 – 6900 K with little variation between calculus compositions. In deionised water the plasma temperature was estimated to be marginally lower at 6600 K, although this was not statistically significant given the uncertainties in the measurement. Plasma temperature in water on the calculus surface was ~ 6500 K, again not a significant variation. Interestingly, Jiang et al (1992c) reported higher plasma temperatures of ~ 10,000 K for similar laser parameters on immersed calculi, this may be due to an increased concentration of calcium in their sample or better laser absorption. The plasma intensity was found to be dependent upon the laser pulse energy, as expected, however the dependence became non-linear at higher pulse energies due to a saturation effect attributed to plasma shielding phenomena. The plasma volume increased along the beam axis with increasing laser pulse energy, but there was little effect on the width of the plasma across the beam focus. This was significant in the generation of pressure pulses, which were considered to be a result of the highly localised high temperature and the rapid onset of the laser pulse. The optical breakdown threshold for the Nd:YAG laser was estimated to be similar for initiating a plasma on the calculus surface either in water or in air (~ 8 GW cm^{-2}), but higher by a factor of ~ 1.5 compared to the estimated optical breakdown threshold of water (~ 5 GW cm^{-2}). The values of the optical breakdown threshold are based on an estimated laser spot diameter of 0.15 mm.

For the Ho:YAG laser the evidence for plasma formation was less convincing. Light emission from the irradiated zone appeared to be scattered flashlamp light emanating from the laser system along with the laser beam. Irradiation of calculi in air showed strong thermal effects particularly on calculi of uric acid composition. However, the irradiance required to achieve the effects that appeared to indicate light (plasma) emission was considerably lower than that required by the Nd:YAG laser, by a factor of approximately 10^4, and therefore unlikely to be plasma. Comparison of the temporal light signal from the laser-calculus interaction zone with the temporal light signal from the laser pulse showed significant similarities, again suggesting there was no plasma signal. Digital photography provided further evidence, particularly in water, that in the Ho:YAG laser interaction no optical emissions were present. Therefore, the Ho:YAG

laser was not believed to be generating plasma on calculi material or in water and the thermal and mechanical effects were attributed to absorption of the laser beam leading to direct vaporization, which is consistent with findings of Chan et al (1999a,b). A theoretical treatment of the Ho:YAG laser interaction using Keldysh (1965) equations is consistent with the lack of plasma formation. Sperrin (2000) comments that plasma formation is an important factor in the shockwave dynamics but not necessarily with the Ho:YAG laser. Vogel and Venugopalan (2003), however, report the possibility of high intensity pulse spikes with this laser and that these may lead to optical breakdown in water.

6.3 Shockwave experiments

For the Nd:YAG laser, pressure pulses were evident when plasma formation was observed. However, with the Ho:YAG laser pressure pulses were apparently not plasma-mediated. In both cases the model of vaporization of water leading to an unstable steam bubble that releases an intense pressure pulse on collapse was supported by the observations and measurements. The resulting shock front was found to be of the order of several MPa in amplitude and travelling at the speed of sound in water (~ 1473 ms^{-1}). Three pressure transients were detected with the Ho:YAG laser. An initial weak expansion phase pressure transient was detected at the end of the laser pulse which was believed to correspond to the conversion of water into steam with an accompanying increase in volume. The second (principal) pressure pulse arrived after a significant time delay following the collapse of the steam bubble, the time delay being attributable to the period in which the steam bubble remains stable before its collapse. A secondary pressure pulse was detected a short time later, having a lower amplitude than the primary pulse and believed to be a rebound cavitation.

The difference in the pressure pulse waveform between the Nd:YAG and the Ho:YAG lasers was found to be significant. For the Nd:YAG laser the pressure pulse had a rise time of 60 ns and a duration of around 100 ns (FWHM). The bubble lifetime was estimated at ~ 15 μs which was independent of laser pulse energy. The pressure wave had the form of a rapidly rising positive pressure followed by a tailing off to ambient pressure. In contrast, the Ho:YAG laser-induced pressure pulse had a much longer rise

time of around 500 ns and a longer duration of 1 μs (FWHM), and a bubble lifetime of several hundred microseconds. In this case, the stability of the steam bubble was influenced by the laser pulse energy, and was found to have a linear relationship, indicating the formation of a more stable steam bubble with increasing laser energy. Another significant difference was the presence of a tensile tail in the pressure waveform for the Ho:YAG laser of the order of a few MPa. The tensile component may be significant in the action on calculi as brittle materials will more easily break up under tension than compression forces.

The angular variation of the pressure pulse with the Nd:YAG laser was strongly dependent on the plasma dimensions, which were measured as ~ 0.15 ± 0.05 mm wide and up to ~ 4 ± 1.0 mm in length. In the path of the laser beam where the plasma dimension was largest, the resultant pressure in that direction was lowest compared to that recorded at other angles. The maximum pressures were detected at 90° to the laser beam i.e. where the plasma dimension was at its narrowest. Therefore, it was concluded that to generate the highest pressure pulses in all directions from the emission centre the plasma must be tightly confined. This is in alignment with a reported reduction in energy conversion from laser energy to mechanical pressure pulses with reduced beam focussing angle and increased plasma dimensions (Vogel et al, 1999). In contrast, no variation in pressure amplitude with angle for the Ho:YAG laser-induced pressure pulses at the fibre tip was found i.e. the shock front appeared to diverge spherically from this point. This would also appear to confirm that there was no plasma generation by the Ho:YAG laser, and it also suggests that the steam bubble collapses at a fixed point in front of the fibre tip rather than along the direction of the laser beam. This explanation is, however, in contradiction with reports from some investigators (Chan et al, 1999a,b).

The pressure pulse amplitude for both lasers decreased with distance from the emission centre. For the Nd:YAG laser the fall-off with distance appeared to be exponential and giving an estimated value of ~ 11 MPa at a distance of 1 mm from the emission centre. The Ho:YAG laser showed a stronger dependence with distance. The predicted pressure at 1 mm distance from the fibre is estimated to be significantly greater than that

measured at several millimeters, with a prediction of 50 MPa for the positive pressure and -25 MPa for the negative pressure component. However, these figures are extrapolated from data with large uncertainties and as such may be an overestimate. Nevertheless, this does suggest that the holmium laser is capable of generating higher peak pressure pulses than those by the Nd:YAG laser. The stronger dependence of pressure amplitude with distance for the Ho:YAG laser compared to that for the Nd:YAG laser was considered to be a result of the two different interaction processes with steam micro bubbles and calculus debris playing a part in the apparent higher attenuation. The difference may also be attributed to differences in frequency of the pressure pulses generated by the two lasers.

The magnitude of the pressure pulse with the Ho:YAG laser has been debated in the literature. Reports by Chan et al (1999a,b) and others have indicated the pressures are relatively weak, of the order ~ 2 MPa, whereas Sperrin (2000) found that the corrected pressures to the point of contact with the calculus are considerably higher at ~ 600 MPa. The results of the present study indicate for a variable pulsed Ho:YAG the peak pressures are between these values, but still in excess of the reported failure strength of calculi. The pressures have been recorded using a needle hydrophone which has permitted highly accurate spatial and peak pressure measurements in the vicinity of the laser emission centre, therefore providing a reasonable level of confidence with the findings. Chan (1999a,b) also used a needle hydrophone, but measured pressures at a distance and applied a correction factor, and this may explain the large disagreement as it has been shown in this work that there is a strong dependence with distance. Sperrin (2000), on the other hand, characterised the pressure field but with a large area membrane hydrophone, however, the instrument is both difficult to position close to the source and also susceptible to damage, potentially leading to measurement uncertainties.

Pressure pulse amplitudes were found to be dependent on laser pulse energy, increasing linearly up to a value where a saturation effect appeared. The conversion of laser energy into pressure was gauged from a ratio of MPa per Joule. Taking the value of laser pulse energy close to the onset of saturation and extrapolating to a distance of 1 mm from the emission centre, for the Nd:YAG laser a value of ~ 340 MPa J^{-1}, which is significantly

higher than that for the Ho:YAG laser, having a value of ~ 78 MPa J^{-1}. This suggests that the shockwave formation process with the Nd:YAG laser is more efficient in terms of coupling the laser pulse energy, which may be attributable to a more spherical steam bubble for this laser, or to the shorter pulse duration. A theoretical analysis has shown that the Nd:YAG laser is both thermally and stress confined and this would be expected to lead to good energy transfer to mechanical effects, whereas the Ho:YAG laser was shown to be thermally confined but not stress confined.

Laser pulse duration was also found to be a key parameter in the generation of pressure pulses. An exponential increase in pressure pulse was seen with decreasing laser pulse duration for the Ho:YAG laser for the range 120 – 800 μs. This again suggests a link to the bubble dynamics, as a shorter pulse duration enables a more spherical bubble shape to be formed.

The effect on the pressure pulse amplitude of varying the laser pulse repetition rate was found to be insignificant except for at higher pulse energies. A slight decrease of around 10 % in the peak pressure amplitude was seen for pulse a energy of 87 mJ and a repetition rate of 20 Hz, possibly arising from the effect of residual bubbles or debris remaining in the vicinity from the previous pulse interaction. However, the reduction in peak pressure value was only marginal and probably not an indication to restrict the maximum pulse rate available from the laser.

The introduction of ions into solution, in particular ion chloride (Fe_2Cl_3), showed a significant enhancement in the pressure amplitude for the Nd:YAG laser although no enhancement was seen for the Ho:YAG laser. For solution strength of 1 % Fe_2Cl_3 there was an enhancement in pressure by a factor of around 2 at the highest laser pulse energy available, and also a lowering of the threshold at the lowest laser energies. There was no further enhancement with solution strength of 2.5 %. These results provide further evidence that the shockwave production with the Nd:YAG laser is linked to the plasma formation as free ions may lower the optical breakdown threshold and enable a more intense plasma to be generated. The lack of effect on the Ho:YAG laser-induced pressure pulses again supports the conclusion that there is no plasma formation with this

laser. No significant enhancement of pressures was seen using physiological saline solution.

6.4 LIBS experiments

From the experiments on plasma formation it was concluded that the Ho:YAG laser does not form plasma on calculi, therefore, the Nd:YAG laser was used as an excitation source for LIBS. The experiments using laser induced breakdown spectroscopy to analyse selected calculi samples for the presence of metals in their material composition showed that the technique may be applicable to calculi samples, although would need to be confirmed by another technique. Elements identified included calcium and magnesium, also sodium, strontium, potassium, iron, copper, chromium, zinc, manganese, and lead. Not all of these elements were found in every sample tested, whereas the presence of some metals is entirely expected, for example calcium is a major constituent of a number of types of calculi. The detection of elements such as lead is of interest as it may indicate environmental factors and has been identified in one of the samples. The concentrations of certain elements have been quantified but this area would need to be investigated further to enable more accurate measurements.

The role of trace elements such as heavy metals for example in the formation of calculi or in the prediction of fragility is not fully understood and there is considerable interest in a technique that can provide this information. The presence of zinc, strontium, copper and manganese are believed to be important elements in stone nucleation. The advantage of LIBS is that no sample preparation is required, and it may be a possibility to produce an on-line in vivo system for use in conjunction with the laser-induced fragmentation application.

6.5 Further work

There is a considerable scope for further research on application of lasers to the therapeutic and diagnostic aspects in the treatment of human urinary calculi. An important area is the need for a more cost-effective laser system so that the technique can be practised more widely. Future developments in high-power diode laser technology, or indeed high-power LEDs tailored for such applications, may prove to be

a potential alternative to the Ho:YAG and other lasers currently under trial or use. Also, developments in suitable optical fibres for infra-red lasers, such as the Erbium YAG and carbon dioxide lasers, as well as the high peak power Q-switched lasers, would be a significant step forward for future laser lithotripsy. For example, a Ho:YAG laser with selectable Q-switch operation might provide the benefits of fragmentation by shockwave action plus the ability to carry out plasma spectroscopy.

Further characterisation of the Ho:YAG laser-induced pressure pulse fields is of interest, in particular for the use of pulse durations in the range << 100 μs, as the shorter pulses are expected to generate higher peak pressure pulses. A Ho:YAG laser system with greater control over the pulse duration would allow the choice between a long-pulse drilling action for example on hard calculi, and a short-pulse shockwave action to efficiently fragment friable concrements. At shorter pulse durations the Ho:YAG laser may generate plasma and so the use of spiked solutions may allow further enhancement in pressure as was found with the Nd:YAG laser in this study and reported elsewhere (Reichel et al, 1991).

The work on the application of LIBS for elemental analysis of urinary calculi is an area that can be considerably developed. Laser systems other than the Q-switched Nd:YAG may be better suited for LIBS on calculi and also enable fragmentation of calculi. The use of a high resolution LIBS system to identify major, minor and trace elements in a wider range of calculi could also be investigated. The calibration of such a LIBS tool would require the fabrication of stimulant stones of various concentrations of metals etc. and having properties close to natural samples and would enable more accurate estimates of concentrations. The technique could be used to study a large collection of samples for elemental analysis in particular the elements present and the spatial distribution within the calculi such as the presence of certain heavy metals at the nidus. Such findings may point to a role in stone nucleation. An investigation into the fragility of calculi and the presence of trace metals in their composition may indicate that stone analysis in real time lithotripsy may facilitate control of the laser parameters to optimise the fragmentation process. The development of suitable and cost-effective LIBS apparatus for in vivo analysis would be an advantage particularly as laser fragmentation

is generally highly successful and there is no sample available for laboratory analysis. Thus LIBS may provide benefits in identification of calculi with respect to elemental composition. The use of Raman spectroscopy would also offer additional compositional information which is of great importance in the clinical management of the condition.

In summary, the field of laser application to calculi has so far proved to be of huge benefit to society and yet there is still a need for further basic and applied research into the therapeutic and diagnostic use of lasers for this application. Since the invention of the laser in 1960 and its first use in the destruction of calculi by Mulvaney and Beck (1968), the past 20 years or so have seen considerable scientific and technological advances in the field to which this research has made a contribution and the future promises to be an area of exciting developments.

REFERENCES

Abboud I A. (2008). Concentration effect of trace metals in Jordanian patients of urinary calculi. *Environ Geochem Health.* **30**, 11-20.

Agarwal R & Singh V R. (1991). A comparative study of fracture strength, ultrasonic properties and chemical constituents of kidney stones. *Ultrasonics.* **29**, 89-90.

Al-Kofahi M M & Hallak A B. (1996). Analysis of kidney stones by PIXE and RBS techniques. *X-ray Spectrometry*. 25**, 225-228.**

Anderholm N C. (1970). Laser-generated stress waves. *Applied Physics Letters.* **16**, 113-115.

Atakan I H, Kaplan M, Seren G, Aktoz T, Gül H & Inci O. (2007). Serum, urinary and stone zinc, iron, magnesium and copper levels in idiopathic calcium oxalate stone patients. *Int Urol Nephrol.* **39**, 351-356.

Bader M J, Hecht V, Hocaoglu Y, Tilki D, Staehler M, Wondrazek F, Reich O, Stief C G & Sroka R. (2007). In-vitro comparison of laser-induced lithotripsy on artificial stones by means of different laser systems. *Medical Laser Application*. **22**, 220-226.

Batishche S A. (1995). The features of the gallstones and kidney stones fragmentation by IR pulsed YAG:Nd laser radiation. *Proc. SPIE.* **2395**, 94-97.

Bazin D, Chevallier P, Matzen G, Jungers P & Daudon M. (2007). Heavy elements in urinary stones. *Urol Res*. **35**, 179-184.

Beghuin D, Delecrétaz G, Schmidlin F & Rink K. (1998). Fragmentation process during Ho:YAG laser lithotripsy revealed by time-resolved imaging. *Proc. SPIE.* **3195**, 220-224.

Benaim G, Mattioli S, Cremona M, Pini R, Salimbeni R, Vannini M & Franceschini M A. (1992). In vitro tests of excimer laser lithotripsy in urinary stones. *Proc. SPIE.* **1643**, 73-77.

Berenberg V A, Murzin A G, Polikarpov S S, Soms L N, Vitrishchak I B & Vorontsov V V. (1993a). On physical mechanisms of laser-induced shockwave lithotripsy in the microsecond range of laser pulse durations. *Proc. SPIE*. **1879**, 126-130.

Berenberg V A, Vitrishchak I B, Murzin A G & Soms L N. (1996). Ruby laser with long optical resonator emitting in microsecond range for lithotripsy applications. *Proc. SPIE*. **2928**, 259-261.

Berenberg V A, Vitrishchak I B, Vorontsov V V & Murzin A G. (1994). Microsecond shockwave laser lithotripsy: analysis of induced absorption mechanisms. *Proc. SPIE.* **2129**, 129-140.

Berenberg V A, Vitrishchak I B, Vorontsov V V, Murzin A G, Polikarpov S S & Soms L N. (1993b). Physical mechanisms of laser-induced shockwave lithotripsy with microsecond laser pulses. *Proc. SPIE.* **2097**, 26-35.

Berlien H-P & Müller G J. (2003). *Applied laser Medicine*. Germany: Springer.

Bhatta K M. (1995). Lasers in urology. *Lasers in Surgery and Medicine.* **16**, 312-330.

Bhatta K M & Nishioka N S. (1989a). Effect of pulse duration on microsecond-domain laser lithotripsy. *Lasers in surgery and medicine.* **9**, 454-457.

Bhatta K M, Rosen D I & Dretler S P. (1989b). Plasma shield lasertripsy: in vitro studies. *The Journal of Urology.* **142**, 1110-1112.

Bhatta K M, Rosen D I, Watson G M & Dretler S P. (1989c). Acoustic and plasma guided lasertripsy (APGL) of urinary calculi. *The Journal of Urology.* **142**, 433-437.

Bloch M A, Fedorovskii S L & Suslov A M. (1993). In vitro lithotripsy with Er:Cr:YSGG laser through fiber. *Proc. SPIE.* **1879**, 182-185.

Bloembergen N. (1974). Laser-induced electric breakdown in solids. *IEEE Journal of Quantum Electronics.* **10**, 375-386.

Boulnois J-L. (1986). Photophysical processes in recent medical laser developments: a review. *Lasers in Medical Science.* **1**, 47-66.

Brinkmann R & Bauer K. (1991). Q-switching and pulse shaping with IR-lasers. *Proc. SPIE*. **1421**, 134-139.

Brinkmann R, Meyer W, Engelhardt R & Walling J C. (1990). Laser induced shockwave lithotripsy by use of a 1 μs Alexandrite laser. *Proc. SPIE.* **1200**, 67-74.

Brujan E-A & Vogel A. (2006). Stress wave emission and cavitation bubble dynamics by nanosecond optical breakdown in a tissue phantom. *J. Fluid Mech.* **558**, 281-308.

Carmona P, Bellanato J & Escolar E. (1997). Infrared and Raman spectroscopy of urinary calculi: a review. *Biospectroscopy.* **3**, 331-346.

Carruth J A S & McKenzie A L. (1986). *Medical lasers - science and clinical practice.* Bristol: Adam Hilger Ltd.

Chan K F, Hammer D X, Choi B, Teichman J M H, McGuff H S, Pratisto H, Jansen E D & Welch A J. (2000a). Free electron laser lithotripsy: Threshold radiant exposures. *Journal of Endourology.* **14**, 161-167.

Chan K F, Hammer D X, Choi B, Vargas G, Sorg B, Pfefer T J, Teichman J M H, McGuff H S, Pratisto H, Janson E D & Welch A J. (2000b). The influence of optical absorption on urinary calculus threshold fluence and ablation efficiency during infrared laser ablation. *Proc. SPIE.* **3925,** 60-68.

Chan K F, Lee H, Teichman J M H, Kamerer A, McGuff H S, Vargas G & Welch A J. (2002). Erbium:YAG laser lithotripsy mechanism. *The Journal of Urology.* **168**, 436-441.

Chan K F, Pfefer T J, Teichman J M H & Welch A J. (2001). A perspective on laser lithotripsy: the fragmentation processes. *Journal of Endourology.* **15**, 257-273.

Chan K F, Vargas G, Parker P J, Teichman J M H, Glickman R D, McGuff H S & Welch A J. (2000c). In vitro Erbium:YAG laser lithotripsy. *Proc. SPIE.* **3914**, 198-206.

Chan K F, Vassar G J, Pfefer T J, Teichman J M H, Glickman R D, Weintraub S T & Welch A J. (1999a). Holmium:YAG laser lithotripsy: a dominant photothermal ablative mechanism with chemical decomposition of urinary calculi. *Lasers in Surgery and Medicine.* **25**, 22-37.

Chan K F, Vassar G J, Pfefer T J, Teichman J M H, Glickman R D, Weintraub S E & Welch A J. (1999b). Chemical decomposition of urinary stones during Holmium laser lithotripsy - Part 1: Lack of photomechanical effect. *Proc. SPIE.* **3601**, 377-386.

Chaudhri M A, Watling J & Khan F A. (2007). Spatial distribution of major and trace elements in bladder and kidney stones. *Journal of Radioanalytical and Nuclear Chemistry.* **271**, 713-720.

Chuong C J, Zhong P & Preminger G M. (1993). Acoustic and mechanical properties of renal calculi: implications in shock wave lithotripsy. *Journal of Endourology.* **7**, 437-444.

Coptcoat M J, Ison K T, Watson G & Wickham J E A. (1987). Lasertripsy for ureteral stones: 100 clinical cases. *Journal of Endourology*. **1**, 119-122.

Corbin N S, Teichman J M H, Nguyen T, Glickman R D, Rihbany L, Pearle M S & Bishoff J T. (2000). Laser lithotripsy and cyanide. *Journal of Endourology.* **14**, 169-173.

Crow P, Stone N, Kendall C A, Persad R A & Wright M P J. (2003). Optical diagnostics in urology: current applications and future prospects. *BJU International.* **92**, 400-407.

Daidoh Y, Arai T, Suda A, Kikuchi M, Komine Y, Murai M & Nakamura H. (1991). Discrimination between urinary tract tissue and urinary stones by fiber optic pulsed photo-thermal radiometry method in vivo. *Proc. SPIE.* **1421**, 120-123.

Denstedt J D, Chun S S, Miller M D & Eberwein P M. (1997). Intracorporeal lithotripsy with the Alexandrite laser. *Lasers in Surgery and Medicine.* **20**, 433-436.

Denstedt J D, Razvi H A, Sales J L & Eberwein P M. (1995). Preliminary Experience with Holmium:YAG Laser Lithotripsy. *Journal of Endourology.* **9**, 255-258.

Devarajan R, Ashraf M, Beck R O, Lemberger R J & Taylor M C. (1998). Holmium:YAG lasertripsy for ureteric calculi: an experience of 300 procedures. *BJU.* **82**, 342-347.

Dretler S P. (1990). An evaluation of ureteral laser lithotripsy: 225 consecutive patients. *The Journal of Urology.* **143**, 267-272.

Dretler S P, Watson G, Parrish J A & Murray S. (1987). Pulsed dye laser fragmentation of ureteral calculi: initial clinical experience. *The Journal of Urology.* **137**, 386-389.

Duck, F A. (1990). *Physical properties of tissue. A comprehensive reference book.* London: Academic Press.

Dushinski J W & Lingeman J E. (1998). High-speed photographic evaluation of Holmium laser. *Journal of Endourology.* **12**, 177-181.

D'yakonov G I, Konov V I, Mikhailov V A, Nikolaev D A, Pak S K & Shcherbakov I A. (1991a). Comparative performance of infra-red solid-state lasers in laser lithotripsy. *Proc. SPIE.* **1421**, 156-162.

D'yakonov G I, Mikhailov V A, Pak S K & Shcherbakov I A. (1991b). Q-switched Nd:glass laser induced acoustic pulses in lithotripsy. *Proc. SPIE.* **1421**, 153-155.

Ebrahimi F & Wang F. (1989). Fracture behavior of urinary stones under compression. *Journal of Biomedical Materials Research.* **23**, 507-521.

Estepa L & Daudon M. (1997). Contribution of Fourier Transform Infrared spectroscopy to the identification of urinary stones and kidney crystal deposits. *Biospectroscopy.* **3**, 347-369.

Fair H D. (1978). In vitro destruction of urinary calculi by laser-induced stress waves. *Medical Instrumentation.* **12**, 100-105.

Fang X, Ahmad S R, Mayo M & Iqbal S. (2005). Elemental analysis of urinary calculi by laser induced plasma spectroscopy. *Lasers in Medical Science.* **20**, 132-137.

Farkas A, Péteri L, Lőrincz L, Salah M A, Flaskó, Varga A & Tóth Cs. (2006). Holmium:YAG laser treatment of ureteral calculi: a 5-year experience. *Lasers in Medical Science.* **21**, 170-174.

Felix M P & Ellis A T. (1971). Laser-induced liquid breakdown - a step-by-step account. *Applied physics letters.* **19**, 484-486.

Finley D S, Petersen J, Abdelshehid C, Ahlering M, Chou D, Borin J, Eichel L, McDougall E & Clayman R V. (2005). Effect of Holmium:YAG laser pulse width on lithotripsy retropulsion in vitro. *Journal of Endourology.* **19**, 1041-1044.

Floratos D L & de la Rosette J J M C H. (1999). Lasers in urology. *BJU International.* **84**, 204-211.

Frank F, Eichenlaub M, Hessel St & Wondrazek F. (1990). Application systems for the intracorporal laser-induced shockwave lithotripsy using the Nd:YAG Q-switch laser. *Proc. SPIE.* **1200**, 81-89.

Fried N M. (2005). Thulium fibre laser lithotripsy: an in vitro analysis of stone fragmentation using a modulated 110-watt Thulium fibre laser at 1.94μm. *Lasers in Surgery and Medicine.* **37**, 53-58.

Galassini S, Liu N Q, Moschini G, Tasca A, Villi G & Valkovic V. (1989). Trace Element variability in kidney stones. *Nuclear Instruments and Methods in Physics Research B* **34**, 556-559.

Glickman R D, Teichman J M H, Corbin N S, Vassar G J, Weintraub S E, Chan K F & Welch A J. (1999a). Photothermal ablation is the primary mechanism in Holmium:YAG laser lithotripsy of urinary calculi. *Proc. SPIE.* **3863**, 376-384.

Glickman R D, Teichman J M H, Vassar G J, Weintraub S E, Chan K F, Pfefer T J & Welch A J. (1999b). Chemical decomposition of urinary stones during Holmium-laser lithotripsy. Part II: evidence for photothermal breakdown. *Proc. SPIE.* **3601**, 369-376.

Glickman R D, Weintraub S E, Kumar N, Corbin N S, Lesani O & Teichman J M H. (2000). Further characterization of photothermal breakdown products of uric acid stones following Holmium:YAG laser lithotripsy. *Proc. SPIE.* **3914**, 144-152.

Golovanova O A, Pyatanova P A, Strunina N N & Baisova B T. (2003). Spectral analysis of the microelemental composition of renal calculi. *Journal of Applied Spectroscopy.* **70**, 489-492.

Grasso M, Bagley D & Sullivan K. (1991). Pulsed Dye Laser Lithotripsy- Currently Applied to Urologic and Biliary Calculi. *Journal of Clinical Laser Medicine & Surgery.* October, 355-359.

Grasso M & Chalik Y. (1998). Principles and Applications of Laser Lithotripsy: Experience with the Holmium Laser Lithotrite. *Journal of Clinical Laser Medicine & Surgery.* **16**, 3-7.

Gross A J & Herrmann T R W. (2007). History of lasers. *World J Urol.* **25,** 217-220.

Helfmann J, Döerschel K & Müller G J. (1990). Laser lithotripsy using double pulse technique. *Proc. SPIE.* **1201**, 284-291.

Helfmann J & Müller G. (2001). Laser lithotripsy: process and overview. *Medical Laser Application*. **16**, 30-37.

Hermann T R W & Gross A J. (2007). Lasers in urology. *World J Urol.* **25**, 215-216.

Hofbauer J, Steffan I, Horbath K, Vujicic G, Schwetz H, Reich G & Zechner O. (1991). Trace elements and urinary stone formation: new aspects of the pathological mechanism of urinary stone formation. *The Journal of Urology.* **145**, 93-96.

Hofmann R, Hartung R, Geissdörfer K, Ascherl R, Erhardt W, Schmidt-Kloiber H & Reichel E. (1988). Laser induced shock wave lithotripsy - biologic effects of nanosecond pulses. *The Journal of Urology.* **139**, 1077-1079.

Hofmann R, Hartung R, Schmidt-Kloiber H & Reichel E. (1990). Laser-induced shock wave lithotripsy. Influence of laser pulse energy and irrigation solutions on stone disintegration. Urol Res. **18**, 45-48.

Iwai K, Shi Y-W, Nito K, Matsuura Y, Kasai T, Miyagi M, Saito S, Arai Y, Ioritani N, Okagami Y, Nemec M, Sulc J, Jelinkova H, Zavoral M, Kohler O & Drlik P. (2003). Calculi fragmentation of Er:YAG laser light through a sealed flexible hollow fiber delivery system . *Proc. SPIE.* **4957**, 62-69.

Jansen E D, Asshauer T, Frenz M, Motamedi M, Delacrétaz G & Welch A J. (1996). Effect of pulse duration on bubble formation and laser-induced pressure waves during Holmium laser ablation. *Lasers in Surgery and Medicine.* **18**, 278-293.

Jiang Z X, Giannetas V, Charlton A & King T A. (1993). New, tunable, flashlamp pumped solid state Ti:sapphire laser for laser lithotripsy. *Proc. SPIE.* **1879**, 165-173.

Jiang Z X & King T A. (1994). Laser lithotripsy: the non-destructive measurement of calculus-surface optical absorption coefficients. *Lasers in Medical Science.* **9**, 161-166.

Jiang Z X, King T A, Shah T & Watson G. (1992a). The feasibility of blind fragmentation in laser lithotripsy. *Lasers in Medical Science.* **7**, 319-329.

Jiang Z X, King T A, Shah T & Watson G. (1992b). Spectroscopic feedback in laser lithotripsy and laser angioplasty. *Proc. SPIE.* **1649**, 106-115.

Jiang Z X, Whitehurst C & King T A. (1991a). Fragmentation methods in laser lithotripsy. *Proc. SPIE.* **1421**, 88-99.

Jiang Z X, Whitehurst C & King T A. (1991b). Basic mechanisms in laser lithotripsy. 1: Opto-acoustic-mechanical analysis. *Lasers in Medical Science.* **6**, 443-450.

Jiang Z X, Whitehurst C, King T A & Holden D. (1992c). Basic mechanisms in laser lithotripsy: 2 Spectroscopic analysis. *Lasers in Medical Science.* **7**, 29-37.

Johansson A, Kromer K, Sroka R & Stepp H. (2008). Clinical optical diagnostics – status and perspectives. *Medical Laser Application.* **23**, 155-174.

Johrde L G & Cocks F H. (1985). Fracture strength studies of renal calculi. *Journal of Material Science Letters.* **4**, 1264-1265.

Kang H W, Lee H, Teichman J M H, Oh J, Kim J & Welch A J. (2006). Dependence of calculus retropulsion on pulse duration during Ho:YAG lithotripsy. *Lasers in Surgery and Medicine.* **38**, 762-772.

Kasidas G P, Samuell C T & Weir T B. (2004). Renal stone analysis: why and how? *Annals of Clinical Biochemistry.* **41**, 91-97.

Keldysh L V. (1965). Sov Phys JETP, Volume 20, Part 5, 1307.

Kim K M. (1982). The stones. *Scanning Electron Microscopy.* **IV**, 1635-1660.

Knudsen B E, Glickman R D, Stallman K J, Chew B H, Beiko D T, Denstedt J D & Teichman J M. (2005). Performance and safety of Holmium:YAG laser optical fibers. *Journal of Endourology.* **19**, 1092-1097.

Kokaj J. (2001). High-speed photography during the laser based gall bladder stone lithotripsy. *Proc. SPIE.* **4183**, 949-960.

Koort H j, Tischer C, Rasch R & Thiede C. (2002). Laser-induced shockwave generation for use in lithotripsy. *Proc. SPIE.* **4609**, 137-140.

Kuo R L, Paterson R F, Siqueira (Jr) T M, Evan AP, McAteer J A, Williams J C & Lingeman J E. (2003). In vitro assessment of ultrasonic lithotriptors. *The Journal of Urology.* **170**, 1101-1104.

Langhorst J & Neuhaus H. (2000). Laser lithotripsy. *Digestive Endoscopy.* **12**, 8-18.

Lauterborn von W. (1974). Kavitation durch laserlicht. *Acustica.* **31**, 51-78.

Lauterborn W & Bolle H. (1975). Experimental investigations of cavitation-bubble collapse in the neighbourhood of a solid boundary. *J Fluid Mech*. **72** (2) 391.

Laurent J, Englender J, Antonetti A & Lecarpentier Y. (1991). Electromechanical Effects of Pulsed Lasers. *Journal de Physique IV*. **1**, Decembre 193-197.

Lee H, Kang H W, Teichman J M H, Oh J & Welch A J. (2005). Urinary calculus fragmentation during Ho:YAG and Er:YAG lithotripsy. *Lasers in Surgery and Medicine.* **38**, 39-51.

Lee H O, Ryan R T, Teichman J M H, Kim J, Choi B, Arakeri N V & Welch A J. (2003). Stone retropulsion during Holmium:YAG lithotripsy. *The Journal of Urology.* **169**, 881-885.

Lin S M, Tseng C L & Yang M H. (1987). Determination of major, minor and trace elements on urinary stones by neutron activation analysis. *International Journal of Radiation Applications and Instrumentation. Part A, Applied Radiation and Isotopes.* **38**, 635-639.

Lo E Y, Petschek H & Rosen D I. (1990). A hydrodynamic model for the laser-induced fragmentation of calculi. *Lasers in the life sciences.* **3**, 233-244.

Maghraby H, Engelhardt R, Muschter R & Hofstetter A G. (1990). Laser lithotripsy - in-vitro comparison of different systems. *Proc. SPIE.* **1200**, 106-117.

Maiman T H. (1960). Stimulated optical radiation in ruby. *Nature.* **187**, 493-494.

Marks A J & Teichman J M H. (2007). Lasers in clinical urology: state of the art and new horizons. *World J Urol*. **25**, 227-233.

Marguet C G, Sung J C, Springhart W P, L'Esperance J O, Zhou P, Albala D M & Preminger G M. (2005). In vitro comparison of stone retropulsion and fragmentation of the frequency doubled, double pulse Nd:YAG laser and the Holmium:YAG laser. *The Journal of Urology.* **173,** 1797-1800.

Marjaron B, Plestenjak P & Lukač M. (1999). Thermo-mechanical laser ablation of soft biological tissue: modeling the micro-explosions. *Applied Physics B.* **69,** 71-80.

Matsuoka K, Iida S, Inoue M, Yoshii S, Arai K, Tomiyasu K & Noda S. (1999). Endoscopic Lithotripsy With the Holmium:YAG Laser. *Lasers in Surgery and Medicine.* **25**, 389-395.

Mattioli S, Cremona M, Benaim G & Ferrario A. (1991). Alexandrite laser and blind lithotripsy: Initial experience - first clinical results. *Proc. SPIE.* **1421**, 114-119.

McKenzie A L. (1990). Physics of thermal processes in laser-tissue interaction. *Phys. Med. Biol.* **35**, 1175-1209.

Miller K, Weber H M, Rüschoff J & Hautmann R E. (1991). Experimental and first clinical results with the Alexandrite laserlithotripter. *Proc. SPIE.* **1421**, 108-113.

Müller G J, Berlien P & Scholz C. (2006). The medical laser. *Medical Laser Application.* **21**, 99-108.

Müller G, Helfmann J, Pashinin V P, Pashinin P P, Konov V I, Tumorin V V & Shklosvsky E J. (1993). New alternative for laser lithotripsy, long pulse passively q-switched solid-state laser with fibre-based resonator. *Proc. SPIE*. **2086**, 103-110.

Mulvaney W P & Beck C W. (1968). The laser beam in urology. *The Journal of Urology*. **99**, 112-115.

Muschter R, Knipper A, Maghraby H & Thomas S. (1990). Laser lithotripsy - experience with different laser systems in the treatment of urinary calculi. *Proc. SPIE.* **1200**, 118-123.

Naqvi S, Khaliq M, Zafar M & Rizvi S. (1994). Treatment of ureteric stones. Comparison of laser and pneumatic lithotripsy. *British Journal of Urology*. **74**, 694-698.

Noack J & Vogel A. (1999). Laser-induced plasma formation in water at nanosecond to femtosecond time scales: calculation of thresholds, absorption coefficients, and energy density. *IEEE Journal of Quantum Electronics*. **35**, 1156-1167.

Noor Buchholz N-P. (2002). Intracorporeal lithotripters: selecting the optimum machine. *BJU International*. **89**, 157-161.

Ochmański W, Kmiecik J & Sulowicz W. (1999). Analysis of chemical composition of urinary stones. *International Urology and Nephrology*. **31**, 743-750.

Ooi D S. (1998). Cautionary note regarding urinary calculi analysis with the Merckognost® Kit. *Clinical Chemistry*. **44**, 694-694.

Paluszkiewicz C, Galka M, Kwiatek W, Parczewski A & Walas S. (1997). Renal stone studies using vibrational spectroscopy and trace element analysis. *Biospectroscopy*. **3**, 403-407.

Pearle M S, Sech S M, Cobb C G, Riley J R, Clark P J, Preminger G M, Drach G W & Roehrborn C G. (1998). Safety and efficacy of the Alexandrite laser for the treatment of renal and ureteral calculi. *Urology*. **51**, 33-38.

Peh O H, Lim P H C, Ng F C, Chin C M, Quek P & Ho S H. (2001). Holmium Laser Lithotripsy in the Management of Ureteric Calculi. *Ann Acad Med Singapore.* **30**, 563-567.

Peng Q, Juzeniene A, Chen J, Svaasand L O, Warloe T, Giercksky K-E & Moan J. (2008). Lasers in medicine. *Reports on Progress in Physics.* **71**, 1-28.

Pensel J, Frank F, Rothenberger K, Hofsetter A & Unsold E. (1981). Destruction of urinary calculi by Nd YAG laser irradiation. *Laser Surgery IV. Proceedings of the Fourth International Symposium on Laser Surgery.* **10**, 4-6.

Pierre S & Preminger G M. (2007). Holmium laser for stone management. *World J Urol.* **25**, 235-239.

Pineda C A & Peisach M. (1994). Micro-analysis of kidney stones sequentially excreted from a single patient. *Nuclear Instruments and Methods in Physics Research B* **85**, 896-900.

Pittomvils G, Vandeursen H, Wevers M, Lafaut J P, De Ridder D, De Meester P, Boving R & Baert L. (1994). The influence of internal stone structure upon the fracture behaviour of urinary calculi. *Ultrasound in Med. & Biol.* **20**, 803-810.

Pougnet M A B, Peisach M & Rodgers A L. (1988). The application of a combined PIXE and XRD approach to the analysis of human stones. *Nuclear Instruments and Methods in Physics Research.* **B35**, 472-477.

Puliafito C A & Steinert R F. (1984). Short-pulsed Nd:YAG laser microsurgery of the eye: biophysical considerations. *IEEE Journal of Quantum Electronics.* **QE-20**, 1442-1448.

Pupkova L S, Reznikov L L, Parhomchuk N A, Gomberg V G, Berenberg V G, Murzin A G, Polikarpov S S & Soms L N. (1993). First experience lithotripsy by ruby laser in the microsecond range of pulse duration. *Proc. SPIE.* **2086**, 100-102.

Pupkova L S, Reznikov L L, Sokolovsky A S, Murzin A G, Soms L N, Berenberg V A, Polikarpov S S, Parhomchuk N A & Voskresensky M A. (1994). First experience with blind lithotripsy of ureteral calculi by ruby laser. *Proc. SPIE.* **2129**, 141-150.

Radziemski L J. (2002). From LASER to LIBS, the path of technology development. *Spectrochimica Acta.* Part B **57**, 1109-1113.

Rassweiler J, Irion U, Strauss R, Bub P & Eisenberger F. (1989). Technical Considerations Using a Pulsed Neodym-YAG Laser for Endoscopic Shock Wave Lithotripsy. *Eur Urol.*. **16,** 374-377.

Reichel E, Paltauf G, Schmidt-Kloiber H & Groke K. (1992a). A special irrigation liquid to increase the reliability of laser-induced shockwave lithotripsy. *Lasers in Surgery and Medicine.* **12**, 204-209.

Reichel E & Schmidt-Kloiber H. (1992b). Laser-induced shock wave lithotripsy with a regenerative energy converter. *Lasers in Medical Science.* **7**, 423-425.

Reichel E, Schmidt-Kloiber H, Paltauf G & Groke K. (1991). A bifunctional irrigation liquid as an ideal energy converter for the laserlithotripsy with ns-laserpulses. *Proc. SPIE.* **1421**, 129-133.

Reynard J & Badenoch D. (1997). Laser lithotripsy. *Lasers in Medical Science*. **12**, 3-10.

Rink K, Delacrétaz G & Salathé R P. (1995). Fragmentation process of current laser lithotriptors. *Lasers in Surgery and Medicine.* **16**, 134-146.

Rizvi S A H, Naqvi S A A, Hussain Z, Hashmi A, Hussain M, Zafar M N, Mehdi H & Khalid R. (2002). The management of stone disease. *BJU International.* **89**, Supplement 1, 62-68.

Robertson W G & Peacock M. (1979). Urinary Calculi. In *Urinary calculus disease,* pp 354-374. Edited by J E A Wickham. 1st edition. Edinburgh: Churchill Livingston.

Rosen D I, Bhatta K M & Dretler S P. (1989). Acoustical and optical feedback guidance for pulsed laser lithotripsy and angioplasty. *Proc. SPIE.* **1066**, 262.

Rosen D, Goldey C, Polyakov I & Dretler S. (1993). Real-time optical feedback control of laser lithotripsy. *Proc. SPIE.* **1879**, 149-159.

Rosin D, Brasesco O & Rosenthal R J. (2000). A review of technical and clinical aspects of biliary laser lithotripsy. *Journal of Clinical Laser Medicine & Surgery.* **18**, 301-307.

Rudhart M & Hirth A. (1994). Use of an absorbent in laser lithotripsy with dye lasers: in vitro study of fragmentation efficiency and jet formation. *The Journal of Urology.* **152**, 1005-1008.

Sabot J-F, Bornet C-E, Favre S & Sabot-Gueriaux S. (1999). The analysis of peculiar urinary (and other) calculi: an endless source of challenge. *Clinica Chimica Acta.* **283**, 151-158.

Sayer J, Johnson D E, Price R E & Cromeens D M. (1993a). Endoscopic laser fragmentation of ureteral calculi using the Holmium:YAG. *Proc. SPIE.* **1879**, 143-148.

Sayer J, Johnson D E, Price R E & Cromeens D M. (1993b). Ureteral lithotripsy with the Holmium:YAG laser. *Journal of Clinical Laser Medicine & Surgery.* **11**, 61-65.

Schafer S A, Durville F M, Jassemnejad B, Bartels K E & Powell R C. (1994). Mechanisms of biliary stone fragmentation using the Ho:YAG laser. *IEEE Transactions on Biomedical Engineering.* **41**, 276-283.

Schmidt-Kloiber H. (1991). Laser lithotripsy. *Proc. SPIE.* **1524**, 143-149.
Schmidt-Kloiber H, Reichel E & Schöffmann H. (1985). Laserinduced shock-wave lithotripsy (LISL). *Biomedizinische Technik.* **30**, 173-181.

Scholz C, Gundlach P, Hopf J, Leege N, Tschepe J, Ertl T, Scherer H & Müller G. (1991). The endoscopically controlled laser lithotripsy of salivary stones. *Lasers and Electrooptics.* **13**, 1762-1763.

Shi W Q, Papaioannou T, Vari S, Daykhovsky L & Grundfest W S. (1990). In vitro fragmentation of biliary calculi with a 308 nm Excimer laser. *Proc. SPIE.* **1200**, 75-80.

Shi W Q, Vari S, Papaioannou T, Daykhovsky L & Grundfest W. (1991). Biliary calculi fragmentation by a 308 nm Excimer laser: A preliminary study. *Journal of Clinical Laser Medicine & Surgery.* **April**. 139-141.

Shkadarevich A P, Loyko M M, Satsukevich S V & Buy A A. (1996). Investigation of lithotripsy processes by means of ruby laser. *Proc. SPIE.* **2623**, 498-504.

Siano S, Pini R, Salimbeni R & Vannini M. (1995). Time-resolved imaging of cavitation effects during laser lithotripsy. *Proc. SPIE.* **2323**, 211-217.

Simons D & Koschmann E. (1992). Pulse stretched Alexandrite laser for improved optical fiber reliability for laser lithotripsy. *Proc. SPIE*. **1650**, 78-85.

Singh V K, Rai A K, Rai P K & Jindal P K. (2008). Cross-sectional study of kidney stones by laser-induced breakdown spectroscopy. *Lasers in Medical Science.* **Dec 23**.

Singh V K, Rai V & Rai A K. (2007). Variational study of the constituents of cholesterol stones by laser-induced breakdown spectroscopy. *Lasers in Medical Science.* **24**, 27-33.

Singh V R & Agarwal R. (1990). Mechanical and ultrasonic parameters of kidney stones. *Journal of Lithotripsy and Stone Disease*. **2**, 117-123.

Sofer M, Watterson J D, Wollin T A, Nott L, Razvi H A & Denstedt J D. (2002). Holmium:YAG laser lithotripsy for upper urinary tract calculi in 598 patients. *The Journal of Urology.* **167**, 31-34.

Söhnel O & Grases F. (1993). Fine structure of calcium oxalate monohydrate renal calculi. *Nephron*. **63**, 176-182.

Sperrin M W. (2000). *The Dynamics of Urolith Fragmentation Arising from Laser Induced High Intensity Shockwaves.* PhD Thesis, Cranfield University.

Sperrin M W & Rogers K. (1998). The architecture and composition of uroliths. *British Journal of Urology.* **82**, 781-784.

Sperrin M, Rogers K, Lane D & Southerden P. (2002). An investigation into the architecture and composition of a urinary calculus. *Journal of Materials Science*: Materials in Medicine. **13**, 7-9.

Sperrin M, Rogers K & Reffold N. (1999). Analysing the stress distribution within urinary stones during lithotripsy. *BENCHmark.* **October**, 14-16.

Spore S S, Teichman J M H, Corbin N S, Champion P C, Williamson E A & Glickman R D. (1999). Holmium:YAG lithotripsy: optimal power settings. *Journal of Endourology.* **13**, 559-566.

Steiger E. (1990). Comparison of different pulsed and Q-switched solid-state laser systems for endoscopic laser induced shock wave lithotripsy: performance and laser/stone interactions. *Proc. SPIE.* **1200**, 94-101.

Steiger E. (1991). A new concept of a compact, multiwavelengths solid-state laser for laser induced shock wave lithotripsy. *Proc. SPIE.* **1421**, 140-145.

Steiger E & Geisel G. (1994). Dual-wavelength-Alexandrite-laserlithotripsy: in-vitro results of urinary calculi fragmentation. *Proc. SPIE.* **2129**, 151-155.

Steiner R & Meier T. (1991). Dual wavelengths (750/375nm) laserlithotripsy. *Proc. SPIE.* **1421**, 124-128.

Sterenborg H J C M, de Reijke Th M, Wiersma J, Erckens R C & Jogsma F H M. (1991). High-speed photographic evaluation of endoscopic lithotripsy devices. *Urological Research.* **19**, 381-385.

Tanahashi Y, Orikasa S, Ciba R, Tahira K, Fukatsu T & Miyakawa T. (1979). Disintegration of urinary calculi by laser beam: drilling experiment in extracted urinary stones. *Tohuko J Exp Med* **128**, 189.

Tasca A, Cecchetti W, Zattoni F & Pagano F. (1993). Photosensitization of cystine stones to induce laser lithotripsy. *The Journal of Urology.* **149**, 709-712.

Teichman J M H, Chan K F, Cecconi P P, Corbin N S, Kamerer A D, Glickman R D & Welch A J. (2001). Erbium:YAG versus Holmium:YAG lithotripsy. *The Journal of Urology.* **165**, 876-879.

Teichman J M H, Schwesinger W H, Lackner J & Cossman R M. (2001). Holmium:YAG laser lithotripsy for gallstones. *Surg. Endosc.* **15**, 1034-1037.

Teichman J M H, Vassar G J, Bishoff J T & Bellman G C. (1998a). Holmium:YAG lithotripsy yields smaller fragments than lithoclast, pulsed dye laser or electrohydraulic lithotripsy. *The Journal of Urology.* **159**, 17-23.

Teichman J M H, Vassar G J & Glickman R D. (1998b). Holmium:Yttrium-Aluminium-Garnet lithotripsy efficiency varies with stone composition. *Urology.* **52**, 392-397.

Teichman J M H, Vassar G J, Glickman R D, Beserra C M, Cina S J & Thompson I M. (1998c). Holmium:YAG lithotripsy: photothermal mechanism converts uric acid calculi to cyanide. *The Journal of Urology.* **160**, 320-324.

Teichmann H-O, Herrmann T R & Bach T. (2007). Technical aspects of lasers in urology. *World Journal of Urology.* **25**, 221-225.

Teng P, Nishioka N S, Anderson R R & Deutsch T F. (1987a). Acoustic studies of the role of immersion in plasma-mediated laser ablation. *IEEE Journal of Quantum Electronics.* **QE-23**, 1845-1852.

Teng P, Nishioka N S, Farinelli W A, Anderson R R & Deutsch T F. (1987b). Microsecond-Long flash photography of laser-induced ablation of biliary and urinary calculi. *Lasers in Surgery and Medicine.* **7**, 394-397.

Thomas S, Pensel J, Engelhardt R, Meyer W & Hofstetter A G. (1988). The pulsed dye laser versus the Q-switched Nd:YAG laser in laser-induced shock wave lithotripsy. *Lasers in surgery and medicine*. **8**, 363-370.

Tischer C, Koort H J, Bazo A, Rasch R & Thiede C, World of Medicine Inc., Dept of Medical Lasers, Orlando and Berlin et al. (2002). Clinical experiences with a new Frequency-doubled Double-pulse Nd:YAG Laser (FREDDY) for the treatment of urolithias. *Proc. SPIE*. **4609**, 128-35.

Tiselius H-G. (2003). Epidemiology and medical management of stone disease. *BJU International.* **91**, 758-767.

Turgut M, Unal I, Berber A, Demir T A, Mutlu F & Aydar Y. (2008). The concentration of Zn, Mg and Mn in calcium oxalate monohydrate stones appears to interfere with their fragility in ESWL therapy. *Urol Res.* **36**, 31-38.

Uebelacker W. (1992). Laser lithotripsy with a Q-switched Alexandrite laser system. *Proc. SPIE.* **1643**, 68-72.

Van Swol C F P, Verdaasdonk R M, Zeijlemaker B Y W, Grimbergen M C M & Boon T A. (1998). Optimization of the dosimetry and safety using the Holmium Laser for Urology. *Proc. SPIE*. **3245**, 110-116.

Vassar G J, Chan K F, Teichman J M H, Glickman R D, Weintraub S T, Pfefer T J & Welch A J. (1999). Holmium:YAG lithotripsy: photothermal mechanism. *Journal of Endourology.* **13**, 181-190.

Vassar G J, Teichman J M H & Glickman R D. (1998). Holmium:YAG lithotripsy efficiency varies with energy density. *The Journal of Urology.* **160**, 471-476.

Vergauwe D A G, Verbeeck R M H & Oosterlinck W. (1994). Analysis of urinary calculi. *Acta Urologica Belgica*. **62**, 5-13.

Vogel A. (1997). Nonlinear absorption: intraocular microsurgery and laser lithotripsy. *Phys. Med. Biol.* **42**, 895-912.

Vogel A, Lauterborn W & Timm R. (1989). Optical and acoustic investigations of the dynamics of laser-produced cavitation bubbles near a solid boundary. *Journal of Fluid Mechanics.* **206**, 299-338.

Vogel A, Nahen K, Theisen D & Noack J. (1996). Plasma formation in water by picosecond and nanosecond Nd:YAG laser pulses – part 1: optical breakdown at threshold and superthreshold irradiance. *IEEE Journal of Selected Topics in Quantum Electronics.* **2**, 847-869.

Vogel A, Noack J, Nahen K, Theisen D, Busch S, Parlitz U, Hammer D X, Noojin G D, Rockwell B A & Birngruber R. (1999). Energy balance of optical breakdown in water at nanosecond to femtosecond time scales. *Applied Physics B* **68**, 271-280.

Vogel A & Venugopalan V. (2003). Mechanisms of pulsed laser ablation of biological tissue. *Chem. Rev.* **103**, 577-644.

Waidelich R. (2005). Laser in urology – state of the art. *Medical Laser Application.* **20**, 111-114.

Walter J B & Israel M S. *General Pathology (5th Edition)*. Churchill Livingstone. ISBN 0 443 018901.

Watanabe M, Kajiwara H, Awazu K & Aizawa K. (2001). Bilirubin calculi crushing by laser irradiation at a molecular oscillating region wavelength based on infrared absorption spectrum analysis using a free-electron laser: an experimental study. *Surg Today.* **31**, 626-633.

Watson G, Murray S, Dretler S P & Parrish J A. (1987a). The pulsed dye laser for fragmenting urinary calculi. *The Journal of Urology.* **138**, 195-198.

Watson G, Murray S, Dretler S P & Parrish J A. (1987b). An assessment of the pulsed dye laser for fragmenting calculi in the pig ureter. *The Journal of Urology.* **138**, 199-202.

Watson G, Shroff S, Thomas R, Kellett M & Rickards D. (1994). The Holmium laser for multifunctional use in urology. *Proc. SPIE.* **2129**, 115-118.

Watson G & Smith N. (1993). A comparison of the pulsed dye and Holmium lasers for stone fragmentation: in vitro studies and clinical experience. *Proc. SPIE.* **1879**, 139-142.

Watson G M, Wickham J E A, Mills T N, Bown S G, Swain P & Salmon P R. (1983). Laser fragmentation of renal calculi. *Br J Urol.* **138**, 195-198.

Welch A J. (1984). The thermal response of laser irradiated tissue. *IEEE Journal of Quantum Electronics.* **QE-20**, 1471-1481.

Welch AJ, Kang H W, Lee H & Teichman J M H. (2004). Calculus fragmentation in laser lithotripsy. *Minerva Urol Nefrol.* **56**, 49-63.

Whitfield H N. (1999a). The management of ureteric stones. Part I: diagnosis. *BJU International.* **84**, 911-915.

Whitfield H N. (1999b). The management of ureteric stones. Part II: therapy. *BJU International.* **84**, 916-921.

Wollin T A, Moore R B, Tulip J & McPhee M S. (1996a). In vitro studies investigating the stone fragmenting parameters of the multi-YAG laser. *Proc. SPIE.* **2671**, 359-366.

Wollin T A, Moore R B, Tulip J, Mourad W A & McPhee M S. (1996b). Preclinical assessment of the new 1440 nm wavelength Nd:YAG laser for fragmenting ureteral calculi in an ex vivo pig model. *Proc. SPIE.* **2671**, 367-374.

Zerbib M, Flam T, Belas M, Debre B & Steg A. (1990). Clinical experience with a new pulsed dye laser for ureteral stone lithotripsy. *The Journal of Urology.* **143**, 483-484.

Zhong P, Tong H-L, Cocks F H, Pearle M S & Preminger G M. (1998). Transient cavitation and acoustic emission produced by different laser lithotripters. *Journal of Endourology.* **12**, 371-378.

Zörcher T, Hochberger J, Schrott K-M, Kühn R & Schafhauser W. (1999). In vitro study concerning the efficiency of the frequency-doubled double-pulse Neodymium:YAG laser (FREDDY) for lithotripsy of calculi in the urinary tract. *Lasers in Surgery and Medicine.* **25**, 38-42.

Zumbé J, Fischer H, Kimont H-G & Kierfeld G. (1993). Intracorporal Alexandrite-laser lithotripsy in the treatment of ureteral calculi. *Proc. SPIE.* **2086**, 96-99.

Web sites

History of Lasers, website of the University of Alaska
http://ffden-2.phys.uaf.edu/212_fall2003.web.dir/James_Becwar/history/

Kidneystoneindia.com
http://www.kidneystoneindia.com/laser-kidney-stone-treatment.php

Sialendoscopy.net
http://www.sosromandie.ch/cv/sites/Sialendoscopy/page1.htm

Stubborn Kidney Stones
http://www.nymc.edu/pubs/chironian/fall99/kstones.htm

Theodore Maiman and the laser, website of the IEEE
http://www.ieeeghn.org/wiki/index.php/Theodore_Maiman_and_the_Laser

APPENDIX A

Laser specifications

Table A.1: Nd:YAG laser output specifications

Parameter	Specification
Laser crystal	Nd:YAG
Wavelength	1064 nm
Operating mode	Q-switched (pulsed)
Pulse duration (FWHM)	~ 6 ns
Max. pulse frequency	20 Hz
Max. pulse energy	~ 200 mJ
Max. average power	~ 4 W
Peak pulse power	~ 33 MW
Energy stability	± 5%
Beam diameter (laser aperture)	5 mm
Beam diameter (focussed, 25 mm lens - diffraction limited)	~ 13 μm
Peak pulse irradiance (based on above)	~ 2 x10^{13} W cm^{-2}
Beam divergence from laser cavity	< 2 mrad

Table A.2: Ho:YAG laser output specifications

Parameter	Specification
Laser crystal	Ho:YAG
Wavelength	2.12 μm
Operating mode	Free running (pulsed)
Pulse duration (FWHM)	120 – 800 μs
Max. pulse frequency	30 Hz
Max. pulse energy	3 J
Max. average power	30 W
Peak pulse power	9 kW
Energy stability	N/A
Beam diameter (fibre)	600 μm
Peak pulse irradiance	~ 28 MW cm^{-2}
Beam divergence from fibre	400 – 440 mrad

APPENDIX B

FT-IR spectra of reference compounds

The following FT-IR spectra were obtained for pure laboratory compounds and used as reference spectra in the identification of urinary calculi samples (section 5.1.1).

B.1: FT-IR Cystine ($C_6H_{12}N_2O_4S_2$)

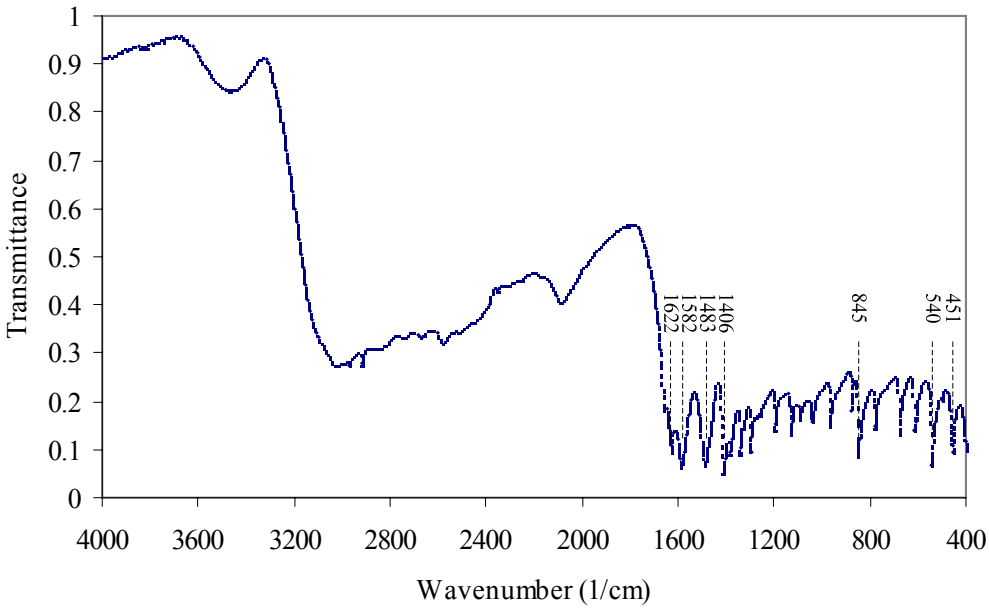

B.2: FT-IR Magnesium Ammonium Phosphate Hexahydrate ($MgNH_4PO_4.6H_2O$)

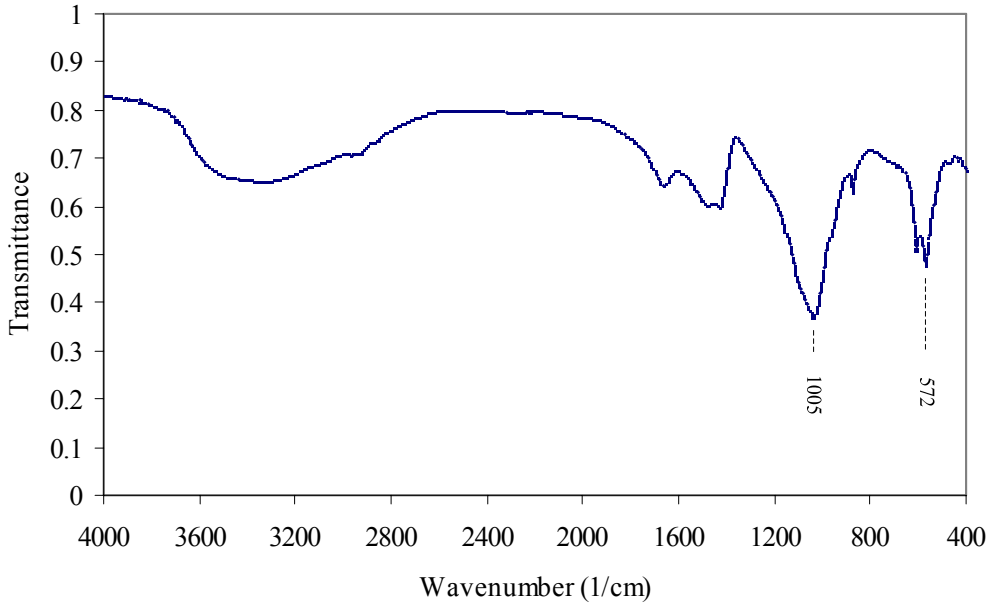

B.3: FT-IR Calcium Hydrogen Phosphate Dihydrate ($CaHPO_4.2H_2O$)

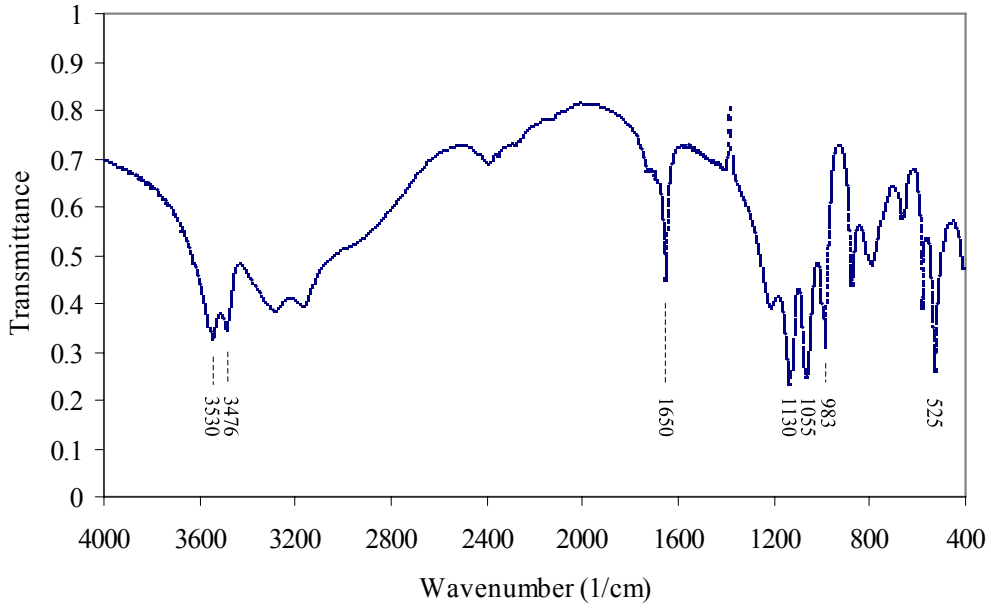

B.4: FT-IR Calcium Oxalate Dihydrate ($CaC_2O_4.2H_2O$)

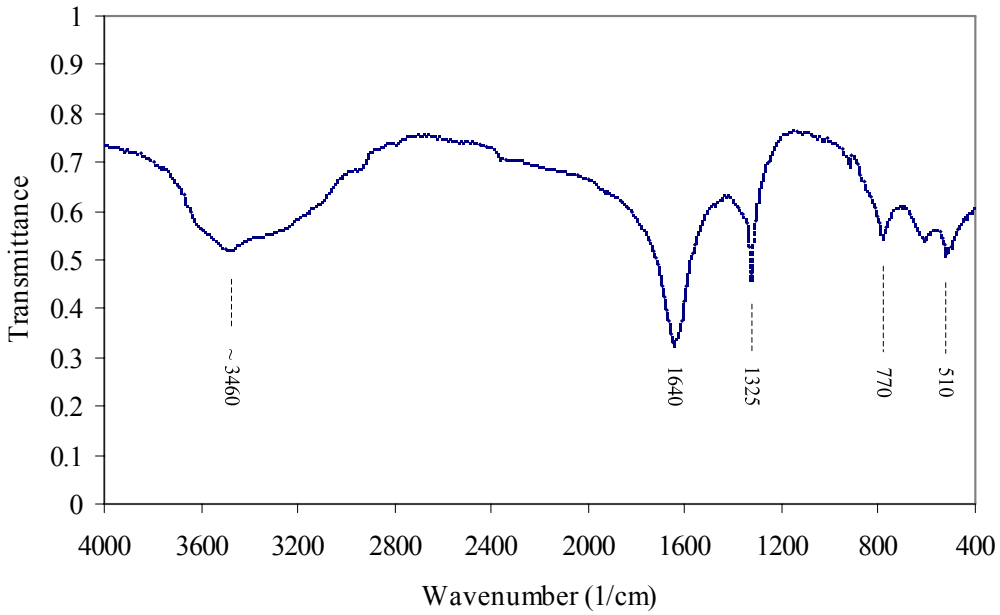

B.5: FT-IR Calcium Oxalate Monohydrate ($CaC_2O_4.H_2O$)

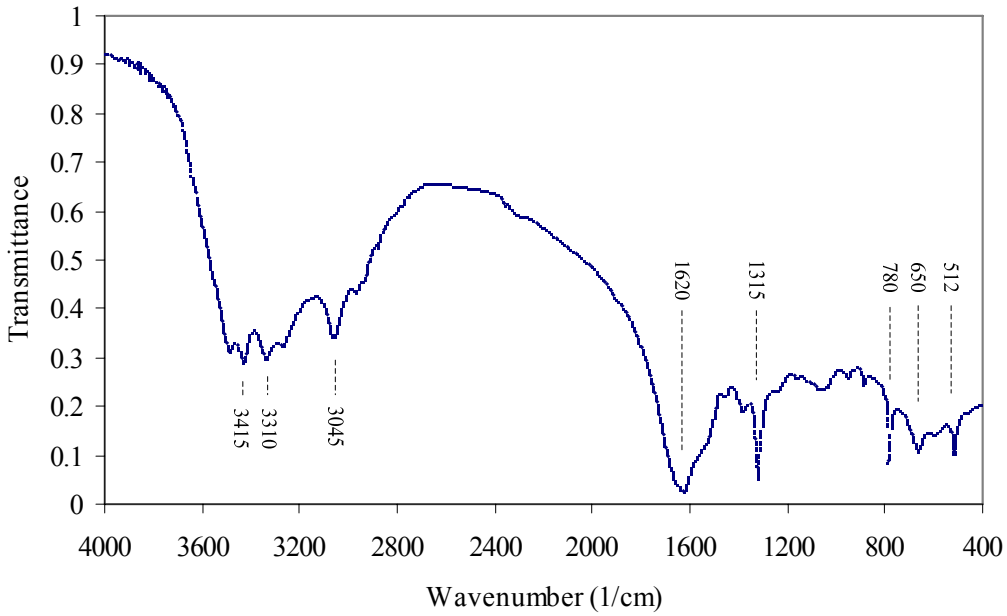

B6: FT-IR Uric Acid ($C_5H_4N_4O_3$)

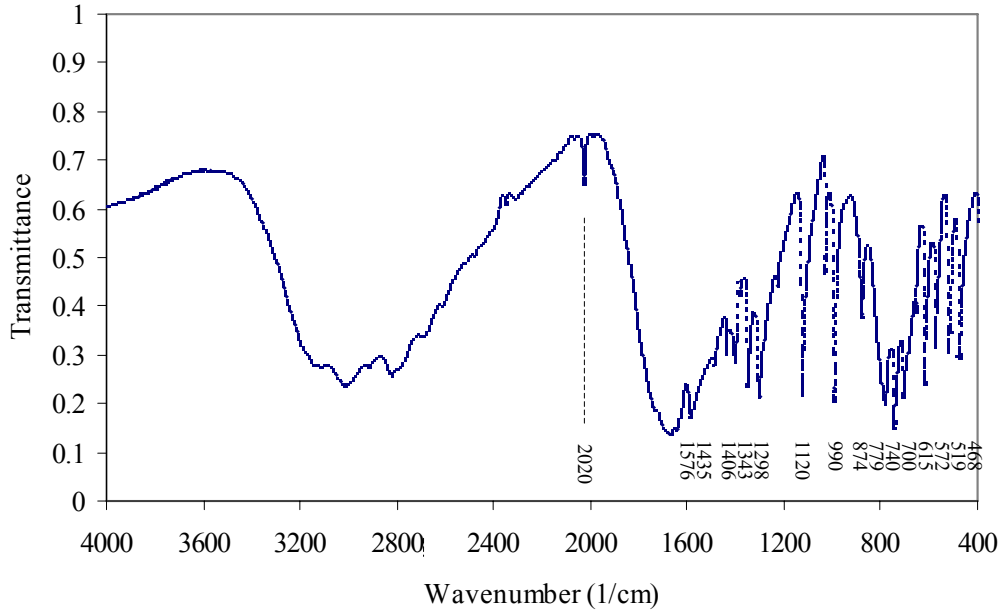

APPENDIX C

Photographs of laser-induced damage on calculi samples

The following photographs show Ho:YAG and Q-switched Nd:YAG laser-induced damage on selected calculi samples. A quantitative investigation of calculus fragmentation with laser parameters was not carried out owing to the limited number of samples available and the destructive nature of such experiments. An appropriate methodology would be to fabricate synthetic calculi with properties closely matching natural human calculi and to carry out systematic ablation of the material for a range of laser parameters and to look for correlation with crater profile. This could form the basis of further work.

Nd:YAG / sample 4

Figure C.1: Photograph showing Q-switched Nd:YAG laser-induced damage on the surface of calculus Sample 4 composed of brushite (calcium hydrogen phosphate dihydrate). 10 shots at ~ 30 mJ per pulse were focussed onto the submerged calculus. The crater appears to be symmetrical in shape and deeper towards the centre. The general absence of blackening suggests that the material has been removed by non-thermal processes i.e. mechanical action from shockwaves. There is, however, some evidence of localised charring at the centre, possibly arising from plasma formation at the beam focus where the temperature (~ 7000 °C) exceeds the decomposition temperature of brushite (~ 350 °C).

Nd:YAG / sample 9

Figure C.2: Q-switched Nd:YAG laser damage on uric acid composition (Sample 9) showing extensive charring from laser action when positioned at the beam focus (parameters ~ 30 mJ per pulse, total approx 100 pulses). In this case the sample was irradiated in air; in water the laser action was seen to easily fragment the calculus with only a few pulses. The evidence of a thermal effect indicates that there must be some absorption at the laser wavelength, leading to temperatures exceeding the material decomposition (> 300 °C).

Ho:YAG / sample 5

Figure C.3: Photograph showing action by Ho:YAG laser on a cystine calculus (Sample 5) immersed in water appears to show strong thermal effect. The crater is charred throughout with evidence of melting suggesting that the laser beam directly irradiated the calculus surface, which supports the 'moses effect' model of vaporising a channel through the water. Cystine has a melting point of 260 °C. The width of the crater was found to be approximately the same as the estimated beam dimension at the fibre exit, providing further confirmation.

Ho:YAG / sample 3

Figure C.4: Photograph showing a series of Ho:YAG laser-induced craters on a struvite calculus (Sample 3: magnesium ammonium phosphate hexahydrate) during irradiation in water. Each crater was formed by 10 laser pulses of ~ 1J per pulse. In this case, there is no apparent charring within the crater suggesting a dominant process of mechanical ablation i.e. possible shockwave action leading to stress fracture within the material. This is supported by the observation that crater size was estimated to be significantly larger than the fibre diameter; hence the action is not purely direct thermal ablation via a vaporised channel through water.

APPENDIX D

LIBS Calibration

The concentrations of the metals in the urinary calculi samples were estimated by comparing signal intensities at the emission wavelengths against signal intensities obtained for reference compounds exposed to identical laser ablation parameters. The reference compounds contained known concentrations of the same elements of interest and this allowed calibration factors to be determined (note this work was not carried out by the author).

An assumption was made that the laser interaction with the reference compounds was comparable to that with urinary calculi i.e. that a similar amount of material would be ablated by the laser pulse. To replicate the density of the stone matrix the powder was fabricated into a pellet by pressing in a die. The reference samples were then placed at the laser beam focus as were the calculi samples, so that all LIBS samples were exposed to identical conditions of laser excitation.

The reference compounds used were obtained in powder form and comprised of calcium chloride ($CaCl_2.2H_2O$), sodium chloride (NaCl), magnesium sulphate ($MgSO_4.7H_2O$), potassium dihydrogen phosphate (KH_2PO_4), strontium chloride ($SrCl_2.6H_2O$), and lead acetate ($(CH_3COO)_2Pb.3H_2O$). The compounds were used in their pure form and not made up in various concentrations in a matrix. With this method there is an assumption of linearity in the signal intensity i.e. that elemental concentration (C(e)) is proportional to signal (counts):

$$C(e)_{\text{sample}} = C(e)_{\text{reference}} \times \text{counts (sample)} / \text{counts (reference)}$$

The molecular weights of the compounds (MW) and the corresponding molecular weights of the metal element (MW(e)) and their concentration by mass (C(e)) are given in Table D1. The counts obtained for the reference emission lines are also shown, and the derived calibration factors of counts per unit concentration of element. These factors were then used for the calculation of concentrations of metal elements in the calculi samples, as shown in Tables D2 – D7. (Note ND = not detected).

Table D.1: LIBS calibration factors derived for reference compounds

Reference compound	MW (g)	MW(e) (g)	C(e)	Ref line (nm)	Counts	Counts / Ce
$CaCl_2.2H_2O$	146.98	40.08	0.27	458.6	530000	1.94×10^6
NaCl	58.44	23	0.39	589.0	170000	4.31×10^5
$MgSO_4.7H_2O$	2246.48	24.3	0.10	407.5	6900	7.00×10^4
KH_2PO_4	136.09	39.1	0.29	404.4	440000	1.53×10^6
$SrCl_2.6H_2O$	266.6	87.6	0.33	460.7	190000000	5.78×10^8
$(CH_3COO)_2Pb.3H_2O$	379.33	207.2	0.55	405.8	2700000	4.94×10^6

Table D.2: LIBS derived concentrations of calcium in calculi samples

Calculus sample (no.)	Calcium counts at ref line (458.6 nm)	Ca C(e)/ppm	Ca %
Struvite / Ca apatite (3)	220000	115000	12
Brushite (4)	710000	364200	36
Cystine (5)	580	300	0.03
COD (6)	300000	153600	15
COM (7)	200000	102200	10
Uric acid (9)	5400	2800	0.3
Struvite (10)	94000	48400	5

Table D.3: LIBS derived concentrations of sodium in calculi samples

Calculus sample (no.)	Sodium counts at ref line (589.0 nm)	Na C(e)/ppm
Struvite / Ca apatite (3)	103	239
Brushite (4)	249	596
Cystine (5)	22.9	53
COD (6)	196	453
COM (7)	138	320
Uric acid (9)	407	942
Struvite (10)	526	1218

Table D.4: LIBS derived concentrations of magnesium in calculi samples

Calculus sample (no.)	Magnesium counts at ref line (407.5 nm)	Mg C(e)/ppm	Mg %
Struvite / Ca apatite (3)	760	10900	1
Brushite (4)	4860	69500	7
Cystine (5)	308	4400	0.4
COD (6)	2590	37000	4
COM (7)	1670	23900	2
Uric acid (9)	0	0	ND
Struvite (10)	5300	76200	8

Table D.5: LIBS derived concentrations of potassium in calculi samples

Calculus sample (no.)	Potassium counts at ref line (404.4 nm)	K C(e)/ppm
Struvite / Ca apatite (3)	48	31
Brushite (4)	0.0	ND
Cystine (5)	0.0	ND
COD (6)	0.0	ND
COM (7)	704	460
Uric acid (9)	0.0	ND
Struvite (10)	179	117

Table D.6: LIBS derived concentrations of strontium in calculi samples

Calculus sample (no.)	Strontium counts at ref line (460.7 nm)	Sr C(e)/ppm
Struvite / Ca apatite (3)	179000	310
Brushite (4)	8100	14
Cystine (5)	3500	6
COD (6)	17300	3
COM (7)	5200	9
Uric acid (9)	580	1
Struvite (10)	62000	107

Table D.7: LIBS derived concentrations of lead in calculi samples

Calculus sample (no.)	Lead counts at ref line (405.8 nm)	Pb C(e)/ppm
Struvite / Ca apatite (3)	0	ND
Brushite (4)	1900	392
Cystine (5)	0	ND
COD (6)	1100	224
COM (7)	0	ND
Uric acid (9)	0	ND
Struvite (10)	0	ND

APPENDIX E

Publication arising from this work

Fang X, Ahmad S R, Mayo M & Iqbal S. (2005). Elemental analysis of urinary calculi by laser induced plasma spectroscopy. *Lasers in Medical Science.* **20**, 132-137.

Lasers in Medical Science (2005) 20: 132–137
DOI 10.1007/s10103-005-0356-8

ORIGINAL ARTICLE

Xiao Fang · S. Rafi Ahmad · Mike Mayo · Syed Iqbal

Elemental analysis of urinary calculi by laser induced plasma spectroscopy

Received: 3 May 2005 / Accepted: 6 September 2005 / Published online: 29 September 2005

Abstract Laser induced plasma spectroscopy (LIPS) has been applied to analyse and identify elemental constituents of urinary calculi. Measurements on seven different urinary stone samples were conducted and the concentrations of some key elemental species were estimated. The elements detected with the present system were: Calcium, Magnesium, Sodium, Samarium, Potassium and Lead. Absolute concentrations of the species were derived from pre-calibration of the system for each element. Their concentrations were found to be widely different in different samples. It was observed that the samples containing a significant amount of lead have large proportion of calcium. It has been established that LIPS would allow real time clinic measurements of elemental contents and the concentrations in the biomaterials without sample preparation. The technique has the potential for routine clinic applications in urological disorder diagnosis.

Keywords Calculi · Urinary · Elements · Spectroscopy · Laser

Introduction

Urinary stones are crystals or agglomerates, composed mainly of oxalate, and/or phosphate and urate, formed in urine or kidney. Stone disease in the Western world has a prevalence of 5–12% and a very high recurrence rate rising to 50% after 10 years. Most stones occur due to dietary factors or metabolic disorders, where abnormally high levels of certain elements, e.g. Calcium, Magnesium, Potassium and Lead, etc. are present in them [1]. It is possible that the chemical compositions of the stones are influenced by the elements as active catalysts or chelating agents. A variety of spectroscopic analytical techniques has been widely used to identify and analyse the structural and elemental compositions of urinary stones. Infrared and Raman spectroscopy and X-ray diffraction [2–6] have been applied for the analysis of structural composition, while inductively coupled plasma atomic emission spectroscopy, graphite furnace atomic absorption spectroscopy and particle induced X-ray emission spectroscopy have been used for the analysis of elemental composition [4, 7–9]. All of these analytical techniques, particularly the ones for elemental analysis, require time and labour intensive specialist sample preparation and presentation protocols. For fast and in situ analysis, laser induced plasma spectroscopy (LIPS) has been found to be a suitable technique for elemental analysis in solid materials [10, 11], although no report on the application of the technique for urinary stone analysis has appeared in the literature as far as we are aware. LIPS has been applied for trace element analysis and on line monitoring of solid material such as metal alloy, limestone, glass, marble and ceramics, etc. [12–16] and also liquid materials such as water, oil and marine sediments, etc. [17–21]. The advantage of the LIPS technique is that it does not require any special sample preparation and presentation efforts. To evaluate the application of this technique to biomaterials and to analyse elemental compositions of urinary stones, a LIPS system was set up and the atomic emission spectra of a variety of urinary stone samples were recorded and analysed.

X. Fang · S. R. Ahmad (✉) · M. Mayo
Centre for Applied Laser Spectroscopy, RMCS, DEOS,
The Defence Academy of the UK, Cranfield University,
SN6 8LA Wiltshire, Shrivenham, UK
E-mail: s.r.ahmad@cranfield.ac.uk

S. Iqbal
Eurology Department,
The Great Western Hospital (NHS Trust),
Marlborough Road, SN3 6BB Wiltshire, Swindon, UK

Materials and methods

A selection of human urinary stones was obtained from a hospital laboratory archive (Chemical Pathology, Great Western Hospital, Swindon). The samples were chosen to represent a range of calculus types, including stones containing calcium and magnesium, and also larger

specimens with the potential to contain a mixture of elements.

As part of routine clinical diagnosis, laboratory tests using a wet chemistry urinary calculus analysis kit (Merckognost by Merck, Germany) were previously performed to determine the chemical composition and stone grouping. This information was available, but further analysis using Fourier Transform Infra-red Spectroscopy (FTIR) was carried out owing to its higher sensitivity. A Bruker Opus FTIR system was utilised, and transmission spectra were obtained for all samples and compared to reference spectra of pure compounds such as calcium oxalate, calcium phosphate, uric acid and cystine. A standard decision tree for identification of calculi was used to interpret the spectra. This established a more accurate identification of the samples based on major composition. However, of particular interest are the metallic elements, including trace metals that may be found in the crystal structure and organic matrix, and it was recognised that only the major elements would be detected.

The stones were supplied dry and stored in sealed pots, having been washed in deionised water following extraction from the patients. Therefore, the samples were examined as received, as all traces of urine, blood and other possible contaminants had been removed. The details of the stone samples used for the experimental analysis are listed in Table 1.

The experimental setup, shown schematically in Fig. 1, consists of a laser source, a sample presentation system, a monochromator/spectrograph and the choice of two detection systems. One of them is based on an intensified diode array/optical multichannel analyser, and the other on a photomultiplier/gated charge integrator. The latter was used in this experiment as it allowed application of gate pulses with adjustable gate width and gate delay to achieve optimum S/N ratio.

The laser source is an Nd-YAG (Litron 200-UK), operating at 1,064 nm wavelength and capable of delivering a maximum energy of 200 mJ over a pulse duration of ~6 ns (FWHM) at a maximum pulse repetition rate of 20 Hz. The beam diameter at the exit is 5 mm and the quoted beam divergence is <2 mrad. A 25 mm focal length lens was used to focus the beam on to the stone sample and the laser pulse energy and pulse repetition rate were maintained at 25 mJ and 20 Hz, respectively, for the present experiments.

The spectral dispersion is achieved by a high-resolution (maximum ~10 cm^{-1}) f/7.8 double monochromator (SPEX 1404). The spectral purity is quoted to be $<10^{-14}$ at wavelength >0.5 nm from a set wavelength. The spectral coverage extends from UV to near IR

Table 1 Sample specifications and structures of urinary stones used for the research (obtained from chemical analysis and IR spectroscopy)

Sample	Specification	Predominant chemical composition	Comments
A	Large pale off-white calculus, oval shaped, slightly rough surface. Size ~70 mm max	Calcium carbonate (apatite) $Ca_{10}(PO_4)_6CO_3$	The sample had been previously cut, revealing a concentric layered structure around a central core. The composition of the core and inner layers was not identified in these experiments but in a large mixed stone these layers are quite possibly of different composition to the outer material
B	Pale cream coloured calculus, smooth surface. Size ~22 mm	Calcium phosphate, $CaHPO_4.2H_2O$	Comparison with FTIR spectrum of reference calcium hydrate phosphate dihydrate (brushite) gave good agreement although likely to be a mixture. The presence of some sharp peaks in the range 650–1,200 cm^{-1} indicates an organic component
C	Grey smooth calculus, size ~30 mm. Lighter coloured material beneath the surface	Cystine $(SCH_2CH(NH_2)COOH)_2$	FTIR spectrum of sample compared to reference sample of pure cystine and showed very close agreement. Laboratory results indicated 50% cystine
D	Brown crystalline calculus with a rough surface. Size ~10 mm	Calcium oxalate CaC_2O_4	Comparison with FTIR spectrum of pure calcium oxalate monohydrate (whewellite) showed good agreement
E	Dark brown calculus of crystalline appearance. Size ~8–10 mm	Calcium oxalate CaC_2O_4	Comparison with FTIR spectrum of pure COM showed good agreement
F	Several small calculi, up to 5 mm in size. Cream coloured and of smooth appearance	Uric acid $C_5H_4N_4O_3$	Comparison with FTIR spectrum of pure uric acid showed very close agreement. Laboratory results indicated monohydrate form
G	Large calculus (size ~50 mm), oval shaped with lobes present. Dark brown surface, underlying material off-white	Magnesium ammonium phosphate (struvite) $MgNH_4PO_4.2H_2O$	Mixed stone (secondary type). Previous wet chemistry analysis by laboratory indicated presence of minor calcium oxalate. However, analysis of FTIR spectrum did not confirm this

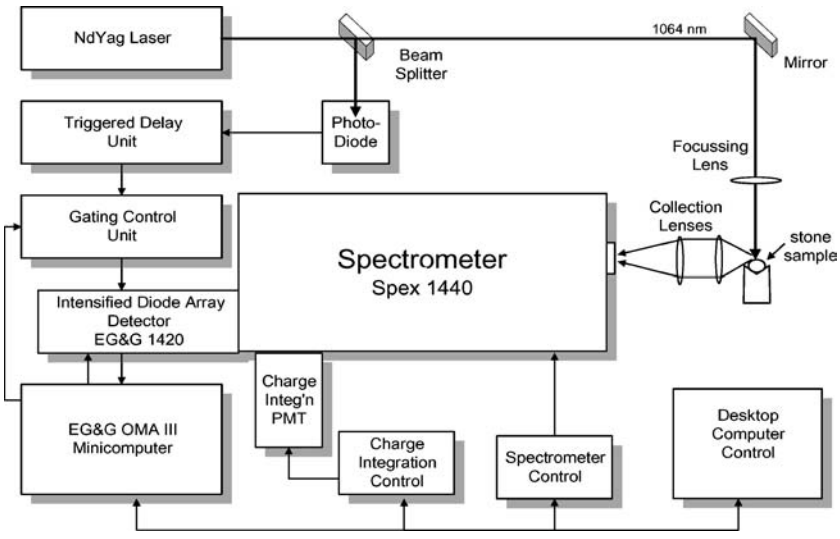

Fig. 1 Schematic of apparatus for laser induced plasma spectroscopy experiments for elemental analysis of solid biomaterials

wavelengths depending upon the grating type being used. The plasma source was imaged on to the entrance slit of the monochromator with collecting lens of 50 mm diameter and a focusing lens ($f = 200$ mm) giving an $f\#$ nearly matching that of the monochromator.

Temporal scans of the emission from plasma were recorded using a digital oscilloscope (Digiscope-HP5 411D-HP, USA). The bandwidth of the instrument was 500 MHz, thus enabling it to faithfully reproduce signals with rise time of ≥2 ns.

The gated charge integrator electronic system (EG&G PARC Model 4420) allowed detection of signals from the plasma through a time gate of width, variable between 2 ns and 2 ms after a time delay from the laser pulse, variable from 50 ns to 2 ms. The photomultiplier (electron Tube-9214B) has a rise time of 2 ns and a spectral window for good response of 300–600 nm. The PM dark current is quoted to be 1 nA (200 counts s^{-1}).

Although relatively low laser power was required to generate plasma, many tightly focused laser pulses, required for good data averaging, bored into the stone material creating a pit. Thus during collection of the LIPS spectra, plasma signal from both the surface and the underlying material was included. Also, as the laser induced pit became more pronounced the material was no longer in the exact focus and so weaker plasma was generated thus requiring the repositioning of the sample several times during signal collection to overcome these difficulties. This offered the added advantage of averaging the signal over a large area of the sample.

Results and discussion

In laser induced plasma, atomic emission from excited metalloid atoms in a solid sample follows the plasma Bremsstrahlung emission by a few microseconds delay. Figure 2 shows the temporal scan of the emission from laser-induced plasma on a NaCl sample at the wavelengths of 589 nm (Na atomic emission line) and 588 nm, respectively. Therefore, a gating method with a proper gate delay and gate width allows the excited atomic emission in the plasma environment to be detected without receiving or with little plasma Bremstrahlung emission as a background. From this measurement a gate width of ~20 μs and a gate delay of ~3 μs with respect to the Bremsstrahlung emission (the first pulse in Fig. 2) were used to detect the LIPS signals

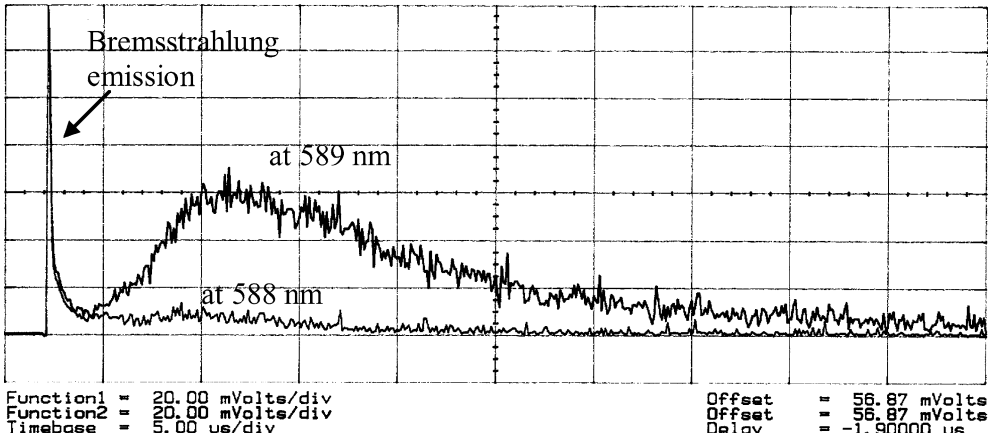

Fig. 2 An example of temporal history of plasma emission from a sample of NaCl

of atomic emission of the stone samples. These were found to be the compromise of best gating parameters for the present measurements.

The atomic emission spectra from laser induced plasma of seven urinary stone samples were recorded and analysed for elemental identification and the comparison of their concentrations. From a detailed analysis and comparison of the data with those obtained from the software database (Optical Emission Lines of the Elements, John Wiley & Sons, 2000) the elements identified in these samples are: Ca, Na, Mg, Sr, K and Pb. At the required data acquisition rate, approximately 40,000 laser pulses would be needed to cover a range of emission wavelengths to record the lines of the studied samples. However, the signal intensity was forced to decrease progressively and disappear after ~800 pulses due to material emission from the beam focused region. Therefore, all the spectra were recorded only over the specific emission lines requiring minimum laser shots (<600 pulses). Figure 3 shows strong Ca atomic lines at 457.9, 458.1 and 458.6 nm having different signal strengths in samples B, D and F. Calcium phosphate (sample B) shows the strongest signal strength among these calcium type samples. Strong Na atomic lines at 589 and 589.6 nm were detected, as shown in Fig. 4, for samples B, C and G. With relatively weaker signal strengths, the emission from Mg at 407.5 nm and Sr at 460.7 nm was detected, in different samples as shown in Figs. 5 and 6, respectively. Relatively weaker signals were observed at 404.4 and 404.7 nm from samples A, E and G, indicating presence of potassium (K) and an emission line from samples B and D at 405.8 nm indicating the presence of lead (Pb), as shown in Figs. 7 and 8, respectively.

The concentrations of these metals in the urinary stone samples were indicated by the signal intensities of the atomic lines provided the specimen was at the focus. Assuming linear calibrations for each element at its detected emission wavelengths, their elemental concentrations in all the samples were estimated and listed in Table 2. At low values of the concentration, the above assumption of linearity with concentration is most likely to be valid. However, at higher concentrations, the signal intensities are expected to be non-linear and likely to saturate at some values of concentration of the species. The saturations were mainly caused by PM tube limitation due to intense emission of strong lines from the elements at high concentrations. The relatively high concentrations of Calcium present in all the samples correspond to their major constituents as specified in Table 1 and the present estimation for Ca and Mg may have large error. However, such error due to saturation is expected to be negligible for other elements and the error due to monitoring methods is estimated to be less than 10%.

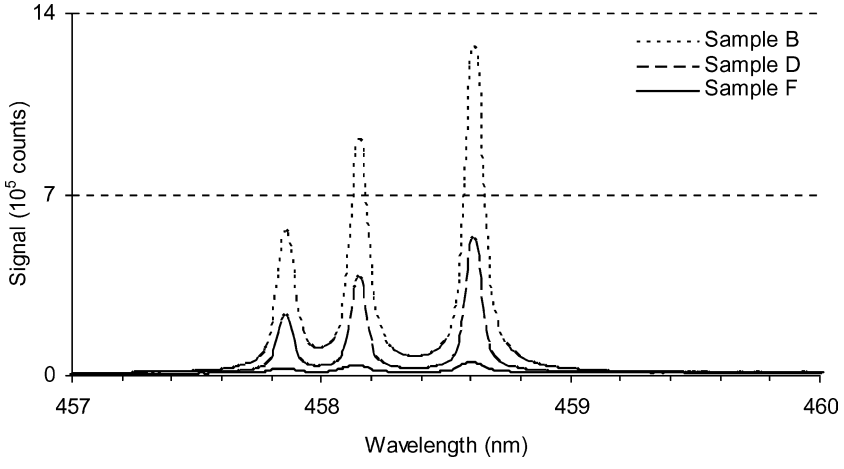

Fig. 3 Calcium atomic emission lines of some urinary stones at 457.9, 458.1 and 458.6 nm

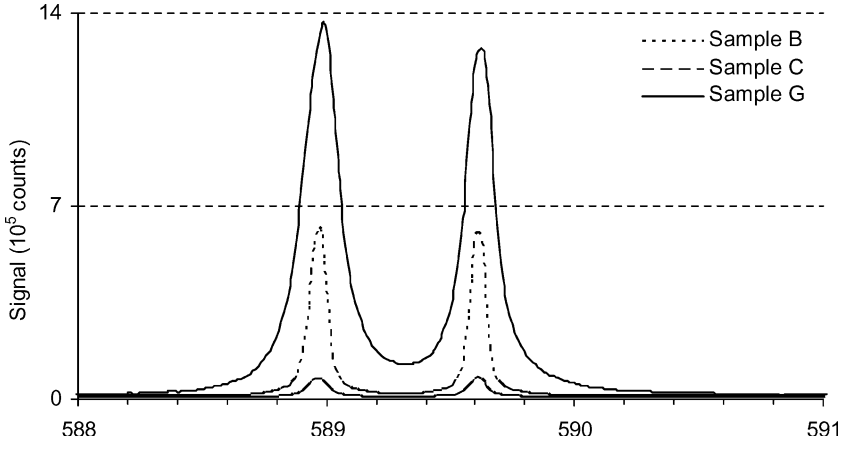

Fig. 4 Sodium atomic emission lines of some urinary stones at 589 and 589.6 nm

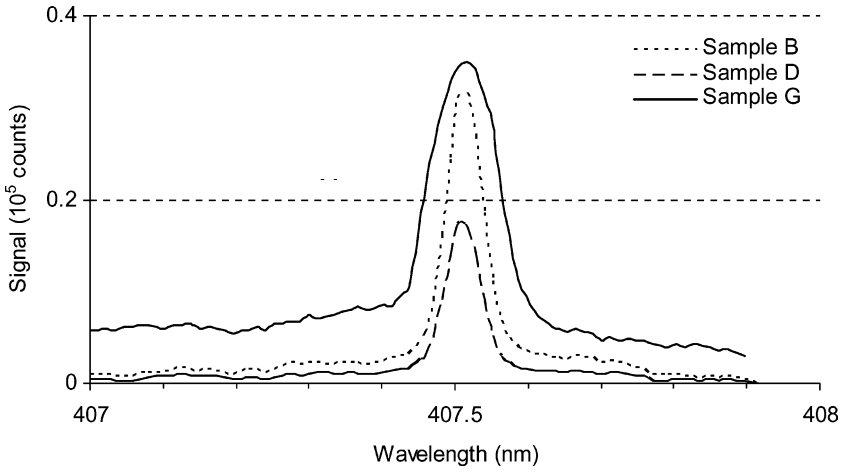

Fig. 5 Magnesium atomic emission line of some urinary stones at 407.5 nm

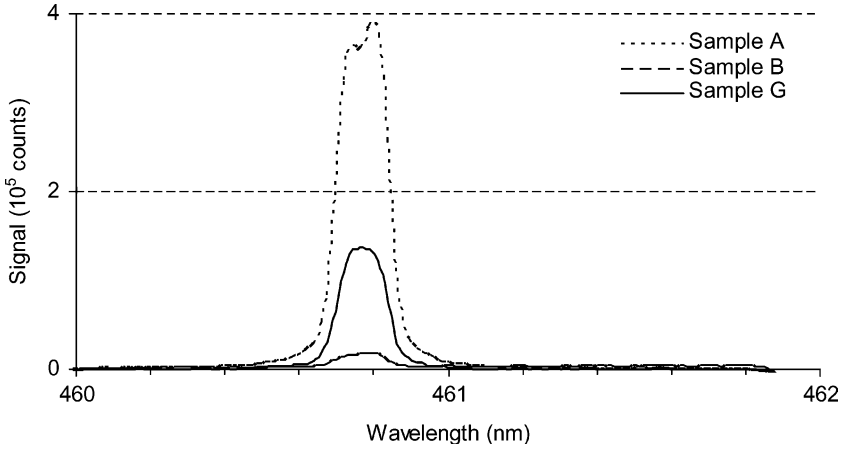

Fig. 6 Strontium atomic emission line of some urinary stones at 460.7 nm

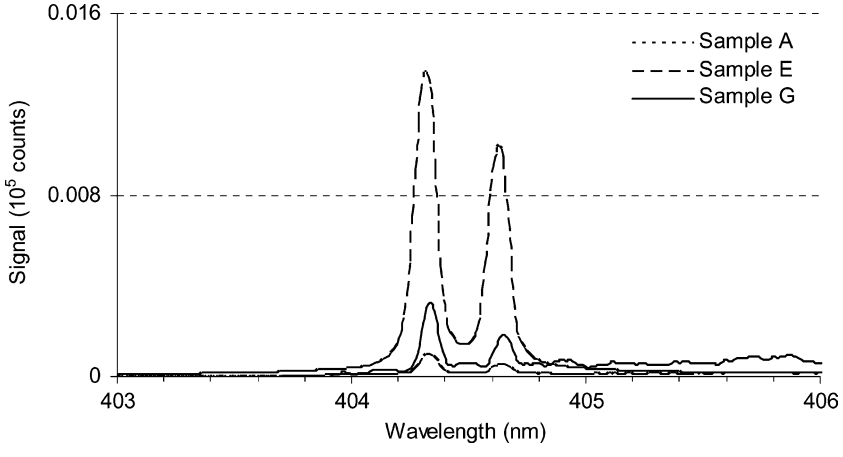

Fig. 7 Potassium atomic emission lines of some urinary stones at 404.4 and 404.7 nm

Sample G shows strong emission of Mg line (407.5 nm) and therefore a relatively high concentration in conformity with the chemical analysis in Table 1. However, high concentration of Mg in the sample B does not confirm with the chemical composition in the table. From the results, it is observed that the samples having significant amount of lead (sample B and D) contain relatively higher concentration of Ca. This observation supports the conclusion made in [4], where data on the relative concentrations of the elements were obtained using FTIR spectroscopy. Although the chemical analysis of the samples did not indicate the presence of Na in any of the samples, the element was detected in all the samples. It is possible that either the element was not a target species in chemical analysis process or the samples were at some stage preserved or soaked in saline water.

Conclusion

Laser induced plasma spectroscopy has been used successfully for the elemental analysis of urinary stones. The technique offers the possibility of accurate measurements

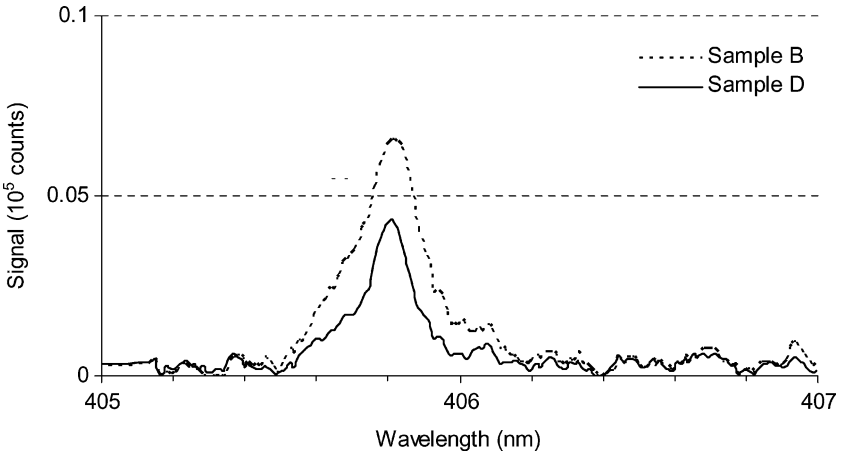

Fig. 8 Lead atomic emission line of some urinary stones at 405.8 nm

Table 2 Elemental concentrations of the urinary stone samples measured with laser induced plasma spectroscopic techniques

	Ca (%)	Mg (%)	Na (ppm)	Sr (ppm)	K (ppm)	Pb (ppm)
Sample A	12	1	239	310	31	ND
Sample B	36	7	596	14	ND	392
Sample C	0.03	0.4	53	6	ND	ND
Sample D	15	4	453	3	ND	224
Sample E	10	2	320	9	460	ND
Sample F	0.3	ND	942	1	ND	ND
Sample G	5	8	1218	107	117	ND

ND, Not detected

of trace elements in such stones without the need for any elaborate sample preparation. However, for quantitative measurements the system needs to be calibrated for each elemental species. It is also possible that the technique may be used for in vitro diagnosis for choosing appropriate laser parameters in laser lithotripsy. Further research on the dependence of signal strengths of the atomic lines on laser wavelength and pulse width will allow optimisation of laser parameter for the design and development of a cost-effective portable laser lithotripter.

References

1. Kasidas GS, Samuell CT, Weir TB (2004) Renal stone analysis: why and how. Ann Clin Biochem 41:91–97
2. Carmona P, Bellanato J, Escolar E (1997) Infrared and Raman spectroscopy of urinary calculi: a review. Biospectroscopy 3:331–346
3. Tunney MM, Bonner MC, Keane PF, Gorman SP (1996) Development of a model for assessment of biomaterial encrustation in the upper urinary tract. Biomaterial 17:1025–1029
4. Paluszkiewicz C, Galka M, Kwiatek W, Parczewski A, Walls S (1997) Renal stone studies using vibrational spectroscopy and trace elemental analysis. Biospectroscopy 3:403–407
5. Estepa L, Daudon M (1997) Contribution of Fourier transformation infrared spectroscopy to the identification of urinary stones and kidney crystal deposites. Biospectroscopy 3:347–369
6. Premasiri WR, Clarke RH, Womble ME (2001) Urine analysis by laser Raman spectroscopy. Laser Surg Med 28:330–334
7. Rodges A, Barbour L, Pougnet B, Lombard C, Ryall R (1994) Urinary element concentrations in kidney stone formers and normal controls: the weekend effect. J Trace Elem Electrolytes Health Dis 8:87–91
8. Perk H, Serel TA, Kobar A, Deniz N, Sayin A (2002) Analysis of the trace element contents of inner nucleus and outer crust parts of urinary calculi. Urol Int 68:286–290
9. Hofbauer J, Steffan I, Hobarth K, Vujicic G, Schwetz H, Reich G, Zechner O (1992) Trace elements and urinary stone information: new aspects of the pathological mechanism of urinary stone formation. J Urol 148:898–901
10. Lee WB, Wu JY, Lee YI, Sneddon J (2004) Recent applications of laser induced breakdown spectroscopy: a review of material approaches. Appl Spectrosc Rev 39:27–97
11. Radziemski LJ (2002) From laser to LIBS, the path of technology development. Spectrochim Acta B57:1109–1113
12. Bassiotis I, Diamantopoulou A, Giannoudakos A, Kalantzopoulou FR, Kompitsas M (2001) Effects of experimental parameters in quantitative analysis of steel alloy by laser-induced breakdown spectroscopy. Spectrochim Acta B56:671–682
13. Fenic C, Dabu R, Stratan A, Blanaru C, Ungureanu C, Luculescu C (2004) Preliminary studies of material surface cleaning with a multi-pulse passively *Q*-switched Nd:YAG laser. Optics Laser Technol 36:125–130
14. Klein S, Stratoudaki T, Zafiropulos V, Hildenhagen J, Dickmann K, Lehmkuhl T (1999) Laser-induced breakdown spectroscopy for on-line control of laser cleaning of sandstones and stained glass. Appl Phys A-Mater Sci Process 69:441–444
15. Kalaitzaki PM, Anglos D, Kilikoglou V, Zafiropulos V (2001) Compositional characterisation of encrustation on marble with laser induced breakdown spectroscopy. Spectrochim Acta B56:887–903
16. Kuzuya M, Murakami M, Maruyama N (2003) Quantitative analysis of ceramics by laser-induced breakdown spectroscopy. Spectrochim Acta B58:957–965
17. Degiacomo A, Dell'aglio M, Depascale O (2004) Single pulse-laser induced breakdown spectroscopy in aqueous solution. Appl Phys A-Mater Sci Process A79:1035–1038
18. Pu XY, Ma WY, Cheung NH (2003) Sensitive elemental analysis of aqueous colloids by laser-induced breakdown spectroscopy. Appl Phys Lett 83:3416–3418
19. Fichet P, Toussaint A, Wagner JF (1999) Laser-induced breakdown spectroscopy: a tool for analysis of different types of liquids. Appl Phys A-Mater Sci Process 69:S591–S592
20. Fichet P, Mauchien P, Wagner JF, Moulin C (2001) Quantitative elemental determination in water and oil by laser induced breakdown spectroscopy. Anal Chim Acta 429:269–278
21. Barbini R, Colao F, Lazic V, Fantoni R, Palucci A, Angelone M (2002) On board LIBS analysis of marine sediments collected during the XVI Italian campaign in Antarctica. Spectrochim Acta B57:1203–1218